TESIS DE LA UNIVERSIDAD DE ZARAGOZA

2021

368

Iván Coarasa Casas

ANAIS-112. Searching for the annual modulation of dark matter with a 112.5 kg NaI(Tl) detector at the Canfranc Underground Laboratory.

Director/es

Dr. D. Jorge Mario Puimedón Santolaria

Dr. D. Miguel Ángel Oliván Monge

ISSN 2254-7606

Prensas de la Universidad Universidad Zaragoza

ISSN 2254-7606

Universidad Zaragoza
1542

Tesis Doctoral

ANAIS-112. SEARCHING FOR THE ANNUAL MODULATION OF DARK MATTER WITH A 112.5 KG NAI(TL) DETECTOR AT THE CANFRANC UNDERGROUND LABORATORY.

Autor

Iván Coarasa Casas

Director/es

Dr. D. Jorge Mario Puimedón Santolaria
Dr. D. Miguel Ángel Oliván Monge

UNIVERSIDAD DE ZARAGOZA
Escuela de Doctorado

2021

ANAIS–112. Searching for the annual modulation of dark matter with a 112.5 kg NaI(Tl) detector at the Canfranc Underground Laboratory

Memoria presentada por

Iván Coarasa Casas

para optar al grado de

Doctor en Física

Grupo de Física Nuclear y Astropartículas
Área de Física Atómica, Molecular y Nuclear
Departamento de Física Teórica
Centro de Astropartículas y Física de Altas Energías (CAPA)
UNIVERSIDAD DE ZARAGOZA

Septiembre 2021

Contents

Preface

The main goal of this work is to contribute to the analysis of the first three years of ANAIS–112 data in the search for the annual modulation reported by the DAMA/ LIBRA experiment. Chapter 1 introduces the need for dark matter in the Universe, its evidences, and the strategies for its detection. Chapters 2 and 3 are mostly devoted to the description of the ANAIS experiment, its goals, history and the experimental performance over the three years, as well as the review of the filtering protocols currently used by ANAIS–112 in its publications. In these chapters, the analysis of the modulation in the rate of muons crossing the ANAIS–112 veto system and the estimation of the radon content in the air filling the inner volume of the ANAIS–112 shielding are original contributions, likewise, this work has also taken part in the calculation of the efficiency of the event selection procedures. The main body of this PhD dissertation is gathered in Chapters 4, 5 and 6. In Chapter 4, the sensitivity prospects of the experiment in the short and long term have been evaluated taking into account different sources of uncertainty and considering various background scenarios. The analysis of the three years of exposure of ANAIS–112 searching for the annual modulation effect is presented in Chapter 5. Finally, Chapter 6 is dedicated to the development and application of a new procedure for filtering low-energy noise events based on machine learning techniques to three years of data.

Chapter 1

Introduction

According to the latest data released from the Planck satellite, the Universe is spatially-flat, with an accelerated expansion, and is composed of 69% dark energy and 26% non-baryonic dark matter [1]. Despite the consistency between these results and the standard cosmological model (see Section 1.1), the nature of dark matter still remains one of the most puzzling questions in Fundamental Physics today.

There exists a large amount of cosmological and astrophysical observations from gravitational interactions between baryonic and a new form of non-luminous matter at very different length scales (see Section 1.2), which supports the existence of dark matter in the Universe. The most compelling solution to the dark matter enigma requires the existence of some new non-zero-mass elementary particle beyond the Standard Model which is expected to be electrically neutral, uncoloured, weakly-interacting with baryonic matter and stable. Many candidates have been proposed to constitute the galactic dark matter, but axions and Weakly Interacting Massive Particles (WIMPs) are the preferred [2] (see Section 1.3).

Different experimental strategies have been applied in order to detect the elusive dark matter particles (see Section 1.4). They are based on the direct detection, by searching for interactions of dark particles with the nuclei of a convenient detector; indirect searches, by identifying the products of the dark matter annihilation in the galactic halos or galaxy clusters; and production at colliders, by observing events with missing transferred momentum and energy after the collision of very energetic ordinary particles [3].

In spite of the wide experimental effort devoted to the understanding of the dark matter nature, no unequivocal answer has been reported until now. Only the DAMA/LIBRA experiment, which uses NaI(Tl) crystal detectors at the Gran

Sasso National Laboratory (LNGS) in Italy, has provided a long-standing positive result [4–7]: the observation of a highly statistically significant annual modulation in the detection rate, which is compatible with that expected for galactic halo dark matter particles. This result has neither been reproduced by any other experiment, nor ruled out in a model independent way. For years, the most plausible scenarios have been ruled out by results obtained in other experiments with different target materials and detection techniques, like those from CDMS [8], CRESST [9], EDELWEISS [10], KIMS [11], LUX [12], PICO [13] or XENON [14] collaborations.

The ANAIS (Annual modulation with NaI Scintillators) experiment [15] (see Chapter 2) is intended to search for dark matter annual modulation with ultrapure NaI(Tl) scintillators at the Canfranc Underground Laboratory (LSC) in Spain. Its main goal is to provide a model independent confirmation or refutation of the annual modulation positive signal reported by DAMA/LIBRA using the same target and technique, but different experimental conditions. ANAIS–112 consisting of 112.5 kg of NaI(Tl) detectors was installed in 2017 at the LSC, and data taking started on the 3^{rd} of August 2017. After 5 years of measurement, ANAIS–112 can test the DAMA/LIBRA result in a model independent way at 3σ confidence level (C.L.), having a significant discovery potential if the modulation signal is effectively due to dark matter particles [16] (see Chapter 4). There are also other projects which share the ANAIS goal, such as the COSINE–100 experiment, taking data at Yang-Yang Underground Laboratory (Y2L) in South Korea since the end of September 2016 [17], and, in the longer-term, the SABRE project, aiming at installing twin detectors in Australia and Italy [18], the COSINUS project, which is developing cryogenic detectors based on NaI [19] and PICOLON project, which is working in the development of highly radiopure NaI(Tl) scintillators after several recrystallisation processes [20].

1.1 The Standard Model of Cosmology

Human understanding of the Universe has evolved significantly over time. From geocentric models, which placed the Earth as the center of the Universe, to the heliocentric model proposed by Nicolaus Copernicus in the 16^{th} century, which suggested that the Earth and the other planets of the Solar System orbited around the Sun. But it was not until the early 20^{th} century that the Milky Way was dicovered to be a small drop in the enormous universe. The development of Einstein's Theory of General Relativity in 1915, coupled with high-precision observation carried out during the last decade of the past century, led to the birth of modern cosmology.

Cosmology aims to provide a description of the largest-scale structures and global dynamics of the Universe, allowing study fundamental issues about its origin, structure, evolution and ultimate fate. Currently, the model that best describes the Universe is the so-called Lambda-Cold Dark Matter (ΛCDM) or concordance model [21–25]. It is based on the Cosmological Principle, which states that the Universe is statistically homogeneous and isotropic in space and matter at sufficiently large scales ($\gtrsim$100 Mpc), and assumes that the Universe presents four fundamental components: dark energy (represented by the cosmological constant Λ), non-baryonic cold dark matter (CDM), ordinary matter (baryons and leptons) and radiation (photons, neutrinos).

The ΛCDM model is commonly referred as the Standard Model of Cosmology, due to its simplicity and great predictability. The overwhelming success of the model lies in explaining a wide spectrum of cosmological observations, such as the accelerating expansion of the Universe [26, 27], the power spectrum and statistical properties of the Cosmic Microwave Background (CMB) anisotropies [28], the spectrum and statistical properties of large scale structures of the Universe [23, 29] and the observed abundances of different light elements [30–33].

The first evidence that the Universe is expanding came from Edwin Hubble in 1929 [34, 35]. Hubble's experimental observations revealed that galaxies are moving away in all directions at velocities directly proportional to their distance from the Earth and from each other following the Hubble-Lemaître's law:

$$v = H_0 r \tag{1.1}$$

being H_0 the Hubble's parameter, v the galaxy velocity and r its distance to the observer. In 1931, Georges Lemaître proposed that if the evident expansion of the Universe was projected back in time, it meant that the Universe was smaller, until at some finite time in the past when the mass of the whole Universe would have been concentrated on a single point, what he called the primeval atom or cosmic egg [36, 37].

During the 1940s, and based on the Lemaître's hypothesis, George Gamow and his collaborators, Ralph Alpher and Robert Herman, formulated the Big Bang theory [38–41]. This theory assumes that the early Universe was once so hot and dense enough which allowed primordial nucleosynthesis. Furthermore, the Big Bang model predicted the presence of a relic background radiation with a temperature of order a few K [42, 43]. The discovery of the CMB radiation by Arno Penzias and Robert

Wilson in 1964 [44] was soon identified as the relic radiation from the epoch of recombination or photon decoupling in Big Bang cosmology, singling out the Big Bang model as the prime candidate to describe the Universe.

Recombination occurred about 380000 years after the Big Bang, when the Universe was at a temperature of some 3000 K, allowing the formation of neutral atoms. The Universe, consisted of a highly-ionized plasma effectively opaque to electromagnetic radiation, changed into a gas of neutral atoms, transparent to photons. After this photon decoupling from matter, radiation traveled freely through the space, being redshifted by the expansion of the Universe, and constituting what is observed nowadays as CMB. This radiation, in the microwave frequency range, follows a blackbody spectrum, corresponding today to a temperature of 2.72548 ± 0.00057 K [45].

Both Hubble-Lemaître's law and the CMB radiation are two strong observational evidences for the homogeneity and isotropy of the Universe. The condition of a homogeneous and isotropic space requires the description of the spacetime by the Friedmann-Lemaître-Robertson-Walker (FLRW) metric in comoving coordinates. This geometry is specified by a curvature parameter k and a time-dependent scale factor $a(t)$. The unknown quantities k and $a(t)$ are to be determined by the matter/energy sources through the Einstein field equations, which in the ΛCDM model frame, are applied to the physical system of the cosmic fluid [24, 46–48]. The FLRW line element expressed in terms of the comoving coordinates is:

$$ds^2 = g_{\mu\nu}dx^\mu dx^\nu = -c^2dt^2 + a^2(t)\left[\frac{dr^2}{1-kr^2} + r^2\left(d\theta^2 + \sin^2\theta d\phi^2\right)\right], \tag{1.2}$$

where $g_{\mu\nu}$ is the metric tensor and $x^\mu = (ct, r, \theta, \phi)$. The possible values of the curvature parameter k are $+1$, 0 or -1 for a closed, spatially flat or open Universe, respectively.

The Einstein equations relate the geometry of the spacetime on one side and the mass/energy distribution on another:

$$R_{\mu\nu} - \frac{1}{2}Rg_{\mu\nu} + \Lambda g_{\mu\nu} = \frac{8\pi G}{c^4}T_{\mu\nu}, \tag{1.3}$$

being $R_{\mu\nu}$ the Ricci curvature tensor, $R = g^{\mu\nu}R_{\mu\nu}$ the scalar curvature or Ricci scalar, Λ the cosmological constant, G the Newtonian gravitational constant and

$T_{\mu\nu}$ the energy-momentum tensor. This tensor can be written in the form:

$$T_{\mu\nu} = \left(\rho + \frac{P}{c^2}\right) u_\mu u_\nu + P g_{\mu\nu} \tag{1.4}$$

for a perfect fluid (without shear stress, viscosity or heat conduction), with u_μ the four-velocity of the fluid element, P the pressure and ρ the density.

The Einstein equations with the FLRW metric and ideal fluid source leads to the basic set of cosmic equations called the Friedmann equations. The time component of the Einstein equations becomes the first Friedmann equation and the spatial component (unique by isotropy) leads to the second Friedmann equation:

$$H^2(t) \equiv \left(\frac{\dot{a}}{a}\right)^2 = \frac{8\pi G}{3}\rho - \frac{kc^2}{a^2} \qquad\qquad \frac{\ddot{a}}{a} = -\frac{4\pi G}{3c^2}\left(\rho c^2 + 3P\right) \tag{1.5}$$

with ρ the total matter and energy density of the Universe and $H(t)$ the Hubble's parameter, being $H(t_0) = H_0$ its present value. Contributions to this density coming from matter, radiation and dark energy or vacuum energy, with $\rho_\Lambda = \frac{\Lambda c^2}{8\pi G}$. The temporal evolution of the density can be derived from them:

$$\dot{\rho} c^2 = -3\left(\rho c^2 + P\right)\frac{\dot{a}}{a} \tag{1.6}$$

Assuming a perfect fluid model for the Universe, the equation of state that relates the pressure to the density is defined as:

$$P_i = \omega_i \rho_i c^2, \tag{1.7}$$

where i represents the matter, radiation, dark energy or any other component contributing to the energy density of the Universe. Combining Equations 1.6 and 1.7 and integrating by separation of variables, the temporal evolution of the energy density for each component results:

$$\rho_i(t) \propto a(t)^{-3(\omega_i+1)} \tag{1.8}$$

For matter $\omega = 0$, for radiation $\omega = 1/3$ and for dark energy two different models are possible: $\omega = -1$, corresponding to a cosmological constant, or, more generally, any $\omega < -1/3$ value, being possible a time dependence $\omega(t)$.

The first Friedmann equation 1.5 can be used to define the critical density, ρ_c, which corresponds to the energy density setting $k = 0$ (flat Universe) and $\Lambda = 0$:

$$\rho_c = \frac{3H_0^2}{8\pi G}, \tag{1.9}$$

in such a way that $\rho > \rho_c$ corresponds to a closed Universe, $\rho = \rho_c$ to a flat Universe and $\rho < \rho_c$ to an open Universe.

The critical density can be used to define a dimensionless density parameter as the energy density relative to critical density, indicating the contribution of each component to the Universe energy:

$$\Omega_i = \frac{\rho_i}{\rho_c} \tag{1.10}$$

The curvature term can also be absorbed into a curvature energy density $\rho_k = -\frac{3}{8\pi G}\frac{kc^2}{a^2}$, being for this case $\sum_i \Omega_i = 1$.

The Standard Model of Cosmology has been very successful in presenting a self-contained picture of the composition and evolution of the Universe. It explains the expansion and cooling of the Universe after the Big Bang, the formation of the light nuclear elements, and how matter congealed to form stars, galaxies and clusters of galaxies, after the inclusion of the proper density inhomogeneity in an expanding universe. Although the model describes very well the aftermath of the Big Bang, it is not able to explain the nature of the Big Bang itself, such as the origin of matter or the assumption of certain very precise initial conditions. These remaining questions can be solved by introducing an inflationary period, as proposed by Alan Guth in 1981 [49]. During this period of cosmic inflation, the Universe would have expanded sharply by increasing the scale factor by more than 30 orders of magnitude, and matter and radiation would have been created virtually from nothing. Afterwards, the Universe followed an adiabatic expansion and cooling as described by the FLRW metric. In addition, assuming an epoch of extraordinarily rapid expansion for the Universe allows to solve the flatness and horizon problems.

During the last thirty years, high-precision cosmological observations have allowed to test the ΛCDM model and determine its six independent (free) parameters. In particular, the six basic cosmological parameters are: the current baryon ($\Omega_b h^2$) and cold dark matter ($\Omega_c h^2$) densities times h^2, where $H_0 = 100h$ km/s/Mpc; the sound horizon at last scattering (θ_{MC}); the reionization optical depth (τ); the primordial

comoving curvature power spectrum amplitude (A_S); and finally, the scalar spectrum power-law index (n_S). In order to estimate these parameters, especially interesting are the measurements of the CMB anisotropies taken by the Planck satellite [1], with a higher precision than its predecessor WMAP [50, 51]. Table 1.1 summarizes the present status of the estimates of the six parameters of the cosmological model, combining information from Planck CMB power spectra, CMB lensing reconstruction and Baryon Acoustic Oscillations (BAO).

Parameter	Symbol	Planck+lensing+BAO
Fit parameters:		
Baryon density today ($\times h^2$)	$\Omega_b h^2$	0.02242 ± 0.00014
Cold dark matter density today ($\times h^2$)	$\Omega_c h^2$	0.11933 ± 0.00091
Approximation to the acoustic scale angle ($\times 100$)	$100\theta_{MC}$	1.04101 ± 0.00029
Reionization optical depth	τ	0.0561 ± 0.0071
Primordial scalar fluctuations amplitude	$\ln(10^{10} A_S)$	3.047 ± 0.014
Scalar spectrum power-law index	n_S	0.9665 ± 0.0038
Derived parameters:		
Hubble parameter (km s^{-1} Mpc^{-1})	H_0	67.66 ± 0.42
Age of the Universe (Gyr)	t_0	13.787 ± 0.020
Dark energy density today	Ω_Λ	0.6889 ± 0.0056
Matter density today	Ω_m	0.3111 ± 0.0056
Spatial curvature density today	Ω_k	0.0007 ± 0.0019

Table 1.1: *Fit parameters: Fitted values for the ΛCDM model parameters (68% C.L.) from Planck CMB power spectra, in combination with CMB lensing reconstruction and BAO. Derived parameters are obtained from the former. From Ref. [1].*

According to these results, and based on the Standard Model of Cosmology, the total mass-energy budget of the Universe is about: 69% of unknown dark energy, 26% of non-baryonic dark matter and 5% of ordinary matter, being negligible the present contribution from the radiation. A more detailed analysis on the CMB anisotropies supporting that the Universe has a large amount of non-baryonic, beyond the Standard Model, cold dark matter is covered in Section 1.2.3. Finally, a flat Universe ($\Omega_k \approx 0$) in accelerated expansion is also supported by observational data.

1.2 Dark matter evidences

The term "dark matter" was firstly used in 1922 by Jacobus Kapteyn in order to explain measurements of the dynamics of stars in the Milky Way [52], although it did not have the modern connotations of an unknown and new type of matter, but referred to any non-luminous astronomical objects. The first evidence correctly attributed to the existence of dark matter comes from 1933, when, studying the Coma cluster, Fritz Zwicky observed a discrepancy between the visible matter and the total matter of the cluster [53]. Using the virial theorem, he found that the gravitational attraction of the visible stars and gas was not sufficient to explain the unexpected high velocity of the galaxies on the edge of the cluster. Since then, a large amount of observations have arosen that point to the existence of dark matter at very different scales, from galactic to cosmological scales.

1.2.1 Galaxy rotation curves

On the galactic scale, one of the most strongest evidences for dark matter existence comes from studying the galactic rotation curves, first measured by Vera Rubin in 1975 [54].

According to Newtonian mechanics, the rotational velocity of bodies bound to a galaxy (stars, gas clouds) at a distance r from the galactic center can be expressed as:

$$v(r) = \sqrt{\frac{GM(r)}{r}} \tag{1.11}$$

if a spherical mass distribution $M(r)$ is assumed for the galaxy, and being G the Newtonian gravitational constant. For distances that extend beyond the galactic disk ($r \gtrsim R_{disk}$), Gauss' Law supports that $M(r)$ should remain constant assuming all the mass is concentrated in the disk, and the velocity is expected to decrease as $v(r) \sim 1/\sqrt{r}$. On the contrary, Vera Rubin's observations indicated that rotation velocities of stars in galaxies stayed approximately constant at these distances (see Figure 1.1), implying that $M(r) \sim r$. The existence of a dark matter halo, extending much farther than the visible matter in the disk and whose density profile varies with the distance in such a way that $v(r) = cte$, is the most extended explanation of these rotation curves (see e.g. Ref. [55]).

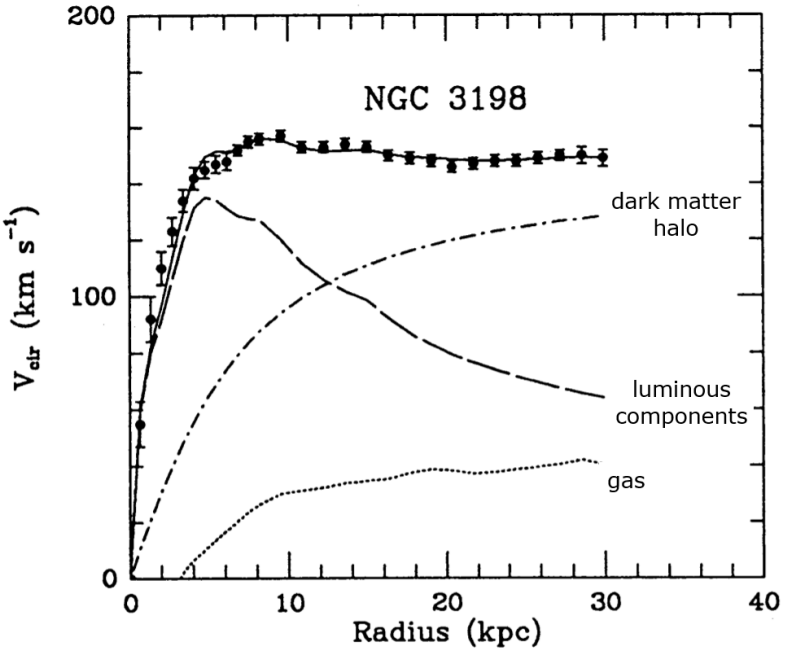

Figure 1.1: *Example of galactic rotation curve. The rotation velocity contributions of the individual components are also shown: the dotted, the dashed and the dashed-dotted lines correspond to gas, luminous components and dark matter halo, respectively. From Ref. [56].*

1.2.2 Gravitational lenses and galaxy clusters

On the scale of galaxy clusters, measurements of the velocity dispersion of galaxies constituted the first evidence of the existence of unseen matter whose contribution to the total mass of the cluster was much greater than that of visible matter. In addition to using the virial theorem to determine the mass of a cluster (as Zwicky did with the Coma cluster in 1933), there are other methods such as studying the profile of X-ray emission that traces the distribution of hot emitting gas in rich clusters, or analyzing the gravitational lensing effect. In particular, X-ray measurements reveal that the temperature of the hot gas observed in the galaxy clusters cannot be explained by considering only the gravitational attraction due to visible matter of the clusters. Regarding gravitational lenses measurements, based on the deflection of the observed light coming from a distant source when there exists a large amount of mass between the source and the observer, they also confirm the existence of an enormous quantity of unseen matter in clusters [57, 58]. As a result of the gravitational lensing effect, multiple images of the source are obtained (see Figure 1.2).

Figure 1.2: *Gravitational lensing effect in galaxy cluster 0024+1654 (picture taken by Hubble Space Telescope in 1996). The blue, loop-shaped objects are multiple images of the same galaxy, duplicated by the gravitational lens of the cluster of yellow, elliptical and spiral galaxies near the photograph's center. From Ref. [58].*

The most direct observational evidence to date for dark matter comes from a system known as the Bullet cluster [59, 60]. In most regions of the universe, dark matter and visible matter meet together, due to their mutual gravitational attraction. However, in the Bullet cluster, a collision between two galaxy clusters appears to have caused a separation of dark matter and baryonic matter (see Figure 1.3). X-ray observations show that much of the baryonic (gas) matter in the cluster is concentrated in the center of the system (in pink in the figure). Electromagnetic interactions between the gas particles caused them to slow down and settle near the point of impact of those galaxies. Nevertheless, weak gravitational lens observations of the same system show that most of the mass resides outside the central baryon gas region (in blue). Since dark matter does not interact electromagnetically, it would not have been slowed down like gas visible by X-rays, so the dark matter components of the two clusters would pass each other without being substantially slowed, being further apart than those of baryonic gas. This accounts for the separation. Unlike galactic rotation curves, this evidence for dark matter is independent of the details of Newtonian gravity, thus it is claimed to be direct evidence for the existence of dark matter.

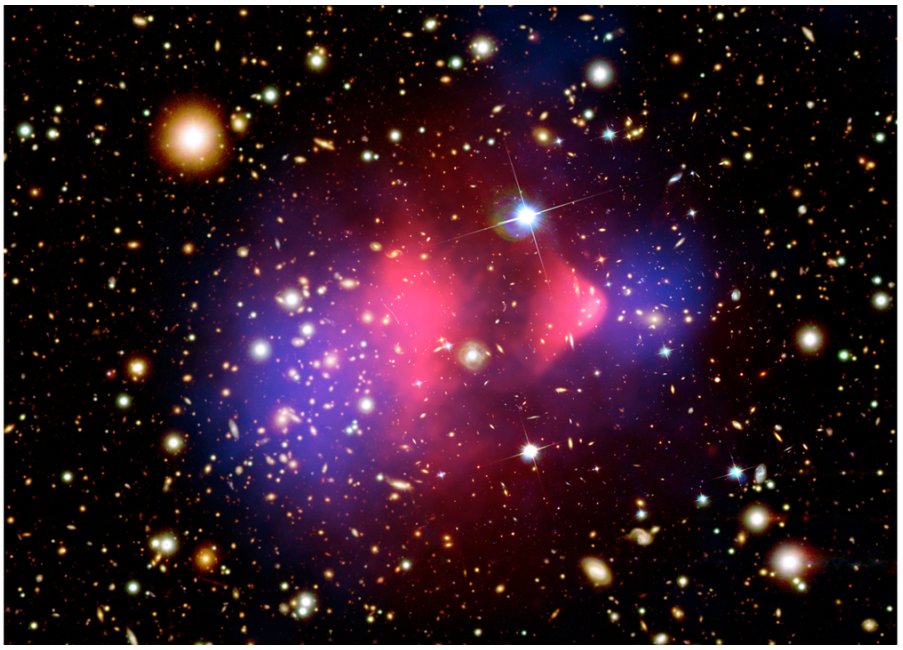

Figure 1.3: *Composite image of the Bullet cluster (1E 0657-556). Hot gas detected by Chandra X-ray telescope (in pink) is superimposed on the optical image of the galaxies from Magellan and Hubble Space Telescope (in orange and white). The mass distribution deduced by gravitational lensing is shown in blue. From Ref. [61].*

1.2.3 CMB anisotropies

The total amount of dark matter in the Universe cannot be determined on the scales of galaxies or galaxy clusters, but requires accurate observations on the cosmological scale. More specifically, this information can be extracted from the analysis of the CMB anisotropies [62, 63].

The first measurement of the CMB inhomogeneities came from the NASA's COBE (Cosmic Background Explorer) satellite in 1992 [64]. These are very small temperature variations, at 10^{-5} level. Since then, there has been intense activity to map the sky at increasing levels of sensitivity and angular resolution. NASA's second-generation satellite, WMAP (Wilkinson Microwave Anisotropy Probe), which was taking data for nine years (2001–2010) at 20 times better resolution than COBE, detected the polarization of the CMB photons for the first time [28, 50, 51]. The last complete (and most accurate) map of the CMB fluctuations is drawn by the European Planck satellite (see Figure 1.4) [65]. This map represents the temperature distribution of the early Universe at the time of recombination: the red dots, hottest on average; the blue spots, colder. In that plasma, the hottest areas were also the densest, so the temperature map is also a density map of the early Universe.

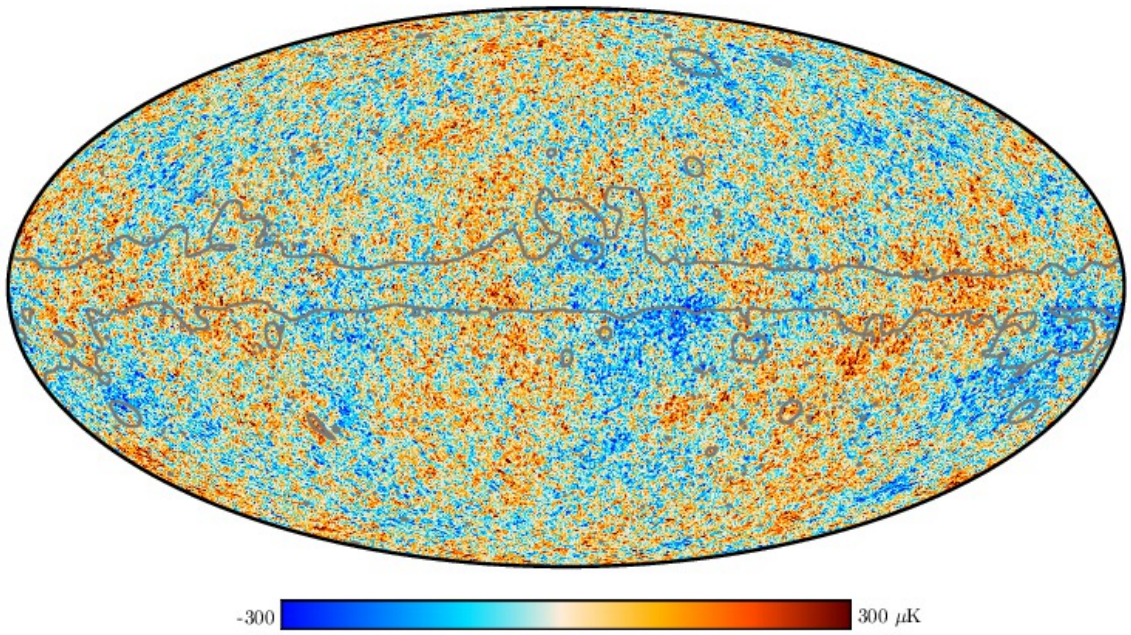

Figure 1.4: *Full-sky map of the small CMB temperature anisotropies over an average temperature of 2.725 K. The grey lines/contours show the position of the microwave emissions in the Milky Way and local structures, which have been removed from the data. From Ref. [65].*

The analysis of the temperature map is performed by expanding the angular distribution of the anisotropies of T as a function of spherical harmonics:

$$\frac{\Delta T}{T}(\theta, \phi) = \sum_{\ell m} a_{\ell m} Y_{\ell m}(\theta, \phi) \tag{1.12}$$

One of the most interesting observables obtained from the analysis is the power spectrum, in which the magnitude usually represented is $\mathcal{D}_\ell = \ell(\ell+1)C_\ell/(2\pi)$, where $C_\ell = \frac{1}{2\ell+1}\sum_m |a_{\ell m}|^2$ measures the amplitude of the multipole ℓ. Figure 1.5 shows the comparison between the measured power spectrum of the CMB temperature anisotropy by Planck satellite and the predictions from the six-parameter concordance ΛCDM model using the best-fit parameter values (see Table 1.1), in terms of the angular scale. It can be observed that there is a very good agreement between the experimental data and the predictions of the ΛCDM model at high multipoles, being determined the acoustic peaks amplitude with an excellent accuracy. It is worth mentioning that the variations in the CMB temperature map associated with perturbations in the density of the early Universe are those with $\ell \geq 2$ multipole

value. The monopole component ($\ell = 0$) is considered to be the mean temperature of the CMB (2.72548 ± 0.00057 K), whereas the dipole ($\ell = 1$) is interpreted as the result of the Doppler shift caused by the motion of the Solar System relative to the nearly isotropic black-body field. The average temperature and the dipole pattern have been subtracted from the data shown in Figure 1.5 because they are not relevant to understand the perturbations in the density of the early Universe.

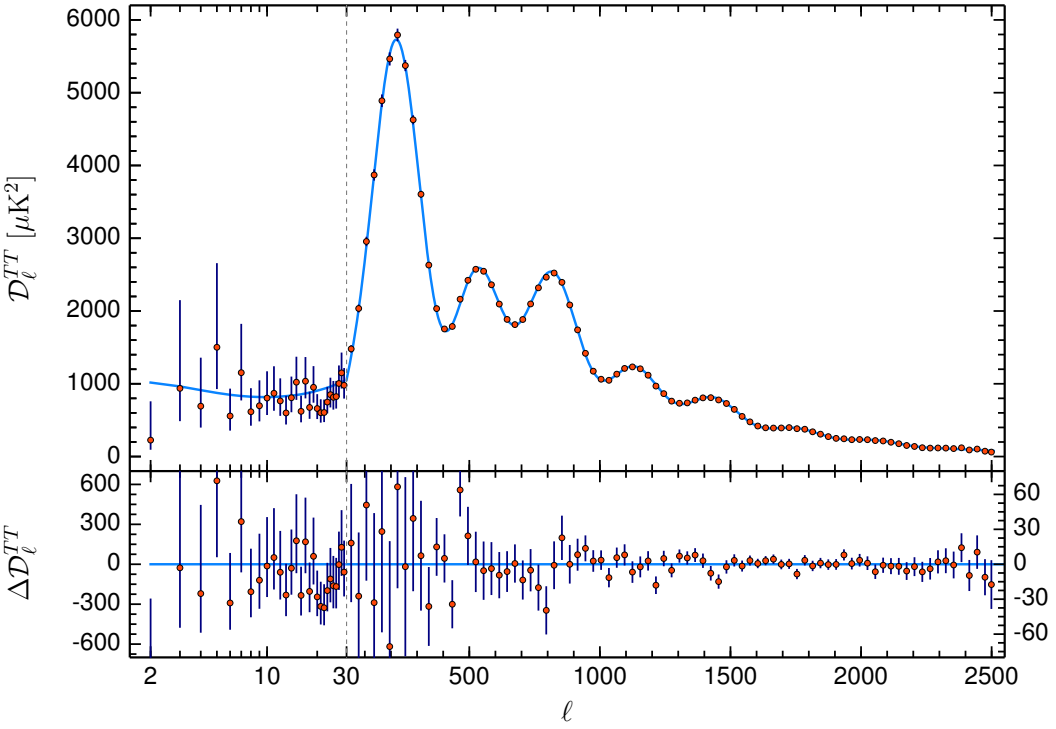

Figure 1.5: *Planck 2018 temperature power spectrum (orange dots) compared with the predictions of the ΛCDM cosmological model (blue line). Residuals are also shown. From Ref. [66].*

From the analysis of the height of the first two acoustic peaks in the power spectrum of the CMB anisotropy, it is possible to determine the amount of baryonic and non-baryonic matter present in the Universe. Thus, the height of the first peak is related to the total density of matter in the Universe, which results to be approximately 31% of the critical density. On the other hand, the height of the second peak is related to the amount of ordinary matter. And what follows from this height is that the density of baryonic matter is about 5% of the critical density. This means that the remaining 26% is a type of non-baryonic matter: dark matter (see Table 1.1 for present best fit parameters values).

In addition to temperature, it is also possible to perform a multipole expansion as indicated in Equation 1.12 for different polarization modes in the CMB photons. The corresponding power spectra are C_ℓ^E, C_ℓ^B and C_ℓ^{TE} for E-modes, B-modes and correlations between density and velocity perturbations at last scattering surface, respectively. Complementary model parameters constraints can be obtained by analyzing CMB polarization (see Ref. [66] for more information).

1.2.4 Big Bang nucleosynthesis and light elements abundances

Big Bang nucleosynthesis (BBN) is an essential ingredient in the study of the current composition of the Universe, since it provides an estimate of the density of baryons (Ω_b) independent of that supplied by the analysis of the CMB anisotropies.

In the first moments of the Universe, the temperature was of the order of $k_BT \sim 100$ MeV and the cosmic plasma was made of photons, neutrinos, electrons and positrons in thermal equilibrium, and of baryons. The charged-current weak interactions proceed sufficiently rapidily to maintain the neutron-proton ratio close to its equilibrium value, given by the Boltzmann factor: $(n/p)_{eq} = e^{-\Delta m/(k_BT)}$, where $\Delta m = m_n - m_p = 1.29$ MeV is the neutron-proton mass difference. As the Universe continues to expand and cool, the heavier neutrons are disfavored over the lighter protons and the n/p ratio decreases, initially following the equilibrium expression. Nevertheless, when the temperature drops below $k_BT \sim 0.8$ MeV, the weak interactions becomes too slow, the baryons decouple from the leptons, and the n/p ratio is frozen at a constant value. Simultaneously, neutrons and protons could combine to form deuterons ($n+p \rightleftharpoons D^+ + \gamma$), but they were immediately dissociated by the abundant and energetic photons from the background bath. This bottleneck to BBN remains until the temperature decreases even further below the deuteron binding energy (2.22 MeV), when the number of photons energetic enough to dissociate D is negligible. At that time ($k_BT \sim 80$ keV), the combination of protons and neutrons to form deuterons stopped the decay of free neutrons ($\tau_n \simeq 880$ s), when the n/p ratio was 1/7, launching primordial nucleosynthesis [31].

According to BBN, the fusion of protons and neutrons generated a large quantity of helium nuclei and smaller amounts of other light nuclei, such as deuterium, helium-3, and lithium-7. By solving the Friedmann equations and computing the forward and reverse nuclear reaction rates in the context of nuclear physics, it is possible to calculate what percentage of helium and other nuclei was formed in those first minutes. The abundance of a given nucleus is defined as the ratio of the

nucleus density to the baryon density, but since the latter is unknown (as baryons had non-relativistic velocities and were not in thermal equilibrium during BBN), the ratio of baryon number density to photon number density is used, which has been obtained from the CMB to be $\eta = 6.09 \times 10^{-10}$ [40]. Table 1.2 collects the theoretical predictions for the abundances of the light elements [24], in comparison with the observational values [40]. An excellent agreement for deuterium, ^{3}He and ^{4}He is found, whereas there is a large discrepancy for ^{7}Li: this is the well-known lithium problem [40, 67, 68], which could simply reflect difficulty in determining the primordial ^{7}Li abundance, or could be a sign of new physics. Figure 1.6 shows the elemental abundances as a function of the baryon-to-photon ratio, η, predicted by the standard model of Big Bang nucleosynthesis (the bands show the 95% C.L. range). The narrow vertical band represents the baryon density estimated from CMB, and results to be consistent with the BBN range for the value inferred from high-redshift D/H measurements and local ^{4}He determinations. The yellow boxes in Figure 1.6 show the observationally inferred primordial abundances with their associated uncertainties.

Primordial abundance	Theoretical	Observational
^{4}He/H	0.2473 ± 0.0003	0.2450 ± 0.0030
D/H	$(2.463 \pm 0.038) \times 10^{-5}$	$(2.569 \pm 0.027) \times 10^{-5}$
^{3}He/H	$(1.034 \pm 0.016) \times 10^{-5}$	$(1.1 \pm 0.2) \times 10^{-5}$
^{7}Li/H	$(5.376 \pm 0.352) \times 10^{-10}$	$(1.6 \pm 0.3) \times 10^{-10}$

Table 1.2: *Comparison between the theoretical predictions of the primordial abundances of light elements and their observational values.*

From the agreement between the abundance of light elements calculated from the BBN and the observations, it follows that the amount of ordinary matter is of the order of 5% and that, therefore, dark matter cannot be baryonic.

1.2.5 Alternatives to dark matter

Since all the observational evidence for the existence of dark matter comes from its gravitational interactions, over the years alternative theories based on the modification of the law of gravity have been proposed to explain these observations [69]. The leading alternative to dark matter is known as modified Newtonian dynamics (MOND) [70], and is able to explain the observed rotation curves of many spiral and

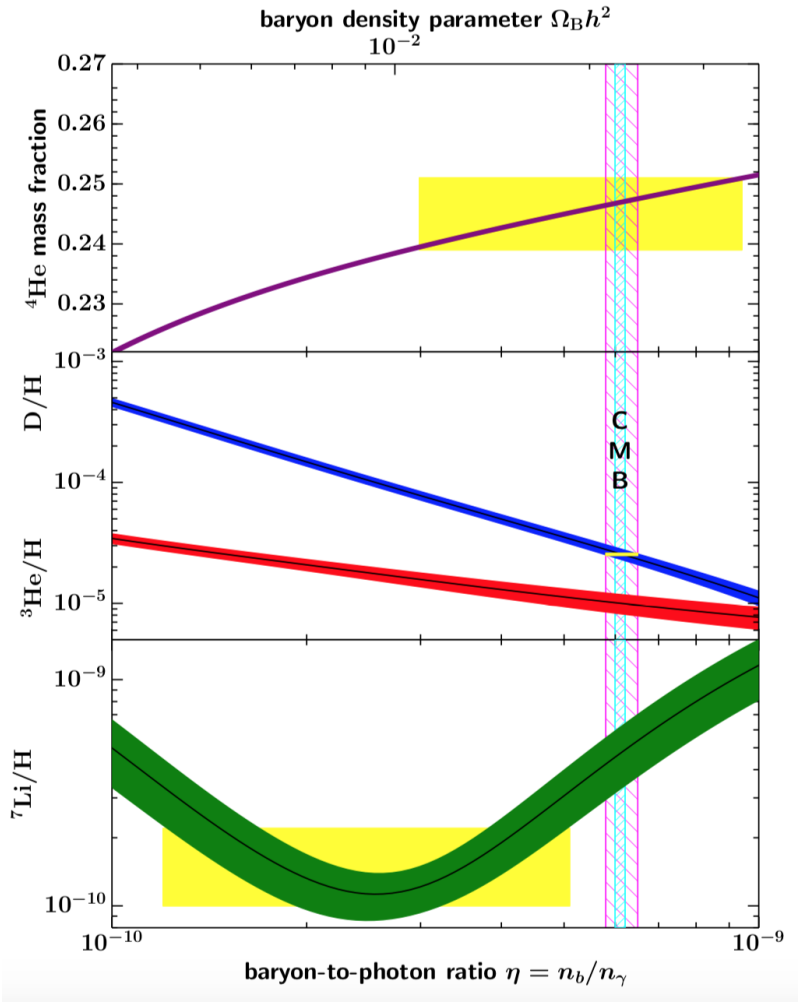

Figure 1.6: *The primordial abundances of ^{4}He, D, ^{3}He, and ^{7}Li as predicted by the standard model of BBN (the bands show the 95% C.L. range). Yellow boxes indicate the observed light element abundances. The narrow vertical band indicates the CMB measure of the cosmic baryon density, while the wider band indicates the BBN D+^{4}He concordance range (both at 95% C.L.). From Ref. [40].*

elliptical galaxies without postulating the presence of any dark or otherwise hidden matter, as well as the empirical Tully-Fisher formula, which relates the intrinsic luminosities and rotational velocities of spiral galaxies. However, MOND is not successful on the scale of galaxy clusters, requiring the incorporation of significant amounts of dark matter. To deal with the cosmological scale, a relativistic generalization of the theory was proposed: TeVeS (tensor-vector-scalar gravity) [71], but they have difficulties explaining the heights of the higher order peaks in the CMB temperature power spectrum [72, 73]. Another challenge is provided by the Bullet cluster, where X-ray observations and gravitational lensing reveal that the

dominant mass component is spatially separated from the baryonic mass (see Section 1.2.2). In summary, there is currently no modified gravity model that explain all the observational evidence for dark matter.

1.3 Dark matter candidates

Dark matter candidates must present a series of general properties in order to explain all the observational evidences described in Section 1.2. From primordial nucleosynthesis and CMB data, it is deduced that dark matter consists of non-baryonic material. In addition, dark matter has to be cold, that is, non-relativistic at the onset of galaxy formation, allowing the gravitational growing of structures at the scales observed in the Universe. Non-baryonic cold dark matter particles are also required to be weakly interacting with ordinary matter, electrically neutral, massive and stable or very long-lived on cosmological timescales [74].

The only particle in the Standard Model of Particle Physics that could partially satisfy the properties described for dark matter would be the neutrino. However, ordinary neutrinos were relativistic particles at the time of decoupling (hot dark matter), so they could not produce as many small scale structures as observed in the Universe. Cosmological observations and simulations are incompatible with neutrinos being the only particle composing dark matter.

After ruling out the neutrino as the unique candidate to compose dark matter, the search for candidates beyond the Standard Model becomes necessary. A plethora of candidates have been proposed to form dark matter, spanning 90 orders of magnitude in mass, ranging from ultralight bosons (fuzzy dark matter) to massive Primordial Black Holes (PBHs). Among the preferred candidates are axions and WIMPs. Both are well-motivated candidates because they were proposed to solve other problems in particle physics unrelated to dark matter, and their properties can be calculated from a well-defined model of particle physics [74–76].

- **Axions**. Axions were first introduced by Peccei and Quinn in 1977 as a solution to the strong CP problem in QCD (quantum chromodynamics) [77], which would predict an electric dipole moment for the neutron about 10^{10} larger than the current limit [78]. They are only a suitable dark matter candidate in a small mass range, from about 1 μeV to 1 meV. Several constraints from laboratory searches and astrophysical observations restrict the axion mass to be less than 3 meV [2]. Nevertheless, more general axion-like particles (ALPs)

could be viable dark matter candidates for any mass up to ∼1 eV. Its detection is usually based on the Primakoff effect, or axion-to-photons conversion in the presence of very strong electromagnetic field. Among the different experimental strategies, it is worth highlighting axion haloscopes, dedicated to measure the coupling of cold dark matter axion or ALPs, such as the Axion Dark Matter Experiment (ADMX) [79, 80]; and axion helioscopes, which look for axions or ALPs that might be produced in the Sun, such as the CAST (CERN Axion Solar Telescope) experiment [81] or the next-generation IAXO (International Axion Observatory) helioscope [82].

- **WIMPs**. Weakly Interacting Massive Particles have been the most attractive candidate to form dark matter since they were proposed by Steigman and Turner in 1985 [83]. They are defined to be particles that would interact with Standard Model particles via weak nuclear force, with a mass range between 10 GeV and 1 TeV. These particles with weak interaction cross section and mass in the range of hundreds of GeV naturally provide a candidate for cold dark matter, whose primordial abundance (in the early Universe) would be in agreement with the currently observed abundance of dark matter. This feature of WIMPs is called the "WIMP miracle". The most popular and theoretically well-motivated example of framework containing a paradigmatic WIMP is the supersymmetric (SUSY) extension of the Standard Model [84]. Although SUSY was initially developed to solve the hierarchy problem, WIMPs are obtained as byproduct. The simplest supersymmetric extension to the Standard Model is the Minimal Supersymmetric Standard Model (MSSM). MSSM gives naturally superpartners for every Standard Model particle: every boson has a fermion partner, and vice versa. The lighest neutralino in the MSSM, i.e., the lowest-mass eigenstate of the supersymmetric partners of neutral Standard Model gauge bosons, is a good and natural dark matter candidate. Nevertheless, most of the parameter space of natural simple SUSY models is essentially ruled out. In the absence of evidence from supersymmetry, and leaving naturalness behind, WIMPs have evolved into a more general class of particles that would have reached the appropiate relic density through self-annihilation. In this wider context, the expected mass range for WIMPs extends from 10 MeV to 100 TeV [75, 76]. Other non-supersymmetric WIMP models include universal extra dimensions models [85], in which the lighest Kaluza-Klein particle emerges as a candidate for dark matter. The different experimental strategies followed for the detection of WIMPs are widely covered in Section 1.4.

Other plausible candidates for dark matter are sterile neutrinos and primordial black holes.

- **Sterile neutrinos**. Sterile neutrinos emerge as a gauge-singlet (likely with right-handed chirality) in an extension of the Standard Model. They are called sterile because they do not interact with the electroweak force, apart for the mixing with the ordinary neutrinos. Their mass range varies between keV and MeV. Although the lifetime of sterile neutrinos must be greater than the age of the Universe to be a candidate for dark matter, some of them may have decayed through various channels. Particularly interesting from an observational perspective is the radiative decay mode to one neutrino plus a photon, leading to a source of mono-energetic photons with energy close to half of the sterile neutrino mass. Recently, an unidentified emission line at 3.5 keV in the X-ray spectra of galaxy clusters has been reported, which might be a hint of the decay of sterile neutrinos with a mass of $\sim$7 keV, although the debate on the origin of this line is still ongoing [76, 86].

- **PBHs**. Primordial Black Holes are thought to originate from gravitational collapse of large density fluctuations in the early Universe. Since they formed in the radiation-dominated era, before BBN, PBHs are effectively non-baryonic. Although the calculation of their lifetime depends on the details of the gravitational collapse, if their mass is greater than $5 \cdot 10^{11}$ kg, their lifetime is longer than the age of the Universe. Several constraints from gravitational waves (recently discovered in binary black holes [87, 88]) in combination with the dynamical heating of dwarf galaxies, supernova lensing, distortions of the CMB, and radio and X-ray emission due to the accretion of interstellar gas onto PBHs keep Primordial Black Holes as viable candidates to form all dark matter or to be a subdominant component. Definitely, PBHs remain a suitable candidate for cold dark matter, despite not being elementary particles [74, 76, 89].

1.4 Dark matter detection

Different experimental approaches are followed in order to detect the elusive dark matter particles: direct detection, indirect detection and production at colliders. Indirect searches are based on the detection of annihilation products of dark matter particles, such as gamma rays, neutrinos, antiprotons and positrons. Direct search attempts to detect nuclear recoils produced by the elastic scattering of dark matter particles in the target nuclei of the detector. Finally, experiments at colliders search for dark matter production in high energy particle collisions. These experimental strategies are complementary to one another, and a schematic representation of the interplay between them is shown in Figure 1.7.

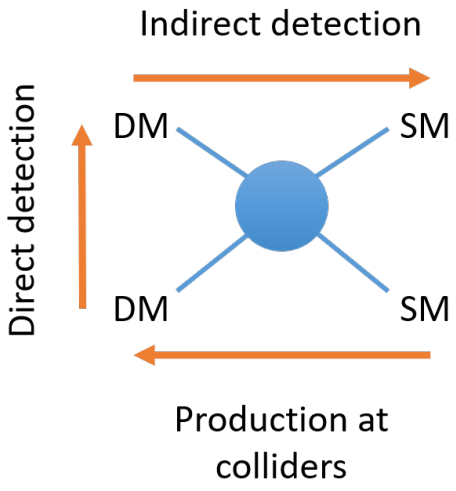

Figure 1.7: *Schematic view of the three different dark matter detection channels.*

Dark matter searches at the Large Hadron Collider (LHC) are briefly described in Section 1.4.1, indirect searches are detailed in Section 1.4.2 and the relevant aspects and results of direct detection are covered in Section 1.4.3.

1.4.1 Dark matter production at LHC

Since the LHC began operating at CERN in 2008, the two multipurpose detectors ATLAS [90] and CMS [91] have searched for new particles in proton-proton collisions at an unprecedented center-of-mass energy (7 TeV during 2010-2012 and 13 TeV during 2015-2018). In order to detect the presence of dark matter, these experiments exploit two similar analysis techniques [92, 93]:

- **Mono-X searches**. They are based on the production of a dark matter mediator by the annihilation of a pair of quarks or gluons, which subsequently decays into a pair of WIMPs that escape the experimental device undetected. The presence of such dark matter particles would be inferred by observing events with missing momentum and energy accompanied by a so-called mono-object (denoted by X: a high energy jet, a photon or a leptonically decaying Z or W boson) which has generally been produced as initial state radiation.

- **Mediator searches**. They are based on the decay of the dark matter mediation into a pair of quarks or leptons, producing a localized excess of events (resonance) in the invariant mass spectrum, or in specifically chosen angular distributions.

ATLAS and CMS experiments have not found significant discrepancies with regard to Standard Model predictions; therefore, their results can be interpreted as limits on the coupling of dark matter mediators to Standard Model particles or as limits on the masses of the mediator and the dark matter particles. Comparison between these results and those from direct detection experiments shows that collider searches are competitive especially for low dark matter particles masses, although this comparison is strongly dependent on the choice of the couplings between dark matter and Standard Model particles [93].

1.4.2 Indirect dark matter detection

Indirect dark matter detection is based on observing the radiation produced when dark matter particles annihilate or decay. WIMPs are expected to self-annihilate into primary Standard Model particles, such as W^+W^-, $\mu^+\mu^-$, $\tau^+\tau^-$, $b\bar{b}$, etc, which subsequently decay and lead to energetic cosmic rays, such as gamma rays, neutrinos, positrons or antiprotons. Since the fluxes of annihilation and decay products are proportional to dark matter density (quadratically and linearly for annihilation and decay processes, respectively), the largest number of particles is expected to come from astronomical objects. In this sense, potential signatures are gamma rays from the Galactic Centre, neutrinos from the Sun's core, and positrons and antiprotons from the galactic halo [2].

Gamma rays

Due to their charge neutrality, gamma rays propagate almost unperturbed and pointing directly to the source where they were produced. They are relatively easy to detect, but can be affected by absorption in the interstellar medium and their background can be large. The direct observation of gamma rays is carried out with gamma-rays telescopes on space, being able to point to the source with great accuracy (about 0.1° for single photons above 10 GeV in Fermi-LAT [94]). However, higher-energy gamma rays must be detected indirectly with ground-based Cherenkov telescopes [95] like MAGIC [96], H.E.S.S. [97] or VERITAS [98] (above about 100 GeV). Some intriguing excesses of gamma rays over the expected astrophysical flux in the few GeV region have been reported by several experiments, for instance, the Fermi-LAT excess from the Galactic Centre [99, 100], but they remain unconfirmed until now. In addition to this, such excesses of gamma rays are in tension with the dwarf spheroid galaxies constraints [101], which are considered the most dark-matter-dominated objects known and provide the most stringent limits to

the dark matter annihilation cross section. The future Cherenkov Telescope Array (CTA) [102, 103] could significantly improve the sensitivity in this search.

Neutrinos

As gamma rays, neutrinos have also an unaffected propagation and therefore point to their source. Nevertheless, due to their extremely low cross section with ordinary matter, their detection is a real challenge, requiring large detectors and exposure times, or even having to correlate their detection with that of other dark matter messengers. Moreover, the angular resolution of neutrino detectors is limited, of the order of 1° for energies around 100 GeV, being less than one degree only for TeV energies, complicating their pointing in searches for relatively low-mass dark matter candidates. In spite of everything, neutrinos remain an attractive signature for dark matter searches because they do not lose energy or are absorbed through their propagation over cosmic distances, nor do they present a significant background source from astrophysical objects. The Sun and the Earth are two very promising sources of neutrinos from WIMPs annihilation. Looking inside the Sun, the comparison between the measured and expected neutrino flux could give information about the capture rate in the Sun or the elastic scattering cross section of dark matter particles with ordinary matter [95]. Large neutrino telescopes like IceCube [104], ANTARES [105] or Super-Kamiokande [106] are able to search for dark matter annihilations into neutrinos. Particularly interesting is the recent discovery of a high-energy cosmic neutrino flux by IceCube [107, 108], opening the door to different dark matter scenarios, specifically those related to annihilation or decay of very heavy dark matter particles (of the order of PeV). In the absence of confirming this evidence, very competitive constraints on the dark matter elastic cross section and on the proton and dark matter annihilation cross section are set by neutrino telescopes [95]. The next generation of neutrino telescopes like IceCube-Gen2 [109], KM3NET 2.0 [110] or Hyper-Kamiokande [111] could increase the sensitivity of indirect detection of dark matter.

Cosmic rays

Finally, cosmic-ray charged particles (like electrons, positrons, protons or antiprotons) can also be produced by the annihilation or decay of dark matter, but determining their source is a great challenge because they are strongly affected by the interstellar magnetic fields. Besides, charged particles can also lose energy during propagation through inverse Compton scattering or synchrotron radiation, therefore their observed energy spectrum can differ from the original one. Nevertheless,

the detection of some antimatter particles could be an indication of the presence of dark matter, since antimatter from astrophysical sources is relatively rare at the Earth. In any case, these antiparticles would come from nearby sources such as the Galactic Center or Halo due to their high probability of annihilation with ordinary matter. Measurements on the steadily increasing positron fraction from 10 GeV to 1 TeV by PAMELA [112] and AMS-02 [113] satellites have tried to be explained involving dark matter annihilations; however, conventional explanations based on positron production by astrophysical sources like pulsars or supernova remnants are also possible. In comparison to the other two techniques mentioned, cosmic rays also provide competitive results in the indirect search for dark matter [95].

1.4.3 Direct dark matter detection

Direct dark matter detection experiments aim to identify nuclear recoils produced by the collisions between dark matter particles and detector's target nuclei. The elastic scattering of WIMPs with masses in the 10–100 GeV would produce typical nuclear recoils energies in the range of 1–100 keV [114]. In order to unequivocally identify such low-energy interactions, a good understanding of the signal signatures is required, as well as fundamentals of particle and nuclear physics. In addition to this, radioactive ultra-low background conditions are mandatory to observe such feeble WIMP-matter interactions, so ultrapure detectors and underground facilities are essential for this type of experiments.

1.4.3.1 WIMP detection rate

The interaction rate of a WIMP in the detector is directly proportional to the number of target nuclei N_T ($= M_{det}/m_N$ for a detector with only one type of nucleus, being M_{det} the detector mass and m_N the nucleus mass), the number of WIMPs per unit volume $n_W = \rho_0/m_W$ (where ρ_0 is the local WIMP density in the galactic halo and m_W is the WIMP mass), its relative velocity with respect to the detector $\vec{v}$ and the cross section of the process σ_{WN}, which generally depends on the energy of the incident particle and of the transferred momentum. Therefore, considering the WIMPs velocity distribution in the detector's reference frame, $f(\vec{v})$, the differential interaction rate can be expressed as [114–116]:

$$\frac{dR}{dE_R} = \frac{\rho_0}{m_W}\frac{M_{det}}{m_N}\int_{v_{min}}^{v_{max}} v f(\vec{v})\frac{d\sigma_{WN}}{dE_R}(\vec{v}, E_R)d\vec{v}, \tag{1.13}$$

where E_R is the energy transferred to the recoiling nucleus and $d\sigma_{WN}/dE_R(\vec{v}, E_R)$ is the WIMP-nucleus differential cross section. The recoil energy of the nucleus

depends on the scattering angle θ^* (calculated in the center-of-mass reference frame) as:

$$E_R = \frac{p^2}{2m_N} = \frac{\mu_{WN}^2 v^2}{m_N}(1 - \cos\theta^*), \tag{1.14}$$

being p the momentum transfer and $\mu_{WN} = \dfrac{m_W m_N}{(m_W + m_N)}$ the WIMP-nucleus reduced mass. The minimum WIMP velocity needed to produce a recoil is:

$$v_{min} = \sqrt{\frac{m_N E_{th}}{2\mu_{WN}^2}}, \tag{1.15}$$

with E_{th} the energy threshold of the detector (the smallest recoil energy that the detector is able to measure); whereas the maximum velocity of the WIMP, v_{max}, is given by the escape WIMP velocity in the detector's reference frame (v_{esc}, given in the halo reference system). Thus, the total rate of observed events (usually calculated per mass unit of target and then, expressed in counts/kg/day) is computed by integrating Equation 1.13 from the threshold energy to the maximum recoil energy, E_{max}.

$$R = \int_{E_{th}}^{E_{max}} dE_R \varepsilon(E_R) \frac{\rho_0}{m_W} \frac{M_{det}}{m_N} \int_{v_{min}}^{v_{max}} v f(\vec{v}) \frac{d\sigma_{WN}}{dE_R}(\vec{v}, E_R) d\vec{v}, \tag{1.16}$$

where $\varepsilon(E_R)$ is the detection efficiency due to, for example, data cuts designed to reduce backgrounds, and which is typically energy-dependent. The maximum recoil energy $E_{max} = 2\mu_{WN}^2 v_{esc}^2 / m_N$ is given by kinematics and it is usually less relevant than E_{th}.

Input from particle and nuclear physics

Additional assumptions on the specific particle physics model and the involved nuclear physics processes have to be made in order to interpret dark matter experiments data. Using Fermi's Golden Rule, the WIMP-nucleus differential cross section can be divided into two terms: one independent of the momentum transfer and the other $F^2(p)$ (known as the form factor), which arises from the finite size of the nucleus, containing the entire dependence on the momentum transfer. Apart from this, the WIMP-nucleus differential cross section can be generally separated

into a spin-independent (SI) contribution and a spin-dependent (SD) one:

$$\frac{d\sigma_{WN}}{dE_R} = \left(\frac{d\sigma_{WN}}{dE_R}\right)_{SI} + \left(\frac{d\sigma_{WN}}{dE_R}\right)_{SD} = \frac{m_N}{2\mu_{WN}^2 v^2}\left[\sigma_0^{SI} F_{SI}^2(E_R) + \sigma_0^{SD} F_{SD}^2(E_R)\right], \tag{1.17}$$

where σ_0^{SI} and σ_0^{SD} are the SI and SD components of the WIMP-nucleus cross sections at zero momentum transfer, and F_{SI} and F_{SD} are the corresponding form factors. The relationship between the transferred momentum and the energy is given by kinematics, such that: $p = \sqrt{2m_N E_R}$.

Spin-independent. For spin-independent WIMP interactions, this nuclear point-like cross section can be expressed as:

$$\sigma_0^{SI} = \frac{4\mu_{WN}^2}{\pi}\left[Z f_p + (A - Z) f_n\right]^2. \tag{1.18}$$

Here Z is the number of protons, $A - Z$ is the number of neutrons, and f_p and f_n are the effective WIMP couplings to protons and neutrons, respectively. A usual simplification so as to compare the results of experiments using different target nuclei is to consider that $f_p = f_n$, and define the WIMP-nucleus cross section in terms of the WIMP-nucleon cross section:

$$\sigma_0^{SI} = \left(\frac{\mu_{WN}}{\mu_{Wn}}\right)^2 A^2 \sigma_{SI}, \tag{1.19}$$

with $\mu_{Wn} = \dfrac{m_W m_n}{m_W + m_n}$ the WIMP-nucleon reduced mass (being $m_n = 0.939$ GeV the mass of a nucleon), A the mass number of the target nucleus and $\sigma_{SI} = \frac{4\mu_{Wn}^2 f_n^2}{\pi}$ the spin-independent WIMP-nucleon cross section.

The nuclear form factor is calculated as the Fourier transform of the nuclear mass density function. A usual choice for the SI form factor is the analytical approximation of Helm [117] using the dimensionless parameter $x = pr_n/\hbar$:

$$F_{SI}(x) = \frac{3\left(\sin x - x\cos x\right)}{x^3} e^{-(xs)^2/(2r_n^2)}, \tag{1.20}$$

where $s = 0.9$ fm is a measure of the nuclear skin thickness and $r_n^2 = (1.23A^{1/3} - 0.60)^2 + \frac{7}{3}(0.52\pi)^2 - 5s^2$ is an effective nuclear radius (in fm) [114]. F_{SI} is only relevant for WIMP targets with high mass numbers $A \gtrsim 100$ and at high recoil energies E_R.

Spin-dependent. For spin-dependent WIMP interactions, the nuclear point-like cross section can be written as:

$$\sigma_0^{SD} = \frac{32\mu_{WN}^2}{\pi} G_F^2 \frac{J+1}{J} \left(a_p \langle S_p \rangle + a_n \langle S_n \rangle\right)^2 . \tag{1.21}$$

Here, G_F is the Fermi coupling constant, J is the total nuclear spin, a_p and a_n are the effective WIMP couplings to protons and neutrons, respectively, and $\langle S_{p,n} \rangle = \langle N|S_{p,n}|N\rangle$ are the expectation values of total proton and neutron spin operators in the limit of zero momentum transfer in the target nucleus (N), and must be estimated using detailed nuclear model calculations.

Input from astrophysics

The dark matter density in the Milky Way and its velocity distribution govern the expected signal for direct detection experiments, and thus are essential for the interpretation of the experimental results. Although its exact distribution has not yet been measured, it can be modelled taking into account the gravity-based observational evidence (see Section 1.2.1).

Standard Halo Model. The simplest model commonly used for the interpretation of direct detection experiments is the Standard Halo Model (SHM) [118]. The SHM assumes that the dark matter particles are distributed in an isotropic and isothermal sphere of collissionless particles with density profile $\rho(r) \sim 1/r^2$ and a Maxwellian velocity distribution truncated at some escape velocity v_{esc} [119]:

$$f(v) = \begin{cases} \dfrac{1}{N_{esc}} \dfrac{1}{v_0^3 \pi^{3/2}} e^{-v^2/v_0^2} & \text{if } v < v_{esc} \\ 0 & \text{otherwise} \end{cases} \tag{1.22}$$

where

$$N_{esc} = \text{erf}\left(\frac{v_{esc}}{v_0}\right) - \frac{2}{\sqrt{\pi}} \frac{v_{esc}}{v_0} e^{-(v_{esc}/v_0)^2} \tag{1.23}$$

is a normalization factor (being $\text{erf}(x) = \frac{2}{\sqrt{\pi}} \int_0^x e^{-t^2} dt$ the error function) and v_0 the most probable WIMP velocity, related with the root mean square velocity of such a distribution by $v_{rms} = \sqrt{3/2} v_0$. Typical values are: $v_0 = 220$ km/s, $v_{rms} = 270$ km/s and $v_{esc} = 650$ km/s. For distributions without an escape velocity ($v_{esc} \to \infty$), $N_{esc} = 1$; whereas, $N_{esc} = 0.9994$ for $v_{esc} = 650$ km/s.

Dark matter density. The precise shape of the density profile of the dark matter halo at the Galactic Center is unknown; however, it is irrelevant for direct dark matter detection experiments because all models give the same value for local density [116]. The local dark matter density ρ_0 can be estimated from the measured rotation curve of the Milky Way, resulting in $\rho_0 = 0.3$ GeV/c^2/cm^3 the common value adopted by direct detection experiments in pursuit of comparing their results.

Predicted signatures

The most usual approach in direct detection experiments consists in measuring the energy dependence of dark matter interactions. Considering the SHM, the differential rate expected by the interaction of a WIMP in the detector (Equation 1.13) can be written as:

$$\frac{dR}{dE_R} = \frac{R_0}{E_0 r} F^2(E_R) e^{-E_R/E_0 r}, \tag{1.24}$$

where R_0 is the total rate of events per unit mass, $E_0 = \frac{1}{2} m_W v_0^2$ is the most probable WIMP incident kinetic energy and $r = \frac{4 m_W m_N}{(m_W + m_N)^2}$ is a kinematic factor. Note that the escape velocity has not been taken into account in this expression. It can be seen that the shape of the nuclear recoil energy spectrum strongly depends on the mass of the nucleus via the nuclear form factor and also on the WIMP mass. For the sake of illustration, Figure 1.8 shows nuclear recoil spectra induced by a $m_W = 100$ GeV WIMP for several common target materials, assuming a spin-independent WIMP-nucleon cross section $\sigma_{SI} = 1 \times 10^{-47}$ cm^2. Even though the rate for SI interactions increases with A^2, the rate for heavy nuclei (Xe, in black) decreases at higher energies due to the nuclear form factor suppression. For extreme cases: if the WIMP mass is negligible compared to the mass of the target ($m_W \ll m_N$), $E_R \sim m_W^2$ and $dR/dE_R \sim m_W^{-2}$; whereas if $m_W \gg m_N$, the energy spectrum is independent of the WIMP mass. This implies that the WIMP mass can be more accurately determined when its mass is comparable to that of the target nucleus, and therefore, the use of different target materials can help to explore the mass range of WIMPs with greater sensitivity.

Detecting dark matter based on the shape of the energy spectrum is a great challenge, since it is a continuous spectrum that is indistinguishable from that produced by backgrounds. The main contributions to the background for direct dark matter detection experiments come from the environmental radioactivity, the internal radioactive contamination due to the presence of primordial isotopes in the detector

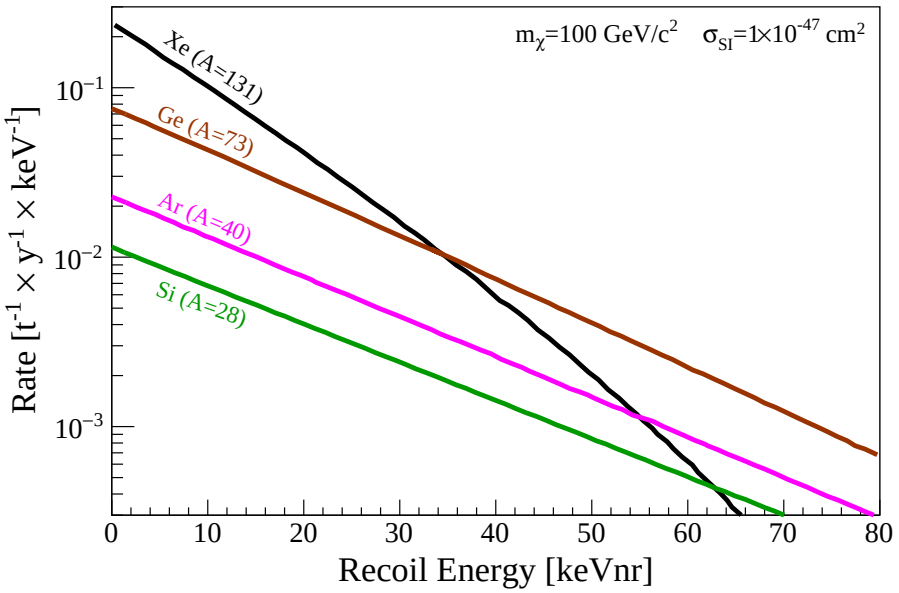

Figure 1.8: *Nuclear recoil energy spectra induced by a $m_W = 100$ GeV WIMP for several target materials considering $\sigma_{SI} = 1 \times 10^{-47}$ cm^2. From Ref. [116].*

construction materials, and finally, cosmic radiation and cosmogenic activation in the detector materials owing to previous exposure to cosmic rays. The ultimate limit in the background will come from the irreducible neutrino flux. Some background mitigation strategies (often summarised as "low-background techniques") are used in this kind of experiments in order to achieve as much sensitivity as possible [115, 116, 120].

- **External backgrounds**. The contribution of cosmic radiation can be greatly reduced by placing the detector in an underground facility. Although the hadronic component is easily suppressed by a few tens of meters water equivalent overburden, muons are more difficult to attenuate. The residual muon flux can directly produce events in the detectors and also secondary particles in the detector surroundings such as neutrons (so-called cosmogenic neutrons), which can produce keV nuclear recoils in elastic scatters with detector nuclei. In order to reduce this background, active veto detectors can be used to tag high-energy deposits by the original muon or its associated cascade. In addition to these cosmogenic neutrons, radiogenic neutrons can be produced from (α, n) reactions, where an α particle emitted by a radioactive decay, usually from the primordial decay chains, is absorbed by a nucleus and releases a neutron, or via spontaneous fission reactions in isotopes like ^{238}U and ^{235}U, present in the materials. A passive shielding based on water or dense materials

with high hydrogen content (e.g. polyethylene or paraffin) are typically used to moderate (and eventually absorb) neutrons. In order to minimize environmental gamma radiation coming from the decays in the natural uranium and thorium chains outside the experimental set-up, as well as from decays of common isotopes such as ^{40}K, ^{60}Co or ^{137}Cs present in the surrounding materials, a passive shielding composed of high-Z materials with low radioactivity content (typically lead and copper) is often used to enclose the detector. Finally, to reduce the γ-ray activity from airborne radon, the inner part of the detector shielding can be flushed with clean nitrogen or radon-free air.

- **Internal backgrounds**. The internal background of the detector materials is a very harmful contribution to the sensitivity. The isotopes more typically contributing to the background are: long-lived natural radioisotopes (^{232}Th, ^{238}U chains and their daughters; ^{40}K), cosmogenic activation isotopes (such as ^{3}H, ^{39}Ar) and anthropogenic isotopes (e.g., ^{60}Co, ^{85}Kr, ^{110m}Ag, ^{137}Cs). In order to minimize the internal radioactive contamination, all detector and target materials are selected in terms of their low radioactivity with various analytical methods, for instance, being previously screened by high purity germanium (HPGe) spectrometry. With regard to isotopes produced by cosmogenic activation due to previous exposure of detector materials to cosmic radiation, they can be reduced by minimizing the exposure time at surface and avoiding air transport. Finally, special care must be taken with ^{222}Rn (and daughters) deposit on surfaces, which can be removed by acid treating or electropolishing the surfaces.

Despite using the low-background techniques described above, the background of the direct detection experiments is still higher than expected from the interaction of dark matter particles (typically lower than 1 count/kg/year). Most of this background can be reduced with the implementation of active background rejection techniques during data analysis such as Pulse Shape Discrimination, volume fiducialisation if spatial information of events is available, or even the discrimination of nuclear from electronic recoils by measuring different observables (heat, light and charge) [121].

Differentiation between nuclear and electronic recoils events is possible due to their different energy-loss mechanisms. In particular, the amplitude of the electrical signal that is generated in a detector when a nucleus recoils with a certain energy is less than that corresponding to the recoil of an electron with equal energy (fewer electron-hole pairs are released in a semiconductor detector or fewer scintillation photons in a scintillator). In order to be able to compare the theoretical nuclear

recoils spectrum with the experimental spectrum, calibrated with electronic recoils, it is necessary to introduce a correction factor: the so-called Relative Efficiency Factor (REF) or quenching factor (Q), defined as the ratio between the pulses amplitudes of a nuclear recoil and an electronic recoil for the same energy deposition: $E_R(\mathrm{keV_{ee}}) = Q \cdot E_R(\mathrm{keV_{nr}})$. Unless otherwise stated, all energies present in this work are referred to electron equivalents ($\mathrm{keV_{ee}}$ or just keV). In view of the above, a precise knowledge of the quenching factor is mandatory for the correct calibration of the recoil energy for the experiments; however, over the years, different values and energy dependences have been reported for some targets, such as sodium and iodine for NaI(Tl) scintillators. Old measurements of quenching factor for NaI(Tl) scintillators reported energy-independent values of ∼0.3 for Na recoils and ∼0.1 for I recoils [122–125], whereas more recent measurements show smaller Q values for Na in the low-energy region and a strong energy dependence [126, 127] (see Figure 1.9). This result would imply an important shift in the WIMP parameter space region within reach of the ANAIS experiment, and consequently, a much better knowledge of this parameter is required to compare data from NaI(Tl) experiments and those from other targets. It is worth noting that quenching factors for ANAIS crystals have been recently measured at the Triangle Universities Nuclear Laboratory (TUNL), but data analysis is still ongoing. Lastly, Figure 1.10 shows the impact of quenching factor uncertainties in the expected rate of WIMPs for WIMP masses of 10 and 50 GeV, and assuming a spin-independent WIMP-nucleon cross section of $\sigma_{SI} = 1 \times 10^{-5}$ pb.

In addition to keeping the background as low as possible, other main characteristics that direct detection experiments must fulfill are: very low energy threshold, the accumulation of a large amount of target material, very long data taking periods and control of the stability of the environmental conditions as well as the operational conditions of the detector. Despite satisfying all these essentials, it would be very difficult to distinguish the hypothetical signal produced by a dark matter particle from that produced by a neutron. A distinctive behaviour must be searched for WIMPs that would allow a positive identification of a dark matter signal unambiguously. In particular, the Earth's motion through the galaxy induces both a seasonal variation of the total rate [118, 131] and a forward-backward asymmetry in a directional signal [132, 133]. As a result of the Earth rotation around the Sun, the velocity of the dark matter particles in the Milky Way halo relative to the Earth varies seasonally, producing an annual modulation of the rate of nuclear recoils in the detectors. Given its relevance to this work, this effect is analyzed in more detail in Section 1.4.4. An even stronger distinctive signature, which can be used to reduce backgrounds, is to exploit the fact that the motion of the Earth in the

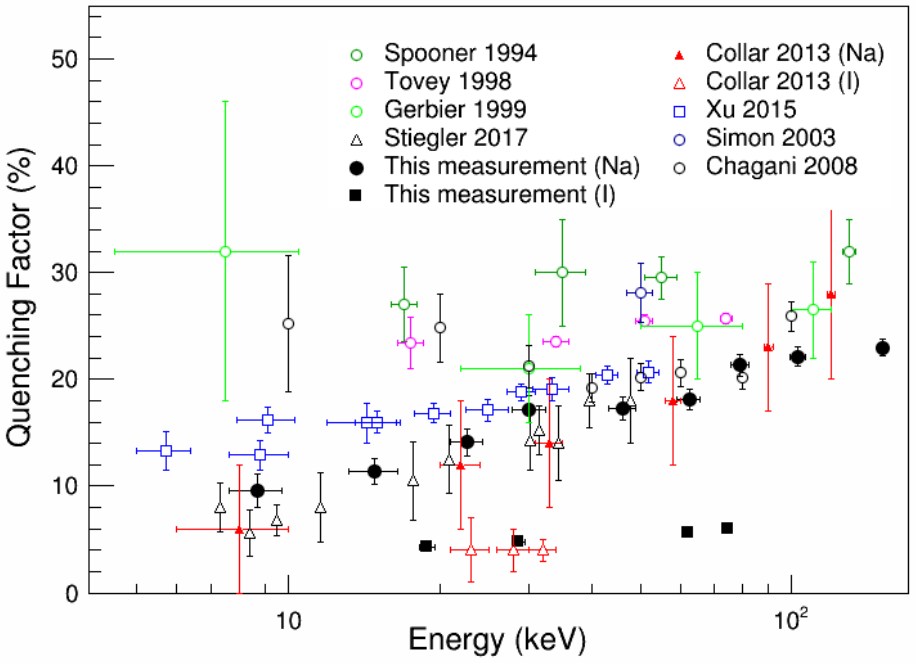

Figure 1.9: *Comparison of quenching factor values for Na and I recoils from different measurements. The closed black circles and squares labeled as "this measurement" refer to those obtained by the COSINE–100 collaboration for Na and I, respectively. From Ref. [127].*

Galaxy towards the Cygnus constellation causes the WIMP flux in the laboratory frame sharply peaked ("WIMP wind"), resulting in a higher rate of recoils from the direction of Cygnus. A detector capable of determining the direction of the WIMP-induced nuclear recoil would provide a powerful tool to confirm the detection of dark matter particles.

1.4.3.2 Direct detection technologies: status and future

As previously commented, direct dark matter detection experiments aim to detect nuclear recoils produced by the elastic scattering of dark matter particles. Such recoil energy of the detector's target nuclei can be observed through three different signals: by measuring the phonon excitations produced by the conversion of the kinetic energy of the scattering particles to lattice vibrations in solid targets (heat), by measuring the scintillation photons released after de-excitation of the target nuclei in scintillating materials (light) and by direct measurement of the ionization produced in the target atoms (charge). There are different experimental approaches depending on which observable is exploited, although the simultaneous measure-

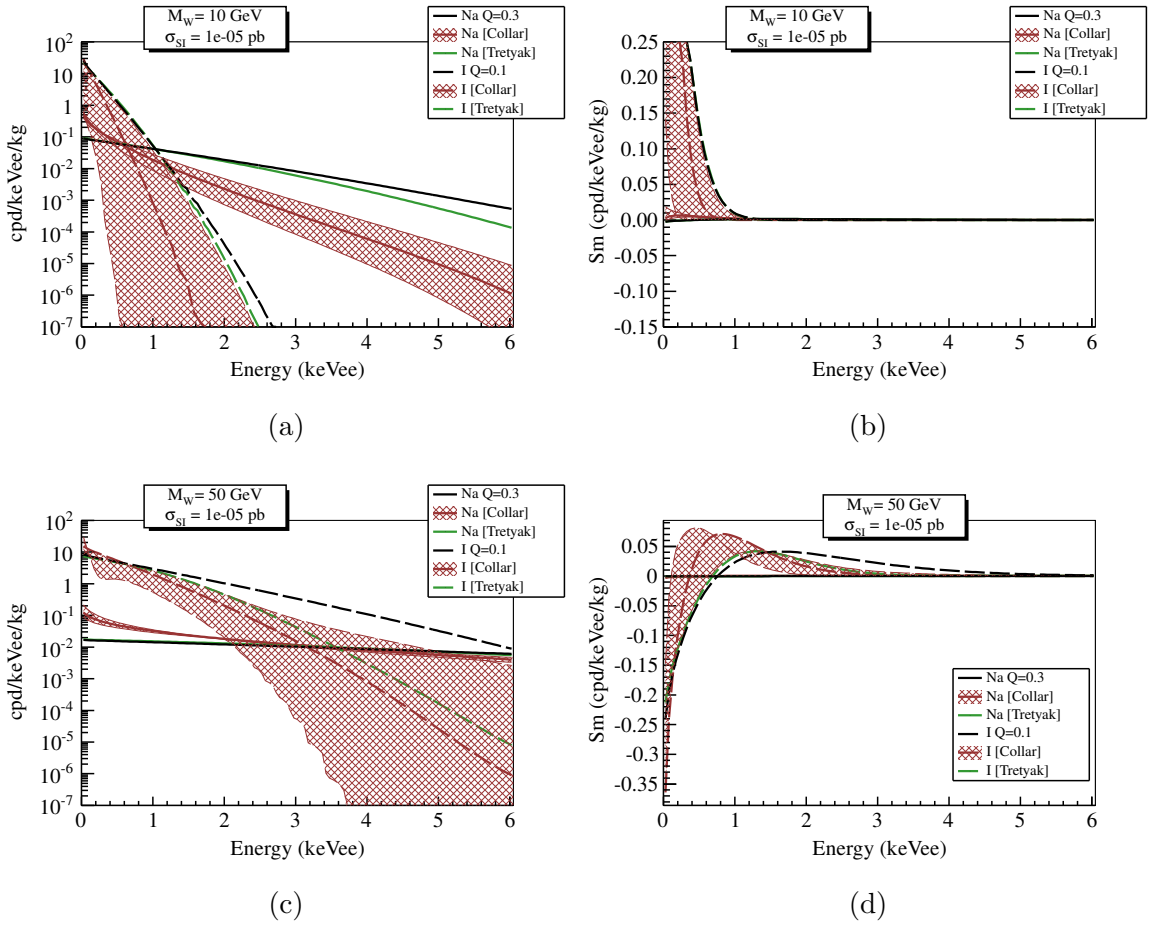

Figure 1.10: *Expected WIMP rates (left) and modulation amplitude (right) in NaI for WIMP masses of 10 GeV (top) and 50 GeV (bottom) assuming* $\sigma_{SI} = 1 \times 10^{-5}$ *pb and different values of Na and I nuclear recoils quenching factors, as reported in Ref. [126] (Collar) and Ref. [128, 129] (Tretyak). From Ref. [130].*

ment of two observables allows a powerful discrimination of nuclear recoils from electronic recoils, considerably reducing the background of the experiment. Figure 1.11 displays a scheme of the three signal channels, as well as the most common detector technologies. To date, there is no detector that measures all three channels simultaneously.

The main technologies used by direct dark matter detection experiments are described below, as well as the current status and future prospects of the most relevant experiments [74, 115, 116, 121, 134]. Negative results have been presented in most of the cases, but the comparison between the measured rate in the detector and the expected rate for a particular WIMP candidate and halo model, allows to rule out said candidate when the measured rate is lower than expected. Even though this exclu-

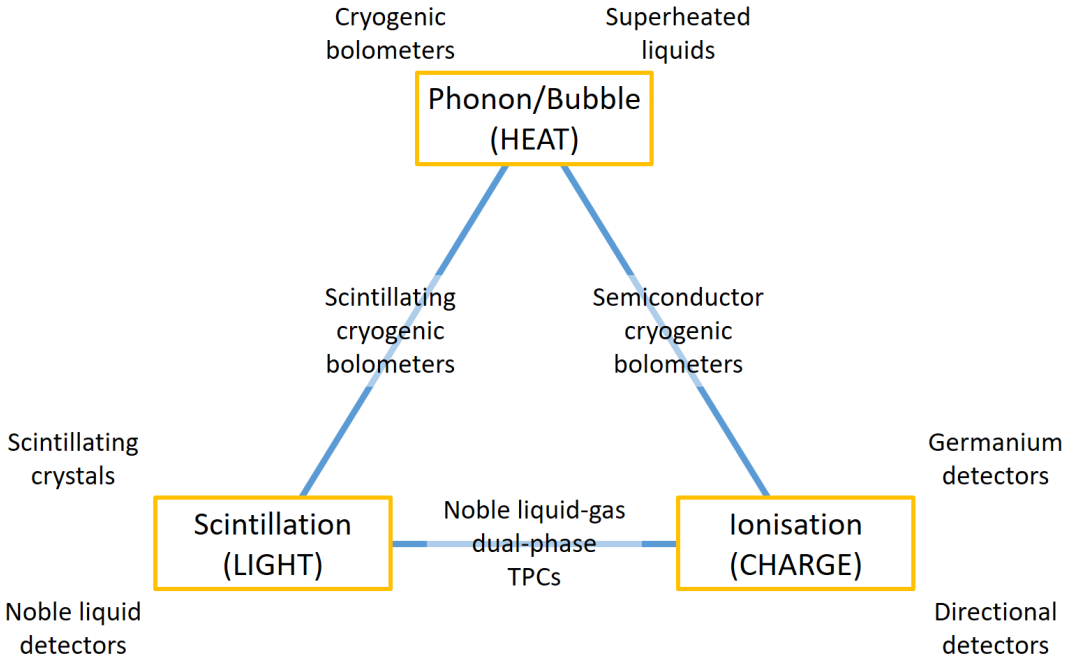

Figure 1.11: *Schematic view of the three signal detection channels together with the most common technologies used in direct detection experiments.*

sion is dependent on the specific model of halo and dark matter particle, it makes it possible to compare the results obtained by other experiments with different targets in terms of the so-called exclusion plots in the cross section-WIMP mass parameter space. Figure 1.12 shows the main recent experimental results and prospects for spin-independent interaction in the (σ_{SI}, m_W) plane, including the regions singled out by the DAMA/LIBRA positive signal.

Room temperature ionisation detectors

Silicon charge-coupled devices (CCDs) allow to explore low-mass WIMPs region. The charge generated by the interaction is drifted towards the pixel gates, until readout. The 3D position of any energy deposit can be reconstructed due to the correlation between the interaction depth and the lateral charge diffusion, leading to an effective particle identification for background rejection. The DAMIC (DArk Matter In CCDs) experiment [136, 137], consisting of 7 CCDs with a total mass of 40 g, has been operating at SNOLAB since 2017, reaching a leakage current of $2\ e^-/mm^2/day$ and 50 eV energy threshold. An excess of ionisation events above the analysis threshold has been observed from an exposure of 11 kg×day, but further investigation is required. Updated constraints on SI WIMP-nucleon cross section have

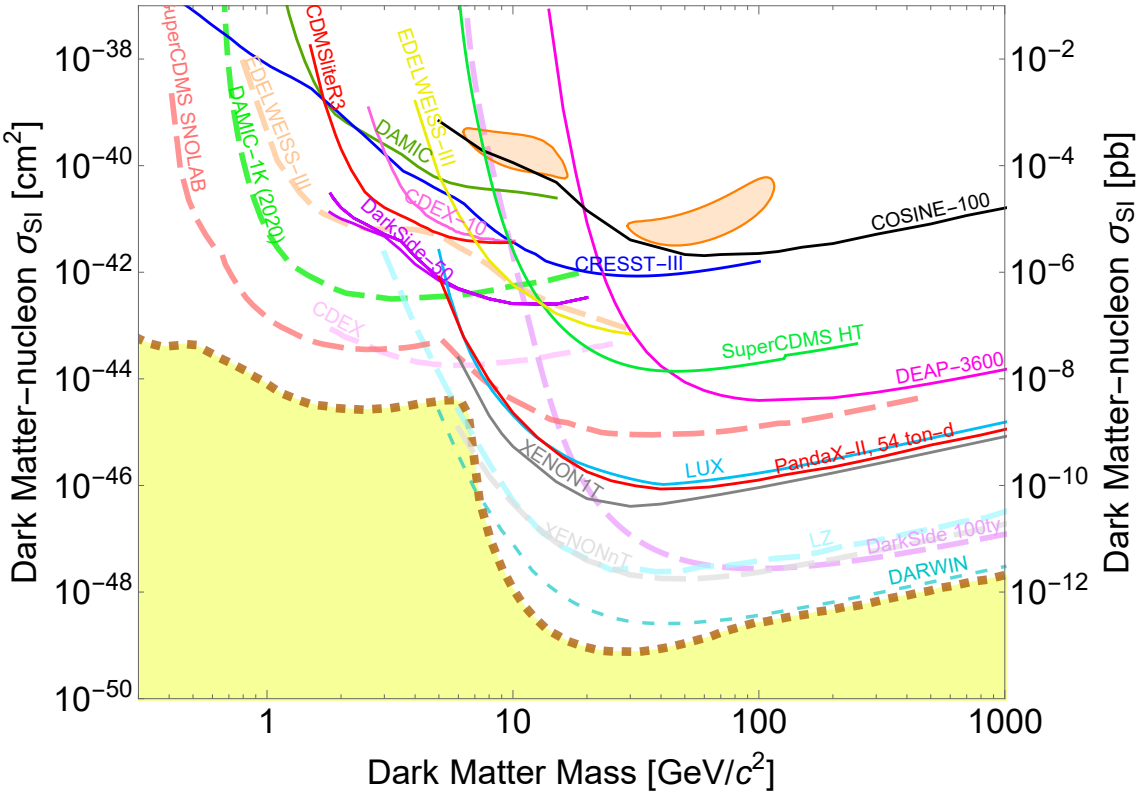

Figure 1.12: *Spin-independent exclusion plot with current limits (solid lines) and prospect projections (dashed lines) for the experiments mentioned in the text, generated using SuperCDMS Dark Matter Limit Plotter [135]. The orange shaded islands represent the positive signal reported by DAMA/LIBRA, whereas the lower yellow limit is the Solar neutrino floor with a xenon target.*

been obtained from these results [138]. The next phase of the experiment, DAMIC–M (DAMIC at Modane) [139], to be operated at the Modane Underground Laboratory (LSM) in France, will consist of an array of low-background 50-CCD array based on the Skipper CCD with a mass of 1 kg and a detection threshold of subelectron. DAMIC–M is now in preparation and commissioning is expected at 2023. Assuming an exposure of 1 kg×yr and an expected background of 0.1 c/keV/kg/d, DAMIC–M will explore SI WIMP-nucleon scattering at the GeV range with an unprecedented sensitivity. Furthermore, DAMIC–M will be able to probe WIMP-electron interactions for WIMP masses in the range of 1 MeV–1 GeV and hidden-sector dark matter candidates.

Room temperature scintillators

Scintillating crystals such as NaI(Tl) and CsI(Tl) can be used to detect dark matter particle interactions via the scintillation mechanism. After the interaction of a particle, the crystal is excited and the subsequent de-excitation releases scintillation light, which can be easily collected by photomultipliers (PMTs). The simplicity of this technology allows the detectors to operate stably for long periods of time and accumulate large amounts of target mass. Nevertheless, the shape of the scintillation pulse acquired by these detectors does not permit to discriminate nuclear recoils from electronic recoils at low energy, so achieving an ultra-low background is mandatory. The experiments using scintillators thus concentrate on exploiting the expected annual modulation signature induced by dark matter particles above a constant contribution from backgrounds and the much larger non-modulating WIMP signal fraction. By using ultrapure NaI(Tl) scintillators, the DAMA/LIBRA experiment at the LNGS in Italy has reported a long-standing positive result compatible with the dark matter annual modulation expected from the SHM (see Section 1.4.4.1). This modulation has been observed over a total of 20 annual cycles, with a total exposure of 2.46 t×yr and reaching a statistical significance of 12.9σ. This result has been excluded by other experiments using different targets or techniques, but the comparison of their results are strongly dependent of the dark matter model. Consequently, a similar annual modulation search using the same target is compulsory to solve the DAMA/LIBRA conundrum. Among the experiments seeking to confirm or refute the DAMA/LIBRA result in a model independent way are COSINE–100 (see Section 1.4.4.2) and ANAIS–112 (see Chapter 2), currently running, and SABRE, COSINUS and PICOLON, in preparation.

Solid-state cryogenic detectors

Germanium ionisation detectors operated at 77 K can reach sub-keV energy thresholds combined with excellent intrinsic radiopurity; however, the charge produced after particle interaction is unable to distinguish nuclear from electronic recoils. The current CDEX–10 (China Dark matter EXperiment) experiment [140], located at the China Jinping Underground Laboratory (CJPL) in China, is using an array of 3×3 p-type Point-Contact Ge detectors immersed in liquid nitrogen with a total mass of about 10 kg. First results from an exposure of 102.8 kg×day with an analysis threshold of 160 eV have been released, and constraints on both SI and SD WIMP-nucleon interactions have been derived. The preparation of future set-ups with significantly larger masses (100 kg in CDEX–100 and a ton-scale in CDEX–1T), devoted to both the search for dark matter and ^{76}Ge neutrinoless double beta

decay proccess, is underway [141].

Other experiments exploit the bolometer technique in combination with charge or light measurement. The main characteristic of bolometers is the conversion of the collected energy into a thermal signal (phonons). Since almost all the released energy is finally converted into heat independently of the interacting particle, non-quenched signal is obtained. These detectors must operate at extremely low temperatures, typically tens of mK or even below, in order to minimize thermal fluctuations, allowing to measure temperature increases of the order of μK.

Semiconductor cryogenic detectors measure simultaneously ionisation and heat signals, making the discrimination between nuclear and electronic recoils possible. The EDELWEISS (Expérience pour DEtecter Les WIMPs En SIte Souterrain) experiment [142], located at the LSM, uses cryogenic germanium detectors. EDELWEISS–III operated an array of 24 FID (Fully Inter-Digitized) cryogenic Ge detectors of 820–890 g each, equipped with two NTD (Neutron Transmutation Doped) Ge sensors for heat signal and aluminium electrodes for charge collection, reporting very good exclusion limits on SI interactions for WIMP mass from 5 to 30 GeV [143], as well as results on ALPs candidates [144]. The next phase of the experiment, EDELWEISS–SubGeV, plans to explore dark matter particles with masses in the range from eV to GeV via electronic or nuclear interactions [145].

The SuperCDMS (Cryogenic Dark Matter Search) experiment [146], placed at the Soudan Underground Laboratory in USA, has operated Si and Ge bolometers at the scale of hundreds of grams each. In 2016, SuperCDMS achieved world leading Ge-based WIMP dark matter constraints from about 1.5 to 250 GeV for both SI and SD interactions combining different analyses in high and low voltages regimes [147]. Recently, sub-MeV WIMP-electron constraints have been derived from the surface operation of very small Si crystals [148]. The next phase of SuperCDMS, at the Sudbury Neutrino Observatory Laboratory (SNOLAB) in Canada, will combine Si and Ge detectors with a total mass of about 30 kg, and is scheduled to start in mid-2021.

Scintillating cryogenic detectors detect simultaneously scintillation and heat signals. The double readout system allows to distinguish nuclear from electronic recoils. The CRESST (Cryogenic Rare Event Search with Superconducting Thermometers) experiment [149], located at the LNGS, uses scintillating bolometers of $CaWO_4$. CRESST–III operates 10 $CaWO_4$ crystals of 24 g each with an achieved energy threshold of 30.1 eV. This unprecedented threshold in combination with the

presence of oxygen in the target has allowed to set the best bounds for SI WIMP-nucleon interaction up to 160 MeV [9]. CRESST–III is planned to be upgraded to a second phase with 100 higher quality crystals with thresholds of the order of 10 eV, which would allow increasing the sensitivity several orders of magnitude.

Noble liquid detectors

The noble gases argon and xenon produced scintillation and ionisation signals after particles interaction inside them, and can be liquefied to build dense and compact dark matter targets. Ton-scale experiments filled with liquid noble gas target are being currently operated employing two different detection techonologies: single-phase and dual-phase. Nowadays, dual-phase xenon experiments are leading the SI WIMP-nucleon cross section limits for masses higher than ∼6 GeV.

Single-phase detectors. These detectors only measure the scintillation signal and consist typically of a spherical liquid noble target 4π-surrounded by PMTs. This arrangement can be used to reconstruct the interaction position with a typical resolution of a few cm. Since only the light is detected, background discrimination is performed by pulse shape discrimination (Liquid Argon, LAr) or via target fiducialisation (Liquid Xenon, LXe). The DEAP–3600 (Dark matter Experiment using Argon Pulse-shape discrimination) experiment [150], placed at SNOLAB, has achieved an excellent background rejection capability using a single-phase LAr detector with a total mass of 3.3 tons of argon, resulting in the best limit on the SI WIMP-nucleon interaction on a LAr target [151].

Dual-phase detectors, Time Projection Chambers (TPCs). Dual-phase (liquid and gas) TPCs enable to detect simultaneously the scintillation and ionisation signals generated by an energy deposition. After a particle interaction, the primary scintillation signal (called S1) is recorded by two arrays of PMTs on the top and bottom of the detector, and ionisation electrons released are drifted upwards to the gas phase where they generate a secondary light signal (S2) proportional to the charge. The charge-to-light signal ratio (S2/S1) can be used to distinguish electronic from nuclear recoils, and 3D event reconstruction is possible with spatial resolution at the order of mm. The XENON1T experiment [152], at the LNGS, has the best sensitivity to SI WIMP-nucleon interaction for masses above ∼6 GeV using a dual-phase LXe TPC with an active mass of 2.0 tons of xenon and accumulating 1 ton×yr exposure [14]. The next stronger limits on SI WIMP-nucleon cross section are those provided by the PandaX-II (Particle and Astrophysical Xenon Experiments) experiment [153], operating at CJPL using a dual-phase LXe TPC with an

active mass of 580 kg of xenon, and the already finished LUX (Large Underground Xenon experiment) experiment [154], at the Sanford Underground Research Facility (SURF) in USA, which utilised a dual-phase LXe TPC with an active mass of 250 kg of xenon. In the WIMP mass range from 1.8 to 3.5 GeV, the most stringent constraint for SI WIMP-nucleon interaction is given by DarkSide–50 [155], in operation at LNGS using a dual-phase LAr TPC with an active mass of about 46 kg of argon depleted in ^{39}Ar, with an accumulated exposure of 6786.0 kg×day. The next generation of liquefied noble gas detectors is expected to increase the sensitivity by 1–2 orders of magnitude. Among them XENONnT [156], PandaX–4T [157], LUX-ZEPLIN (LZ) [158] and DarkSide–20k [159] are in preparation, whereas the multi-tonne DARWIN (DARk matter WImp search with liquid xenoN) observatory [160] is at the design and R&D stage.

Superheated liquid detectors

Metastable superheated liquids are used as WIMP target in bubble chambers. The liquids are kept at a temperature just above their boiling point so that when an energy deposit occurs above some threshold, a bubble is created (bubble nucleation) that can be counted and localized with mm-precision by cameras. These detectors can be tuned in order that only nuclear recoil events will create bubbles. Target fluids with different composition can be operated at bubble chambers. Typically they are refrigerants and most of them contain the isotope ^{19}F, making them the detectors with the highest sensitivity to spin-dependent WIMP-proton couplings; but adding other heavy elements like iodine also offer good sensitivity to spin-independent interactions. The PICO–60 (the merger of PICASSO, Project In CAnada to Search for Supersymmetric Objects, and COUPP, Chicagoland Observatory for Underground Particle Physics) experiment [161], located at SNOLAB, has presented the best limit to date on SD WIMP-proton interactions using 52 kg of C_3F_8 with an accumulated exposure of 2571 kg×day. Some changes in the bubble chamber design have been implemented in the current PICO–40L experiment [162], which is taking data with 40 L of C_3F_8, and will also be used in the future PICO–500 experiment, which will utilise a ton-scale bubble chamber.

Directional detectors

As previously mentioned, due to the Sun's motion relative to the Galactic rest frame, the directional WIMP-induced nuclear recoil rate would be peaked around the opposite of the direction of Solar motion. Directional detectors are based on the

measurement of the direction of the recoiling nucleus, which would lead to the unambiguously confirmation of the Galactic origin of the signal. The nuclear recoil track reconstruction results very challenging because the range of WIMP-induced nuclear recoils is below 100 nm for energies less than 200 keV in liquid and solid materials. Nevertheless, the track length of these nuclear recoils is increased through the use of low pressure gases ($\sim$0.1 atm), allowing them to be resolved. The operation of the low pressure gases as target material is carried out in TPCs with different electron amplification devices and track readouts. Even though the full determination of the nuclear recoil direction would require recording both axis and sense, detecting the so-called head-tail asymmetry by measuring the relative energy loss along the track can also help improve sensitivity. Nowadays, directional detectors are not competitive in the search for dark matter due to their technological challenges. Among the pioneering experiments in the use of this technique is the DRIFT (Directional Recoil Identification From Tracks) experiment [163]. DRIFT operated at the Boulby Underground Laboratory in UK over more than a decade using 0.140 kg of CS_2+CF_4+O_2 mixture at a pressure of 55 mbar, deriving from 54.7 live-days the best limits for SD WIMP-proton interaction from directional detectors [164, 165]. Regarding the future of this technique, many groups working on directional dark matter detection have joined in the CYGNUS proto-collaboration with the aim of developing a multi-target and multi-site observatory capable of measuring the dark matter directionality and exploring the neutrino floor [166].

1.4.4 Annual modulation of dark matter

As discussed in the previous section, the detection of a distinctive dark matter signature such as annual modulation would imply an unequivocal identification of dark matter. Originally suggested in the 1980s [118, 131], the annual modulation signature exploits the effect of the Earth's revolution around the Sun on the number of events induced by the dark matter particles. In fact, as a result of its annual revolution, the Earth should be traversed by a larger number of dark matter particles around the 2^{nd} of June (when its rotational velocity is added to that of the Solar System relative to the Galaxy) and by a smaller number around the 2^{nd} of December (when the two velocities are subtracted) [167]. Figure 1.13 illustrates this effect.

Thus, the differential rate expected by the interaction of WIMPs does not depend only on the velocity distribution of the dark matter particles, but also on the Earth's velocity in the Galactic frame, $\vec{v}_E(t)$. The full expression for the differential interaction rate taking into consideration the SHM, the Earth's velocity and the Galaxy's

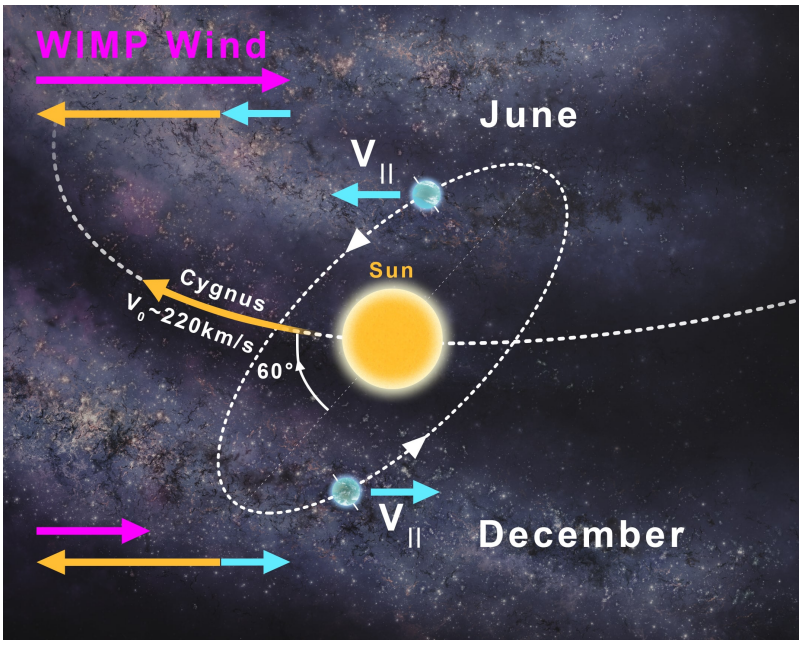

Figure 1.13: *Schematic representation of the Earth's rotation around the Sun as well as the Sun's rotation around the Galactic Center, resulting in a WIMP wind with a predictable variation of intensity throughout the year. From Ref. [168].*

escape velocity can be written as [114, 119, 169]:

$$\frac{dR}{dE_R}(E_R,t) = \frac{1}{N_{esc}}\frac{R_0}{E_0 r}F^2(E_R)\times\begin{cases}\Theta_1(E_R,t) & \text{if } v_{min}(E_R) < |v_{esc}-v_E(t)|\\ \Theta_2(E_R,t) & \text{if } |v_{esc}-v_E(t)| < v_{min}(E_R) < v_{esc}+v_E(t)\\ 0 & \text{if } v_{min}(E_R) > v_{esc}+v_E(t)\end{cases}$$

$$\Theta_1(E_R,t) = \frac{v_0\sqrt{\pi}}{4v_E}\left[\text{erf}\left(\frac{v_{min}+v_E}{v_0}\right)-\text{erf}\left(\frac{v_{min}-v_E}{v_0}\right)\right]-e^{-(v_{esc}/v_0)^2}$$

$$\Theta_2(E_R,t) = \frac{v_0\sqrt{\pi}}{4v_E}\left[\text{erf}\left(\frac{v_{esc}}{v_0}\right)-\text{erf}\left(\frac{v_{min}-v_E}{v_0}\right)\right]-\frac{v_{esc}+v_E-v_{min}}{2v_E}e^{-(v_{esc}/v_0)^2} \tag{1.25}$$

Here, $v_E(t)$ has been obtained by projecting $\vec{v}_E(t)$ onto the Galactic plane, such that:

$$v_E(t) = v_\odot + v_\oplus \cos\gamma\cos\omega\,(t-t_0)\,, \tag{1.26}$$

where $v_\odot$ is the Sun's velocity with respect to the Galactic halo ($v_\odot \simeq v_0 + 12$ km/s), $v_\oplus = 30$ km/s is the Earth's orbital velocity around the Sun on a plane with inclination $\gamma = 60°$ relative to the Galactic plane. Moreover, $\omega = 2\pi/T$ with $T = 1$ year

and t_0 is approximately the 2^{nd} of June, when the Earth's velocity is maximum. Finally, the Earth's velocity can be expressed as a function of the day of the year t as:

$$v_E(t) = 232 + 15 \cdot \cos\left(2\pi \frac{t - 152.5}{365}\right) \text{ km/s}, \tag{1.27}$$

with the maximum at $t = 152.5$ days, the 2^{nd} of June.

Since the Earth's orbital velocity is much smaller than the Sun's velocity with respect to the Galactic halo ($15/232 \simeq 0.07$), the amplitude of the modulation is expected to be small, and the temporal variation of the differential rate in the SHM can be approximated by a first-order Taylor expansion [168]:

$$\frac{dR}{dE_R} \approx S_0(E_R) + S_m(E_R) \cos\omega\,(t - t_0)\,, \tag{1.28}$$

where $S_0(E_R)$ is the time-averaged differential rate, $S_m(E_R)$ is the modulation amplitude and the contribution from higher-order terms is negligible ($<0.1\%$). In these conditions, the dark matter annual modulation signature becomes a very distinctive signal because all of these requirements must be simultaneously satisfied [167]:

- the rate must have a component that modulates as a cosine function, with a period of 1 year and a phase reaching its maximum around the 2^{nd} of June;
- this modulation must only be found in a well-defined low-energy range, where events induced by dark matter particles can be present;
- in the case of a multi-detector configuration, only those events that give a signal in a single detector (single-hit events) must be used, since the probability that a dark matter particle interacts with more than one detector is negligible;
- for usually adopted halo distributions (SHM), the modulation amplitude in the region of maximum sensitivity must be $\leq 7\%$, although it may be higher in other scenarios.

Only systematic effects fulfilling all these requirements could mimic the annual modulation signature, so it is crucial for experiments searching for the annual modulation of dark matter have under control all those experimental parameters which could induce a time-variable behaviour. In the same way, a robust background understanding is mandatory because some background components could be responsible for a modulation in the expected rate.

1.4.4.1 The DAMA/NaI and DAMA/LIBRA experiments

Only the DAMA (DArk MAtter) experiment, which uses NaI(Tl) crystal detectors at the LNGS in Italy, under 1400 meter of rock (about 3600 m.w.e.), has provided a long-standing positive result [4–7]: the observation of a highly statistically significant annual modulation in the detection rate, which is compatible with that expected for galactic halo dark matter particles.

Description of the DAMA experiment set-ups

The DAMA experiment has operated different set-ups over the years [170]: DAMA/NaI from 1995-2002, DAMA/LIBRA-phase1 from 2003-2010 and DAMA/LIBRA-phase2 from 2011 onward. The pioneer DAMA/NaI, consisted of nine 9.7 kg highly radiopure NaI(Tl) detectors, amounting 87.3 kg of mass in total, acquired data for 7 annual cycles, reporting the first direct model independent evidence for the presence of dark matter particles in the galactic halo with a 6.3σ C.L. from an exposure of 295.15 kg×yr [171]. The DAMA/NaI apparatus was replaced by the second generation DAMA/LIBRA (DArk MAtter/Large sodium Iodide Bulk for RAre processes), consisting of 25 highly radiopure NaI(Tl) crystals produced by Saint-Gobain company [172] of 9.7 kg mass each in a 5×5 matrix configuration. The DAMA/LIBRA experiment has been operated in two different measurement phases: DAMA/LIBRA-phase1, which accumulated data for 7 annual cycles (the first five with 232.8 kg because of a broken PMT and the last two with 242.5 kg after the PMT replacement), and DAMA/LIBRA-phase2, currently running. Both DAMA/LIBRA-phase1 and phase2 have confirmed with higher statistical significance the DAMA/NaI results, achieving a 12.9σ C.L. for the full exposure collected by the three experimental set-ups (2462.09 kg×year) [170]. Table 1.4 reports on the details of the three experimental phases of the DAMA experiment.

Apparatus	Period	Mass (kg)	Exposure (kg×yr)	Mean Live Time (%)	Energy threshold (keV)
DAMA/NaI	1995–2002	87.3	295.15	∼48	2.0
DAMA/LIBRA-phase1	2003–2008	232.8	709.39	62	2.0
	2008–2010	242.5	331.14	76	2.0
	Total		1040.53	65 (49–83)	2.0
DAMA/LIBRA-phase2	2011–2017	242.5	1126.40	80 (76–85)	1.0

Table 1.3: *Details about the three experimental phases of the DAMA experiment.*

The NaI(Tl) crystals are coupled to two PMTs on each side of the crystal through 10 cm Suprasil-B light guides (acting also as optical windows) and surrounded by low-radioactive OFHC (Oxygen Free High Conductivity) freshly electrolyzed copper shields. The detectors are enclosed in a sealed low-radioactive OFHC Cu box continuously flushed with high-purity nitrogen gas (anti-radon box) in slight overpressure relative to the external environment. Outside the Cu box, the passive shield is made by $\geq$10 cm of OFHC low-radioactive Cu, 15 cm of low-radioactive lead, 1.5 mm of cadmium foil, about 10-40 cm of polyethylene/paraffin and roughly 1 m of concrete made of the Gran Sasso rock (see Figure 1.14). The whole installation is under air conditioning to assure a suitable and stable working temperature for the electronics. Furthermore, the stability of several parameters and the running conditions is monitored along all the data taking.

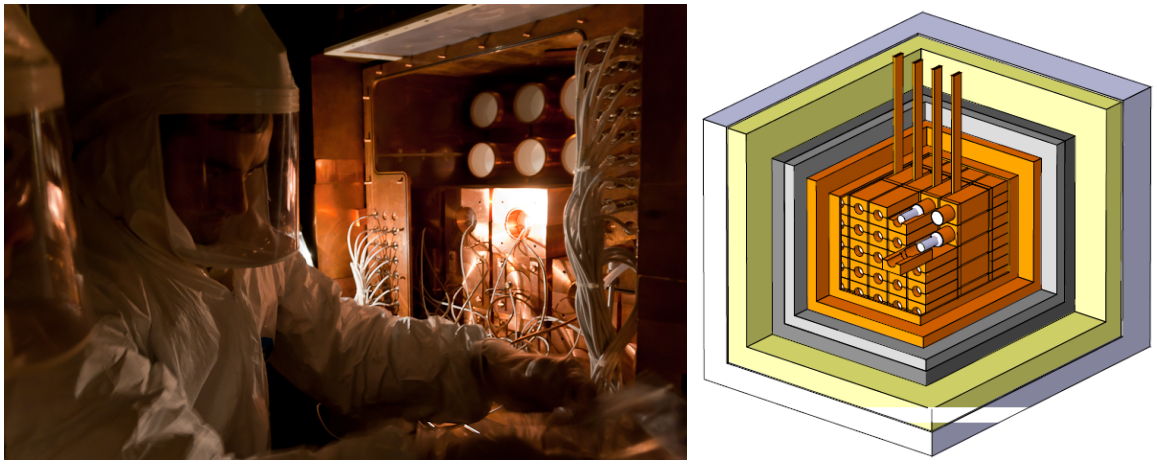

(a) (b)

Figure 1.14: *Picture taken during the installation of DAMA/LIBRA-phase2 (a) and artistic view of the DAMA/LIBRA experimental set-up (b). From Ref. [170].*

The signal of each detector is obtained as the linear sum of the signals of the two PMTs and the trigger is produced by the coincidence of the two PMTs in a 50 ns (100 ns) window for DAMA/LIBRA-phase1 (DAMA/LIBRA-phase2). During DAMA/LIBRA-phase1, the software energy threshold was established at 2 keV to keep a high acceptance efficiency for the single-hit events near the threshold ($\sim$60% in the 2-3 keV bin). In order to reduce the energy threshold, all the ETL (Electron Tubes Limited) PMTs were replaced by a second generation PMTs Hamamatsu, with higher quantum efficiency (around 40% versus 30% in phase1) and with lower background with respect to those used in phase1. During the commissioning run of phase2, the achievement of the 1 keV energy threshold was successfully confirmed

and the acceptance efficiency for the single-hit events was estimated at 70% for the 1-2 keV bin (75% in the 2-3 keV bin). Other improvements of some detector's features was also reached such as energy resolution or the light response, which was typically in the range 5.5–7.5 photoelectrons/keV for DAMA/LIBRA-phase1 and rose to 6–10 photoelectrons/keV for DAMA/LIBRA-phase2.

The annual modulation signal

A combined dataset of DAMA/NaI and DAMA/LIBRA has collected 2.46 ton×yr exposure showing a peculiar annual modulation of the single-hit scintillation events in the lowest energy region (below 6 keV) which satisfies all the requirements of the dark matter annual modulation signature. In particular, the single-hit events show a clear cosine-like modulation with a period of (0.999 ± 0.001) yr and reaching its maximum at (145 ± 5) days well compatible with that predicted for the dark matter particles in the SHM (1 yr period and 152.5 days phase). In addition, the modulation is only present for the single-hit events in the lowest energy interval and not in other higher energy regions, nor in multiple-hit events, also consistent with expectation for the dark matter signal. The measured modulation amplitude of the single-hit events in the [2,6] keV energy region over 20 annual cycles is $S_m = (0.0103 \pm 0.0008)$ c/keV/kg/d (12.9σ C.L.), which represents a variation of the order of 1% with respect to the total event rate in such energy interval. Moreover, due to the reduction of the energy threhsold from 2 to 1 keV, DAMA/LIBRA-phase2 has also been able to observed the modulation in the [1,6] keV energy range for six annual cycles, reporting a modulation amplitude of $S_m = (0.0106 \pm 0.0011)$ c/keV/kg/d with a statistical significance of 9.6σ. Table 1.4 summarized the results of the best fits of the single-hit residual rates for DAMA/NaI, DAMA/LIBRA-phase1 and DAMA/LIBRA-phase2, considering both the free and fixed period and phase. The residuals are calculated from the single-hit event rate after subtracting the averaged detection rate in 1 keV energy bins for every annual cycle. Figure 1.15 shows the residuals of the DAMA/NaI data (a) and DAMA/LIBRA-phase1 and DAMA/LIBRA-phase2 data (b) between 2 and 6 keV, as well as those obtained by DAMA/LIBRA-phase2 from 1 to 6 keV (c). The superimposed curves are the cosinusoidal functional forms $S_m \cos \omega(t - t_0)$ with a period $T = 2\pi/\omega = 1$ yr, a phase $t_0 = 152.5$ days (the 2^{nd} of June) and a modulation amplitude S_m equal to the best fit of all corresponding data.

This modulation signal of such high statistical significance could not be related to other non-WIMP explanations. No systematic or side processes able to simultaneously fulfil all the requirements of the annual modulation singature and to account for

Apparatus	S_m (c/keV/kg/d)	Period (yr)	Phase (days)	C.L.
From 2 to 6 keV				
DAMA/NaI	0.0192 ± 0.0031	1.0	152.5	6.2σ
	0.0200 ± 0.0032	1.00 ± 0.01	140 ± 22	6.3σ
DAMA/LIBRA-phase1	0.0096 ± 0.0013	1.0	152.5	7.4σ
	0.0097 ± 0.0013	0.998 ± 0.002	144 ± 8	7.5σ
DAMA/LIBRA-phase2	0.0095 ± 0.0011	1.0	152.5	8.6σ
	0.0096 ± 0.0011	0.9989 ± 0.0010	145 ± 7	8.7σ
DAMA/LIBRA-phase1+	0.0095 ± 0.0008	1.0	152.5	11.9σ
DAMA/LIBRA-phase2	0.0096 ± 0.0008	0.9987 ± 0.0008	145 ± 5	12.0σ
DAMA/NaI+	0.0102 ± 0.0008	1.0	152.5	12.8σ
DAMA/LIBRA-phase1+	0.0103 ± 0.0008	0.9987 ± 0.0008	145 ± 5	12.9σ
DAMA/LIBRA-phase2				
From 1 to 6 keV				
DAMA/LIBRA-phase2	0.0105 ± 0.0011	1.0	152.5	9.5σ
	0.0106 ± 0.0011	0.9993 ± 0.0008	148 ± 6	9.6σ

Table 1.4: *Results of the best fits of the single-hit residual rates for DAMA/NaI [171], DAMA/LIBRA-phase1 [6] and DAMA/LIBRA-phase2 [7] in [1,6] and [2,6] keV energy regions, considering both the free and fixed period and phase.*

the whole measured modulation amplitude have been found by DAMA/LIBRA collaboration. In particular, upper limits on the possible contributions to the DAMA/LIBRA measured modulation amplitude from radon, temperature, background rejection procedures and acceptance efficiences, energy calibration and other sources of background have been estimated [170]. In addition to this, any possible role of some natural periodical phenomena have been quantitatively demonstrated to be unable to mimic the observed effect [173, 174].

If the DAMA signal is interpreted as that caused by the elastic interactions of WIMPs with the detector's target materials, two favoured regions should appear at 10–15 GeV for scattering off sodium and 60–100 GeV for scattering off iodine [119]. As previously mentioned, the conversion from measured recoil energy into WIMP mass and WIMP-nucleon cross section involves depends on the quenching factors of the target materials. DAMA reports constant quenching factors of 0.3 for Na and 0.09 for I [124], whereas the recent measurements indicate an energy dependency with smaller quenching factors in the region of interest (see Figure 1.9). Using the DAMA/NaI and DAMA/LIBRA-phase1 data and considering the canonical (isospin-

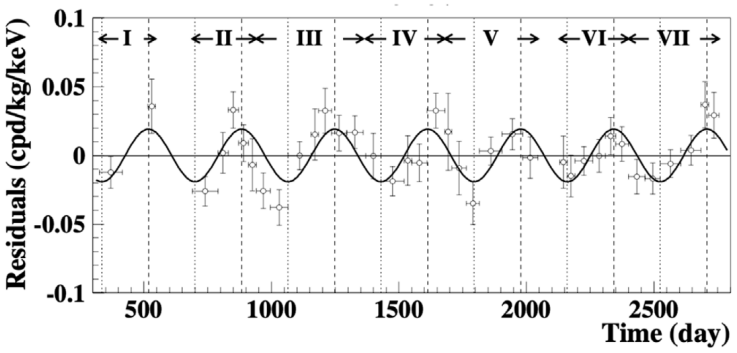

(a)

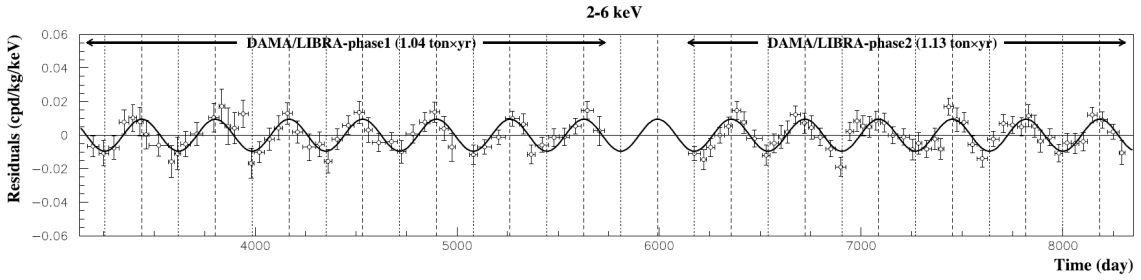

(b)

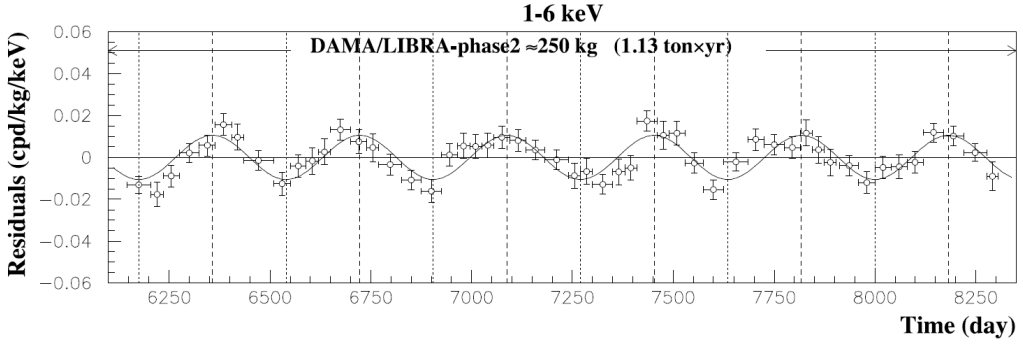

(c)

Figure 1.15: *Experimental residual rate of the single-hit scintillation events measured in the [2,6] keV energy region by DAMA/NaI (a) and DAMA/LIBRA (b), as well as in the [1,6] keV energy range for DAMA/LIBRA-phase2 (c). From Ref. [170].*

conserving) SI interaction scenario, two WIMP candidates emerged with a good fit for masses of about 10 and 70 GeV. Taking into account the new data obtained by DAMA/LIBRA-phase2, the best fit high mass shifts to ∼54 GeV and to ∼8 GeV for the low mass. Nevertheless, the goodness of fit in the SI interaction scenario is not good with the new data, being disfavored at 5.2σ for the low mass region and at 2.5σ for the high mass region [175]. Despite this, the DAMA/LIBRA collaboration considers that the purely SI scenario is still supported by the data for both low and

high mass candidates and has evaluated the allowed regions for these candidates by estimating the domains of the $m_W - \sigma_{SI}$ parameter space whose likelihood-function values differ more than 10σ from absence of signal [170]. This estimation has been done considering both the constant Na and I quenching factors and the energy dependence described in Ref. [129] (see Figure 1.10).

In any case, the interpretation of the DAMA signal in the dark matter framework is strongly model dependent, so independent confirmation is mandatory to solve the DAMA/LIBRA conundrum. Currently, the COSINE–100 (see Section 1.4.4.2) and ANAIS–112 (see Chapter 2) experiments are seeking to shed light on this puzzle using the same target and technique.

1.4.4.2 The COSINE experiment

The COSINE–100 (merger of KIMS, Korea Invisible Mass Search, and DM-Ice) experiment [17] have been operating 106 kg of low-background NaI(Tl) crystals since the 30^{th} of September 2016 at the Y2L in South Korea. The eight NaI(Tl) crystals were produced by Alpha Spectra Inc. from four different powder grades and are hermetically encased in OFC (Oxygen-Free Copper) tubes with quartz windows attached at the end and light-coupled to two Hamamatsu PMTs. The Cu encapsulation of the crystals have a calibration window with either a reduced Cu thickness or a thin Mylar cover to facilitate low energy source calibrations. The NaI(Tl) crystals are arranged in a 4×2 matrix configuration and are housed in a 1 cm thick acrylic box, immersed in 2200 L of Linear Alkyl-Benzene-based liquid scintillator, which allows to veto mainly the ^{40}K emissions from the NaI(Tl) crystals. The inner walls of the acrylic container and the outer surfaces of the crystal assemblies are wrapped with specular reflective films to increase the light collection efficiency of the liquid scintillator. Eighteen Hamamatsu PMTs are attached to the two sides of the box to detect the photons generated in the liquid scintillator. From inside outward, the acrylic box is surrounded by a 3 cm-thick OFC box, a 20 cm-thick lead-brick castle and 3 cm of 37 plastic scintillator panels for cosmic ray muon tagging (see Figure 1.16). Finally, the shield is supported by a steel skeleton.

COSINE–100 established the analysis energy threshold at 2 keV in six of the eight crystals with an oustanding light collection of about 15 photoelectrons/keV. Nevertheless, due to the lower light collection and higher thresholds, the remaining two crystals (C5 and C8 of masses 18.0 and 18.3 kg, respectively) were removed from any further analysis. From the analysis of the first 59.5 days of data collected, COSINE–100 excluded the DAMA/LIBRA signal in the SI interaction framework [176]. A first

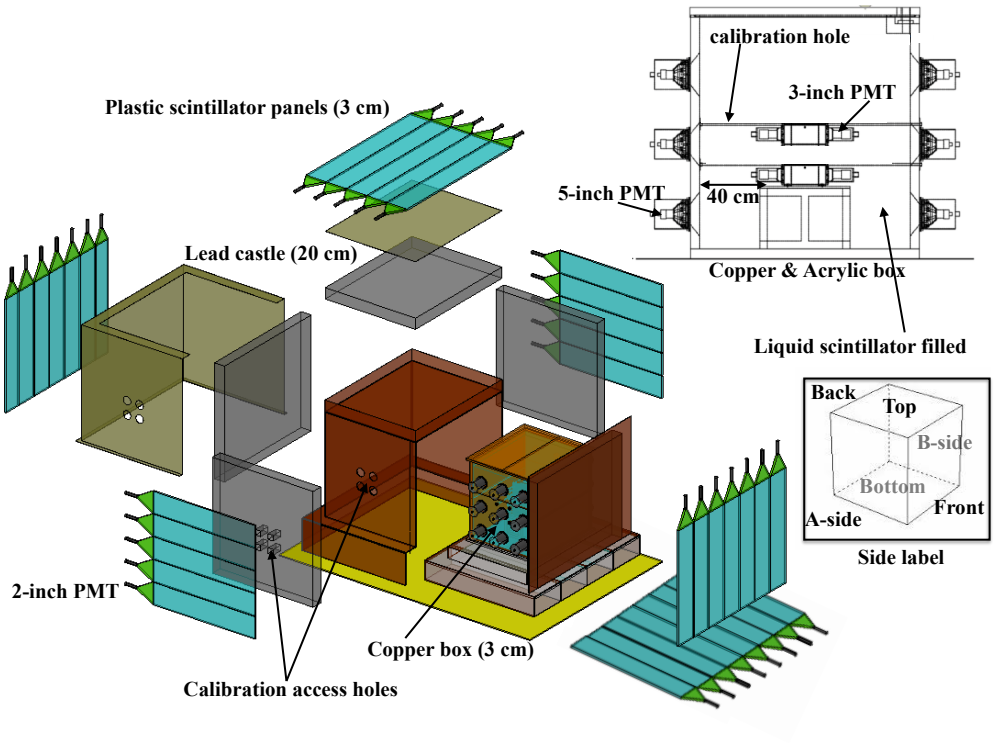

Figure 1.16: *Artistic view of the COSINE–100 experimental set-up. From Ref. [17].*

analysis of annual modulation from 1.7 years of data has also been presented [177], corresponding to a total exposure of 97.7 kg×yr, as another detector (C1 with a mass of 8.3 kg) was excluded due to its high noise rate, leading to a total effective mass of 61.4 kg. The best fit for the modulation amplitude of the single-hit events in the [2,6] keV energy region, when the period and phase are fixed, is $S_m = (0.0083 \pm 0.0068)$ c/keV/kg/d, consistent with both the null hypothesis and the DAMA/LIBRA's best fit value at 1σ C.L. More data are needed to confirm or refute the DAMA/LIBRA signal. The COSINE–100 experiment expects to reach 3σ coverage of DAMA/LIBRA region within 5 years of data exposure and with lower energy threshold.

Recently, the COSINE–100 experiment has demonstrated to have reached the energy threshold of 1 keV by using machine learning techniques for the rejection of noise events [178], but annual modulation results have not yet been reported. In parallel, the development of crystals with higher radiopurity is ongoing in Korea for a second phase of the experiment using about 200 kg of NaI(Tl) (COSINE–200) [179]. In fact, first results from small crystals (∼0.7 kg) have shown a reduction of ^{210}Pb activity [180].

Chapter 2

The ANAIS experiment

The ANAIS (Annual modulation with NaI Scintillators) experiment is intended to search for dark matter annual modulation with ultrapure NaI(Tl) scintillators at the Canfranc Underground Laboratory (LSC) in Spain, in order to provide a model independent confirmation of the signal reported by the DAMA/LIBRA collaboration using the same target and technique.

The ANAIS experiment, led by the Nuclear Physics and Astroparticles Group of the University of Zaragoza, is the result of the long expertise acquired in the operation of NaI(Tl) scintillators over more than twenty years with different prototypes for ANAIS. The NaI32 [181–183] experiment was the precursor of ANAIS. It was operating for two years at the LSC and consisted of three BICRON hexagonal NaI detectors with 32.1 kg of total mass. In the search for the annual modulation effect, no positive signal was found, but bounds to WIMP mass and cross section were established.

Subsequently, one of the NaI32 detectors was modified to build the ANAIS prototype I [184] and, after decoupling the photomultiplier and removing the original encapsulation, it was used in ANAIS prototypes II [185] and III. These prototypes allowed the development of pulse shape discrimination techniques, the optimization of light collection and the measurement of the potassium content of the bulk crystal. Nevertheless, the use of the old BICRON crystals for a dark matter experiment was ruled out due to their high potassium content at the level of 0.5 ppm [186] and the high ^{210}Pb contamination.

The next step was the testing of a new 9.6 kg NaI(Tl) parallelepipedic crystal made by Saint-Gobain and with the same shape and size as those of DAMA/LIBRA [187], named ANAIS–0. This set-up permited the characterization and understand-

ing of the background at low energy, the optimization of NaI bulk event selection, determining the calibration method and testing the electronics. Although its high potassium content at the same level than that found in the latter [130, 186] was the reason why its use was again discarded, many technical aspects of the set-up and data-taking system were established to be used in next ANAIS prototypes.

The latest ANAIS prototypes were built by Alpha Spectra Inc. (AS), Colorado (US) [188], because of the low potassium content in the purified NaI powder provided by the company. Two modules were purchased for quality assessment in radiopurity and light collection. Each cylindrical module consists of a 12.5 kg NaI(Tl) crystal, housed in OFE (Oxygen Free Electronic) copper and coupled through quartz windows to two Hamamatsu photomultipliers (PMTs) at the LSC clean room in a second step. These two detectors constituted the ANAIS–25 set-up [189], and were found to have an acceptable content in ^{40}K, but a high ^{210}Pb contamination. The origin of this large ^{210}Pb contamination was identified at the end of the purification process and growing of the crystal. As a result, the company modified its procedures in order to reduce the ^{210}Pb content in the next crystals produced for ANAIS. A new module was incorporated later to form ANAIS–37 set-up [190], and the reduction of the ^{210}Pb content in comparison with previous modules was confirmed.

Finally, the full ANAIS experiment set-up, named ANAIS–112, was installed at LSC Hall B in 2017. After the commissioning run for calibration and general assessment, ANAIS–112 started data taking in "dark matter search" mode on the 3^{rd} of August 2017. It consists of nine 12.5 kg NaI(Tl) modules in a 3×3 matrix configuration, amounting 112.5 kg of mass in total. All the crystals are cylindrical (4.75" diameter and 11.75" length) and are housed in OFE copper; the encapsulation has a Mylar window in the lateral face allowing low energy calibration using external gamma sources. Every crystal was coupled through synthetic quartz windows to two Hamamatsu PMTs at the LSC clean room. Different PMT models were tested in order to choose the best option in terms of light collection and background [130], selecting finally the R12669SEL2 model.

In this chapter, the ANAIS experimental requirements and the achievements of ANAIS–112 are described (Section 2.1), as well as all the elements of the experimental set-up like crystals (Section 2.2) and photomultipliers (Section 2.3), electronic and data acquisition (Section 2.4) or the muon veto system (Section 2.5). The ANAIS–112 data analysis and blinding strategy are explained in Section 2.6. Section 2.7 focuses on the energy calibration of the experiment at both low and high energy. The light collection of ANAIS–112 modules is reported in Section 2.8. In

Section 2.9, the temporal variability of relevant experimental parameters along the three years of data taking are described. The background model of ANAIS–112 is summarized in Section 2.10, together with the measurement of an upper limit for the ^{222}Rn content in the internal cavity of the shielding containing the ANAIS–112 detectors. Finally, the description of the Blank module is conducted in Section 2.11.

2.1 ANAIS experimental requirements and achievements of ANAIS–112

Several requirements must be satisfied by an experiment devoted to the search for dark matter annual modulation to reach its goal. The region of interest of the expected signal is at very low energies, where the background level must be low enough to detect a variation corresponding to about 0.01 c/keV/kg/d above 1 keV. For these reasons, an energy threshold as low as possible is desirable and maximum suppression of any background source must be achieved. Additionally, very stable operational conditions and a long exposure time are also necessary to have enough statistical significance in the search for a seasonal variation.

2.1.1 Low energy threshold

WIMPs interaction is expected to be produced below 100 keV of nuclear recoil energy or even at lower energies depending on the WIMP mass. This implies electron equivalent energies below approximately 30 keV for Na recoils and below 10 keV for I recoils. The energy threshold depends on experimental aspects such as the light collection efficiency (dependent on the optical quality of the crystal, the light collection system of the modules and the PMT quantum efficiency) and the hardware trigger level. Efficiently triggering each PMT at the photoelectron (phe) level is very important owing to the nature of the low energy events, consisting on few separate photons. To ensure the acquisition of all relevant events but without increasing the dead time, each crystal coupled to two PMTs is triggering in logical AND mode between the two PMT signals. Furthermore, robust noise filtering protocols are mandatory so as to guarantee the quality of low energy events.

The analysis energy threshold of ANAIS–112 has been set at 1 keV$_{ee}$. This has been possible thanks to the outstanding light collection of all the modules, at the level of 15 phe/keV$_{ee}$ (see Section 2.8), and the good low energy calibration (see Section 2.7.2) due to the presence of the coincidence events of ^{22}Na (0.87 keV) and ^{40}K (3.20 keV). It is important to note that the 0.87 keV peak from ^{22}Na is actually below the analysis threshold, but it was established at 1 keV$_{ee}$ because the total

detection efficiency of some modules is 15% at this energy (see Section 3.2.4). In connection with the trigger efficiency at the energy threshold, it is higher than 98% for all detectors (see Section 3.2.1).

2.1.2 Low background level in the region of interest

The region of interest (ROI) for the WIMP annual modulation in target detectors is below 6 keV$_{ee}$. This annual modulation signal is expected to be less than a 10% of the total interaction rate of dark matter particles, but in a much lower percentage of the total events rate if other background contributions are present. In order to keep the known background as low as possible in the ROI, an ultrapure NaI powder must be used, a careful crystal growing and detector manufacturing must be done, and external radiopure materials must be carefully selected. For instance, internal contamination of the ^{22}Na and ^{40}K isotopes in NaI(Tl) crystals were identified as especially harmful for dark matter search experiments since they produce a line at 0.87 keV and 3.20 keV, respectively, corresponding to the K-shell electron binding energy released following electron capture.

Besides internal contamination, the possible influence of external backgrounds also has to be taken into consideration. For this purpose, a passive shield consisting of lead, boron-loaded water and polyethylene was specifically designed for ANAIS–112 detectors. Figure 2.1 shows an artistic view of the ANAIS–112 full experimental set-up, in which all the nine detectors arranged in a 3×3 matrix are enclosed in several layers of shielding. From inner to outer layer: 10 cm of archaeological lead plus 20 cm of low activity lead to attenuate the external gamma background; a stainless steel anti-radon box continuously flushed with radon-free nitrogen gas to prevent the entrance of airborne radon inside the lead shielding; 16 plastic scintillators covering the top and the lateral faces of the anti-radon box so as to act as active shielding against muons and muon-related events; and finally, a 40 cm-thick neutron moderator consisting of a combination of boron-loaded water and polyethylene blocks.

By installing ANAIS–112 at the LSC, under 2450 m.w.e. (meter water equivalent), the flux of muons from cosmic rays is reduced by approximately a factor of 10^5 compared to that measured at sea level. Nevertheless, a residual muon flux (of the order of 5.26×10^{-3} μ m^{-2} s^{-1} at LSC Hall A [191]) still survives the rock shielding, and could produce secondary neutrons in the set-up materials which could contribute to the background in the region of interest. These muon-related events can be

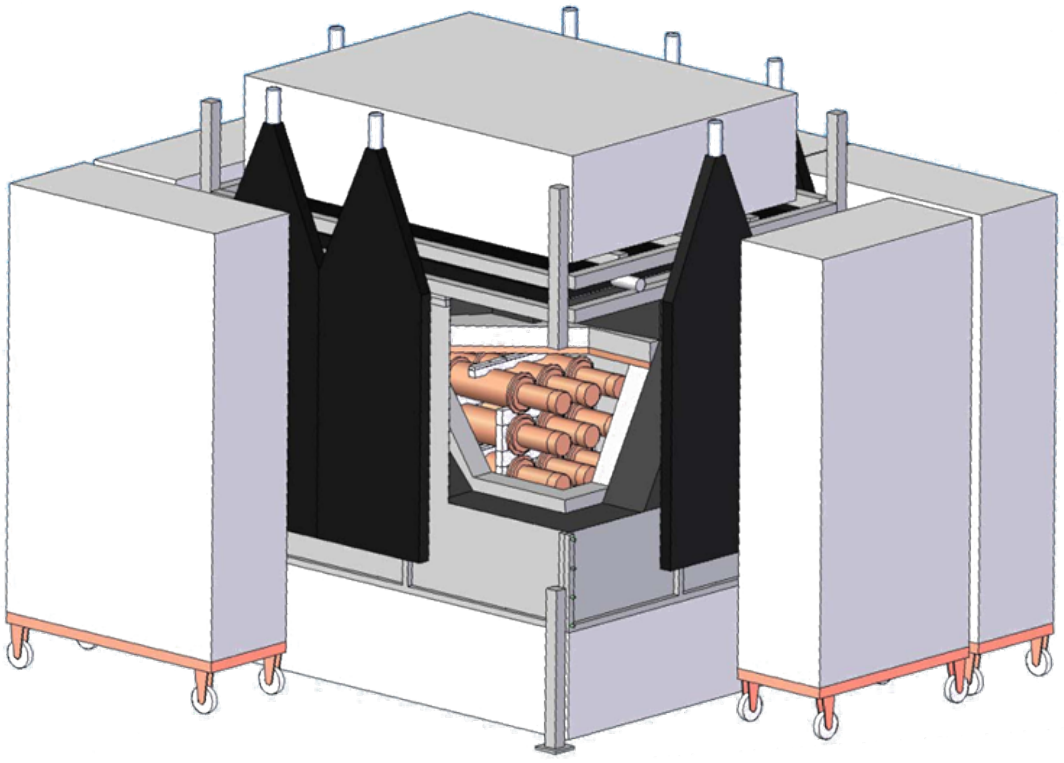

Figure 2.1: *Artistic view of the ANAIS–112 experimental set-up.*

removed by tagging muon interactions in the active muon veto system composed of plastic scintillators. This system is described in Section 2.5.

2.1.3 Stability

The stability of the environmental and experimental parameters is one of the most important experimental requirements for dark matter annual modulation searches, since data taking is performed over several annual cycles. Therefore, it is mandatory to check any seasonal variation or anomalous behaviour that could affect to the gain, threshold, background or trigger efficiency of the experiment. To have under control as many parameters as possible, all relevant environmental and external parameters must be monitored. For this purpose, a slow-control system was designed for the ANAIS–112 experiment. This system and the stability of the environmental conditions and data aquisition parameters, such as the gain, are described in Section 2.9. The study of stability for several background event populations for which no modulation is expected is covered in Section 5.1.

2.1.4 Exposure maximization

Once the target mass is fixed, the exposure of the experiment is marked by the effective measurement time: the live time. Consequently, the system has to maintain as low as possible the dead and down times. The former is related to the time after each event during which the system is not able to record another event, whereas the latter corresponds to the maintenance or system malfunction time. Live and dead times are precisely determined by using specific counters (see Ref. [192]).

The evolution of the live time for the three years of ANAIS–112 set-up can be seen in Figure 2.2, in which the dead time and the down time contribution to total time are also shown. Down time is mostly due to periodical calibration of the modules using external gamma sources (seen as periodical spikes in the figure), and a few incidences affecting electrical supply of the LSC and maintenance labours along the three years of operation. Anyway, the total live time percentage is over 95% of the elapsed time and the dead time a 2.4% of the total time. This excellent duty cycle guarantees that the data are evenly distributed along the year, reducing possible systematic contributions in the annual modulation analysis. The percentages of live, down and dead times, total live time accumulated and exposure per operation year are collected in Table 2.1. Total numbers for the full exposure are also given.

Year	Time period	Live Time (days)	Exposure (kg×yr)	Live Time (%)	Dead Time (%)	Down Time (%)
1	03/08/2017 - 31/07/2018	340.11	104.83	94.5	2.9	2.6
2	01/08/2018 - 01/08/2019	348.24	107.33	95.5	2.1	2.4
3	02/08/2019 - 13/08/2020	359.04	110.66	95.3	2.3	2.4
Total	03/08/2017 - 13/08/2020	1047.38	322.82	95.1	2.4	2.5

Table 2.1: *Distribution of live, dead and down times during ANAIS–112 data taking, total live time accumulated and exposure per operation year. Numbers for the full exposure are also given.*

In any case, these live time percentages are above the live time reported by DAMA, ranging from 49% to 83% (from 76% to 85%) depending on the annual cycle in DAMA/LIBRA–phase1 (DAMA/LIBRA–phase2) [170]. ANAIS–112 data also show a good homogeneous distribution of the live time along the elapsed time.

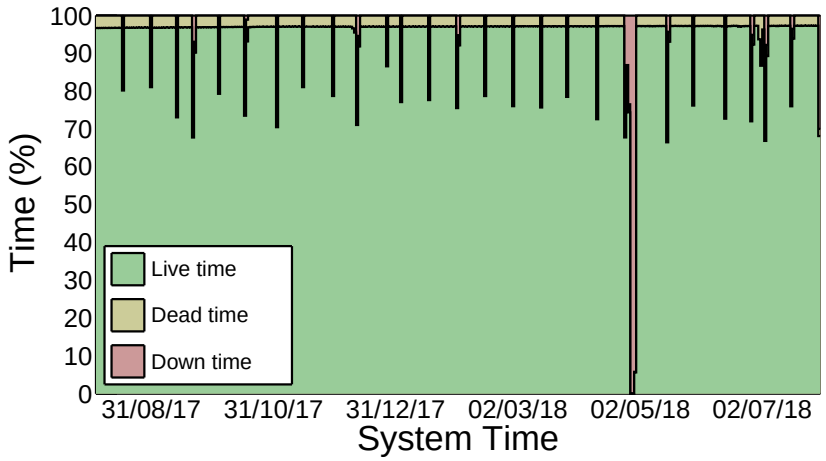

(a) *First year.*

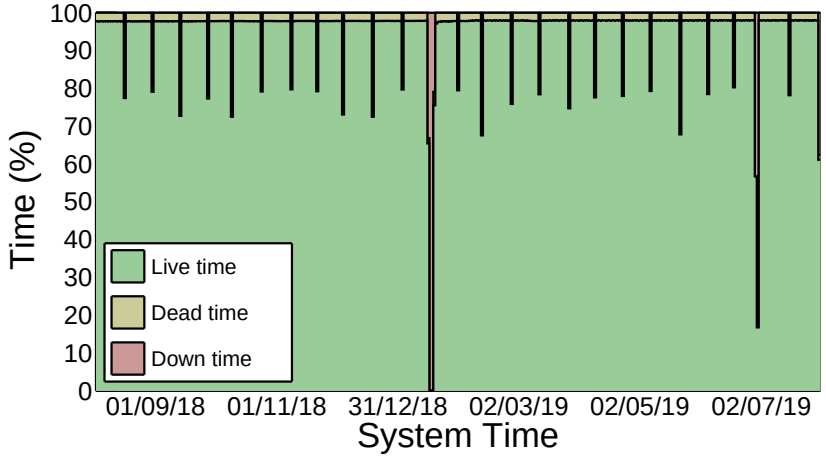

(b) *Second year.*

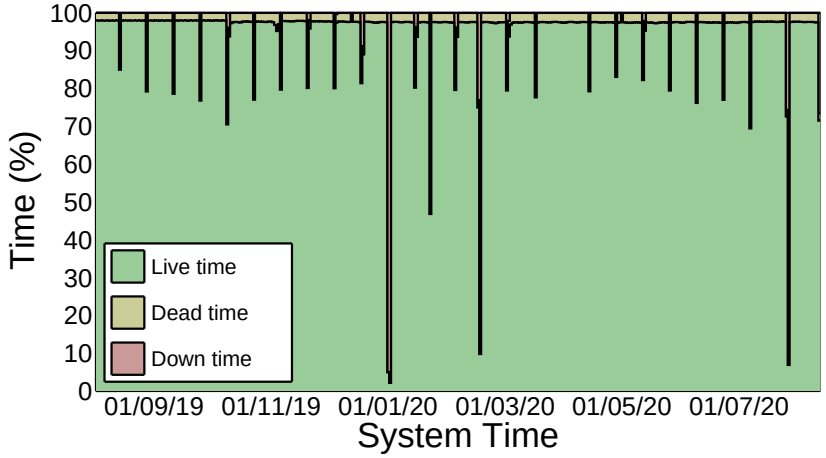

(c) *Third year.*

Figure 2.2: *Distribution of live, dead and down times during the first (a), the second (b) and the third (c) years of ANAIS–112 data taking.*

2.2 Scintillation mechanism

The scintillation detector is based on one of the most useful available techniques to detect ionizing radiation and it is still widely used for spectroscopy of a wide assortment of radiations in nuclear and particle physics experiments. It makes use of the fact that certain materials emit a small flash of light, the so-called scintillation light, when they are struck by some particle. By coupling these detectors to an amplifying device such as a photomultiplier, the scintillation light can be converted into electrical pulses, which can then be analyzed. The scintillation mechanism is exhaustively covered in references [193] and [194].

According to Ref. [194], the ideal scintillator material should possess a few properties:

1. It should convert the kinetic energy of the incident particle into detectable light with a high scintillation efficiency.

2. The light yield should be proportional to deposited energy, i.e., with a linear behaviour.

3. In order to achieve a good light collection, the medium should be transparent to the emitted wavelength.

4. The decay time should be as short as possible so that fast signal pulses can be generated.

5. The material should have good optical quality to manufacture practical large size detectors.

6. Its refractive index should be near that of glass ($\sim$1.5) to allow efficient coupling between the scintillation light and the photomultiplier tube.

The choice of a particular scintillator is always a compromise among these and other factors because no scintillator material simultaneously meets all the aforementioned criteria. There are two most commonly used types of scintillation materials: inorganic and organic-based liquids and plastics. The most widely applied scintillators include the inorganic alkali halide crystals (such as NaI), which tend to have the best light output and linearity, but with a relatively slow response in time. On the other hand, organic scintillators are generally faster but have a lower light yield.

The organic scintillators are aromatic hydrocarbon compounds containing linked or condensed benzene-ring structures. Scintillation light in these compounds arises from transitions in the energy level structure of a single molecule, and therefore can be observed independently of the material physical state. Due to the fact that the delocalized electrons are occupying π-molecular orbitals, the principal emission path has a decay time of the order of a few nanoseconds. In ANAIS–112, plastic organic scintillators surrounding the shielding are used as a muon veto system (see Section 2.5).

In inorganic scintillators, the process of scintillation is clearly characteristic of the electronic band structure found in the crystal lattice of the material. Electrons have available bands of energy in insulators or semiconductor materials. When charged particles produce energy depositions in the crystal, excited electrons from the valence band can fill the conduction band states. However, in pure materials, the recombination of the electron-hole pairs with emission of a photon is not the dominant process for energy relaxation. Only a few photons are released by this mechanism and typical gap widths in pure crystals are such that the emitted photons are too energetic to lie within the visible range. Therefore, this kind of materials is commonly doped with small amounts of impurities, called activators, so as to enhance the probability of UV-visible photon emission during the de-excitation process. These activators create discrete levels in the forbidden gap modifying the normal energy band structure of the pure crystal (see Figure 2.3). Electrons can de-excite back to the valence band with typical half-lives of 50-500 ns.

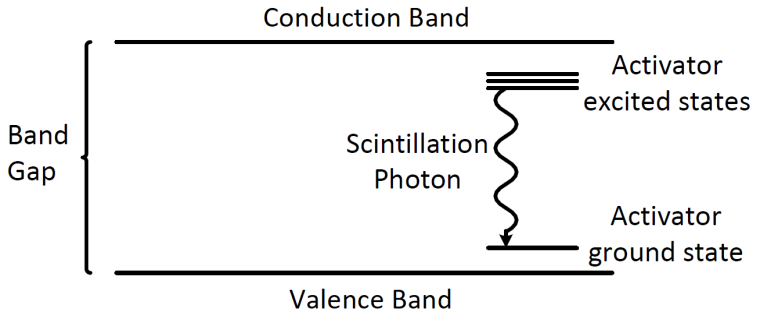

Figure 2.3: *Energy band structure of an inorganic activated crystalline scintillator. From Ref. [194].*

Thallium doped sodium iodide scintillators have been widely used in the gamma spectroscopy field. The material permits the growing of large ingots from high-purity

sodium iodide to which a small fraction of thallium has been added as an activator. Fine-tuning of Tl concentration (typically 10^{-3} mole fraction of thallium) is able to achieve high light yield, while preserving high transparency to its own light emission. In particular, the spectral distribution of the scintillation photons in NaI(Tl) has its maximum around 410 nm.

The disadvantages of NaI(Tl) are its long scintillation decay time (∼230 ns), the crystal fragility and its hygroscopic nature that requires a tight encapsulation.

2.2.1 ANAIS–112 NaI(Tl) crystals

ANAIS–112 consists of nine modules, 12.5 kg each, of ultrapure sodium iodide Thallium doped, NaI(Tl), built by the Alpha Spectra company in Colorado (US) along several years. All the crystals are cylindrical (4.75" diameter and 11.75" length) and are housed in OFE (Oxygen Free Electronic) copper. In a second step, crystals were coupled through synthetic quartz windows to two PMTs at the LSC clean room. Very low energy calibration can be performed thanks to a Mylar window in the lateral face of each module.

Before ANAIS–112 commissioning, some of the modules had been tested and characterized in different smaller but equivalent set-ups: ANAIS–25 [189] took data with D0 and D1 detectors from December 2012 to March 2015; in ANAIS–37, D2 was added [190] and also D3, D4 and D5 detectors were successively operated in three-module set-ups with different detector configurations (A37D3 [195], A37D5). From March to July 2017, the commissioning phase of the full ANAIS–112 experiment took place performing calibration and general assessment, and the dark matter run started on the 3^{rd} of August 2017. Details about the powder name used for the growing of the ANAIS–112 modules and the date of arrival at LSC for the nine NaI(Tl) detectors can be found in Table 2.2. Furthermore, Figure 2.4a shows the 3×3 final configuration of the detectors in the ANAIS–112 set-up, and the detector positions inside the shielding can be seen in Figure 2.4b.

The bulk ^{40}K content of ANAIS–112 crystals has been evaluated by searching for the coincidences between 3.2 keV energy deposition in one detector (following the electron capture decay from K-shell) and the 1460.8 keV gamma line escaping from it and being fully absorbed in other detectors [186, 196]; estimating the efficiency of the coincidence by Monte Carlo simulation. The measured values of ^{40}K activity for the nine crystals from ANAIS–112 data are presented in Table 2.2. They are compatible with previously results found for detectors D0 to D5 using the data from

Detector	Powder name	Date of arrival at LSC	^{40}K (mBq/kg)	^{210}Pb (mBq/kg)
D0	<90 ppb K	December 2012	1.33±0.04	3.15±0.10
D1	<90 ppb K	December 2012	1.21±0.04	3.15±0.10
D2	WIMPScint-II	March 2015	1.07±0.03	0.70±0.10
D3	WIMPScint-III	March 2016	0.70±0.03	1.80±0.10
D4	WIMPScint-III	November 2016	0.54±0.04	1.80±0.10
D5	WIMPScint-III	November 2016	1.11±0.02	0.78±0.01
D6	WIMPScint-III	March 2017	0.95±0.03	0.81±0.01
D7	WIMPScint-III	March 2017	0.96±0.03	0.80±0.01
D8	WIMPScint-III	March 2017	0.76±0.02	0.74±0.01

Table 2.2: *Powder name, date of arrival at LSC and internal contamination measured of ^{40}K and ^{210}Pb for the nine NaI(Tl) detectors of ANAIS–112 produced by Alpha Spectra.*

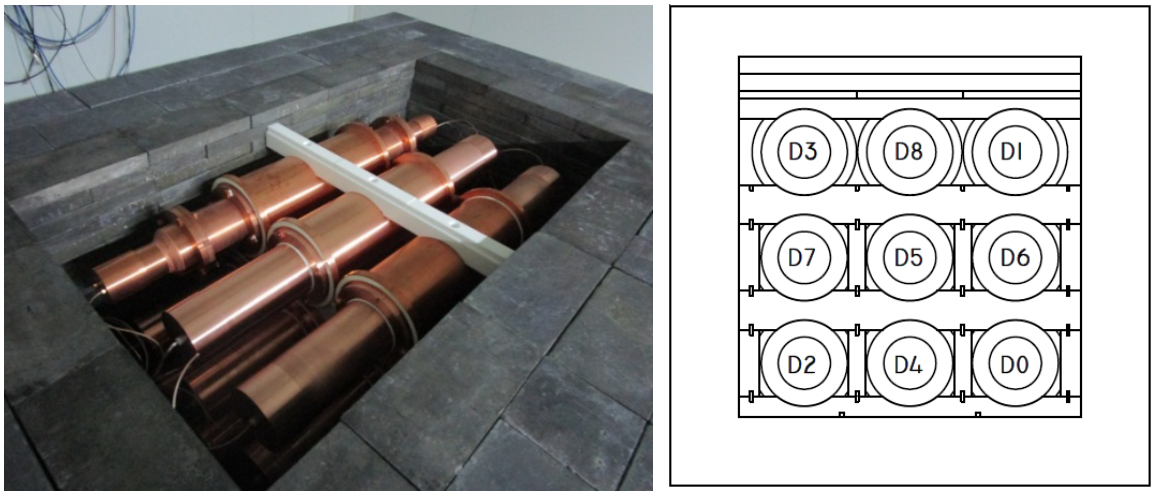

(a) (b)

Figure 2.4: *Picture taken while ANAIS–112 commissioning (a) and East face view of detector positions in the 3×3 modules matrix (b).*

the set-ups with only two or three modules, having lower coincidence probability. On average, the ^{40}K activity in ANAIS–112 crystals is 0.96 mBq/kg, corresponding to 32 ppb of K. Detectors produced by the company Alpha Spectra Inc. have shown to have a potassium activity only slightly higher than that of the DAMA/LIBRA crystals (at or below ∼20 ppb [187]).

The internal contamination of ^{210}Pb in ANAIS–112 crystals have been determined by measuring the alpha events rate, selected through pulse shape analysis (PSA). PSA allows to powerfully discriminate alpha events from $\beta/\gamma/\mu$ events by comparing the area and the amplitude of the pulse, because the former produce a faster scintillation than the latter. The measured values of ^{210}Pb activity for the nine modules of ANAIS–112 are also shown in Table 2.2. It can be verified that the last detectors produced by Alpha Spectra have a significantly lower ^{210}Pb activity compared with that of D0 and D1 modules after modifying the purification and growing procedure of the crystals. Nevertheless, these values are still much higher than those achieved in DAMA/LIBRA crystals, ranging from 5–30 μBq/kg [187].

It is worth noting that the ^{40}K and ^{210}Pb measured activities in ANAIS–112 crystals are similar to those determined for COSINE–100 crystals produced by the same company from the same starting material [197, 198].

2.3 Photomultiplier tubes

A photomultiplier tube is an extremely sensitive light detector providing a current output proportional to light intensity. It consists of an input window, a photochatode made of photosensitive material followed by an electron collection system, an electron multiplier section (or dynode string) and finally an anode from which the final signal can be taken. All parts are housed in an evacuated glass tube which serves as a preassure boundary to sustain vacuum conditions [193, 194].

Photomultipliers convert the incident light, which typically consist of no more than a few hundreds of photons, into a measurable electric current (see Figure 2.5). During operation, a high voltage is applied to the cathode. When an incident photon impacts on the photocathode, an electron is emitted via the photoelectric effect. Due to the applied voltage, the electron is then accelerated in the vacuum and focused onto the first dynode, where it transfers part of its energy to the electrons in the dynode. As a result, secondary electrons are emitted, which are accelerated towards the next dynode, where more electrons are released and further accelerated. An electron cascade down the dynode string is thus created. Finally, the electrons emitted by the last dynode are collected at the anode.

Depending on the material of the photocatode, and the geometric disposition and number of dynodes, there are different types of PMTs. The proper operation of the PMT must be guaranteed by a stable high voltage supply, a good housing system that

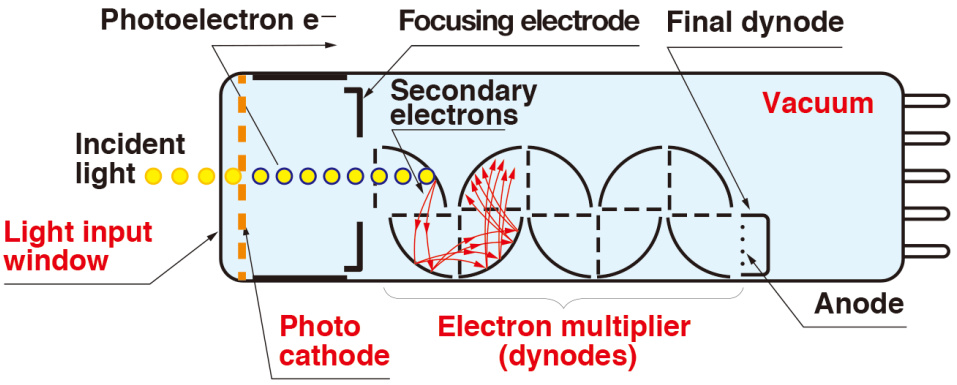

Figure 2.5: *Schematic view of a photomultiplier tube. From Ref. [199].*

shields the photomultiplier tube from external light and avoid electromagnetic interferences and a suitable signal processing set-up. The high voltage supply provides potential difference to the dynodes, allowing the emission of secondary electrons.

A previous characterization of the PMTs is required in order to test some parameters:

- The **quantum efficiency**: it is the ratio between photoelectrons produced and incident photons at photocathode. It depends on the wavelength of the incident photons and the material of the photocathode.
- The **gain**: it is the final number of collected electrons at the anode for each photoelectron produced at the photocathode. It is susceptible to variations in the high voltage power supply, so a stable high voltage supply is crucial to have an stable gain.
- The **rise time** (**fall time**): it quantifies the time required for a single photoelectron signal to change from 10% to 90% (from 90% to 10%).
- The **transit time**: it is the time interval from the arrival of light to the photocathode and the appearance of the output pulse at the anode.
- The **dark current**: it is the rate of dark events produced without light excitation of the photocathode.
- The **single electron response** (**SER**): it is the output signal produced by a single photoelectron.

A compromise between high quantum efficiency, low background and low dark current had to be taken into consideration to select the most suitable photomultiplier for ANAIS. High quantum efficiency is mandatory to achieve a low energy threshold, PMTs must be made of radiopure materials so as to minimize their contribution to the background of the experiment, and low dark rate of the PMT is also important to prevent an undesirable increase in trigger rate, which would increase dead time and further complicate selection of real bulk scintillation events.

Fulfilling all these requirements, the Hamamatsu R12669SEL2 PMT model (previously named as R6956MOD) was selected for ANAIS–112. This model (see Figure 2.6) has a bialkali photocathode, high quantum efficiency (>33%), a maximal response at 420 nm and dark current below 500 Hz. It has ten dynode stages and a gain factor around 10^6 at the nominal voltage value. The full technical information can be seen in Table 2.3. Moreover, this PMT model is similar to the installed in the upgrade of the DAMA/LIBRA experiment (DAMA/LIBRA–phase2) [170, 200], and also the one that the KIMS/COSINE collaboration would later select [17, 201].

Figure 2.6: *Hamamatsu R12669SEL2 photomultipliers.*

A total of 42 units of Hamamatsu R12669SEL2 were received at LSC and tested. The radiopurity levels and the homogeneity among all the units were verified by high purity germanium (HPGe) spectroscopy [192, 202]. The characterization of the PMTs was performed by measuring SER, gain, relative quantum efficiency and dark

Characteristics	
Diameter	3”
Spectral response	300-650 nm
λ of max. response	420 nm
Photocathode material	Bialkali
Photocathode min. effective	70 mm
Dynode structure	Box-and-grid + Linear-focused
Number of stages	10
Operating ambient T	-30/+50 °C
Max. supply voltage	1500 V
Max. avg anode current	0.1 mA
Characteristics at 25 °C	
Cathode luminous sens.	100 μA/lm
Quantum efficiency at peak	$> 33\%$
Anode luminous sens	100 A/lm
Gain	10^6
Anode dark current (max.)	6 (60) nA
Dark current rate	< 500 Hz
Anode pulse rise time	9.5 ns
Electron transit time	60 ns
Transit time spread	13 ns
Pulse linearity	30 ($\pm$ 2%) mA

Table 2.3: *Hamamatsu R12669SEL2 technical data.*

rate in a dedicated test bench at the University of Zaragoza. More information on details and results of these measurements can be found in Ref. [192].

The 18 units eventually used in the ANAIS–112 set-up are listed in Table 2.4 together with the measured activities taken into consideration in the ANAIS–112 background model [196]. It can be seen that compatible levels of activity are found among them. The weighted mean values are also shown in the table.

Detector	PMT reference	^{40}K (mBq/PMT)	^{232}Th (mBq/PMT)	^{238}U (mBq/PMT)	^{226}Ra (mBq/PMT)
D0	ZK5902	97±19	20±2	128±38	84±3
	ZK908	133±13	20±2	150±34	88±3
D1	FA0069	105±15	18±2	159±29	79±3
	FA0119	105±21	22±2	259±59	59±3
D2	FA0034	155±36	20±3	144±33	89±5
	FA0090	136±26	18±2	187±58	59±3
D3	FA0018	108±29	21±3	161±58	79±5
	FA0060	95±24	22±2	145±29	88±4
D4	FA0081	98±24	21±2	162±31	87±4
	FA0088	137±19	26±2	241±46	64±2
D5	FA0100	90±15	21±1	244±49	60±2
	FA0106	128±16	21±1	198±39	65±2
D6	FA0117	83±26	23±2	238±70	53±3
	FA0118	139±21	24±2	228±52	67±3
D7	FA0086	104±25	19±2	300±70	59±3
	FA0101	103±19	26±2	243±57	63±3
D8	FA0104	127±19	23±1	207±47	63±2
	FA0108	124±18	21±2	199±44	61±2
weighted mean		114.9±4.6	21.6±0.4	180.2±9.8	66.7±0.6

Table 2.4: *Measured activity for each Hamamatsu R12669SEL2 PMT unit by HPGe spectrometry at the LSC. The weighted mean for all of them are also reported.*

2.3.1 Single electron response

In order to understand the scintillation signal in the very low energy region, a good knowledge of the PMTs response with low light intensity becomes essential. In particular, the most elementary PMT signal can be understood from characterizing the SER.

The single electron response of the PMTs used in ANAIS–112 was measured in a dedicated test bench at the University of Zaragoza, using an UV LED illumination of very low intensity and triggering with the LED excitation signal. Afterwards, SER was measured again at LSC with the background data taken along the normal operation of the detectors in ultra-low background conditions. This onsite SER extraction was performed using the peak identification algorithm developed for the ANAIS data analysis. The SER is built with peaks at the end of pulses having a very low number of peaks to avoid trigger bias, and prevent from the pile-up of

several photoelectrons. The photoelectron area is integrated in a fixed time window around the peak maximum (from 30 ns before the maximum until 60 ns after) so as to obtain the SER charge distribution. Since no external trigger is possible to determine the onsite SER charge distribution, a software threshold is applied to distinguish the last peak from baseline fluctuations. As a result, information about the SER distribution at low charge is hidden by this threshold, and in order to derive the SER mean value, only the Gaussian part of the onsite SER is fitted [192, 195].

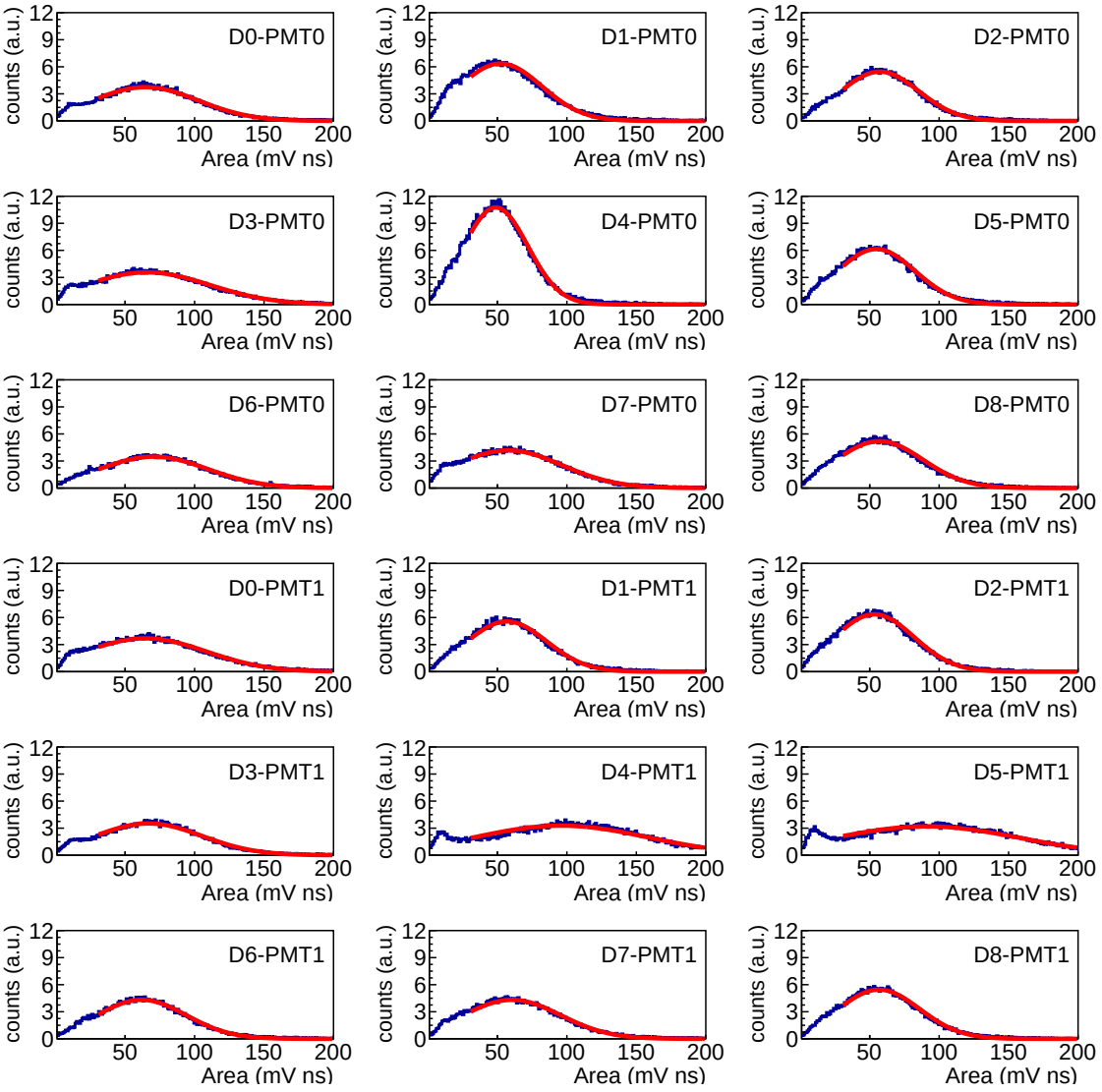

Figure 2.7: *Example of SER charge distributions for the 2 PMT × 9 detectors of ANAIS–112 for the first background run.*

Figure 2.7 shows the SER charge distribution for the 18 PMTs used in the ANAIS–112 set-up from the first background run (a period of approximately two weeks)

selecting the last peak in pulses having a very low number of photoelectrons. The response to individual photons of a PMT unit is characteristic and strongly dependent on the high voltage supply. The PMT1 of detectors D4 and D5 were operated at higher high voltage during the first year of data taking, and this can be observed as a broader SER charge distribution and a higher mean value, since the PMT gain is higher. The mean and standard deviation values obtained from the fits to Gaussian lineshapes for the first background run are summarized in Table 2.5. The PMTs are identified by 0 or 1 depending on its position in the set-up: 0 corresponds to the East side of the shielding, and 1 to the West one. The quantum efficiency (Q.E.) for every PMT unit used in the ANAIS–112 set-up is also reported.

Detector	PMT	Q.E. (%)	SER mean (mV·ns)	SER σ (mV·ns)
D0	PMT0	38.2	64.50±0.31	38.27±0.27
	PMT1	37.2	60.80±0.51	46.66±0.37
D1	PMT0	39.7	44.63±0.55	35.60±0.37
	PMT1	39.7	53.77±0.32	31.44±0.27
D2	PMT0	39.2	56.06±0.25	29.29±0.22
	PMT1	42.6	50.11±0.35	31.28±0.27
D3	PMT0	37.3	64.23±0.42	46.53±0.32
	PMT1	39.4	67.46±0.28	38.16±0.25
D4	PMT0	40.1	46.65±0.26	25.00±0.21
	PMT1	41.8	100.82±0.40	55.87±0.47
D5	PMT0	43.6	51.21±0.33	31.12±0.27
	PMT1	43.9	96.62±0.47	59.86±0.56
D6	PMT0	40.4	68.84±0.36	40.49±0.30
	PMT1	38.9	60.15±0.32	33.88±0.28
D7	PMT0	41.9	55.37±0.50	40.80±0.35
	PMT1	42.5	56.08±0.43	38.75±0.32
D8	PMT0	41.6	52.04±0.38	35.42±0.28
	PMT1	43.4	53.65±0.29	32.15±0.24

Table 2.5: *SER charge distribution fit values for the 18 PMT units of ANAIS–112 for the first background run. The quantum efficiency for every PMT unit is also given [203].*

The evolution of the SER of each PMT allows to monitor the stability of the PMT gain. Figure 2.8 shows the evolution in time of the SER mean values for PMT0 (in

black) and PMT1 (in cyan) coupled to each module in the ANAIS–112 set-up for two-weeks-long background runs along the three years of measurement. It has to be highlighted that the high voltage of PMTs coupled to D4 and D5 detectors was modified after the first year of data taking in order to stabilize the modules behaviour (see Section 2.7.2).

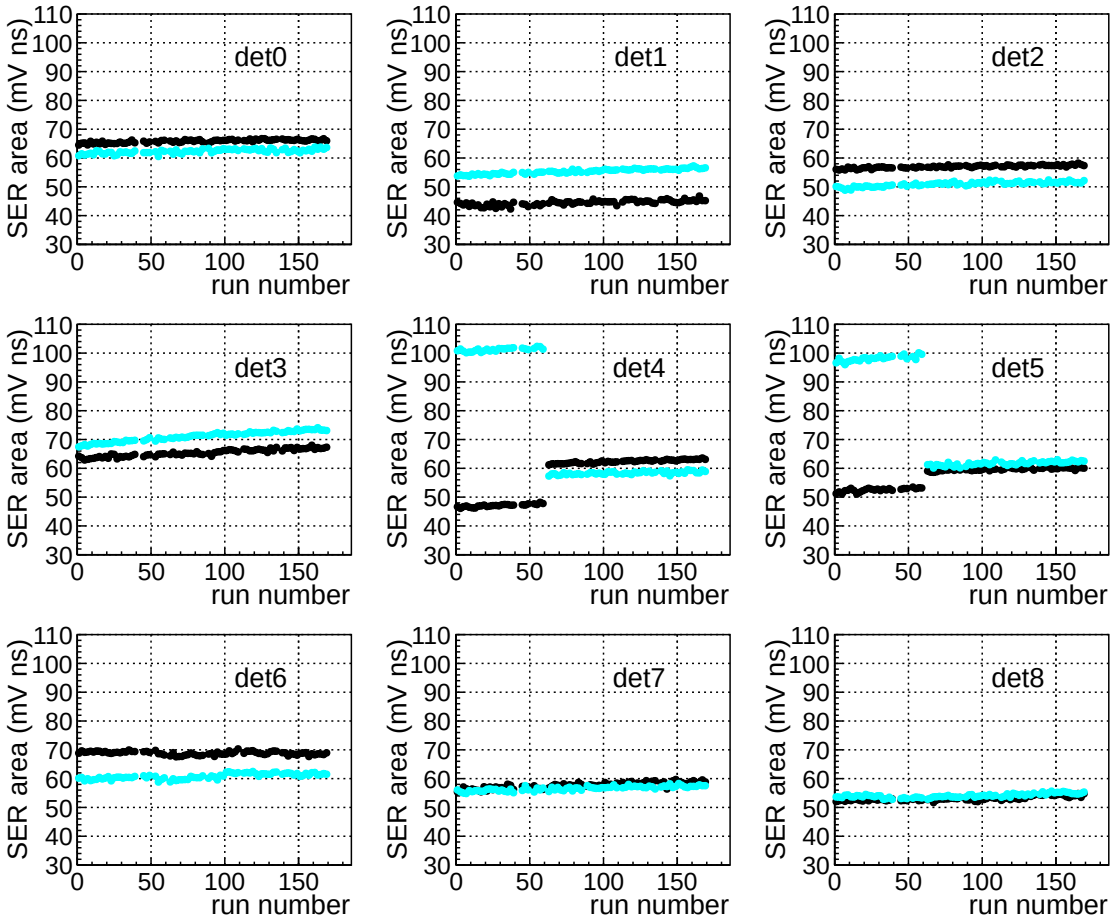

Figure 2.8: *Evolution of the SER mean values for PMT0 (black) and PMT1 (cyan) coupled to each module for two-weeks-long background runs. The high voltage of PMTs coupled to D4 and D5 was modified after the first year of data taking.*

2.4 Electronics and data acquisition system

ANAIS electronics has been tuned-up and tested through the different ANAIS prototypes and set-ups [130, 185, 204]. The final design and characterization of the whole ANAIS acquisition system is the evolution of the front-end of the previous prototypes adapted to VME electronics [192]. ANAIS acquisition hardware and

software design results to be robust and scalable. The electronic front-end has been designed taking into consideration the scintillation signal characteristics described in Section 2.2. It has to be able to get information in a wide range of energies to understand the background of the experiment, and a baseline as clean as possible is also required to reach a low energy threshold.

In summary, the following requirements were considered to the ANAIS front-end design:

- Stable trigger level at the photoelectron level is mandatory.
- Electronic noise must be minimized and controlled.
- Periodic energy calibrations must be possible to control the stability.
- Robustness and scalability are compulsory for the whole system.

For the fulfillment of the aforementioned requirements, the electronic front-end is divided into two main stages as it can be observed in Figure 2.9. These basic stages are:

- **Analog front-end**: it is responsible for processing PMT signals to reach the trigger goal and improve the signal/noise ratio. It consists of a custom-made preamplifier and several NIM modules (see Figure 2.10). The preamplifiers are located just outside the anti-radon box for low background reasons and in order to minimize the length of the cables and then, optimize the signal/noise ratio. They have two output signals: one for digitizing and one for the rest of analog front-end. This last signal is duplicated using Fan-In/Fan-Out from which the trigger signal is obtained. The triggering signal is used as input of a Constant Fraction Discriminator (CDF), which produces the trigger for signals above the threshold at a constant given fraction of the signal maximum.
- **Digital front-end**: it is responsible for digitizing the signal parameters:
  - PMT signal waveforms ($S_0(t)$ and $S_1(t)$ for PMT0 and PMT1, respectively).
  - Charge generated at the PMTs.
  - Pattern of triggering for all detectors.
  - Triggering time for all the PMT signals.
  - Real time of the trigger and accumulated live time.

This stage consists of several VME modules, which are controlled by the trigger of the analog front-end and store digital information in their buffers, which are later read by the data acquisition (DAQ) program. The design of this section can be seen in Figure 2.11. The VME modules are located outside the ANAIS hut, in an air-conditioned room whose temperature is controlled and continuously monitored.

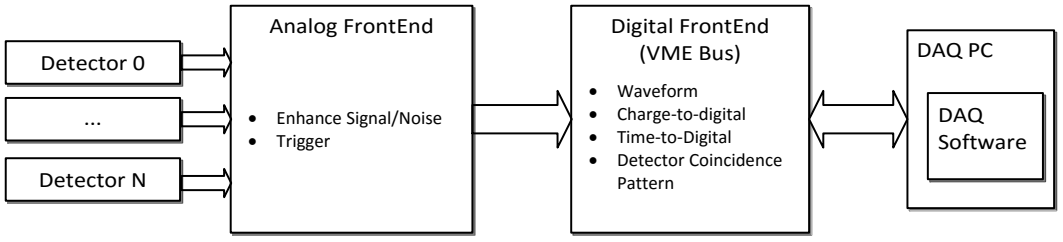

Figure 2.9: *DAQ system block diagram. From Ref. [192].*

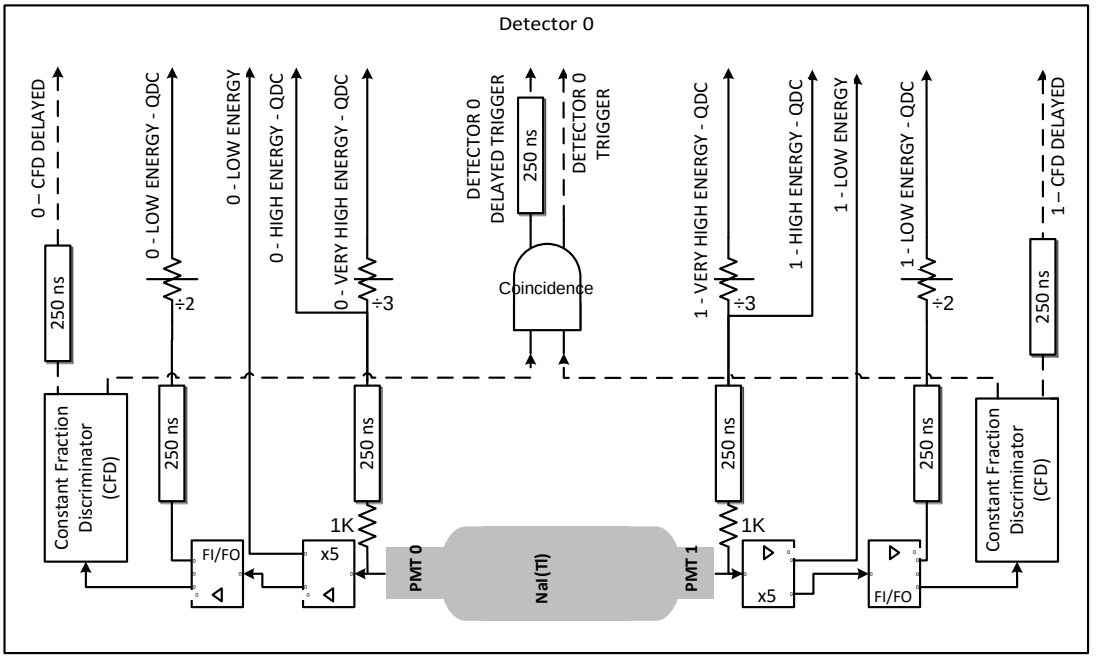

Figure 2.10: *Detector analog front-end. From Ref. [192].*

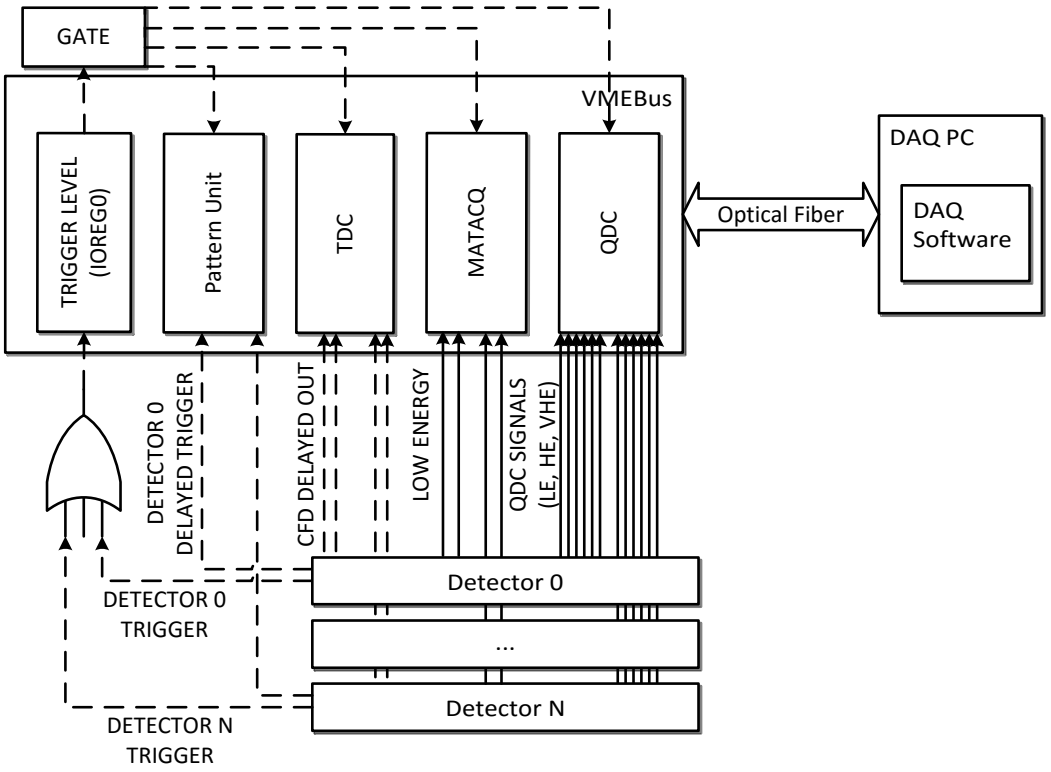

Figure 2.11: *Digital front-end. From Ref. [192].*

The charge signal coming from every PMT is separately processed and recorded. Each one is divided into: a trigger signal, a low energy (LE) signal that goes to the digitizer and a high energy (HE) signal, conveniently attenuated for high energy events. Triggering of every single module is done by the coincidence (logical AND) of the two PMT signals of any detector at photoelectron level in a 200 ns window, while the main acquisition trigger is the logical OR of individual detectors.

The building of the spectra is done by software (off-line) by integrating the $S_0(t)$ and $S_1(t)$ waveforms and adding them for each module (see Section 2.6). These waveforms are also used to discriminate bulk scintillation events in the NaI(Tl) crystals from PMT-origin events (see Chapter 3) and to distinguish alpha interactions from beta/gamma ones (see Section 2.7.1).

2.5 Muon veto system

The underground muon flux is known to have an annual modulation [205] which could mimic the dark matter modulation [173, 174]. Direct interaction of muons in

the NaI(Tl) crystals would produce high energy depositions well above the region of interest for the dark matter modulation analysis; however, muon-related events produced in the shielding (like secondary neutrons) are expected to produce signals in the ROI very similar to those expected for WIMP interactions.

The residual muon flux at LSC Hall A has been recently determined to be $(5.26 \pm 0.21) \times 10^{-3}$ μ m^{-2} s^{-1} [191], being more than four orders of magnitude lower than the surface muon flux (see Figure 2.12), but enough to have some influence in the ANAIS–112 detectors. For this reason, a plastic veto system was implemented in ANAIS–112 in order to tag muon interactions in the plastic scintillators and be able to correlate them with muon-related events in the NaI(Tl) crystals.

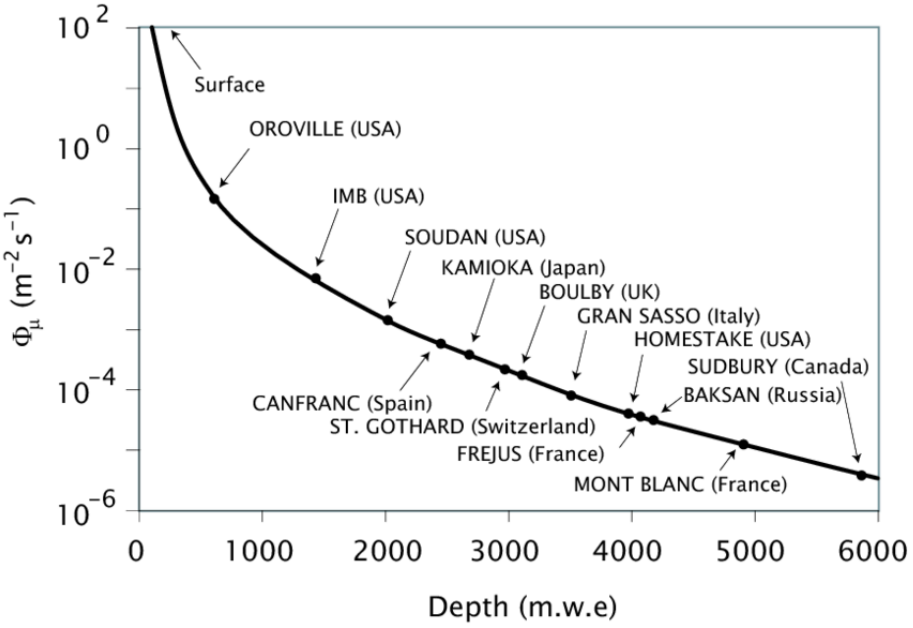

Figure 2.12: *Depths of different underground laboratories as function of muon flux. From Ref. [206].*

ANAIS–112 muon veto system consists of 16 plastic scintillators covering the top and the four sides of the anti-radon box (see Figure 2.13). This system aims to detect the residual muon flux at the detectors position in order to discard coincident events in the NaI(Tl) crystals (see Section 3.1.1) and study the possible correlation between muon interactions in the plastic scintillators and events in the NaI(Tl) crystals. For the latter purpose, a tagging strategy is carried out instead of a hardware vetoing strategy.

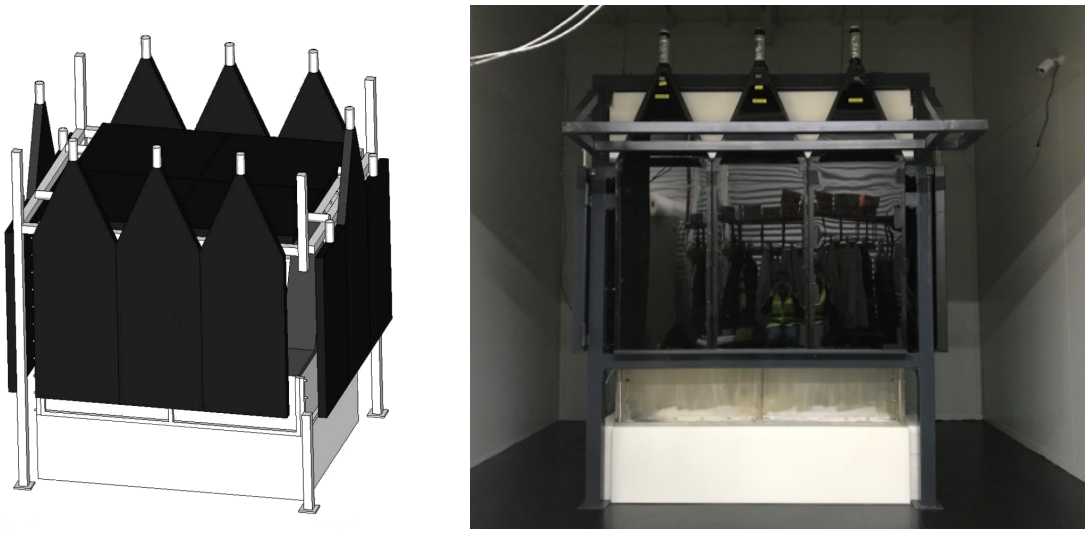

(a) (b)

Figure 2.13: *Artistic view of the ANAIS–112 veto system (a) and picture taken while ANAIS–112 commissioning (b).*

The sixteen plastic scintillators have different origin and dimensions, but all of them are 5 cm thick (see Table 2.6). Eight of them were built and used for the IGEX neutrinoless double-beta decay experiment [207], and the other eight were expressly purchased to Scionix [208] for covering the ANAIS–112 set-up. They all were tested in the previous ANAIS set-ups. The specific position of each plastic scintillator on the different faces of ANAIS–112 can be seen in Figure 2.14.

Face	Veto number	Vendor/Model	Dimensions (mm)	Surface (m^2)
Top	1, 2, 7, 8	Scionix/R500*50B1000-2ME2PX	1000 × 500 × 50	2.00
East	3, 4	Scionix/R700*50B750-2ME2PX	750 × 700 × 50	1.55
	12	Homemade	1000 × 500 × 50	
West	5, 6	Scionix/R700*50B750-2ME2PX	750 × 700 × 50	1.55
	13	Homemade	1000 × 500 × 50	
South	9, 10, 11	Homemade	1000 × 500 × 50	1.50
North	14, 15, 16	Homemade	1000 × 500 × 50	1.50

Table 2.6: *Plastic scintillators models and dimensions for the ANAIS–112 muon veto system. The equivalent surface of each face is also given.*

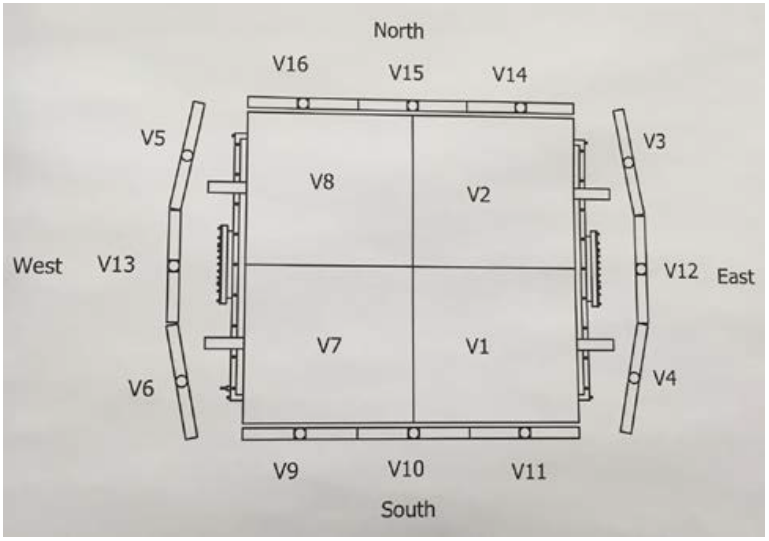

Figure 2.14: *Top view of the ANAIS–112 veto scintillators layout.*

A specific data acquisition system is used for reading the 16 plastic scintillators signals. For each event, the muon detection front-end electronics provides information on pulse digitization, multiplicity trigger pattern and real time tagging. A preliminary pulse shape analysis developed for the previous ANAIS set-ups is applied to select events attributable to muons [192]. It is based on the strong particle discrimination capability of the plastic scintillators. Background events (noise from coupled PMTs) in plastic scintillators are much faster than muon events and, therefore, the ratio of the tail pulse area to the whole pulse area becomes a quite efficient discriminating parameter. Muon selection parameters and operation conditions of the plastic scintillators have been chosen to ensure a high acceptance of real muon events and a high rejection of background events.

Table 2.7 collects the average muon rates measured along the three years of operation of ANAIS–112 for each face of the experiment layout. A higher muon flux is observed in the top vetoes than in the lateral ones, in agreement with the expected angular distribution [209, 210]. In addition, more events have been measured on the north and south faces than on the east and west faces, which is consistent with the non-homogeneous rock overburden profile at the LSC Hall B position [191]. It has to be remarked that these results are preliminary because the efficiency of the muon events selection procedure has not been taken into account. The possible contribution of background events in the plastic scintillators to the measured muon rates has not been estimated either. In any case, it can be seen that the average rate of muons measured by the top plastic scintillators of the ANAIS–112 veto system is compatible with the integrated muon flux in LSC Hall A of $(5.26 \pm 0.21) \times 10^{-3}$ μ m^{-2} s^{-1} [191].

Face	Average muon rate (10^{-3} μ m^{-2} s^{-1})
Top	5.299±0.005
North	4.805±0.006
South	4.885±0.006
East	3.491±0.005
West	3.439±0.005

Table 2.7: *Average rate of muons after applying the pulse shape analysis in the five faces of the ANAIS–112 veto system.*

It is worth noting that the DAMA/LIBRA experiment does not have any muon detection system. Although the muon flux in the LNGS [170] is one order of magnitude lower than that of the LSC, the residual muon flux could cause both direct interactions with DAMA/LIBRA crystals as well as muon-related events, as secondary neutrons, which could mimic the dark matter modulation. Nevertheless, DAMA/LIBRA collaboration completely discards muons as possible explanation of their observed signal [173, 174].

The ANAIS–112 veto system also allows for monitoring the muon interaction rates onsite along ANAIS–112 data taking, as can be seen in Figure 2.15. The figure shows the muon rate measured by each face of the veto system after applying the pulse shape analysis on a monthly basis.

2.5.1 Annual modulation search in the coincident muon rate

The seasonal time variations of the underground muon flux is a well measured effect [205, 209–220], which is correlated with the temperature of the upper atmosphere. An increase in temperature of the stratosphere causes a decrease of the air density, thus resulting in a larger fraction of π and K mesons decaying into muons energetic enough to reach underground detectors. Therefore, the atmospheric muon rate changes during the year increasing in summer and decreasing in winter.

In order to search for hints on annual modulation in the muon rate at the ANAIS–112 position, the coincident muon rates between two different faces of the veto system are considered. While most of the non-coincident events in the plastic scintillators of the ANAIS–112 veto system come from natural radioactive background or have a PMT origin, coincident events can undoubtedly be attributed to muons. Figure 2.16

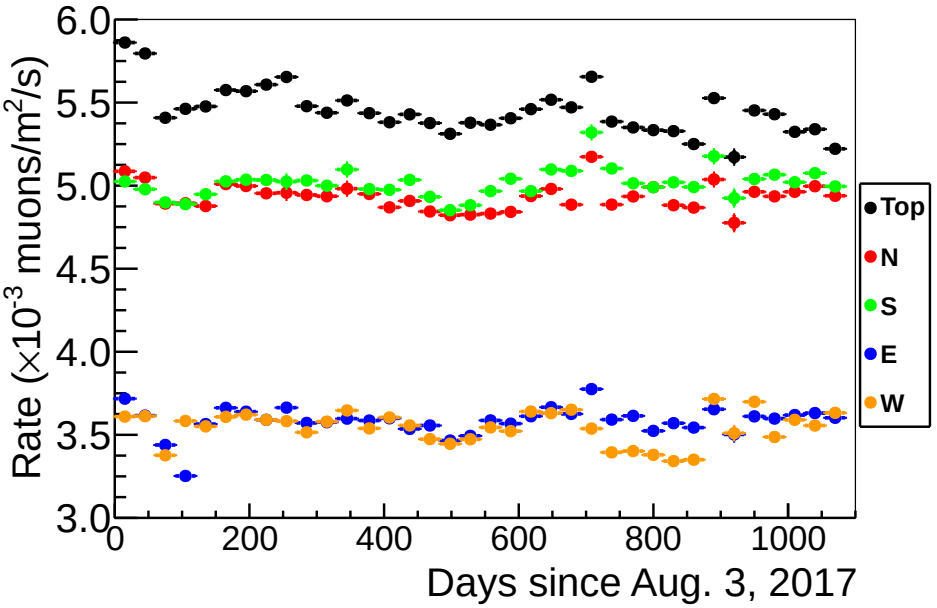

Figure 2.15: *Evolution of the muon rate on each face of the ANAIS–112 scintillator veto system on a monthly basis since August 2017.*

shows the rates of coincidences between two faces of the veto system on a monthly basis: Top-North (a), Top-South (b), Top-East (c), Top-West (d), North-South (e) and East-West (f). The variation of the coincident muon rate has been modelled with a cosine function plus a constant term:

$$R(t) = R_0 + R_m \cos \omega(t - t_0), \tag{2.1}$$

where R_0 is the non-modulated component, R_m is the modulation amplitude, $\omega = 2\pi/365$ days^{-1} and t_0 is the phase.

The results of fitting the coincident muon rates to Equation 2.1 are gathered in Table 2.8. As mentioned above, the rate of muons crossing two faces of the veto system depends on the rock overburden profile at the ANAIS–112 position and also on the size of the plastic scintillators on each of the faces considered. For this reason, the percentage of fluctuation with respect to the average in each of the face-face coincidences is used as an estimator of the muon flux variation. On average, this modulation results to be $(1.8 \pm 0.2)\%$ relative amplitude, peaking around the 20^{th} of June – 2^{nd} of July. It has to be remarked that this percentage of modulation is slightly overestimated ($\sim 0.04\%$) due to the bias (see Section 5.2.3) produced on the estimator of the modulation amplitude when a fit to a non-linear function is performed.

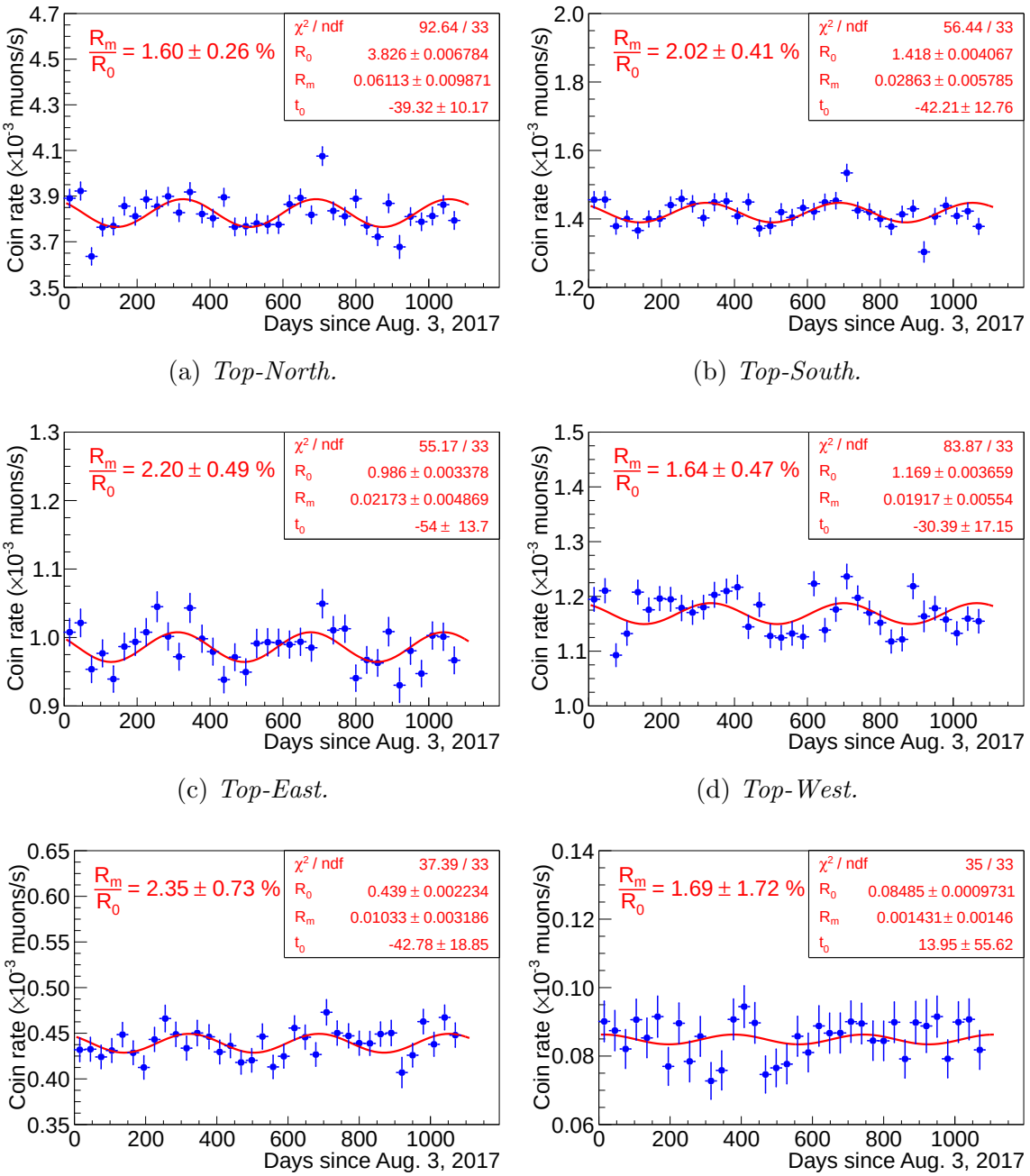

(a) *Top-North.* (b) *Top-South.*

(c) *Top-East.* (d) *Top-West.*

(e) *North-South.* (f) *East-West.*

Figure 2.16: *Fit results of the rates of coincidences between two faces of the ANAIS–112 veto system for three years of data on a monthly basis.*

In order to compare the preliminary results obtained for the modulation of the rate of coincident muons in ANAIS–112, Table 2.9 shows the results on modulation of the muon rate reported by other experiments in different underground facilities. From these results, it can be deduced that the muon rate presents a seasonal variation

Face-face coincidence	R_0 (10^{-3} μ s^{-1})	R_m (10^{-3} μ s^{-1})	R_m/R_0 (%)	t_0 (days)	χ^2 / NDF
Top-North	3.826±0.007	0.06±0.01	1.60±0.26	-39±10	92.6 / 33
Top-South	1.418±0.004	0.029±0.006	2.02±0.41	-42±13	56.4 / 33
Top-East	0.986±0.003	0.022±0.005	2.20±0.49	-54±14	55.2 / 33
Top-West	1.169±0.004	0.019±0.006	1.64±0.47	-30±17	83.9 / 33
North-South	0.439±0.002	0.010±0.003	2.35±0.73	-43±19	37.4 / 33
East-West	0.085±0.001	<0.004	<4.5	14±56	35.0 / 33

Table 2.8: *Best fit results of the rates of coincidences between two faces of the ANAIS–112 veto system for three years of data with period fixed to 1 year and unconstrained phase. Note that for east-west coincidences, an upper limit (95% C.L.) is given.*

with a relative amplitude of the order of 1.5–2%, reaching the maximum around the end of June or the beginning of July. The results obtained by ANAIS–112 at LSC are compatible with those measured in LNGS; however, the COSINE–100 experiment at Y2L has reported a lower relative modulation amplitude than the rest of experiments. Regarding the phase, the maximum obtained for the muon rate is delayed with respect to that expected for the annual modulation of dark matter (around the 2^{nd} of June).

Experiment	Location	Ref.	Live time (days)	R_m/R_0 (%)	Phase, t_0
MACRO	LNGS	[211]	608	$\simeq 2$	middle of July
MACRO	LNGS	[216]	2145	1.95±0.03	29^{th} June - 1^{st} July
LVD	LNGS	[212]	2724	1.49±0.06	20^{th} June - 20^{th} July
LVD	LNGS	[217]	8403	1.56±0.09	4^{th} July - 10^{th} July
Borexino	LNGS	[214]	1063	1.29±0.07	23^{rd} June - 5^{th} July
Borexino	LNGS	[218]	3218	1.36±0.04	1^{st} July - 2^{nd} July
OPERA	LNGS	[205]	1274	1.55±0.08	28^{th} June - 14^{th} July
COSINE–100	Y2L	[220]	952	0.6±0.2	10^{th} June - 18^{th} July
ANAIS–112	LSC	This work	1090	1.8±0.2	20^{th} June - 2^{nd} July

Table 2.9: *Results of the annual modulation of the muon rate obtained by some experiments in different underground facilities.*

2.6 ANAIS–112 data analysis and blinding strategy

The software framework used for the analysis of the ANAIS–112 data is ROOT [221]. The data acquisition system directly saves ROOT files with all the available information read from the electronic modules, mainly the PMT waveforms, QDCs values and clocks readouts (real and live times). In order to get the relevant pulse information without increasing the acquisition dead time, the required analysis is done off-line.

Each ROOT file stores the information of 25000 triggered events. These files are grouped into measurements runs as follows:

- **Background run**: package of approximately 15 days with the background data of each detector. They are numbered with an odd number.
- **Calibration run**. Approximately every two weeks the background acquisition is stopped to calibrate the detectors in energy. For this purpose, an external ^{109}Cd source is used for about 3–4 hours. They are numbered with an even number.
- **Veto run**. The acquisition of plastic scintillators of the veto system is launched independently. The saved files are numbered with odd numbers as the background runs.

The analysis of these data runs is carried out in three subsequent levels:

1. **First level**. Pulse parameters like baseline level and root mean square, pulse onset, pulse area and some pulse shape analysis parameters are calculated. The time elapsed since the last muon interaction in the veto system is also computed. Finally, the peak-searching algorithm is applied.
    - **Baseline level (DC) and root mean square (RMS)**. The mean value and standard deviation of the DC level are derived from the first points of the pulse (pretrigger region). The pretrigger region is a configurable parameter.
    - **Pulse onset (t_0)**. The pulse onset is assigned to the point where the signal overtakes a threshold level. The threshold level is configured for each PMT.
    - **Pulse area**. The pulse area is calculated as the addition of the two PMT signals since the pulse onset, subtracting the corresponding DC

contribution. It is one of the most important parameters extracted in the analysis software due to its expected linear behaviour with energy.

- **Time since the last muon veto (vts)**. The time elapsed (in seconds) since the last muon interaction in any of the plastic scintillators of the ANAIS–112 veto system.
- **Peaks in the pulse**. The number and position of peaks detected by the peak-finding algorithm [192] in each PMT signal are stored. First, the algorithm applies a low pass filter (cut frequency = 100 MHz) to eliminate the higher frequencies of the signal. Second, the minima are located from the change of sign of the first derivative of the pulse. The minima must have a height less than a software threshold to be considered as peaks. This threshold is also a configurable parameter.

2. **Second level**. The energy response of every detector is calibrated in two different ranges: high energy (HE) and low energy (LE). As explained in Section 2.7, the high energy calibration is performed with the background runs, while the ^{109}Cd calibration runs are used for the low energy calibration. Finally, the LE region is recalibrated by combining three background runs ($\sim$1.5 months) and the corresponding ^{109}Cd calibration run.

3. **Third level**. The pulse shape cut is optimized and the corresponding efficiency is calculated. In this level of analysis, LE variable is blinded for single-hit events (multiplicity 1), whereas it remains unblinded for multiple-hit events. The latter are used to estimate event selection efficiencies (see Section 3.2.2) and as control populations in the search for annual modulation (see Section 5.1).

The blind protocol for the annual modulation analysis of ANAIS–112 data was designed before data taking started. Both energy and time distribution from single-hit events in the region of interest were kept blinded since the beginning of the data taking. The fine tuning of the event rejection procedures [15], general background assessment [196] and sensitivity estimate [16] were performed using $\sim$10% of the data from the first year of measurement (34 days randomly distributed along the data taking period amounting to 32.9 days live time).

2.7 Energy calibration

The ANAIS–112 energy calibration is performed with external ^{109}Cd sources every two weeks. In order to minimize down time during the dark matter run, all the

nine modules are simultaneously calibrated using a multi-source system built in a flexible wire. The sources are outside the shielding and they are introduced inside the shielding facing the Mylar windows during the calibration keeping the system closed and guaranteeing radon-free operation. The design and implementation of this system can be seen in Figure 2.17.

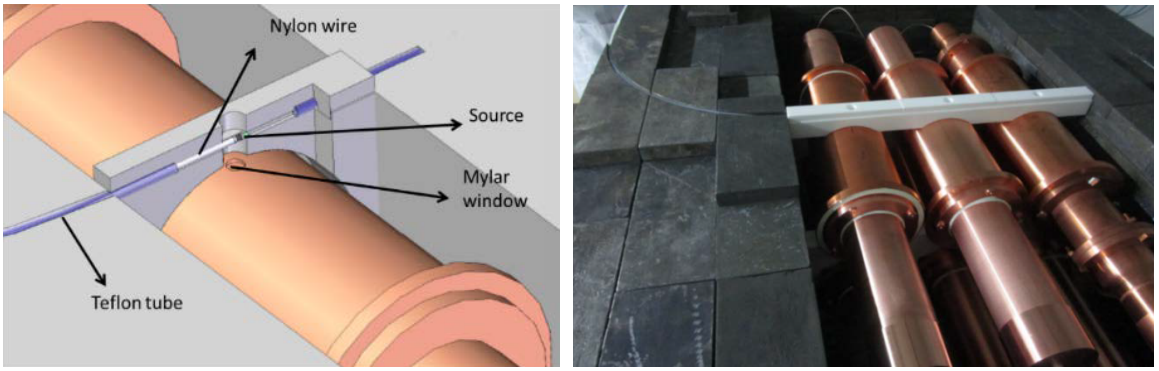

(a) (b)

Figure 2.17: *Calibration system design (a) and its implementation (b).*

^{109}Cd ($T_{1/2}$ = 461.9 days) decays by electron capture to the isomeric state of ^{109}Ag, emitting a gamma of 88.0 keV in 3.6% of the cases. K_α and K_β X-rays are also emitted with average energies of 22.1 and 25.0 keV and intensities of 69.8% and 13.8%, respectively. ANAIS–112 NaI(Tl) crystals cannot discriminate these X-rays of such close energies, and therefore a compound peak of average energy 22.6 keV is observed in the calibration spectrum. In addition to these lines, the calibration spectrum features a peak due to the presence of a cover of heat-shrink tube with Br content. The tube is used to ensure the junction of the sources to the wire. The new calibration line corresponds to 11.9 keV, the average of the two more intense K_α Br X-rays produced after photoelectric absorption of ^{109}Cd photons by Br.

In Figure 2.18 the calibration spectra for the nine modules corresponding to the first calibration run can be seen. As energy estimator, the pulse area of the sum of the digitized waveforms is used: $S_{sum}(t) = S_0(t) + S_1(t)$. The 11.9 and 88.0 keV lines are fitted to single Gaussian lineshapes added to a second-degree polynomial, while the 22.6 keV line is fitted to two Gaussian lineshapes with the same standard deviation added to a first-degree polynomial. All the three fits are shown as solid lines and the corresponding chi-squared values are given. 11.9, 22.6 and 88.0 keV lines are shown in black, red and blue, respectively.

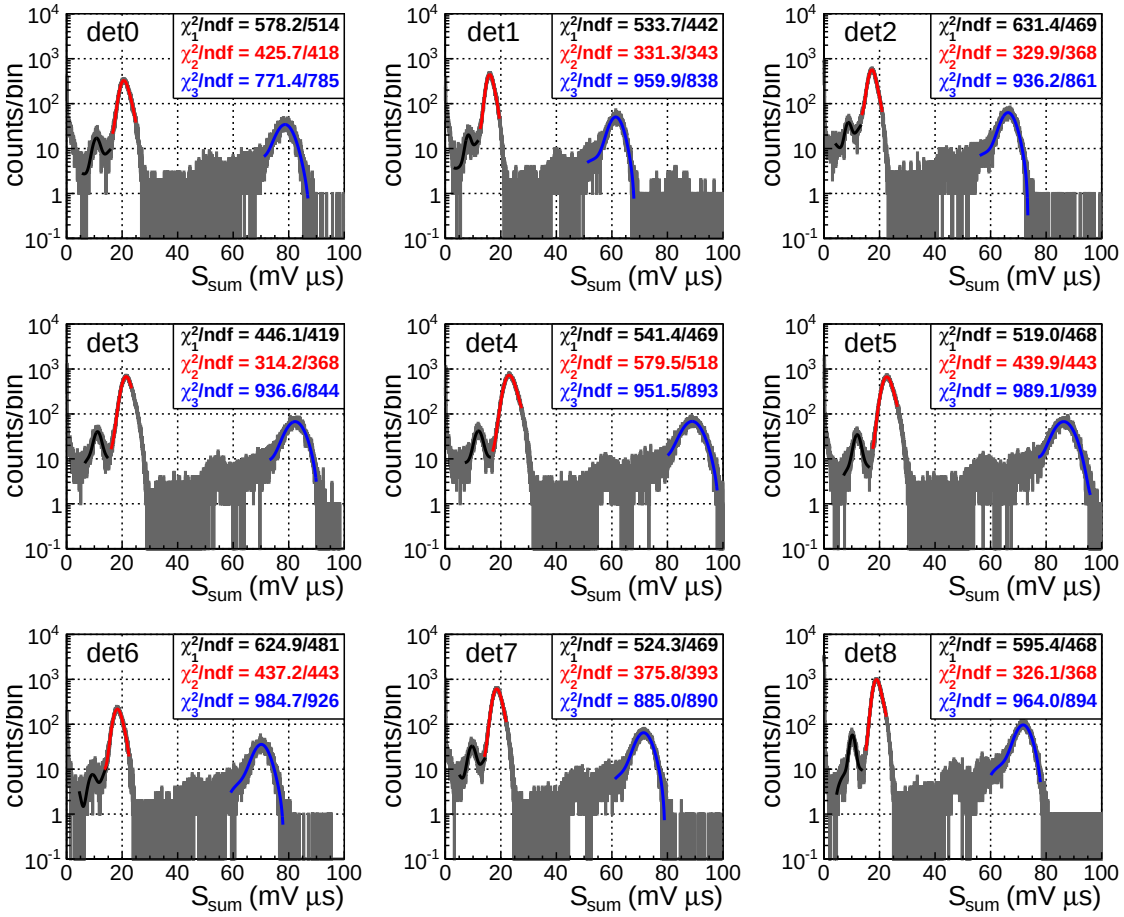

Figure 2.18: *Calibration spectra for the nine modules in the first ANAIS–112 calibration run. Fits to the 11.9, 22.6 and 88.0 keV lines are shown in black, red and blue solid lines, respectively. The chi-squared values are also given.*

These lines are used for monitoring gain stability and to correct any possible gain drift. Figure 2.19 shows the evolution of the positions of these three lines along the three years of operation. It can be observed that most of the modules have been stable during the whole period of data taking, but D4 and D5. D4 and D5 showed deviations of near 10% in the first year of operation, not related neither with high voltage instabilities in the PMT supply nor temperature, but with a change in the light sharing between the two PMTs of the module (see Section 2.8). After completing the first year of ANAIS–112 operation, D4 and D5 high voltage operation point was changed in order to reach more stable behaviour (run numbers from 62).

As commented above, the region of interest for the dark matter annual modulation search is at very low energy, below 10 keV. Nevertheless, a good high energy calibration is mandatory to validate the ANAIS–112 background model and prop-

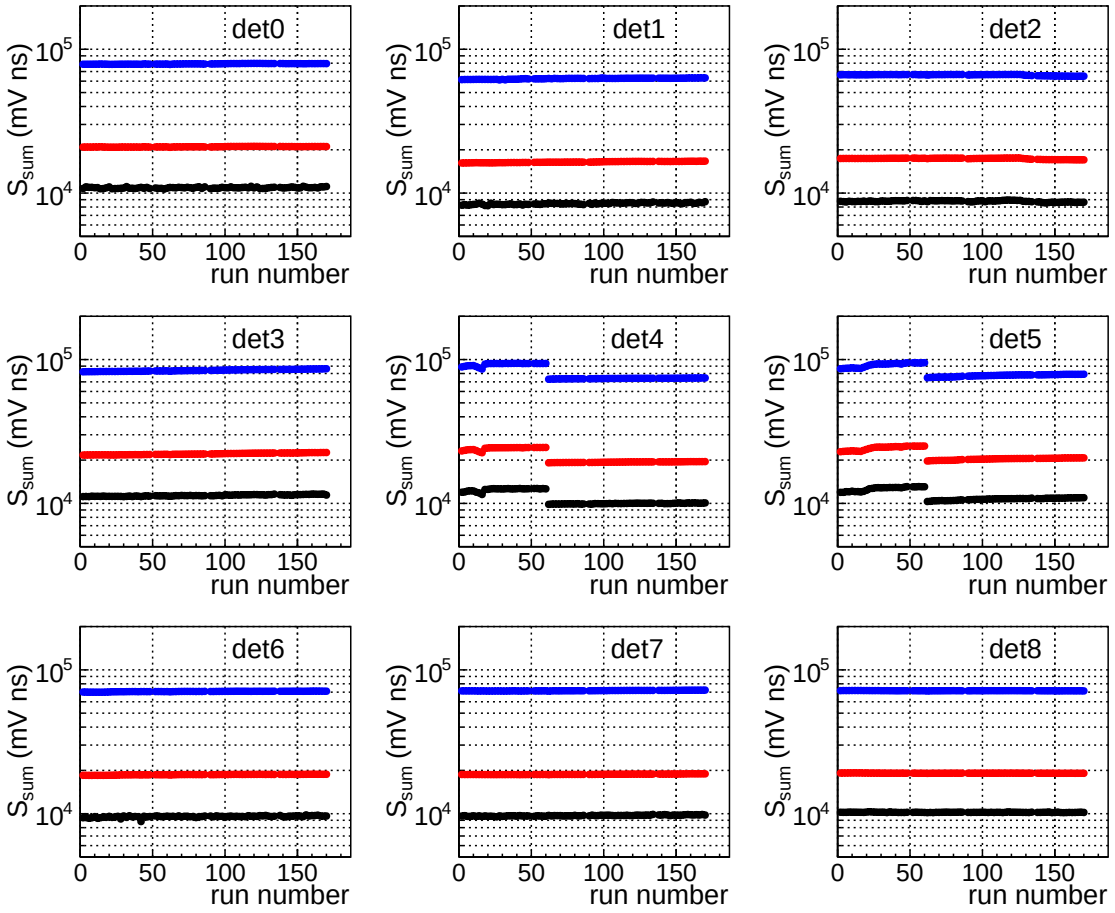

Figure 2.19: *Mean positions of the three ^{109}Cd lines in the S_{sum} variable along the three years of operation for the nine ANAIS–112 modules. In black 11.9 keV line, in red 22.6 keV line, and in blue 88.0 keV line.*

erly select ^{22}Na/^{40}K low energy events from coincidences with high energy gammas. Non-linearities in the detector response have been observed in ANAIS–112 modules, due to intrinsic non-linearities of the scintillator itself [194] and PMTs saturation effects. For this reason, specific strategies for energy calibration have been applied to ANAIS–112 data, both in the high energy (Section 2.7.1) and low energy (Section 2.7.2) ranges.

2.7.1 High energy calibration

The digitalization scale is optimized for the study of the low energy events, so the events above ∼500 keV are out of the digitizer dynamic range and pulse area energy estimator saturates. For this reason, the ANAIS–112 DAQ system (see Section 2.4) incorporates a second signal line conveniently attenuated to retain information on

the energy released by every high energy event through the use of charge-to-digital converters (QDC).

Figure 2.20 represents the pulse area versus the corresponding QDC value for detector D3 during the two first weeks of data taking. It can be observed that the pulse area parameter is clearly saturated above QDC$\simeq$700. In order to estimate the energy of events above $\sim$50 keV, the linearization of the S_{sum} response is performed using a modified logistic function (green line).

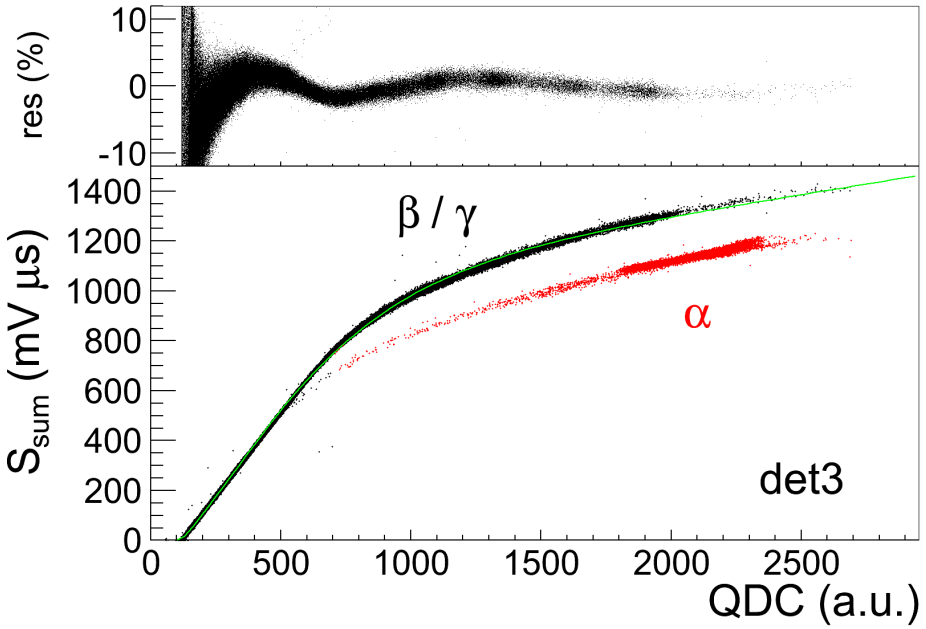

Figure 2.20: *Total pulse area for detector D3 during the two first weeks of data taking as a function of the QDC readout. The linearization of the S_{sum} signal is performed with the green line. The α population (red dots) is clearly separated from the β/γ one (black dots). The top panel shows the residuals of the β/γ population fitting to the green line.*

This double readout system also allows to discriminate α events (shown in red in Figure 2.20) from β/γ events (depicted in black). For high energy events the digitized pulses are saturated and, since α events are faster than β/γ, the integral of the pulse in the microsecond window is smaller for the same QDC value.

As there are no high energy external sources available to calibrate ANAIS–112 high energy regime, calibration of events above $\sim$50 keV is performed for each background run independently using several peaks that are easily identified in the background

data. For every detector and run, between 6 and 8 peaks are used depending on their presence in the spectrum. Among them are: 238.6 keV (^{212}Pb), 295.2 keV (^{214}Pb), 338.3 keV (^{228}Ac) together with 351.9 keV (^{214}Pb), 583.2 keV (^{208}Tl) combined with 609.3 keV (^{214}Bi), 1120.3 keV (^{214}Bi), 1274.5 keV (^{22}Na), 1460.8 keV (^{40}K) and 1764.5 keV (^{214}Bi). Each peak is fitted to one (or several, as noted) Gaussian lineshapes plus a second-degree polynomial. Eventually, the calibration is carried out by means of a linear regression between the nominal energies of the peaks and the Gaussian means.

Figure 2.21 shows the high-energy calibrated background spectrum for single-hit events (in anticoincidence, i.e., discarding coincidence events among different modules) adding all the ANAIS–112 detectors during the three years of operation. The upper panel shows the residuals ((fit – nominal)/nominal) for the positions of the main peaks identified in the background, being all of them below 5%.

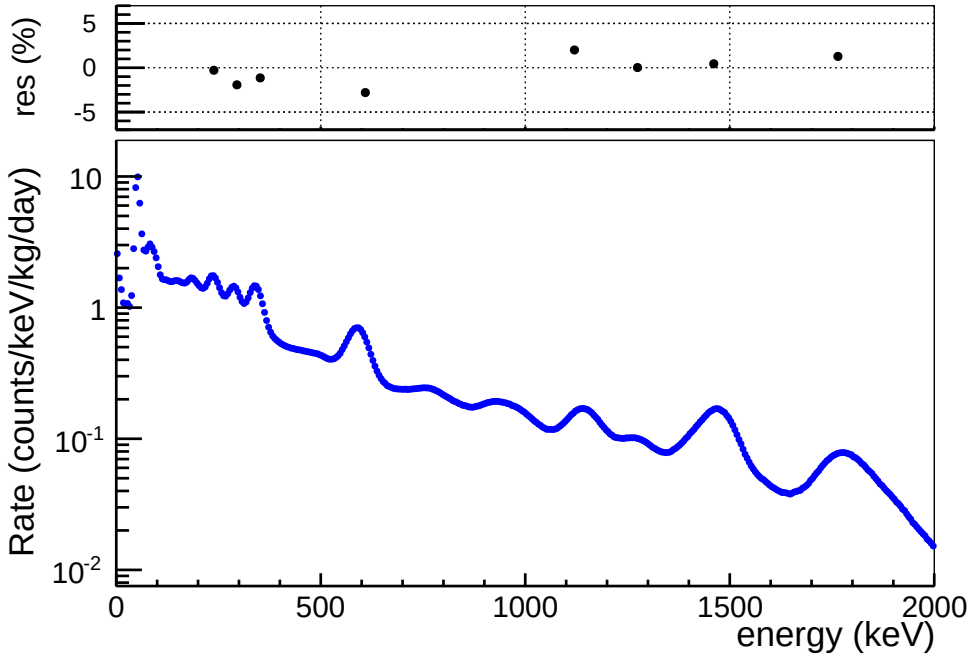

Figure 2.21: *Total high energy anticoincidence spectrum measured along the three years of ANAIS–112 operation. The top panel shows the residuals for the positions of the main peaks identified in the background.*

2.7.2 Low energy calibration

The ^{109}Cd calibration provides two peaks very close to the region of interest, namely: 11.9 and 22.6 keV. In addition to these lines, two internal lines present in the background can be added to increase the reliability of the energy calibration in the ROI,

since they are actually either in the ROI or very close to the threshold. The latter correspond to an internal contamination of ^{40}K in the bulk and the presence of ^{22}Na as a result of cosmogenic activation. These isotopes may decay via electron capture (EC), with the emission of a γ from the daughter nucleus de-excitation. The atomic de-excitation energy (0.87 keV for ^{22}Na and 3.2 keV for ^{40}K for K-shell EC, which has the largest probability) is fully contained in the crystal where the decay occurs, while the high energy γ (1274.5 and 1460.8 keV, respectively) can escape and hit another detector, thus producing a coincidence event. Figure 2.22 shows the low energy events recorded in one detector when another detector has triggered in coincidence for the three years of ANAIS–112 exposure. The spots at (1274.5 keV, 0.87 keV) and (1460.8 keV, 3.2 keV) can be ascribed to ^{22}Na and ^{40}K bulk contamination in the NaI(Tl) crystals, respectively.

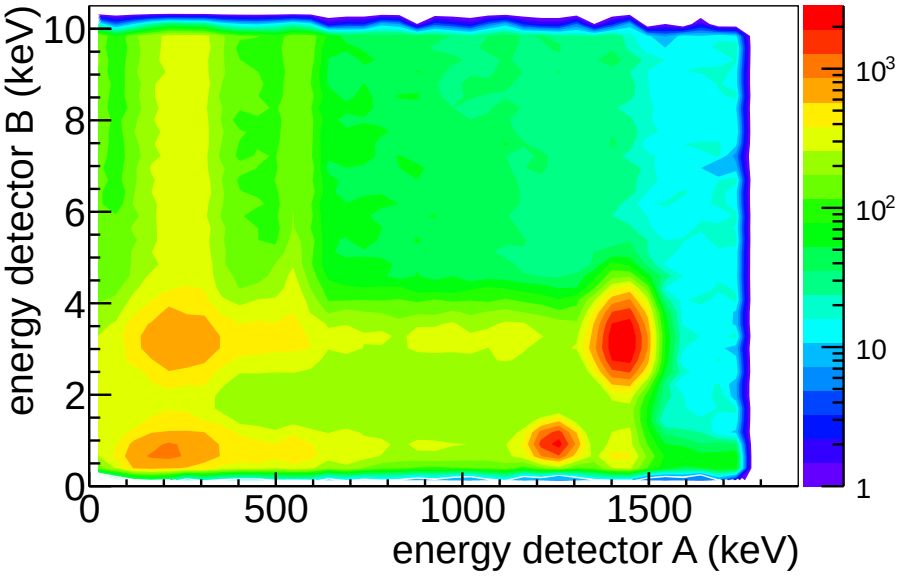

Figure 2.22: *Scatter plot of the energies recorded in two detectors triggered in coincidence when one of them has an energy deposition below 10 keV for the three years of ANAIS–112 exposure. The spots at (1274.5 keV, 0.87 keV) and (1460.8 keV, 3.2 keV) correspond to K-shell EC decays from ^{22}Na and ^{40}K in the NaI crystal, respectively.*

The ^{22}Na/^{40}K low energy peaks are excellent for LE calibration. Therefore, they are used in conjunction with the two lowest energy peaks of ^{109}Cd (11.9 and 22.6 keV) to calibrate the ROI. Whereas the calibration with the external ^{109}Cd sources is carried out periodically every two weeks, the ^{22}Na and ^{40}K peaks are obtained by accumulating three background runs ($\sim$1.5 months) in order to increase their low statistics.

The peaks registered during calibration runs are fitted to Gaussian lineshapes, while for the ^{22}Na and ^{40}K peaks, the median of the distribution is taken due to the low number of events. Figure 2.23 shows the evolution of the median positions of the ^{22}Na/^{40}K lines along the three years of operation. As was observed in Figure 2.19 for the ^{109}Cd peaks, most of the modules show a stable behaviour during the three years of data taking, except for detectors D4 and D5 until their high voltage change at the end of the first year of operation. It is worth mentioning that the ^{22}Na/^{40}K peaks selected by coincidence requirement are polluted with a population of very fast low energy events (likely Cherenkov light from PMTs) in coincidence with a high energy deposition in another crystal. As explained in Section 3.1.2, they can be removed with a pulse shape cut.

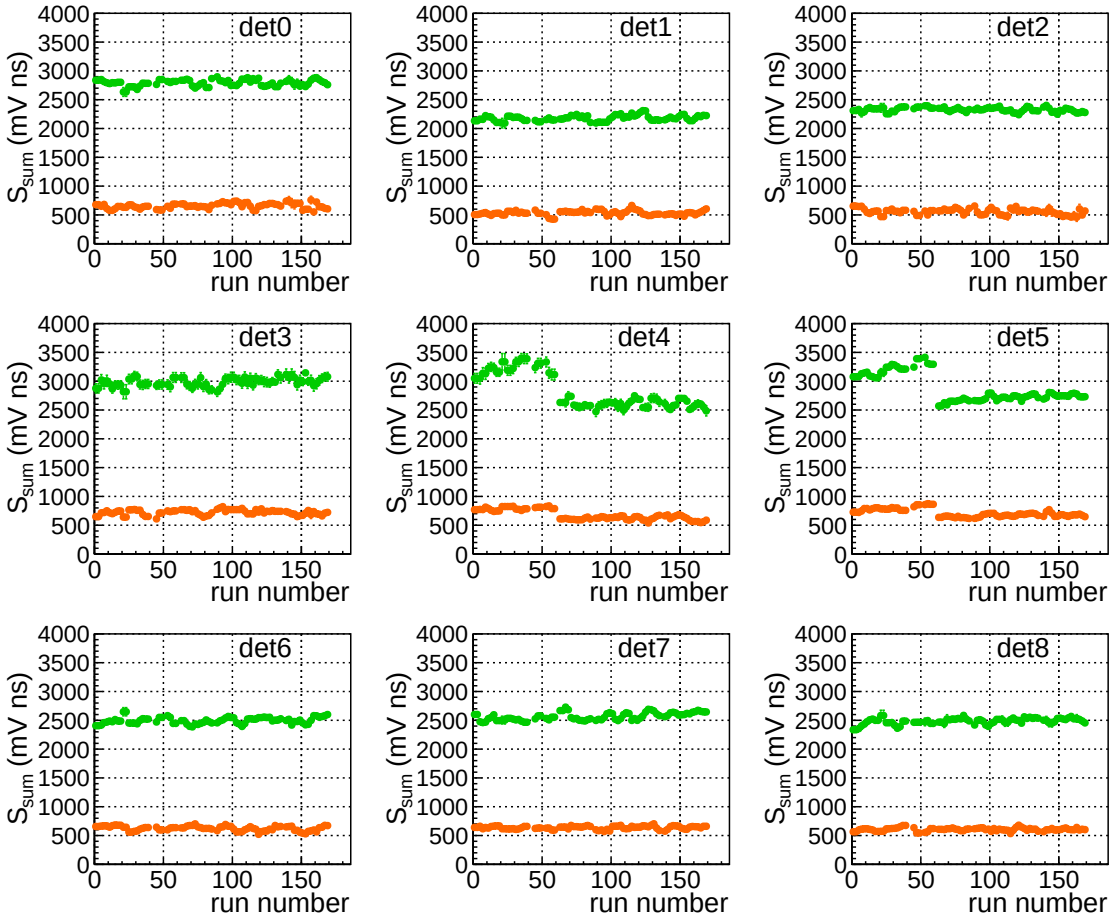

Figure 2.23: *Median positions of the ^{22}Na and ^{40}K lines in the S_{sum} variable along the three years of operation for the nine ANAIS–112 modules. In orange 0.87 keV line, and in green 3.2 keV line.*

Finally, an unweighted linear fit on the expected energies against the positions of the peaks for every detector is performed using a linear function (see Figure 2.24), and the recalibration of the low energy events (below 50 keV) is carried out. In spite of accumulating 1.5 months of background runs to estimate the position of the coincident ^{22}Na and ^{40}K peaks, their uncertainty is still much higher than that of the ^{109}Cd peaks. For this reason, an unweighted linear fit is decided to be used and, subsequently, a Monte Carlo simulation is used to estimate the effect that the uncertainty in the calibration peaks has on the rate of events in the region of interest (see Section 4.1.4).

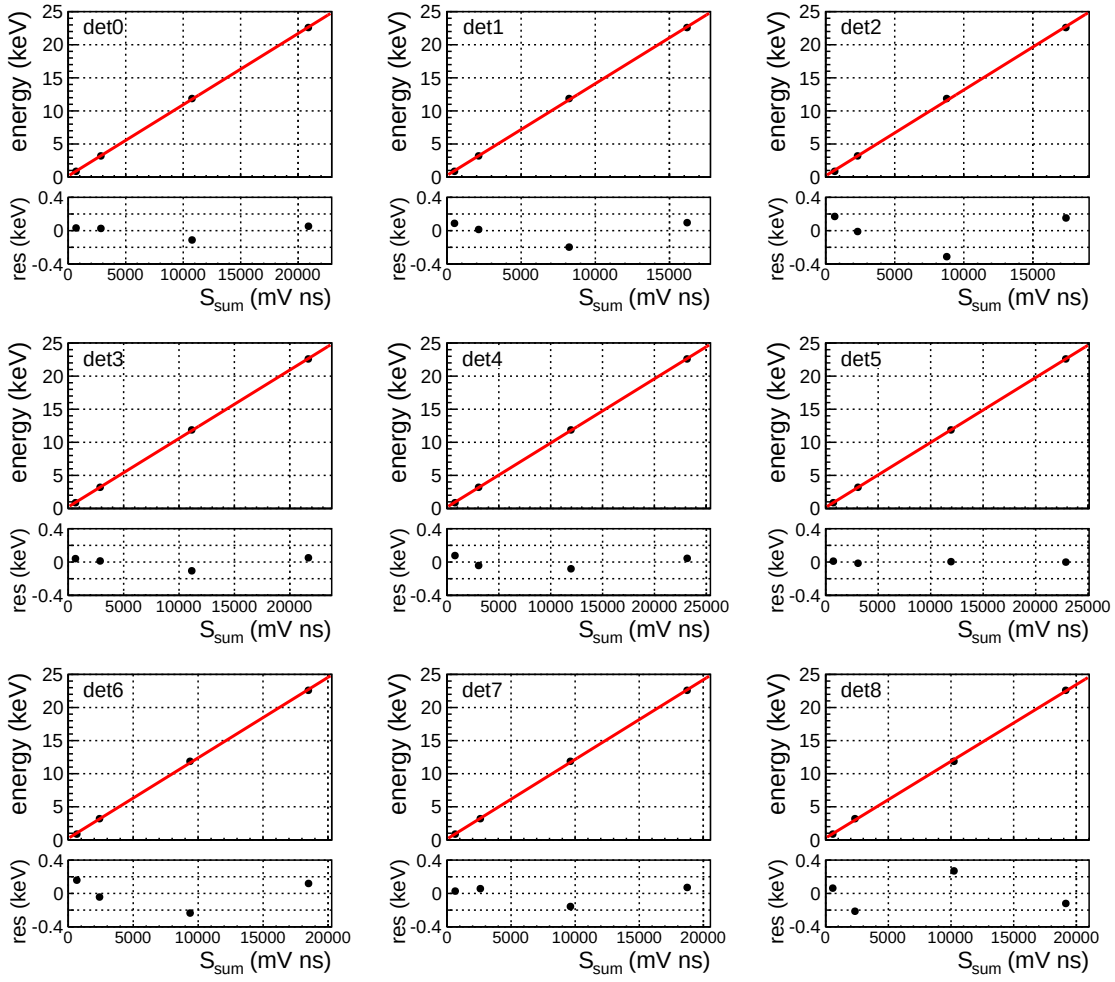

Figure 2.24: *Low energy calibration for all the ANAIS–112 detectors during the two first weeks of data taking, combining information from ^{109}Cd calibration runs and 0.87 keV and 3.2 keV lines from ^{22}Na and ^{40}K in the background, respectively, selected by coincidences. Residuals of the linear fit for each module are also shown.*

The calibration peaks are also used to compute the resolution of ANAIS–112 in the low energy region. All background runs and all calibration runs are added to estimate the standard deviation of the ^{22}Na/^{40}K and ^{109}Cd peak relative to their mean position, respectively. The ^{22}Na and ^{40}K peaks are fitted to a Gaussian lineshape plus a linear background, whereas the 11.9 and 22.6 keV peaks from ^{109}Cd are fitted to two and four Gaussian functions plus a quadratic background, respectively. The Gaussians for the 11.9 and 22.6 keV lines are constrained to have the same width and their relative intensities and positions are fixed to the two K_α Br X-rays and the four more intense Ag X-rays, respectively. Figure 2.25 shows the energy resolution as a function of energy. It is very well reproduced by a $\alpha + \beta \cdot \sqrt{E}$ function. Fit results are shown in the upper panel, while residuals are displayed in the lower panel.

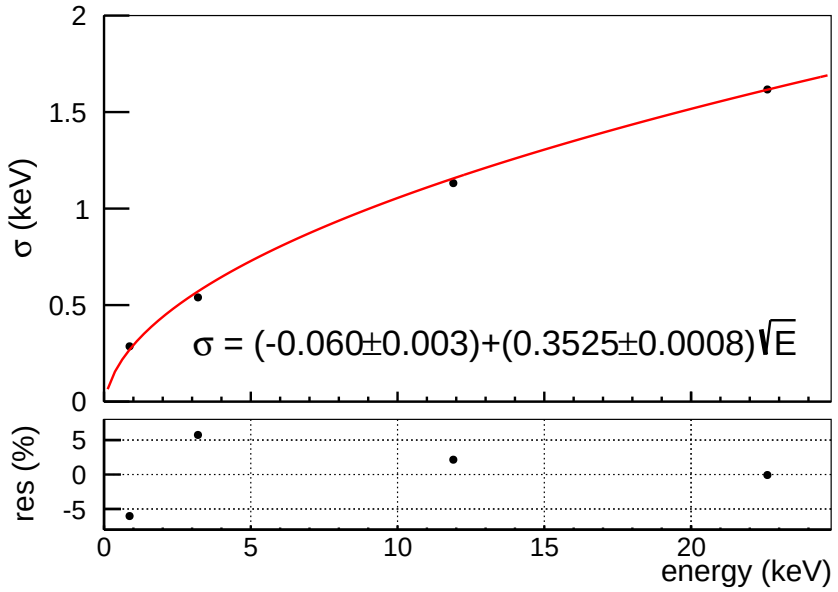

Figure 2.25: *Energy resolution of the calibration peaks as a function of energy. Red line corresponds to the fit to a $\alpha + \beta \cdot \sqrt{E}$ function, showing in the upper panel the values of the fitted parameters. The lower panel shows the residuals for the positions of the calibration peaks.*

2.8 Light collection

The light collection is one of the most relevant parameters in a low threshold scintillation experiment because it contributes strongly to the achievable energy threshold, succesful implementation of PMT noise rejection procedures, and energy resolution. Because of this, careful studies have been carried out on ANAIS prototypes [130] and for Alpha Spectra modules in previous ANAIS set-ups [192, 195].

In order to derive the total light collected, the single electron response (SER) charge distribution for every PMT has to be measured, and then compared to the charge response for a well-known deposited energy in the NaI(Tl) crystals. For this purpose, the 22.6 keV line from ^{109}Cd calibration source is used.

The light collected by each of the PMTs coupled to the ANAIS–112 modules is calculated as the ratio between the mean pulse area corresponding to the 22.6 keV calibration line and the mean of the SER pulse area distribution described in Section 2.3.1. Table 2.10 summarizes the global light collection of the nine ANAIS–112 detectors derived from three years exposure, as well as the light collection at every PMT. It must be remarked the outstanding light collection measured for the nine modules, at the level of 15 photoelectrons/keV. Only D6 module shows a light collection slightly below 13 phe/keV.

Detector	PMT light collection (phe/keV/PMT)	Total light collection (phe/keV/module)
D0	7.060±0.005 7.418±0.008	14.48±0.01
D1	7.76±0.01 6.891±0.008	14.65±0.02
D2	6.59±0.01 7.68±0.02	14.27±0.03
D3	7.111±0.009 7.230±0.007	14.34±0.01
D4	7.01±0.03 7.33±0.03	14.34±0.01
D5	7.54±0.04 7.26±0.06	14.80±0.03
D6	6.379±0.008 6.355±0.008	12.73±0.01
D7	7.24±0.01 7.32±0.01	14.56±0.02
D8	7.99±0.01 7.84±0.01	15.83±0.02

Table 2.10: *Total light collected per unit of deposited energy by the nine NaI(Tl) modules of ANAIS–112 derived from three years exposure. The light collection at every PMT is also reported.*

These light collection values are higher and more homogeneous than those reported for the DAMA/LIBRA modules (5.5–7.5 phe/keV) [200], and similar to those of the modules used by COSINE–100 [17]. The very good optical properties of our crystals, the high quantum efficiency Hamamatsu PMTs (see Table 2.5) and the good optical coupling between crystals and quartz windows and between quartz windows and PMTs are some of the reasons why the light collection is so high.

Light collection is continuously monitored by using periodic external calibrations with ^{109}Cd sources and the SER derived from the background run closer to every calibration run. Figure 2.26 shows the evolution of the light collected per PMT (black for PMT0, cyan for PMT1) and per module (in red) along the three years of ANAIS–112 data taking. It has to be highlighted that all the modules show a quite stable total light collection along the three years of operation. Slight decreases are observed in most of them, but module D5. Regarding the light collected at each PMT, all of them also show a quite stable behaviour, except D4 and D5 modules during the first months of measurement. D4 and D5 detectors showed a still unexplained anticorrelation in the light collected at each PMT. This behaviour, which was correlated with the instability in the gain observed in these two modules (see Figure 2.19), was corrected after the high voltage change carried out at the end of the first year of data taking.

2.9 ANAIS–112 stability

As commented in Section 2.1.3, monitoring the stability of all environmental and experimental parameters is mandatory for an experiment devoted to search for the annual modulation of dark matter. For this reason, the temporal evolution of some critical data acquisition parameters and different environmental parameters are studied in Section 2.9.1 and Section 2.9.2, respectively. For the latter, a slow-control system has been specifically designed.

2.9.1 Data taking stability

In this section, it is studied the evolution of some acquisition parameters, such as gain, light collection or acquisition rate, whose variations could mimic an annual modulation.

The stability of the energy calibration of all ANAIS–112 modules is crucial. The total response of each module to a given energy deposition can be modified by

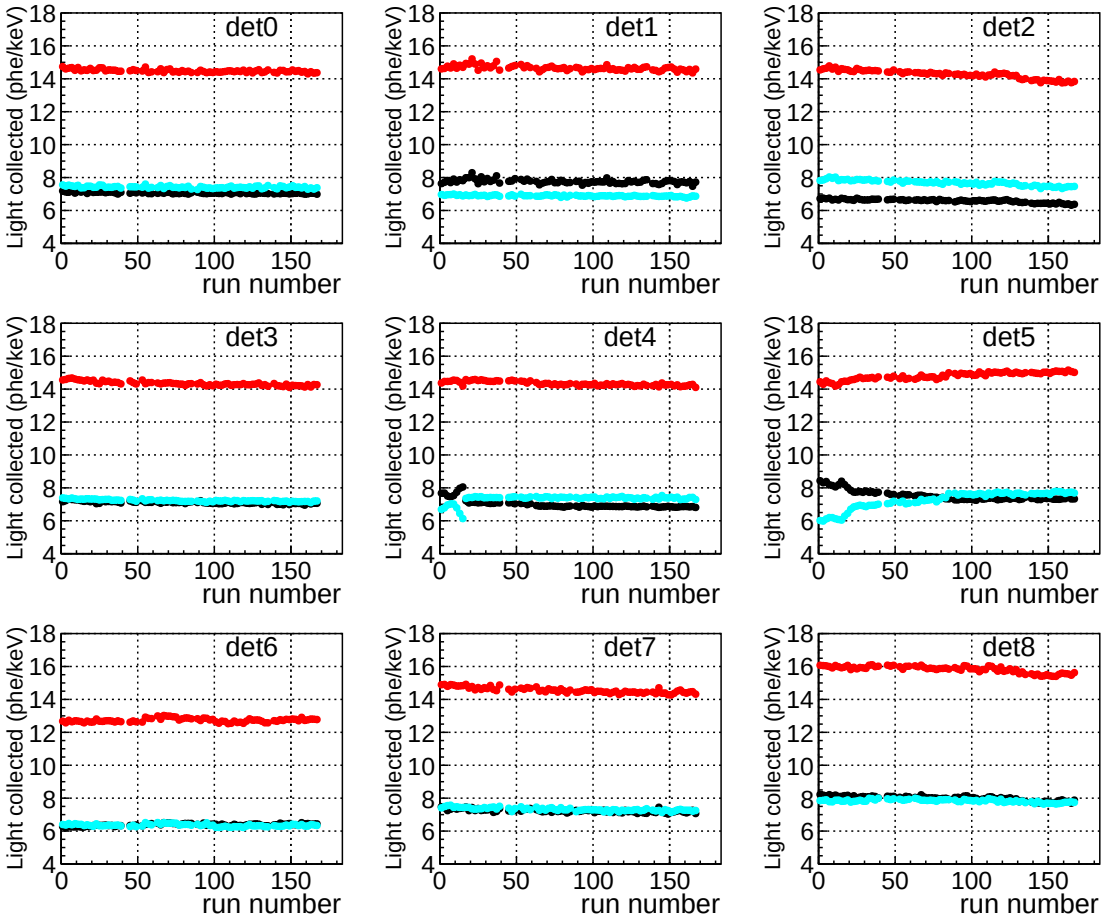

Figure 2.26: *Evolution of the light collection for the nine NaI(Tl) modules along the three years of ANAIS–112 data taking. Solid red dots correspond to the total light collected per module, whereas black and cyan dots correspond to the PMT0 and the PMT1 values, respectively.*

changes in the light collection and PMT gain, but the calibration in energy is able to correct it.

- **PMT gain stability**. As discussed in Section 2.3.1, the gain of the photomultipliers coupled to each ANAIS–112 module is directly monitored by the single electron response. The evolution of the SER mean values for PMTs has been shown in Figure 2.8 and a very stable behaviour during the three years of data taking is observed, except for PMTs coupled to D4 and D5 modules until their high voltage change at the end of the first year of operation.

- **Light collection stability**. As can be seen in Figure 2.26, no large variations are observed in the light collected by each ANAIS–112 module, with the exception of D4 and D5 modules for the reason just explained above. To better observe these variations, the deviations of the light collection with respect to

the mean value have been displayed in Figure 2.27. The upper panels show the deviation of the light collection per module (in red), while the lower panels show it per PMT (black for PMT0, cyan for PMT1). For D4 and D5, different average values have been considered for the periods before and after the high voltage change. The strong variability (∼10%) shown during the first year of the PMTs coupled to D4 and D5 has turned out to be corrected in subsequent years (<2%). The rest of the modules show a very stable behaviour during the three years of data taking, with a deviation in the light collected per module and per PMT of less than 2%, which increases to 4% for D2 module.

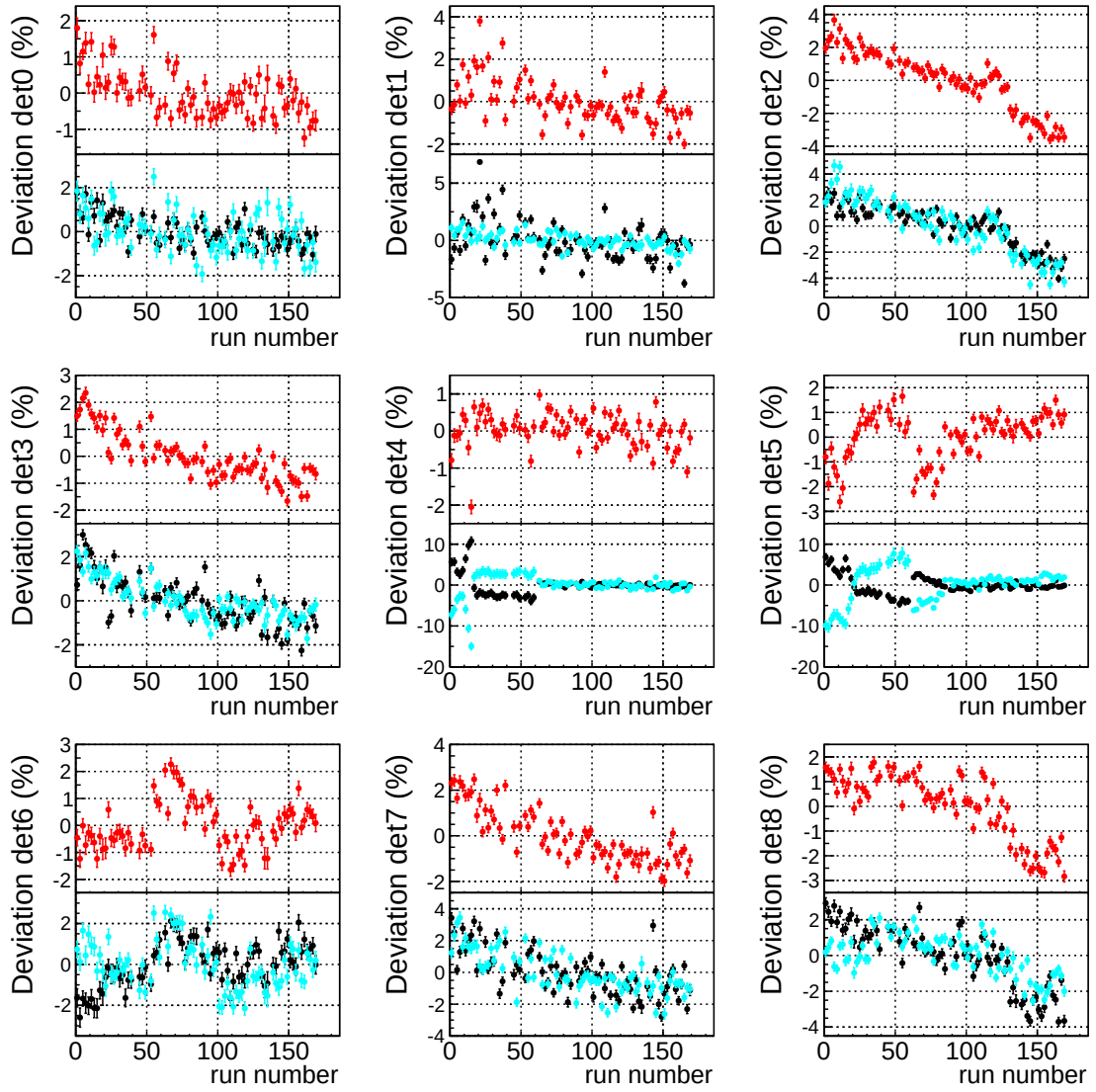

Figure 2.27: *Evolution of the light collection for the nine NaI(Tl) modules along the three years of ANAIS–112 data taking, shown as relative deviation with respect to the average values. The total light collected per module is shown in red in the upper panels, whereas the light collected per PMT is shown in black for PMT0 and cyan for PMT1 in the lower panels.*

- **Calibration stability**. The upper panels in Figure 2.28 show the relative deviation in the position of the three lines observed in the ^{109}Cd calibration runs along the three years of data taking: 11.9 keV in black, 22.6 keV in red and 88.0 keV in blue. The lower panels show the deviations in the position of the 0.87 keV (in orange) and 3.2 keV (in green) lines from ^{22}Na and ^{40}K in the background, respectively, selected by coincidences. Regarding the ^{109}Cd lines, the largest variability ($\sim$10%) is observed in detectors D4 and D5 during the first year of measurement before the high voltage change. The behaviour of the different modules has been quite different in the three years of data taking: D0, D6 and D7 are stable at the level of $\pm$1%, D8 is very stable at the level of $\pm$0.5%, D1 and D3 present a similar drift to higher values (of the order of 1.3%/year), as also do D4 and D5 after the high voltage (1.3%/year for D4 and 3%/year for D5), whereas D2 suffered a sudden gain change ($\sim$4%) in November 2019 (run number 131). With respect to the ^{22}Na/^{40}K coincidence lines, most of the detectors show fluctuations of the order of $\pm$10% in the S_{sum} value of the 0.87 keV from ^{22}Na, except D0, D1 and D2 which reach up 20%. The fluctuations in the S_{sum} value of the 3.2 keV from ^{40}K are less than $\pm$5% for all detectors. In any case, the calibration procedure allows to correct for drifts or changes in the detector response.

- **Trigger rate stability**. Figure 2.29 shows in black the total acquisition rate of ANAIS–112 along the three years of operation, as well as the trigger rate per module in different colours properly indicated in the legend. It is observed that the total trigger rate is $\sim$6 Hz, being the acquisition rate of each detector below 1 Hz. High-trigger periods are also observed in the figure. All of them are related with changes occurring with the supply of gas overpressure to prevent radon entrance into ANAIS–112 shielding. In the first year, the gas used for flushing ANAIS–112 shielding was provided by the LSC general gas supply, by boiling off commercial liquid nitrogen, and the high-trigger rate periods correspond to dewar exhaustion. Afterwards, boiled-off liquid nitrogen was replaced by nitrogen from pressurized gas bottles. In January 2019, a new high-trigger period was observed as a consequence of the replacement of the nitrogen gas supply by radon-free air provided by the LSC to all experiments. Although the LSC radon-free system works properly for the rest of the experiments located in the LSC, it produces an undesired effect on ANAIS–112, so nitrogen gas bottles were used again to purge the ANAIS–112 shielding. Since October 2019, boiled-off nitrogen was again used to flush ANAIS–112 shielding, but this time, the liquid nitrogen was produced at the LSC new air liquefaction system and a dewar specifically devoted to ANAIS used for the evaporation.

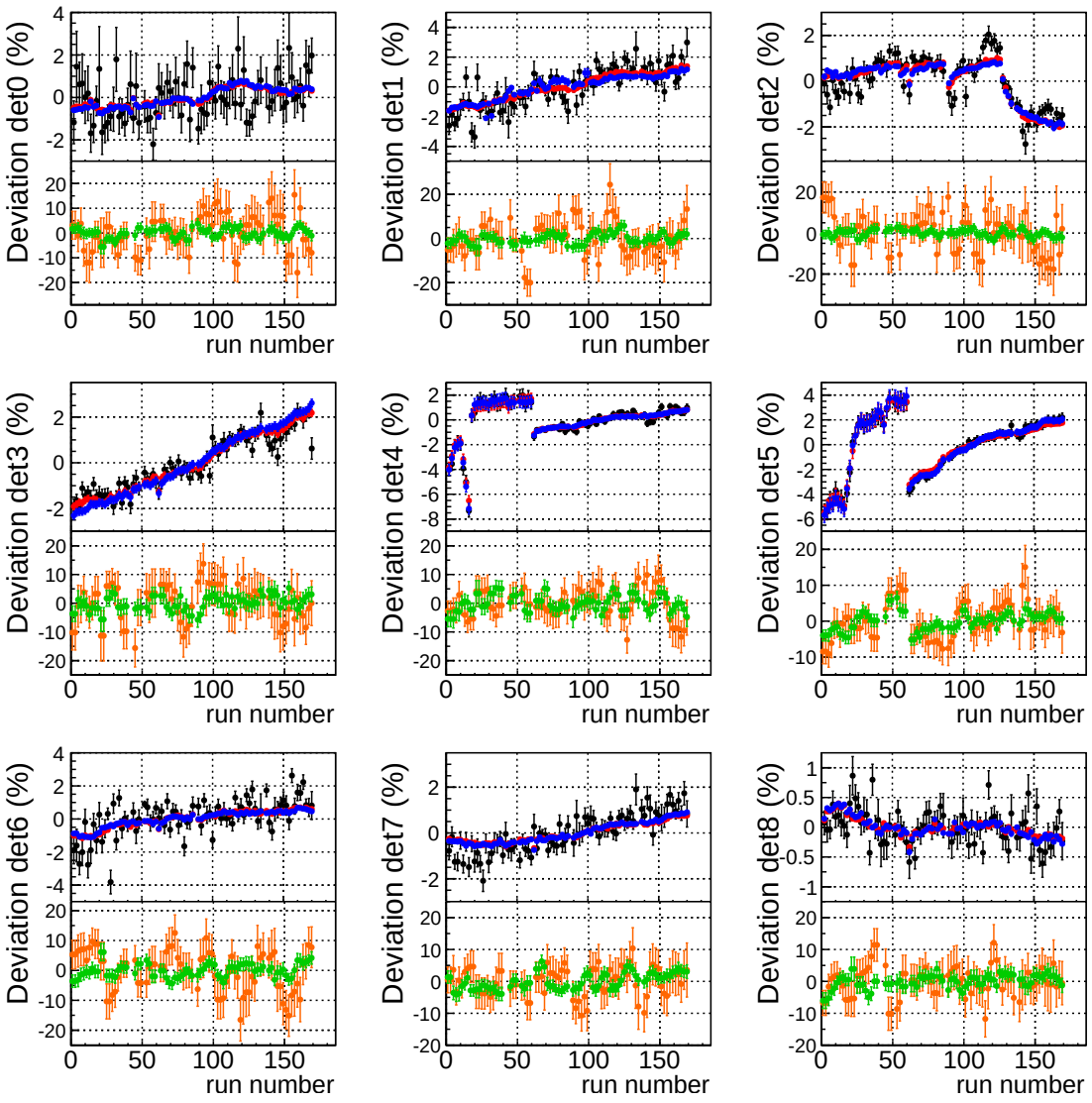

Figure 2.28: *Evolution of the S_{sum} value of the calibration lines along the three years of ANAIS–112 data taking, shown as relative deviation with respect to the average values. Upper panels show the relative position of the lines 11.9, 22.6 and 88.0 keV from ^{109}Cd in black, red and blue, respectively. Lower panels show the deviation of the lines 0.87 and 3.2 keV from ^{22}Na and ^{40}K in orange and green, respectively.*

This change produced both a small increase and instabilities in the acquisition rate, fluctuating along the week, in correlation with the level of nitrogen in the ANAIS dewar. In March 2020, an attempt was made again to change the ANAIS–112 purge system to the radon-free air provided by the LSC, but after observing the increase in the trigger rate, it was returned to boiled-off nitrogen gas from LSC liquified air.

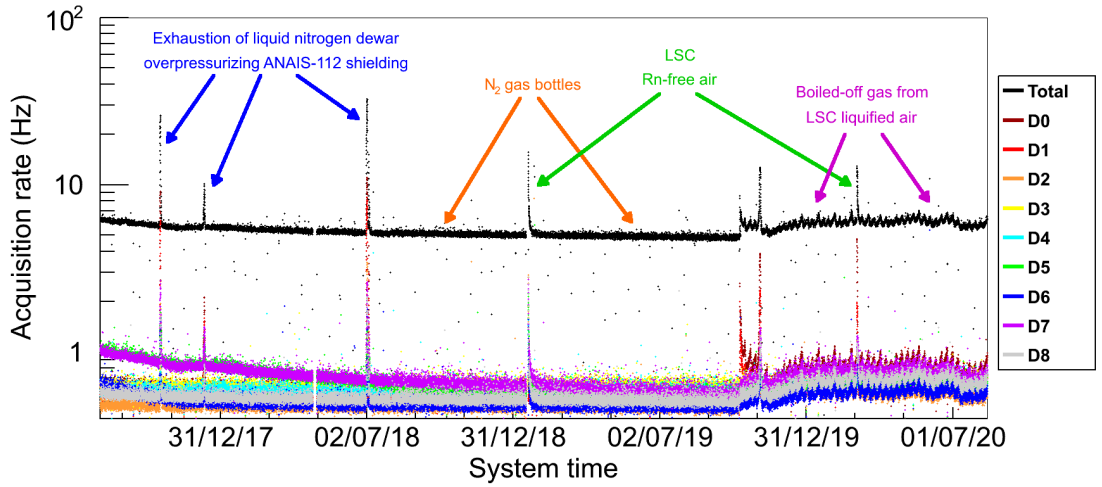

Figure 2.29: *The ANAIS–112 trigger rate (calculated in 3600 s time bins) from August 2017 until August 2020. Total rate is shown in black, whereas the acquisition rate of each detector is shown in different colours indicated in the legend.*

The increase in total trigger rate since October 2019 is responsible of the small increase in the dead time observed in the third year of data (see Table 2.1).

There is still no explanation for the increase in the acquisition rate of ANAIS–112 when using the radon-free air provided by the LSC. However, the effect is clearly not related with radon content in the air, because coincidence rates are very stable and not affected, and the effect is by about one order of magnitude too large to be due to gammas from radon progeny. In either case, ANAIS–112 total trigger rate is dominated by random photoelectron coincidences which can be easily removed requiring more than one peak in the pulse at every PMT of a given ANAIS–112 module, as can be seen in Figure 2.30 (red dots). The event rate after rejecting those events having only one peak in each PMT results to be approximately 3 Hz, with a very stable behaviour. It has to be remarked that the ANAIS–112 event selection protocol (see Section 3.1.3) requires more than 4 peaks in each PMT signal to be considered a bulk scintillation event. Therefore, the total rate of selected events is not affected by the high-trigger periods occurred along the three years of operation.

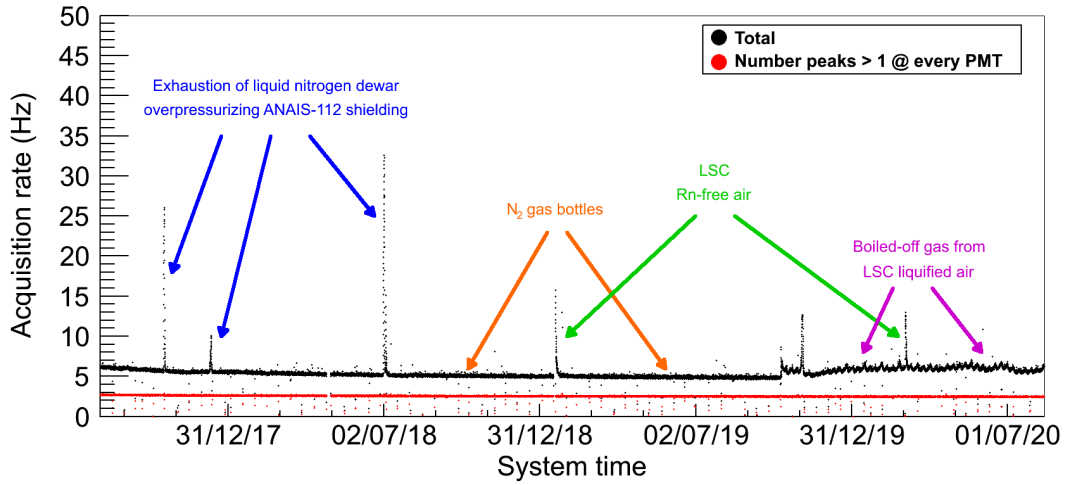

Figure 2.30: *The ANAIS–112 trigger rate (calculated in 3600 s time bins) from August 2017 until August 2020. Total rate is shown in black, and the rate of events having more than one peak detected by the peak-finding algorithm in every PMT in red.*

2.9.2 Slow-control and environmental parameters

The ANAIS–112 slow-control system is responsible for the monitoring and storage of all relevant environmental parameters, such as temperature. All the data are saved every few minutes and alarms have been set on the most relevant parameters sending an alarm message to ANAIS GLIMOS through Telegram in order to restore the standard conditions as soon as possible. Figure 2.31 displays the graphics user interface of the slow-control system.

The list of parameters monitored in ANAIS–112 is:

- **Temperature**. A relation between the acquisition rate and the temperature at the electronics rack has been observed in previous ANAIS set-ups [192], as well as between the coincidence window and temperature. The temperature instability can have a large effect in all the acquisition stages, and therefore, temperature is measured at different locations: inside the shielding, inside the ANAIS hut and at the electronics.

  Figure 2.32a shows the evolution in time along the three years of ANAIS–112 data taking of the temperature inside the ANAIS–112 shielding (T_{int}) where the detectors are located. This temperature follows the external conditions at the LSC Hall B. It varies from 18.1 to 20.3 °C, having a mean value of 19.5 °C and standard deviation of 1.7 °C. Especially relevant is the observed decrease (and subsequent increase) in temperature in the Hall B and inside the ANAIS–

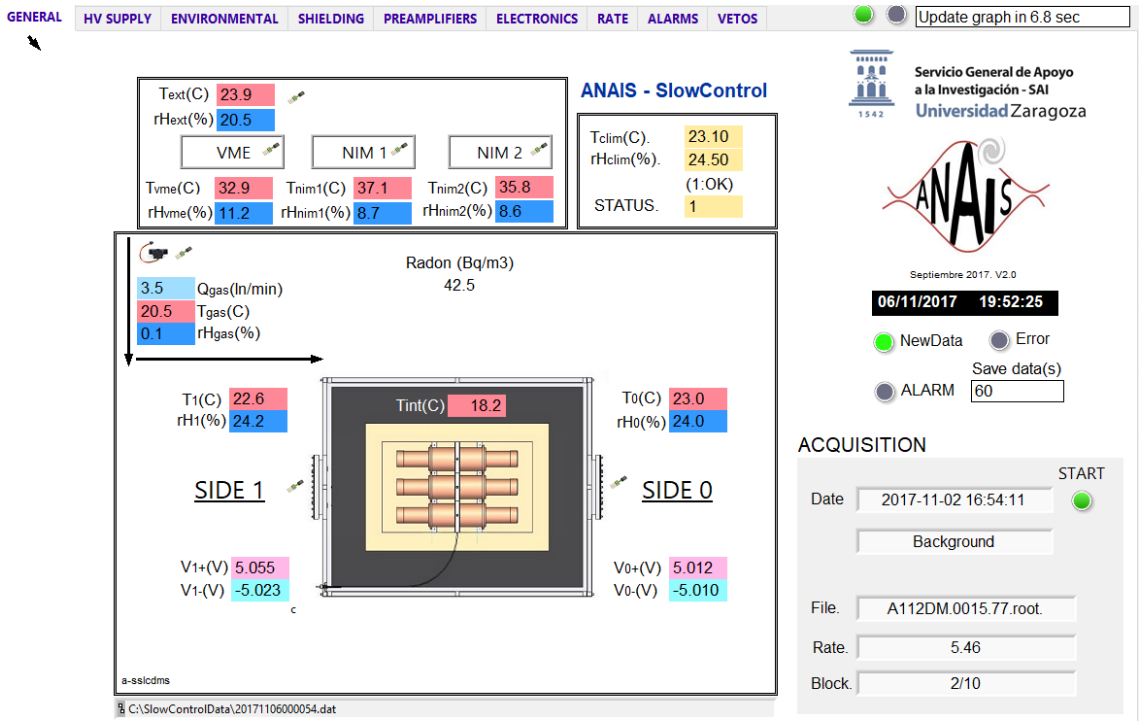

Figure 2.31: *ANAIS–112 slow-control system interface.*

112 shielding since the starting of the Ar-DM cooling down in Hall A (at the end of September 2017). In April 2019, LSC staff modified the configuration of the air-conditioning system of the underground facilities in order to solve these instabilitites in Hall B temperature. Since then, the stability in temperature has been greater, with a standard deviation of 0.2 °C, although it has changed abruptly twice in this period.

Figure 2.32b displays the evolution in time along the three years exposure of ANAIS–112 of the temperature at the electronics air-conditioned space (Telcabin) and the temperatures at VME and NIM racks placed inside that conditioned space (Tvme, Tnim1, Tnim2). The temperature of the preamplifiers follows exactly the same trend as T_{int}, whereas on the other hand, temperature at the VME and NIM electronics racks is fully decoupled from Hall B temperature.

- **Nitrogen flux**. The ANAIS–112 anti-radon box is continuously flushed with radon-free nitrogen gas to prevent the entrance of airborne radon inside the lead shielding. This flux is monitored to register any variation that could affect the experiment. As explained in Section 2.9.1, the observed changes in the acquisition rate are clearly related to the cuts in the nitrogen supply. The time behaviour of the nitrogen gas flux entering into the ANAIS–112 shielding

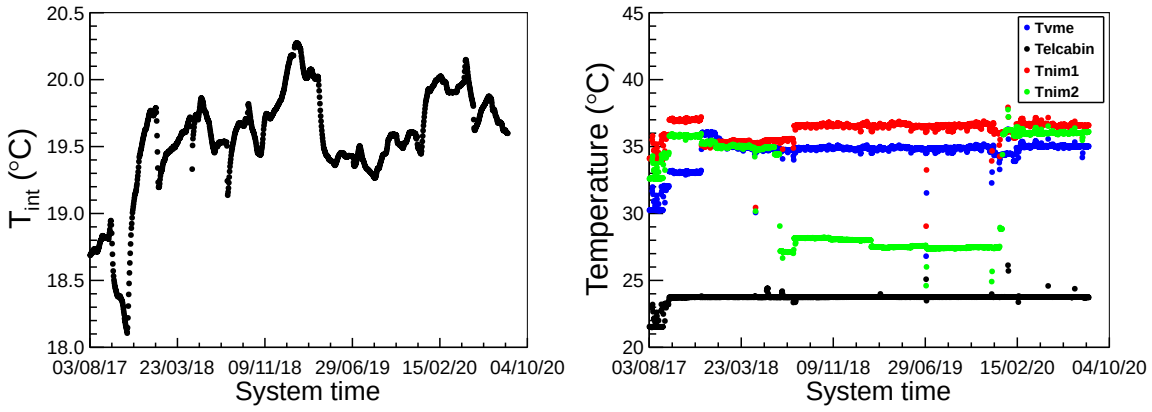

(a) (b)

Figure 2.32: *Left panel (a): Evolution of the temperature inside the ANAIS–112 shielding (T_{int}). Right panel (b): Evolution of the temperatures inside the ANAIS–112 electronics air-conditioned room (Telcabin), and at different positions of the electronics racks (Tvme, Tnim1, Tnim2). All of them have been averaged per day.*

is shown in Figure 2.33. It can be observed in the figure that the nitrogen gas flux reduced down to zero three times (once) in the first (third) year of data taking.

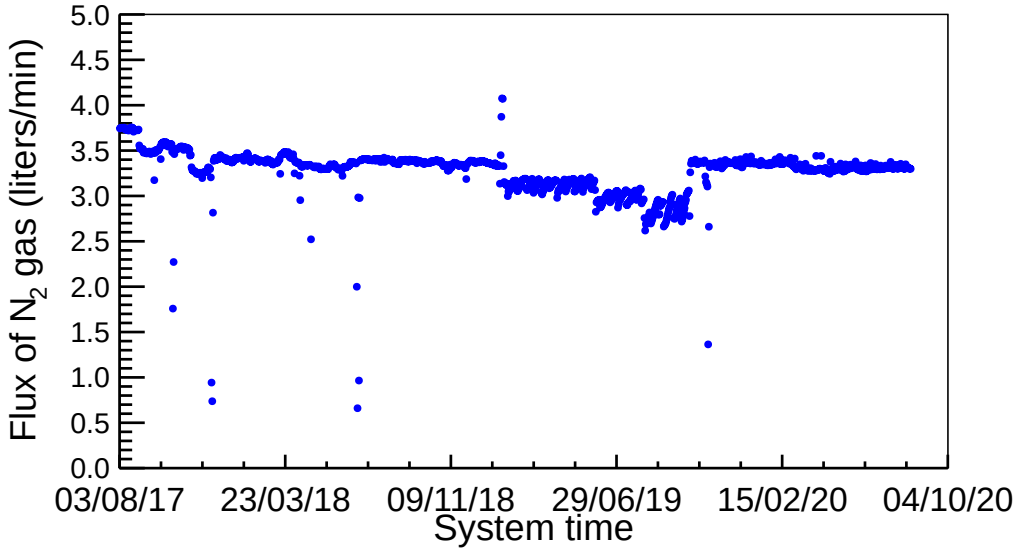

Figure 2.33: *Evolution of the nitrogen gas flux entering into the ANAIS–112 shielding to prevent radon intrusion, averaged per day.*

- **Radon concentration in the laboratory**. The ^{222}Rn activity is one of the most common sources of radioactive background. Because of this, the radon concentration in the air surrounding the ANAIS hut (outside the shielding) is monitored by a Genitron (now Saphymo) AlphaGuard system which also records the pressure, humidity and temperature environmental parameters. It is worth highlighting that ANAIS–112 shielding is designed to prevent radon intrusion, being the inner space continuously flushed with radon-free gas, and therefore, the radon content in the ANAIS–112 inner volume is below sensitivity (see Section 2.10.1). Nevertheless, monitoring external environmental radon content is interesting to have under control possible systematics in the annual modulation analysis.

  The temporal behaviour of radon concentration and humidity in LSC Hall B along the three years of ANAIS–112 operation can be seen in Figure 2.34. Both of them have been averaged per day (a, c) and month (b, d). A seasonal variation can be clearly identified in the radon and humidity values along the measurement period. The monthly averaged values have been fitted to a cosinoidal function ($y(t) = y_0 + A\cos(\frac{2\pi}{T}(t - t_0))$) leaving unconstrained the amplitude of the fluctuation (A), the mean value (y_0), the period (T) and the phase (t_0). The results of the fit are collected in Table 2.11. They are compatible with an annual modulation, having the maximum around the 28^{th} of July with an error of 17 (6) days for radon content (humidity). Both modulations are clearly correlated, although the amplitude of humidity (30%) is twice that of radon (14%). However, more data are needed to confirm such a modulation and to identify its origin.

Parameter	Radon content	Humidity
y_0	79.8±1.2 Bq/m^3	34.60±0.37 %
A	11.2±1.6 Bq/m^3	10.36±0.51 %
T	362±10 days	369.5±3.5 days
t_0	26^{th} July ± 17 days	31^{st} July ± 6 days

Table 2.11: *Results of the fit to cosinoidal function for the monthly averaged values of radon content and humidity in LSC Hall B along the three years of ANAIS–112 operation.*

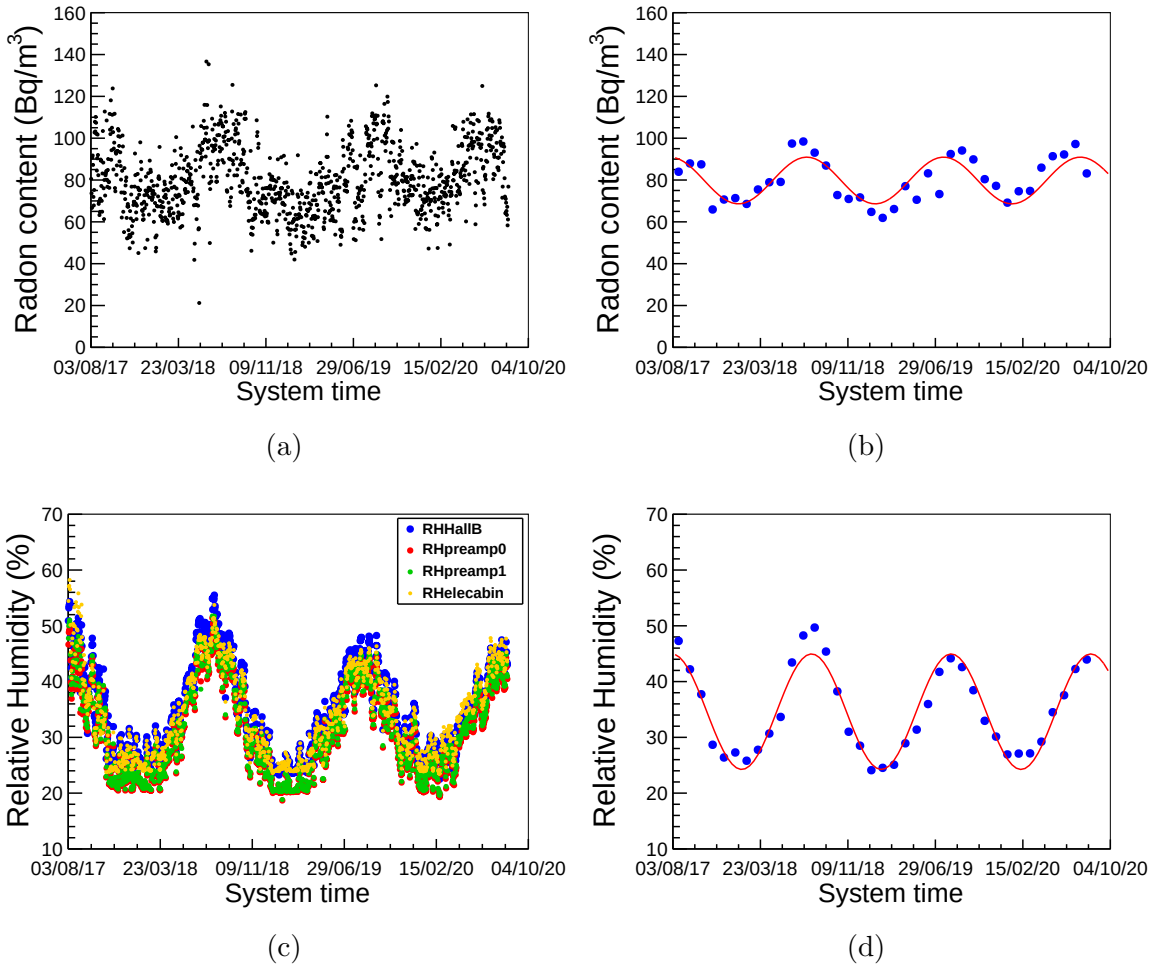

Figure 2.34: *Daily mean values (left) and monthly mean values (right) fitted to cosinoidal function for radon content (top) and humidity (bottom). The results of the fit are shown in Table 2.11.*

- **PMT high voltage and intensity**. The electrical signal of PMTs is very dependent on the high voltage supplied, and therefore, it has to be very stable to assure the gain stability of all the photomultipliers. Figure 2.35 shows the evolution in time of the PMT high voltage for all the nine ANAIS–112 detectors along the three years of operation. It can be observed that all the PMTs show a very stable behaviour during the three years of data taking, except those of the D4 and D5 modules, whose voltages were changed at the end of the first year as previously mentioned. Two power outages can also be observed in late April 2018 and another in mid-February 2020 that were quickly restored. In addition, PMTs current can be also monitored to detect any variation in its value.

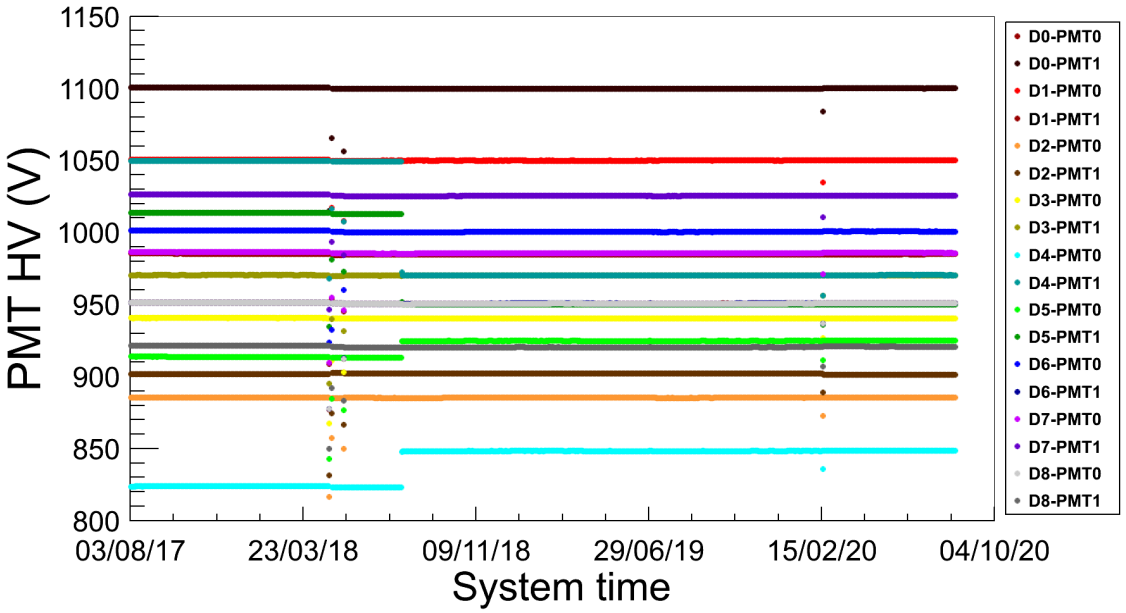

Figure 2.35: *Evolution of the PMT high voltage for all the nine ANAIS–112 detectors, averaged per day.*

2.10 Background model

A good knowledge of background is crucial for experiments demanding ultra low background conditions, such as those searching for a dark matter signal. The construction of reliable background models provide guidance for design and for analyzing any possible systematics, while allowing robust estimates of the ultimate experiment sensitivity. It should be noted that the reliability of these studies is based on three key aspects: an accurate assay of background sources, a careful computation of their contribution to the experiment (made by Monte Carlo simulation) and continuous validation of the obtained results against experimental data in different experimental conditions and energy ranges.

The ANAIS experiment has always attended to the background characterization of the different prototypes and set-ups over the years [130, 186, 190, 202, 222–225]. A complete description of the background model for the ANAIS–112 set-up can be found in Ref. [196]. The most important aspects of such a model are described below.

The background sources considered for the ANAIS–112 detectors include activities from Alpha Spectra NaI(Tl) crystals and from external components.

External radioactive contaminants

Activities of most of the external components were measured by HPGe spectrometry at LSC before being installed in the set-up.

- **PMTs**. The most important external contribution to the background comes from the photomultipliers. Every PMT unit used in the full experiment has been screened, finding compatible levels of activity among them (see Table 2.4).
- **Crystals housing**. There are not direct measurements of most of the materials used in the encapsulation of the NaI(Tl) crystals, but upper limits and values for similar quality copper and synthetic quartz from ANAIS–0 prototype have been considered.
- **Archaeological lead**. Upper limits on ^{210}Pb, ^{232}Th and ^{238}U activities quoted in Ref. [226] have been used for archaeological lead used in the passive shielding.
- **^{222}Rn in the inner volume atmosphere**. Until now, there was no direct measurement of the radon content in the air filling the inner volume of the shielding, so a concentration two orders of magnitude lower than the radon concentration in LSC Hall B due to nitrogen gas flushing was assumed in the ANAIS–112 background model (0.6 Bq/m^3). An upper limit one order of magnitude lower than the one previously considered has been determined by screening the same nitrogen gas used to purge the ANAIS–112 shielding using a HPGe detector at LSC (see Section 2.10.1).
- **External neutrons and gammas**. Contributions from fast neutrons and environmental gamma background have also been estimated and resulted to be negligible compared to the previous contributions.
- **Muons**. Contribution from muons interacting in the crystals (and other muon-related events) are vetoed by the coincidence with a signal in the plastic scintillators covering the ANAIS–112 shielding and then, it has not been taken into consideration in the background model.

Internal radioactive contaminants

Internal contamination from the NaI(Tl) crystals is the dominant background source. The activity of the most relevant primordial and cosmogenic radionuclides has been directly measured for the ANAIS–112 detectors applying different techinques.

- **^{40}K**. The bulk ^{40}K content of ANAIS–112 crystals has been estimated by searching for the coincidences between 3.2 keV energy deposition in one detector (following EC) and the 1460.8 keV gamma line escaping from it and being fully absorbed in other detectors. Efficiency of the coincidence is evaluated by Monte Carlo simulation. The measured values of ^{40}K activity for the nine ANAIS–112 crystals can be seen in Table 2.2. On average, the ^{40}K activity in ANAIS–112 crystals is 0.96 mBq/kg, corresponding to 32 ppb of K.

- **^{210}Pb, ^{232}Th and ^{238}U**. The activities from ^{210}Pb and ^{232}Th and ^{238}U chains have been determined on the one hand, by quantifying Bi/Po and alpha-alpha sequences, and on the other hand, by comparing the total alpha rate, determined through pulse shape analysis, with the low energy depositions attributable to ^{210}Pb, which are fully compatible. For ^{232}Th and ^{238}U chains, very low values of a few μBq/kg have been found for all the detectors. Nevertheless, the measured alpha rate following PSA pointed to a relevant activity of ^{210}Pb out of equilibrium, producing ^{210}Po. The contamination level of ^{210}Pb for each of the ANAIS–112 modules can be observed in Table 2.2. These values are those determined in the characterization performed when detectors arrived to Canfranc, so they are expected to decrease following the ^{210}Pb half-life of 22.2 yr.

- **Cosmogenic activation**. Thanks to the very good detector response and the prompt data taking starting after storing the detectors underground in all ANAIS set-ups, a detailed study of cosmogenic radionuclide production in NaI(Tl) has been possible.

  - ***I and Te isotopes***. For I and Te isotopes, initial activities underground were measured following the evolution of the identifying signatures for each isotope along several months. The evolution in time of the counting rates for these signatures matched single exponential decays following the radioactive decay law and half-lives deduced from the fits agreed with the known values within uncertainties, confirming the identification of: ^{125}I ($T_{1/2}$ = 59.4 days), ^{126}I ($T_{1/2}$ = 12.9 days), ^{121}Te ($T_{1/2}$ = 19.2 days), ^{121m}Te ($T_{1/2}$ = 164.2 days), ^{123m}Te ($T_{1/2}$ = 119.2 days), ^{125m}Te ($T_{1/2}$ = 57.4 days) and ^{127m}Te ($T_{1/2}$ = 106.1 days).
  - ***^{109}Cd and ^{113}Sn***. ^{113}Sn decays by electron capture mainly to a 391.7 keV isomeric state of the daughter, having a half-life of 115.1 days; therefore, a peak at the binding energy of K-shell electrons of In at 27.9 keV is produced, as well as another one for the L-shell at around 4 keV. The ratio between the probabilities of EC for K and L shells is 7.4 for decay

to the isomeric state. Similarly, ^{109}Cd decays by EC to the 88.0 keV isomeric state of ^{109}Ag, having a half-life of 461.9 days, and therefore it gives a peak at the binding energy of the K-shell of Ag at 25.5 keV together with an additional peak around 3.5 keV, corresponding to the Ag L-shell binding energy, being 5.4 the ratio between K and L-shell EC probabilities.

Once the tellurium and iodine cosmogenically produced isotopes in NaI(Tl) and decaying by EC have significantly decayed, these other EC decaying isotopes can be searched for in the background data. Although a precise time analysis cannot be attempted as the peaks are very small, even if accumulated over long times, and cannot be resolved, a quantification of the induced activities of these two isotopes has been attempted. The signals have been analyzed in spectra accumulated over a quite long time to make them measurable; the whole area of the peaks is assigned just to one of the isotopes in the analyzed runs, which means that the initial activities derived could be slightly overestimated.

Peaks around 3.5 and 4 keV from ^{109}Cd and ^{113}Sn decays, respectively, are expected in the region of interest for dark matter searches. Therefore, these isotopes must be taken into account in the background models of NaI(Tl) crystals; since the half-lives, especially for ^{113}Sn, are not too large, they should not be a problem in the long term.

– ^{22}***Na***. ^{22}Na ($T_{1/2} = 2.6$ yr) is specially troubling for dark matter searches considering that the binding energy of the K-shell of its daughter Ne is 0.87 keV, falling the corresponding energy deposition in the region of interest, and having a long enough half-life to compromise the first years of data taking. A direct estimation of ^{22}Na activity in the nine crystals of ANAIS–112 was carried out by looking for coincidences with 1274.5 keV depositions in other detectors. The population of coincidence events having an energy deposition of 0.87 keV in one detector (following the EC decay of ^{22}Na) and the 1274.5 keV gamma line, escaping from it and being fully absorbed in other detector, can be used to cross-check the ^{22}Na activity determination. The measured rate at 0.87 keV (after filtering and efficiency correction) for each ANAIS–112 detector is well reproduced by the corresponding simulation using the deduced ^{22}Na activity values. Moreover, a deviation of only 0.5% is obtained if the measured rate up to 2 keV is compared with the simulated one, averaging all the detectors. Finally, the rate of events at 0.87 keV selected through the coincidence with the high energy gamma has been checked to decay with

$T_{1/2} = 2.82 \pm 0.12$ yr, in good agreement with the half-life of ^{22}Na.

The good description achieved for the coincident 0.87 keV peak also allows to validate the PMTs noise rejection procedures and calculated acceptance efficiencies even below 1 keV (see Chapter 3).

– $^{3}\boldsymbol{H}$. Tritium is a pure beta emitter with transition energy of 18.6 keV and a long half-life of 12.3 yr. Due to 57% of the emitted electrons are in the range from 1 to 7 keV, ^{3}H can be a relevant background in the ROI for the dark matter signal. In the ANAIS–112 detectors, the presence of tritium is inferred in order to explain the differences between the measured background and the background models. Although a direct identification of a ^{3}H content in the crystals has not been possible, the inclusion of a certain activity of ^{3}H homogeneously distributed in the NaI(Tl) crystals provides a very good agreement below 20 keV. The required ^{3}H initial activities to reproduce the data are around 0.20 mBq/kg for D0 and D1, and 0.09 mBq/kg for D2-D8 modules.

The contribution of all the background sources described above to the background levels of the ANAIS–112 detectors has been simulated by Monte Carlo using the Geant4 package [227]. A detailed description of the set-up was implemented including the lead shielding and detectors, considering NaI crystal, teflon wrapping, copper encapsulation with the Mylar window, silicone pads, quartz windows, PMTs, bases and copper enclosure. The energy spectra measured in ANAIS–112 for each one of the nine detectors during the first year of data taking were compared with the background model produced summing all the simulated contributions, in different conditions and energy ranges [196].

- **High energy region**. In the high energy region from 100 to 2000 keV, the model agrees at 5.6% for the total rate obtained by averaging all the ANAIS–112 detectors. Considering the coincidence spectrum from 200 to 2000 keV, which includes events having energy deposited at more than one NaI(Tl) detector, the agreement of the model is at the level of 2.9% on the average of all modules. Indeed, the background model gives a slight overestimation. As can be seen in the lower panel of Figure 2.36 for D3 module, the PMTs activity is the most relevant one in the high energy range.

- **Low energy region**. The anticoincidence background spectrum below 100 keV for detector D3 can be seen in the top panel of Figure 2.36. The background at very low energies is totally dominated by crystal emissions. In particular, ^{210}Pb and ^{3}H continua and ^{40}K, ^{22}Na and ^{109}Cd peaks are the most significant

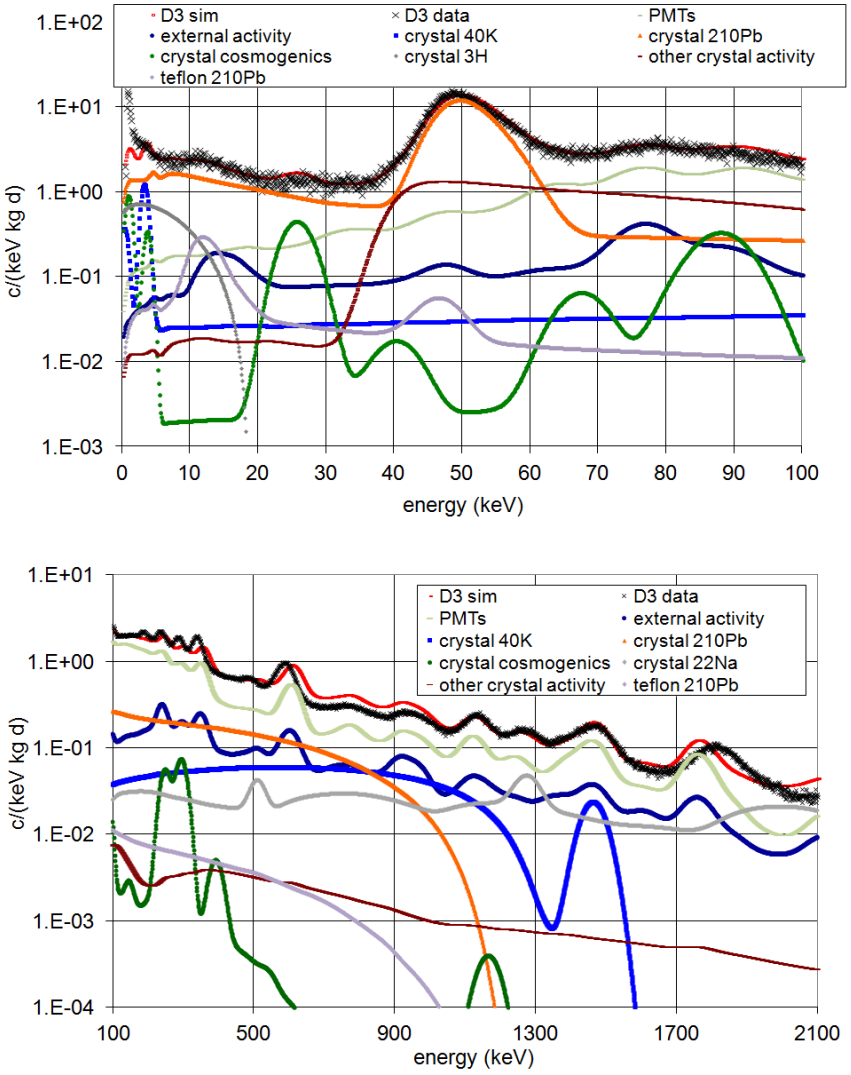

Figure 2.36: *Energy spectra expected from individual background sources, together with the sum of all of them and the measured background. Results are presented for D3 detector, for anticoincidence spectrum in the low energy range (top) and for total spectrum in the high energy region (bottom). From Ref. [196].*

contributions. ^{40}K and ^{22}Na peaks are partially reduced thanks to anticoincidence operation in the 3×3 modules matrix. According to the background model developed, ^{210}Pb, ^{3}H, ^{40}K and ^{22}Na account for 32.5%, 26.5%, 12.0% and 2.0% of the measured rate in ANAIS–112 from 1 to 6 keV, respectively.

The ANAIS–112 background model agrees very well with the data above 2 keV, but below this energy there is some discrepancy. From Table 2.12, it can be seen that the model does not explain 54% of the measured rate in the re-

gion from 1 to 2 keV, but the deviation is of only 10.7% from 2 to 6 keV. The measured rates shown in the table for each detector in ANAIS–112 correspond to the ∼10% of unblinded data from the first year of data taking (see Section 2.6). In Figure 2.37, the comparison for the low energy region of anticoincidence spectra for each ANAIS–112 detector using the ∼10% of unblinded data of the first year of measurement with the corresponding background model summming all the simulated contributions is shown. The same, but for total anticoincidence spectrum is displayed in Figure 2.38.

	[1,2] keV			[2,6] keV		
Detector	Measurement (c/keV/kg/d)	Simulation (c/keV/kg/d)	Deviation (%)	Measurement (c/keV/kg/d)	Simulation (c/keV/kg/d)	Deviation (%)
D0	7.43±0.21	4.37	-41	4.75±0.06	4.53	-4.7
D1	7.30±0.24	4.36	-40	4.80±0.06	4.46	-7.1
D2	4.66±0.18	1.84	-61	2.53±0.04	2.27	-10.2
D3	7.09±0.20	2.77	-61	3.30±0.05	2.97	-10.0
D4	5.83±0.17	2.73	-53	3.20±0.05	2.88	-10.0
D5	6.20±0.18	1.84	-70	3.02±0.04	2.34	-22.5
D6	5.40±0.21	2.04	-62	3.00±0.04	2.42	-19.2
D7	4.20±0.15	2.03	-52	2.69±0.04	2.42	-10.1
D8	3.80±0.14	1.94	-49	2.35±0.04	2.18	-7.4
ANAIS-112	5.77±0.06	2.66	-54	3.29±0.02	2.94	-10.7

Table 2.12: *Measured rates (after correction for efficiency of the filtering procedure) in the regions from 1 to 2 keV and from 2 to 6 keV for each ANAIS–112 detector and on average, from the ∼10% of unblinded data of the first year of data taking. The corresponding simulated rates and their deviation from the measurement are also presented.*

The unexplained events below 2 keV could be attributed to non-bulk scintillation events which have not been rejected or to background sources not included in the described model. More about this issue is covered in Chapter 6.

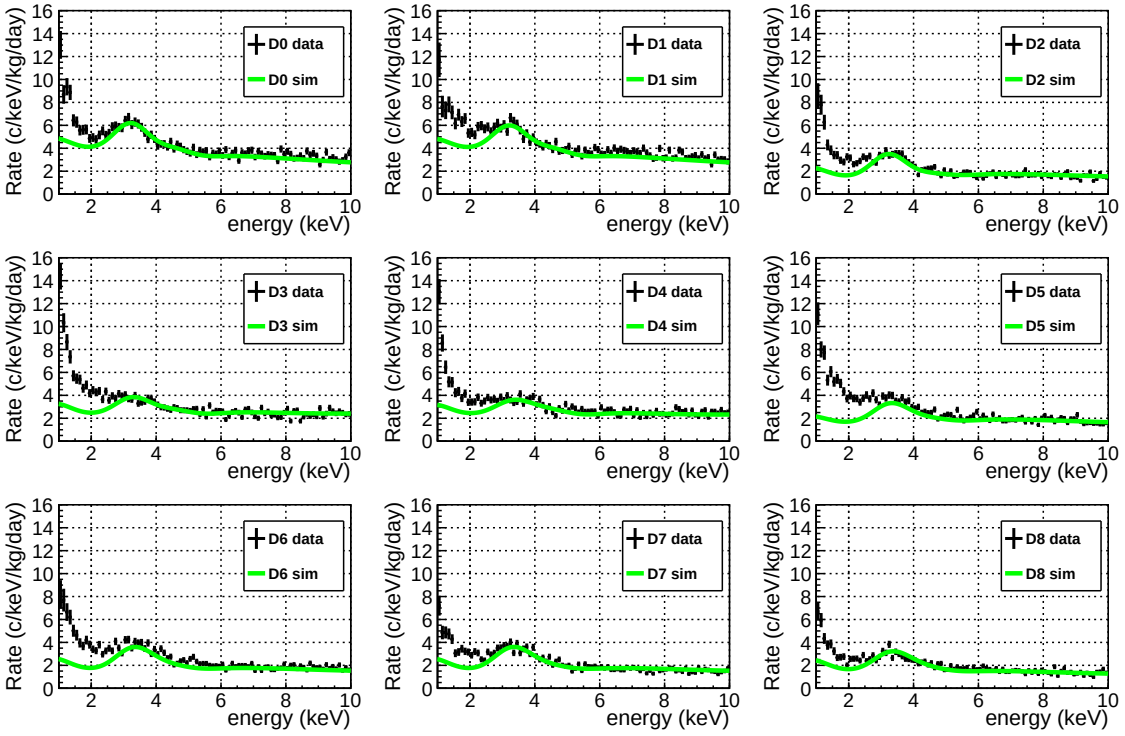

Figure 2.37: *Comparison of the anticoincidence energy spectra in the region of interest measured for each detector with the corresponding background model summing all the simulated contributions. The shown data correspond to the ∼10% of unblinded data of the first year of data taking after filtering and efficiency correction.*

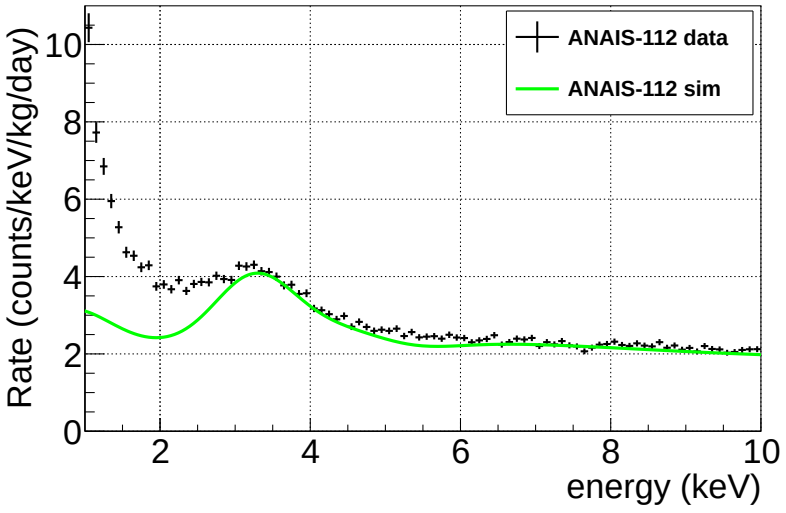

Figure 2.38: *Comparison of the total anticoincidence energy spectrum in the region of interest with the corresponding background model summing all the simulated contributions. The shown data correspond to the ∼10% of unblinded data of the first year of data taking after filtering and efficiency correction.*

2.10.1 Upper limit on the ^{222}Rn content of the nitrogen gas purging ANAIS–112

The ^{222}Rn upper limit presently considered in the ANAIS–112 background model (0.6 Bq/m^3) [196] is two orders of magnitude lower than outside (see Table 2.11) thanks to the radon-free nitrogen gas overpressure provided by the LSC. This arbitrary value is compatible with the absence of lines coming from radon daughter isotopes in the measured background.

Measuring the radon activity inside the ANAIS–112 shielding would require a much more sensitive detector than current commercial radon detectors. For this reason, we proposed to use one of our High Purity Germanium (HPGe) detectors placed at LSC to estimate the radon content in the nitrogen gas used for flushing the ANAIS–112 shielding (see Figure 2.39). In particular, the shielding of the HPGe detector has been purged for two years (2017-2018) with the same radon-free nitrogen gas purging the ANAIS–112 shielding. Figure 2.40 shows the energy spectrum up to 3 MeV for the HPGe detector accumulating the two years of data taking (669.9 days of live time). Some gamma lines can be clearly distinguished in the spectrum such as the 1460.8 keV line from ^{40}K and 2614.5 keV from ^{208}Tl.

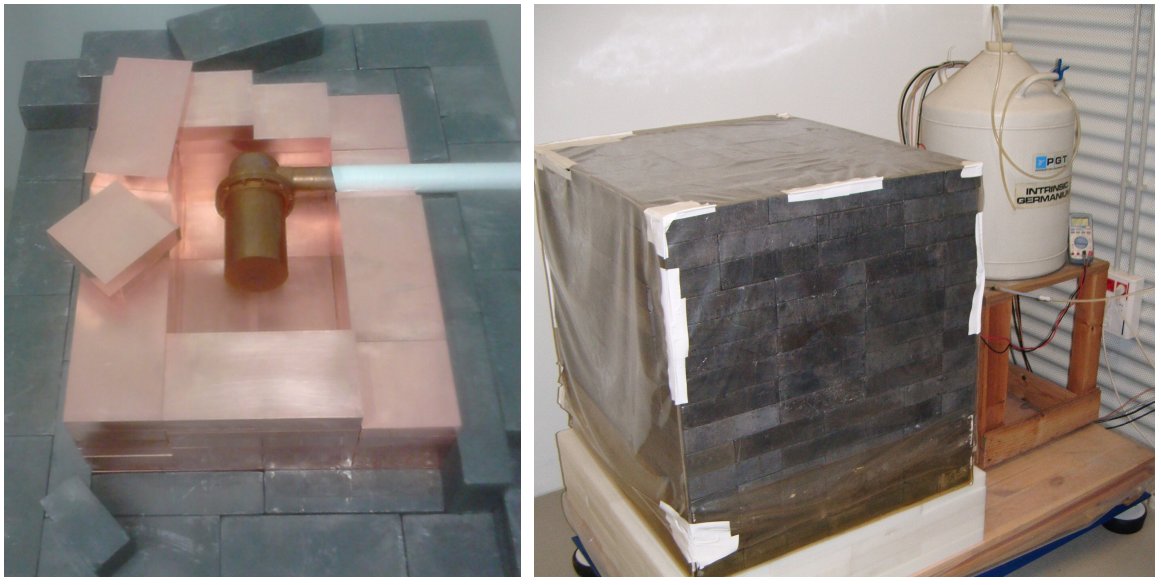

(a) (b)

Figure 2.39: *Picture taken of the inside of the HPGe detector shielding where nitrogen gas is injected (a) and of the external lead shielding together with the dewar which cools the HPGe detector (b).*

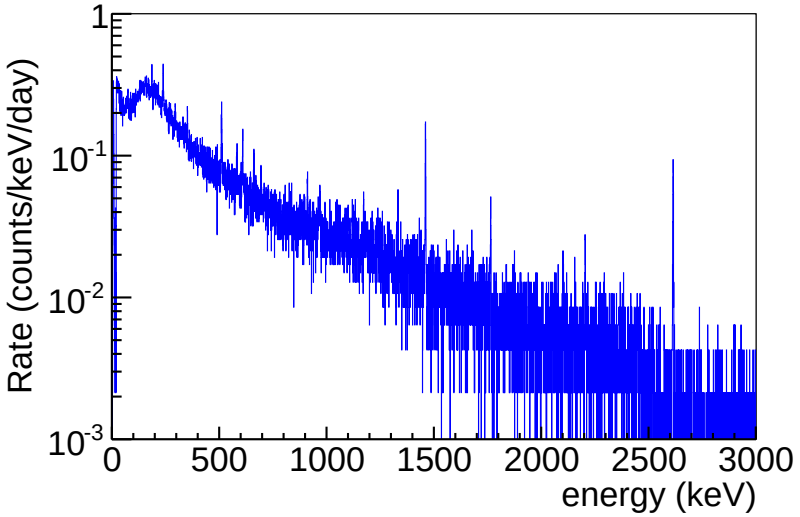

Figure 2.40: *Energy spectrum up to 3 MeV for the HPGe detector accumulating the two years of data taking.*

The HPGe detector is taking data steadily for about a week. After stopping the acquisition, an external ^{22}Na source is introduced through a wire to calibrate for about 15 min. Then, the dewar is filled with liquid nitrogen used to cool the HPGe detector, and again a calibration with ^{22}Na is carried out before restoring data acquisition. The 511 and 1274.5 keV peaks from ^{22}Na are used to perform a linear energy calibration.

The possible presence of residual ^{222}Rn in the nitrogen gas used to purge the inner volume of the shielding would be revealed by observing the gamma lines coming from radon daughter isotopes. Unfortunately, the ^{214}Bi and ^{214}Pb peaks observed by the HPGe detector have a contribution from ^{226}Ra and $^{\text{nat}}$U that cannot be disentangled from the possible residual ^{222}Rn in the nitrogen gas. Figure 2.41 depicts the decay mechanisms of radioactive isotopes from ^{226}Ra sub-chain together with their main gamma emissions, as well as the half-lives of each isotope. Next to the energy of the gamma emission, its intensisty is shown in brackets. The rate of each of these peaks on the HPGe spectrum can be expressed as:

$$R = A \cdot I_\gamma \cdot \varepsilon \tag{2.2}$$

where A is the activity of the isotope, I_γ is the intensity of the gamma ray and ε is the total absorption efficiency. The latter depends on the energy of the gamma ray and the source-detector geometry and distance. For this reason, it is necessary to measure it with a calibration source of known activity.

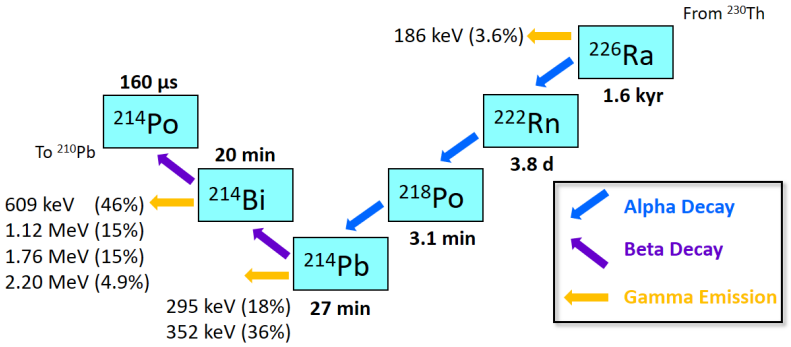

Figure 2.41: ^{226}*Ra sub-chain showing decay mechanisms of the radioactive isotopes together with their main gamma emissions, as well as the half-lives of each isotope. Next to the energy of the gamma emission, its intensity is shown in brackets.*

In order to calculate the absolute efficiency for the energies of the main gamma emissions of the radon daughter isotopes, namely: 295 and 352 keV from ^{214}Pb, and 609, 1120, 1764 and 2204 keV from ^{214}Bi, the following were combined: on the one hand, a calibration performed with a KCl source of known activity and, on the other hand, a Monte Carlo simulation using the Geant4 package. KCl is a natural source of ^{40}K and is used to estimate the absolute efficiency of the HPGe detector at 1460.8 keV at different positions inside the shielding. In particular, several measurements were made in the front part of the detector, as well as in the lateral parts, obtaining an average efficiency of $(0.50 \pm 0.02)\%$. This result serves to validate the Monte Carlo simulation when considering 1460.8-keV photons distributed isotropically around the detector. It is found that the correction factor to be applied to the simulation in order to reproduce the experimental data is 1.34 ± 0.02. It has been assumed that this factor only depends on the source-detector geometry, but not on the energy, so it can be used directly to correct the simulations corresponding to the main gamma emissions of the radon daughter isotopes, thus estimating the absolute efficiency for ^{222}Rn (see Figure 2.42a). For the Monte Carlo simulation, a detailed description of the set-up was implemented including (see Figure 2.42b):

- The external shielding of lead 15 cm thick and the internal shielding of copper 10 cm thick.
- The cylindrical germanium detector with a diameter of 62 mm and a height of 60 mm, encapsulated in a 1 mm thick copper cylinder. The detector has a 1 mm thick dead layer on the front and side.
- The cylindrical copper cryostat measuring 84 mm in diameter and 180 mm in height, counting 1 mm thick. The distance between the detector and the outside of the cryostat window is 5 mm.

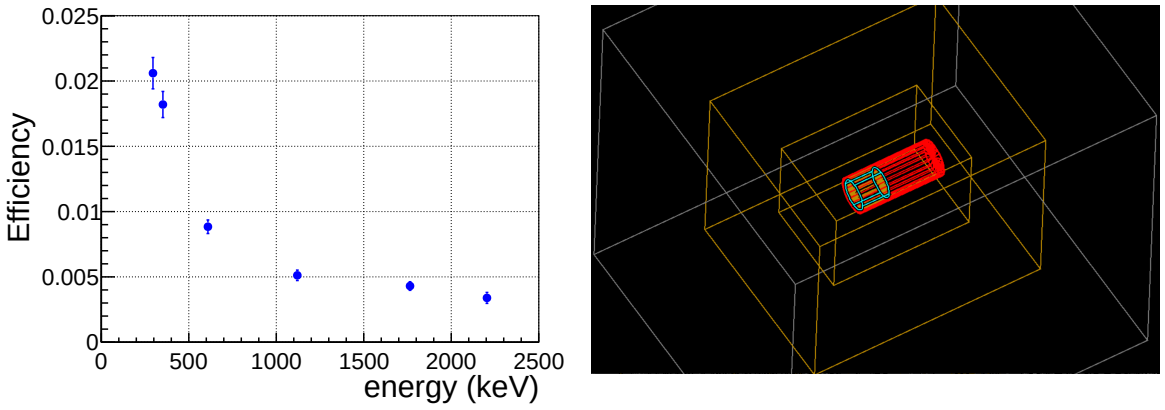

(a) (b)

Figure 2.42: *Left panel (a): Absolute efficiency of the HPGe detector for the main gamma emissions of* ^{222}*Rn daugthers. Right panel (b): Geometry of the HPGe set-up implemented in the Geant4 simulation.*

A small accumulation can be observed around the 352 keV peak, however, as mentioned above, it cannot be deduced if it is only due to the possible residual ^{222}Rn in the nitrogen gas used to purge the shielding, or there could be a small concentration of ^{226}Ra (^{226}Ra has a less intense line at 186 keV which is not distinguishable in the spectrum). Therefore, only an upper limit for the activity of ^{222}Rn in the nitrogen gas provided by the LSC can be obtained. Table 2.13 summarizes the data used to calculate the upper limit for the radon content in the nitrogen gas:

$$A(^{222}\text{Rn}) < 0.04 \text{ Bq/m}^3 \text{ (95\% C.L.)}. \tag{2.3}$$

Rate (counts/day)	0.19±0.04
Intensity (%)	35.60±0.07
Absolute efficiency (%)	1.82±0.10
Inner volume (L)	12
Specific activity (Bq/m^3)	0.028±0.006

Table 2.13: *Summary of the data used to calculate the upper limit for the radon content in the nitrogen gas used to purge shielding.*

This upper limit to the ^{222}Rn content inside the ANAIS–112 shielding is 15 times lower than the previously considered.

The evolution in time of the ^{222}Rn/^{226}Ra content in the HPGe shielding has also been studied by adding the rate of the six peaks from ^{214}Bi and ^{214}Pb. This added rate has been fitted to a constant plus a modulation term with a yearly period (see Figure 2.43). The modulation amplitude resulting from the fit is 0.24±0.11 counts/day, but its statistical significance is so low that the bias produced by the non-linear fit is not negligible (see Section 5.2.3). In particular, a value of 0.03 counts/day is obtained for the bias, so the corrected modulation amplitude results to be 0.21±0.11 counts/day, compatible with the absence of modulation to less than 2σ.

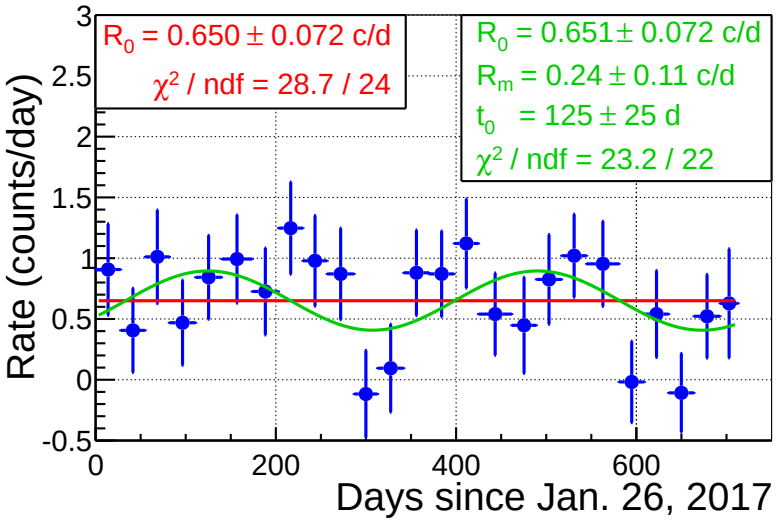

Figure 2.43: *Evolution in time for the rate of the addition of the six peaks of ^{214}Bi and ^{210}Pb for the HPGe detector. The red line represents the fit to a constant rate, whereas the green line is fitted to a constant plus a modulation term with a yearly period.*

According to our background model, even if the upper limit 0.04 Bq/m^3 of ^{222}Rn (see Equation 2.3) with 100% modulation amplitude was assumed to be inside the ANAIS–112 shielding, its contribution to the ANAIS modulation would be $< 2.7 \cdot 10^{-4}$ c/keV/kg/d in the region of [1,6] keV, being negligible compared to the expected modulation deduced from the DAMA/LIBRA result.

2.11 Blank module

A Blank module was installed inside the ANAIS hut at LSC Hall B after the first year of ANAIS–112 data taking, at the beginning of August 2018. This module is similar to the nine modules, but without NaI(Tl) crystal. Two PMTs, identical to those used in ANAIS–112 modules, have been coupled to quartz optical windows

at both sides of the module, which consists of a copper housing with the interior covered by Teflon diffusor film (see Figure 2.44).

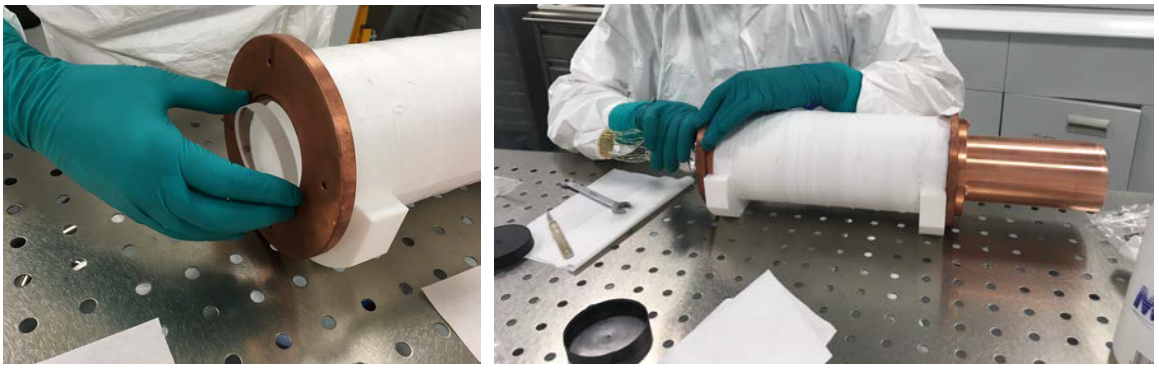

(a) (b)

Figure 2.44: *Mounting the ANAIS Blank module in the LSC clean room: quartz windows (a) and PMTs (b).*

The Blank module is contained within a specific lead shielding next to ANAIS–112 (see Figure 2.45). The PMTs readout of this module uses same homemade preamplifiers and electronic chain than ANAIS–112 modules, but independent high voltage supply. The data acqusition system of the Blank module has been integrated in the ANAIS–112 DAQ system, as detector D9. Data analysis of D9 is carried out using same parameters and procedures than used for the rest of the modules. The goals of the Blank module are to learn as much as possible on the different non-bulk events populations having PMT-origin, which are contributing in the ANAIS–112 noise, and to check the ANAIS experimental conditions stability independently of the ANAIS–112 modules.

Figure 2.46 shows in black the acquisition rate of the Blank module since the start of data taking in August 2018. This module was showing clear instabilities in trigger rate, which are associated to the fact that the module was not in a radon-free environment. The Blank module shielding began to be flushed with bottled nitrogen gas and radon-free air since February 2019, but in a discontinuous regime: some sporadic cuts on the radon-free air supply have occurred since then. The effect can be clearly observed in Figure 2.46 as high-trigger periods. The rate of the Blank module stabilizes strongly in the periods having radon-free gas (either air or nitrogen) coming into the shielding at a level of 0.1 Hz, about a factor of five below the typical level when the flushing is switched off (at about 0.5 Hz). Figure 2.46 also displays the rate of events having more than one peak in each

Figure 2.45: *Setting-up the ANAIS Blank module in the ANAIS hut, inside a specific lead shielding, next to ANAIS–112.*

PMT signal, which increases strongly if radon-free environment is not guaranteed. However, it has been noticed that some of these events correspond to electrical noise, in particular the high-trigger rate period at the end of the summer 2020 (shown in green in Figure 2.46). From July 2019 until February 2020, one of the PMTs was operated at higher voltage, leading to a slight increase in the acquisition rate. Finally, the events with more than one peak at each PMT which are not compatible with electrical noise are shown in orange.

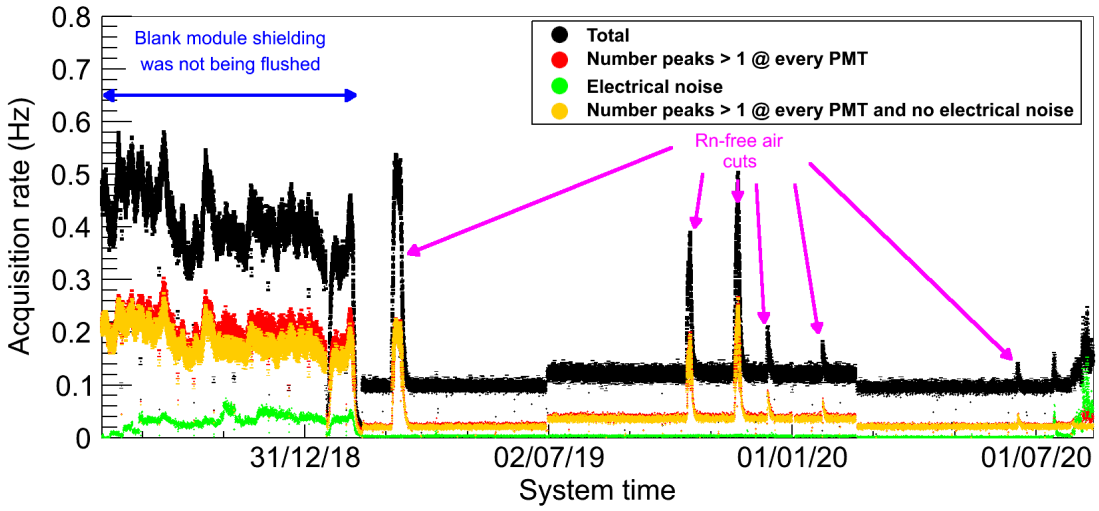

Figure 2.46: *Trigger rate of the Blank module: total acquisition rate is shown in black, events having more than one peak at each PMT in red, events associated to electrical noise in green, and in orange, those events with more than one peak at each PMT which are not compatible with electrical noise.*

It can be concluded that the Blank module is sensitive to the content of radon in the air, but no effect on the trigger rate can be related with the use of the radon-free air provided by LSC or nitrogen gas, unlike ANAIS–112 modules behaviour.

The Blank module can be very useful to understand the excess of events below 2 keV with respect to the background model, if these were due to PMT-generated events which have not been removed by the ANAIS–112 filtering protocols described in the next chapter. Since the Blank module does not house a particle detector, radioactive sources cannot be used to perform an energy calibration of the observed events. Nevertheless, the amount of light collected by the Blank module PMTs can be compared with that collected by the PMTs of any ANAIS–112 modules when events below 2 keV are recorded. In order to do this, the number of photoelectrons (*nphe*) is defined as the area of the PMT waveform divided by the average size of the photoelectron in that PMT, i.e., the mean value of the SER charge distribution of the PMT. Figure 2.47 shows the SER charge distribution for the 2 PMTs coupled to the Blank module from the 93^{rd} run selecting the last peak in pulses having a very low number of photoelectrons, as is done in the ANAIS–112 set-up.

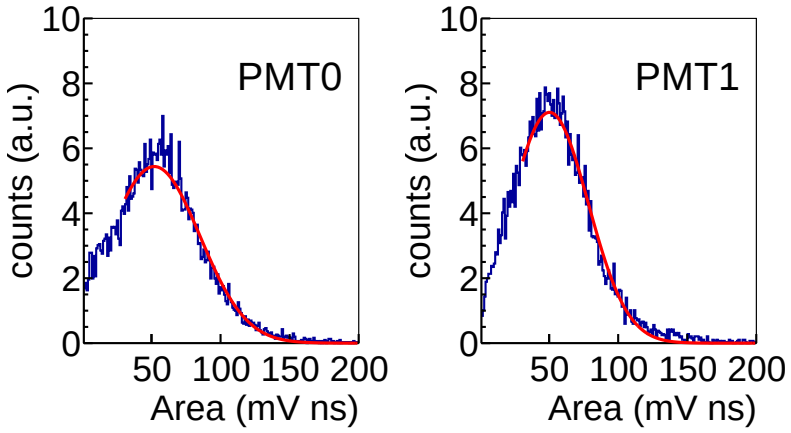

Figure 2.47: *Example of SER charge distributions for the 2 PMT coupled to the Blank module for the 93^{rd} run.*

The evolution of the SER mean values for PMT0 (in black) and PMT1 (in cyan) of the Blank module for two-weeks-long background runs along the last two years of data taking is shown in Figure 2.48. It can be observed in the figure that the mean value of the SER has a great uncertainty before the Blank module shielding purge begins (February 2019, run number 91). It is also confirmed that the PMT1 operated at higher voltage during the period between July 2019 and February 2020 (run numbers from 113 to 147).

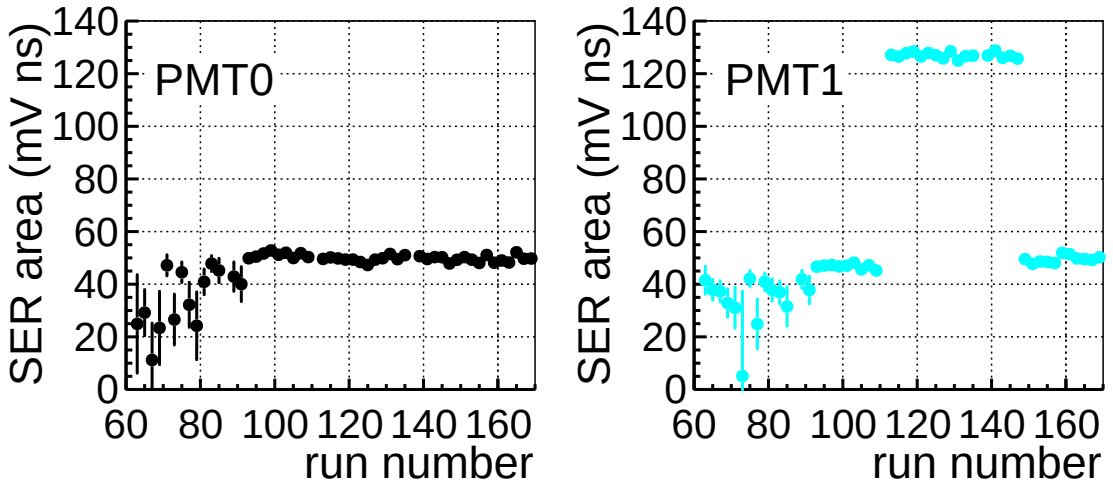

Figure 2.48: *Evolution of the SER mean values for PMT0 (black) and PMT1 (cyan) coupled to Blank module for two-weeks-long background runs. The high voltage of PMT1 was modified between run numbers 113 and 147.*

Figure 2.49 shows the total number of photoelectrons (adding the two PMT vias) of the events between 1 and 2 keV from ^{109}Cd calibration runs for all the ANAIS–112 detectors. In view of the figure, it is concluded that events with energy between 1 and 2 keV produce a signal with a total number of photoelectrons between 10 and 28. This population of events from the Blank module with [10,28] photoelectrons will be used in Chapter 6 as a training population for non-bulk scintillation events.

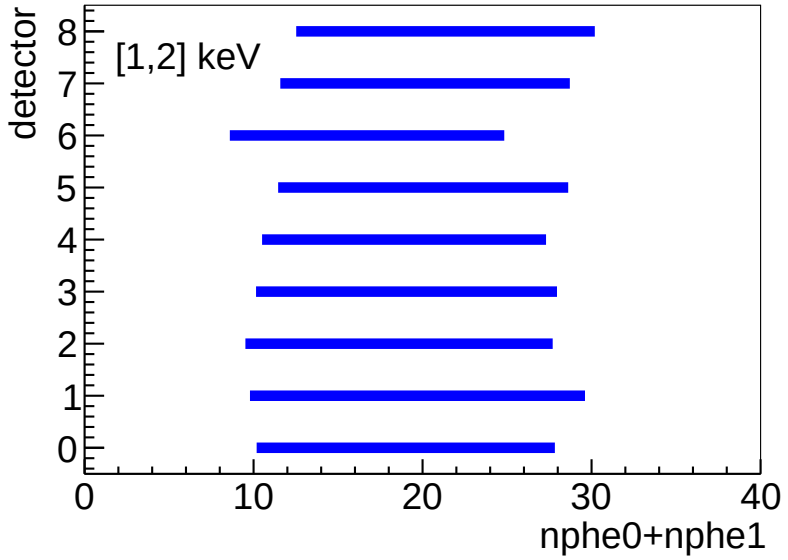

Figure 2.49: *Total number of photoelectrons (adding the two PMT vias) of the events between 1 and 2 keV from ^{109}Cd calibration runs for each ANAIS–112 detector.*

Chapter 3

Bulk NaI(Tl) low energy events selection

There are different light-emitting mechanisms in the components surrounding NaI(Tl) crystals, which contribute significantly to events at low energy region. These light emissions can be originated in the PMTs own structure, the optical windows used to couple the crystal to the PMT, or even the optical grease or silicone pads used in that coupling; but they are definitely not generated by the scintillator crystals, nor by the PMT dark current. Unlike dark current events, which are removed by the trigger in logical AND between the two PMTs, the former events can dominate the trigger rate near the energy threshold and they have to be rejected before any dark matter analysis. Controlling these anomalous or noise event populations in the low energy region is one of the main goals for the ANAIS experiment, since dark matter particles are expected to deposit very small energy in the detector. In particular, dark matter interaction should be produced below 100 keV of nuclear recoil energy or even at much lower energies depending on the candidate (see Section 1.4.3). This implies electron equivalent energies below approximately 30 keV for Na recoils and below 10 keV for I recoils. Thus, a very good knowledge of the detector response for real scintillation events in the bulk and characterization of all background sources in the low energy region are required. Specific filtering protocols for events with origin in the PMT similar to those described for previous ANAIS set-ups [228], but updated and optimized for ANAIS–112 [15] have been designed. Multiparametric cuts based on the temporal parameters of the pulses and the asymmetry in light sharing between PMTs are considered, and the corresponding acceptance efficiencies have been calculated. This filtering procedure has allowed to reach 1 keV analysis threshold.

The ANAIS–112 specific filtering protocols were introduced in Ref. [15] and are summarized in Section 3.1. The total efficiencies estimated for the detection and selection of events in the ROI have been updated using 3 years of data and can be found in Section 3.2. Finally, the low energy spectra for all ANAIS–112 detectors after event selection and efficiency correction are discussed in Section 3.3.

3.1 Filtering protocols

In order to reduce the energy threshold below 2 keV, strong rejection of non-bulk NaI scintillation events is required. Filtering procedure must guarantee a compromise between a high acceptance of bulk NaI scintillation events and a high rejection factor of other non-bulk events. Dark matter particles should interact with our detector through processes having a very low cross section, typically from 10^{-50} to 10^{-40} cm^2 per nucleon in most conventional WIMP scenarios [134]. This means that the probability of a dark matter particle interacting twice while crossing ANAIS–112 set-up is negligible, so, coincidences among different modules are rejected by selecting events compatible with single-hit interactions. This very low interaction cross section also involves that the probability of interacting in the PMT or other set-up components having low mass is insignificant, too, and that the interaction with the Na and I atoms is expected to be dominant. Depending on the dark matter candidate, this interaction could occur only with the nuclei or as well as with the electrons in the target material, although the energy transferred would be much less than that transferred to a nucleus. That is why those events generated in the PMTs, or those which are related with a muon crossing ANAIS–112 set-up (see Section 2.5), should be removed from our analysis.

ANAIS–112 filtering protocols consist of: rejection of muon related events (Section 3.1.1), pulse shape analysis through temporal parameters of the pulses (Section 3.1.2), and asymmetry cut in the energy partition among both PMTs (Section 3.1.3). Rejection of muon related events implies an effective reduction in the acquisition live time, while in the other two, the efficiency of the cut to preserve the bulk scintillation events in NaI(Tl) active volume has to be estimated by studying ^{22}Na and ^{40}K populations (see Section 3.2.2) and ^{109}Cd calibration data (see Section 3.2.3), respectively.

3.1.1 Rejection of muon related events

In Ref. [229], a scintillation with very slow time constant (of the order of 200 ms) was identified in NaI(Tl) crystals after the passage of a very energetic particle, like

a muon. As the trigger is set at the photoelectron level, photons in the tail of such pulses are able to trigger the acquisition multiple times, up to hundreds of ms after the pulse onset. Consequently, the total acquisition rate increases after every high energy deposition event. The ANAIS–112 veto scintillator system (see Section 2.5), which uses the same hardware clock source as the ANAIS–112 modules, allows to correlate muon events in the plastic scintillators with energy depositions in the NaI(Tl) crystals. Figure 3.1 shows in blue the total trigger rate in a period of 1000 s, with a time binning of 0.1 s. Veto scintillators trigger timing is marked as black dots in the figure. As can be observed in the figure, most of the relevant increases in the trigger rate are preceded by the interaction of a muon in the Veto System. These high rate periods can then be related to a direct muon interaction in at least one of the NaI(Tl) crystals, which produce subsequent triggers of the acquisition system. Most of these total trigger rate increases are removed by rejecting events arriving less than one second after a veto scintillation trigger (see red line in Figure 3.1), and the live time of our measurement is corrected off-line by subtracting to the live time one second for every muon veto trigger. The fraction of live time rejected after the application of this filtering amounts only to a 3%.

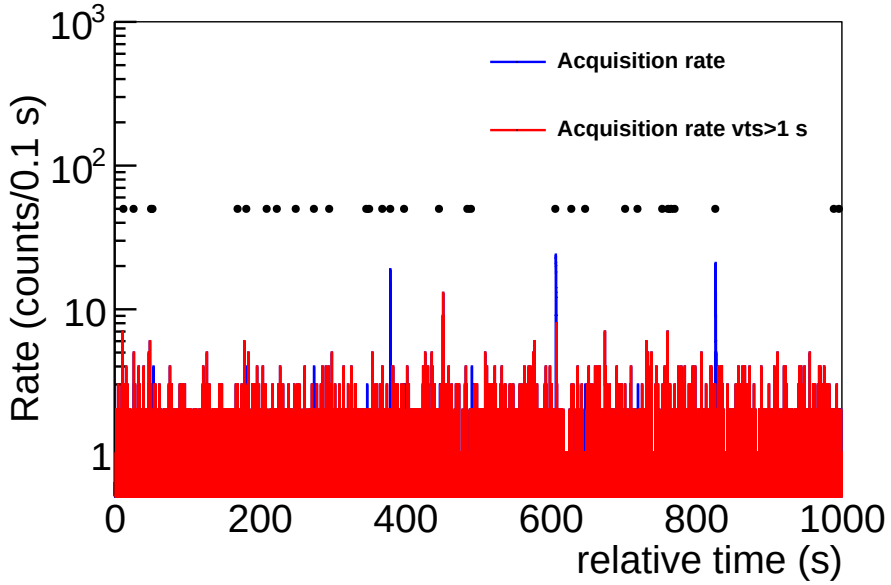

Figure 3.1: *Total trigger rate in ANAIS–112 in a 1000 s period is shown in blue and in red the trigger rate after removing 1 s following a veto trigger. Events in the veto scintillators are marked as black dots, pointing to a correlation between muon crossing ANAIS–112 set-up and total trigger rate increases.*

Unfortunately, all the muon related events are not rejected in this way, because the increase in the acquisition rate lasts more than one second after the passage of

some of these high energetic particles. However, these events are easily removed by impossing an analysis threshold requiring more than one peak in the pulse at every PMT of a given ANAIS–112 module. This analysis threshold is very soft, implying that at least 4 photoelectrons are required to produce an effective trigger (2 at each PMT). According to the light collection of ANAIS–112 modules reported in Section 2.8, it should not compromise the energy threshold level of the experiment at 1 keV or even below. Furthermore, more stringent analysis threshold will be introduced in Section 3.1.3 and more information of the implications of this filter will be given there. The energy distribution of the events removed using the 1 s after a muon filter is shown in Figure 3.2 for the ANAIS–112 unblinded data (see Section 2.6). It is clear these events would contribute to the very low energy region if they were not rejected.

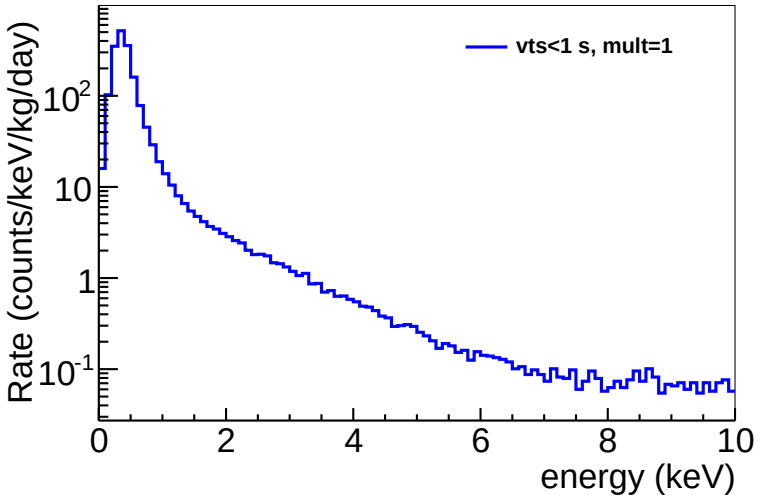

Figure 3.2: *Energy distribution (below 10 keV) of muon related events for the ANAIS–112 unblinded data, i.e. single-hit events arriving less than one second after a trigger of the Veto System.*

3.1.2 Pulse shape cut

As commented in the previous section, slow scintillation components (up to several hundreds of ms) have been measured in NaI(Tl) crystals after large energy depositions (α or $\beta/\gamma/\mu$) [229]. These slow components can trigger the DAQ system several times and result in fake low energy events in the usual NaI(Tl) scintillation time scale if they are not properly identified as pulse tails.

Cherenkov light emission in the PMT glass is the most common light production mechanism in the PMT, which can be generated by radioactive contamination in

the PMT itself or in the environment [194, 230]. These events are very fast, actually they should be dominated by the temporal response of the PMT (around tens of ns), and hence, they should be easily discriminated by pulse-shape analysis (PSA) with respect to NaI(Tl) scintillation events (in the order of hundreds of ns). As an example, Figure 3.3a shows a low energy bulk scintillation event from ^{22}Na decay, whereas a fast pulse coming from the PMT can be seen in Figure 3.3b. Following Ref. [187], the PSA parameter defined to discriminate this kind of events is:

$$P_1 = \frac{\sum_{t=100\ \mathrm{ns}}^{t=600\ \mathrm{ns}}(S_0(t) + S_1(t))}{\sum_{t=0}^{t=600\ \mathrm{ns}}(S_0(t) + S_1(t))}, \tag{3.1}$$

where $S_0(t)$ and $S_1(t)$ are the pulse amplitudes at time t after the trigger position for the waveforms of the PMT0 and PMT1, respectively. Figure 3.4a shows the distribution of P_1 parameter for detector D1 as a function of the energy for ^{109}Cd events from the first calibration run. It can be observed that for NaI(Tl) scintillation pulses (dominated by the scintillation time of $\sim$ 230 ns) this P_1 parameter has a value around 0.65, although the dispersion is greater below 2 keV. The P_1 parameter distribution of detector D1 as a function of the energy for background events from the first dark matter run is shown in Figure 3.4b, in which it can be seen that most of the events have P_1 values lower than 0.3, which are associated to fast scintillation (Cherenkov-like) or single phe events. However, below 2 keV both noise and scintillation populations overlap and a clear separation using the P_1 parameter is no longer possible. Finally, Figure 3.4c show the distribution of P_1 parameter for detector D1 with energy for 3.2 keV bulk events coming from the internal ^{40}K disintegration, which have been selected by the coincidence with the 1460.8 keV γ in another detector, and from which it follows that NaI bulk events have P_1>0.4, in agreement with calibration data.

Random coincidences between individual dark current phe are also removed by this parameter. Nevertheless, it is not useful to discriminate fake low energy events produced by long phosphorescence in the crystal or pulse tails (see Figure 3.3c). In order to do so, a new parameter based on the logarithm of the mean time of the distribution of the individual phe arrival times in the digitized window [231] is defined, $\log(\mu_p)$, where μ_p is evaluated from the software trigger position until the end of the pulse as

$$\mu_p = \frac{\sum_i A_i t_i}{\sum_i A_i}, \tag{3.2}$$

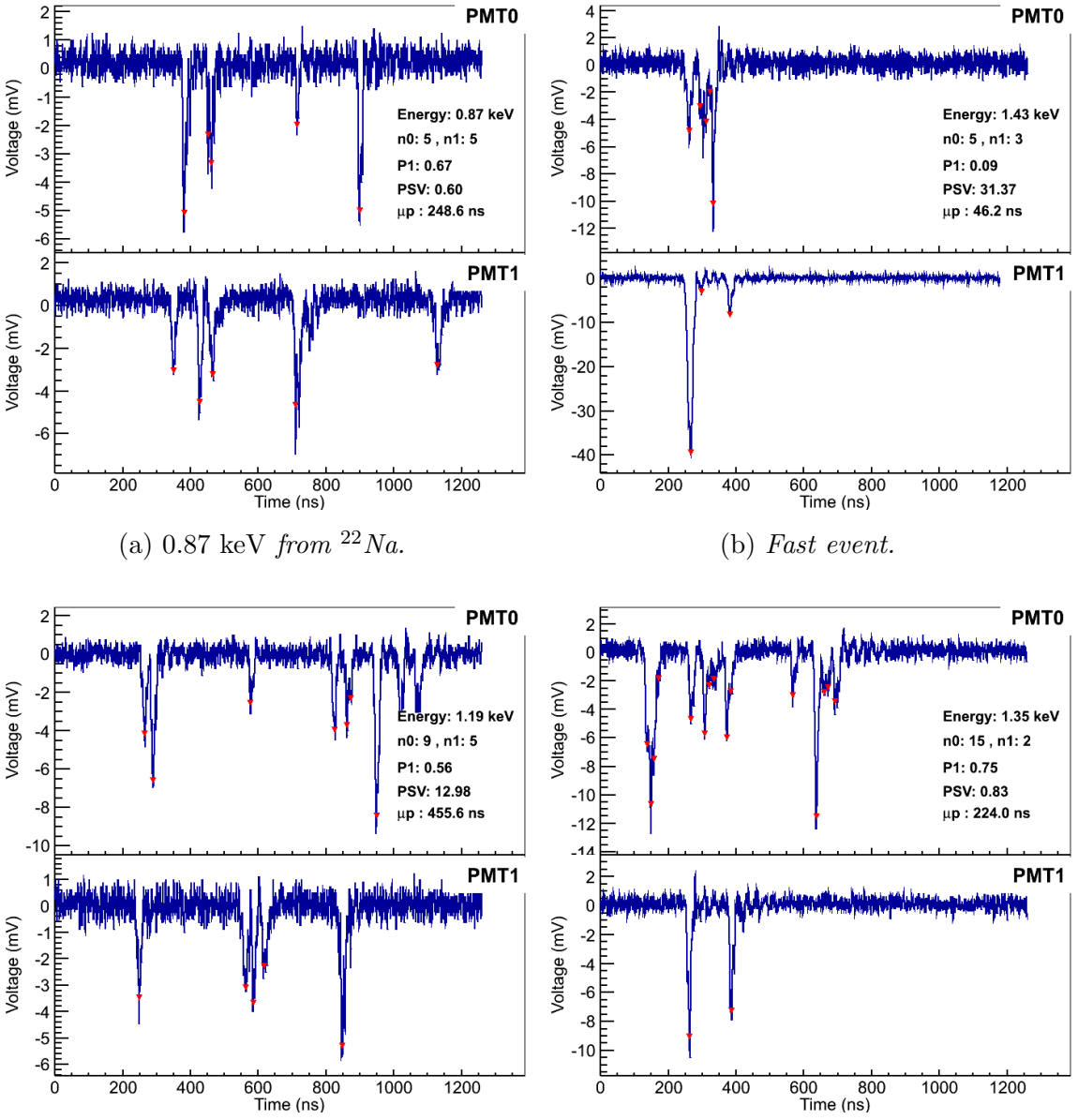

(a) 0.87 keV *from* ^{22}Na.

(b) *Fast event.*

(c) *Long* μ_p *event.*

(d) *Low energy asymmetric event.*

Figure 3.3: *Examples of low energy digitized pulses. The two traces at each panel correspond to the two PMT signals, while the legend display the energy of the event, number of peaks detected by the algorithm at every trace* (n_0 *and* n_1)*, and PSA parameters* P_1*,* PSV *and* μ_p*. Red triangles: phe identified by the peak-searching algorithm. Panel (a): 0.87 keV bulk scintillation event from* ^{22}Na *decay selected by coincidence with a 1274.5 keV deposition in another crystal. Panel (b): fast event, likely a Cherenkov light emission in one PMT that is seen in the opposite PMT. Panel (c): long* μ_p *event, possibly caused by phosphorescence in the NaI(Tl) crystal. Panel (d): low energy asymmetric event. From Ref. [15].*

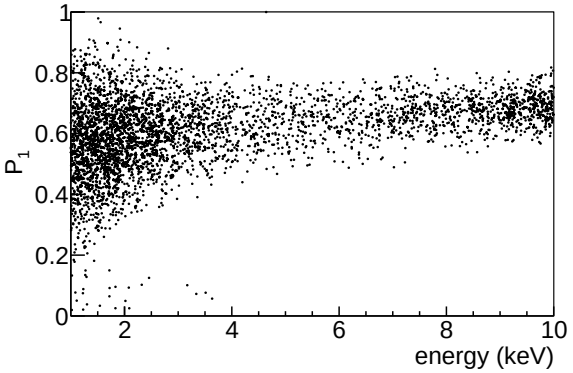

(a) ^{109}Cd *calibration.*

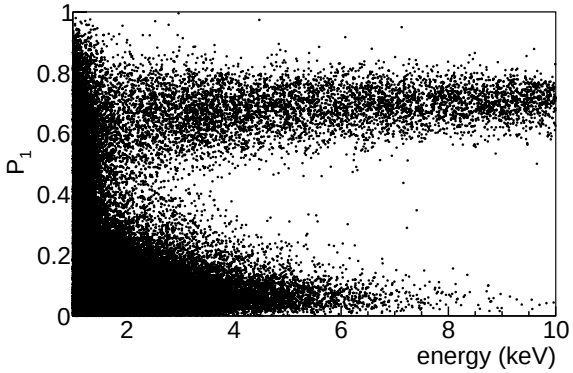

(b) *Background events.*

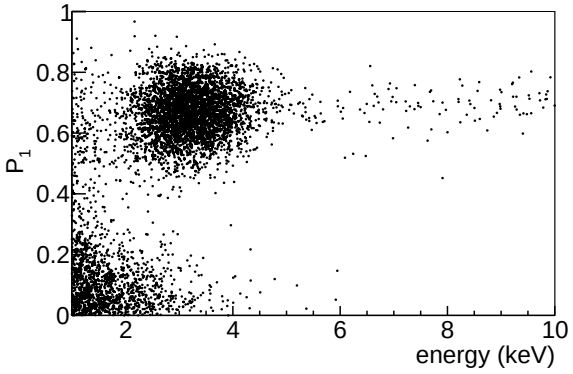

(c) ^{40}K *coincidence.*

Figure 3.4: P_1 *parameter distribution of detector D1 as a function of the energy for* ^{109}Cd *events from the first calibration run (a) and background events from the first dark matter run (b), as well as for 3.2 keV events coming from the internal* ^{40}K *disintegration and selected by the coincidence with the high energy gamma (c).*

being A_i and t_i the amplitude and time of the phe identified in the pulse trace, respectively. For the phe identification, the same peak-searching algorithm developed for the SER construction (see Section 2.3.1) is used.

Figure 3.5 shows the distribution of these pulse shape parameters for the low energy events in [1,2] keV (a) and [2,6] keV (b) of detector D1 for the ∼10% unblinded data. Bulk scintillation events are clustered around (P_1=0.65, log(μ_p)=−1.65), while most background events at these energies correspond to very fast events with P_1<0.2.

Due to the correlation between both parameters, a bivariate analysis is performed, assuming that $\vec{\boldsymbol{x}} = \begin{pmatrix} P_1 \\ \log(\mu_p) \end{pmatrix}$ follows a 2-dimensional Gaussian distribution with mean $\vec{\boldsymbol{\mu}}$ and covariance matrix $\boldsymbol{V}$. Both $\vec{\boldsymbol{\mu}}$ and $\boldsymbol{V}$ are calculated in [1,2] keV win-

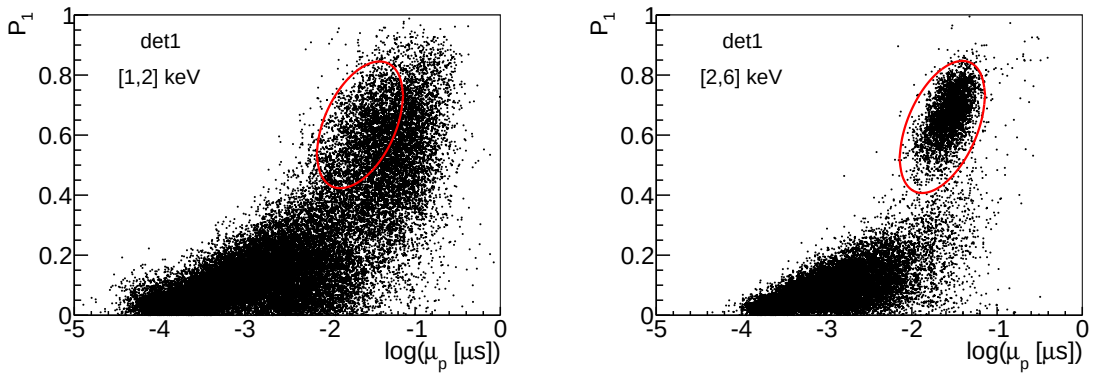

(a) (b)

Figure 3.5: *Distribution of the background events of the ∼10% unblinded data of detector D1 with energies between 1 and 2 keV (a) and from 2 to 6 keV (b) in the* $(P_1, \log(\mu_p))$ *plane. Bulk scintillation events are clustered around* $(0.65, -1.65)$*. The red line encloses the events selected by the PSV cut in this detector.*

dow from the 0.87 keV bulk scintillation population from ^{22}Na decay selected by coincidence with a 1274.5 keV energy deposition in another crystal (the specific distribution of these events can be seen in Figure 3.10a). The resulting parameter is defined as

$$PSV = (\vec{\boldsymbol{x}} - \vec{\boldsymbol{\mu}})^T \boldsymbol{V}^{-1} (\vec{\boldsymbol{x}} - \vec{\boldsymbol{\mu}}). \tag{3.3}$$

For any given value of the parameter PSV_{cut}, the inequality $PSV < PSV_{cut}$ represents an ellipsoid centered at $\vec{\boldsymbol{\mu}}$, and such that the probability that an event $\vec{\boldsymbol{x}}$ lies outside the ellipsoid is given by $1 - F_{\chi^2}(PSV_{cut})$, where F_{χ^2} is the cumulative χ^2 distribution with 2 degrees of freedom [74]. $PSV_{cut} = 3$ (red line in Figure 3.5) is selected, so the efficiency of the cut at [1,2] keV is 77.7%, but as the distribution of the PSA parameters depends on energy, the efficiency of the cut in other energy regions has to be calculated, as it is explained in detail in Section 3.2.2.

3.1.3 Asymmetric events

A different population of background events, which do not have the timing characteristics of afterpulses or pulse tails, is observed below 2 keV. The main characteristic of these events is a strong asymmetry in the energy partition among both PMTs (see an example in Figure 3.3d). They are also observed by the COSINE collaboration [17], and could be related to the light emission observed in PMTs by other experiments [232, 233]. These asymmetric events can be easily distinguished by the

difference in the number of peaks identified in the signals of the two PMTs of every detector (n_0 and n_1) by the peak-finding algorithm. Figure 3.6a shows the distribution of n_0 and n_1 for background events corresponding to the ∼10% unblinded data in the [1,2] keV energy region. Most of them display a very asymmetric distribution, with few peaks (one or two) in one PMT and more than five in the other one. It is worth noting that, with more than 7 phe/keV/PMT, the probability of having 1 or 2 phe in one PMT at 1 keV is around 3%. These events, only visible below 2 keV in dark matter runs (see Figure 3.6b), are not present neither in the ^{109}Cd calibration runs (Figure 3.6c), nor in the 0.87 keV bulk scintillation population from ^{22}Na (Figure 3.6d), so they are presumably fake light events produced at or near the PMTs.

With the PSV parameter, derived from the addition of the two PMT signals, this asymmetric population cannot be distinguished from that of bulk scintillation, so a cut based on the number of peaks detected at every PMT is used to reject them. In particular, an event is required to have more than four peaks identified by the peak-finding algorithm at every PMT signal (see red lines in Figure 3.6). The efficiency of this cut is calculated on calibration runs as explained in Section 3.2.3.

3.2 Efficiency estimate

The total detection efficiency, $\varepsilon(E, d)$, calculated independently for every detector d as a function of the energy E, is factorized as

$$\varepsilon(E, d) = \varepsilon_{trg}(E, d) \times \varepsilon_{PSV}(E, d) \times \varepsilon_{asy}(E, d), \tag{3.4}$$

where $\varepsilon_{trg}(E, d)$ is the trigger efficiency (probability that an event is triggered by the DAQ system), and $\varepsilon_{PSV}(E, d)$ and $\varepsilon_{asy}(E, d)$ are the efficiency of the PSV and asymmetry cuts, respectively. For the muon-vetoed events, no efficiency is required, but a 1 s dead time is calculated for every muon triggering the veto system, that is added to the total dead time of the DAQ system and then, discounted from the total live time. The efficiency of the anticoincidence cut can be safely taken as one, given that, with a total rate below 5 Hz, the probability of an accidental coincidence between two detectors in the digitization window (1.2 μs) is negligible.

3.2.1 Trigger efficiency

The hardware threshold is low enough to efficiently trigger at the photoelectron level each PMT (see Section 2.4). However, at very low energy, very few photoelectrons

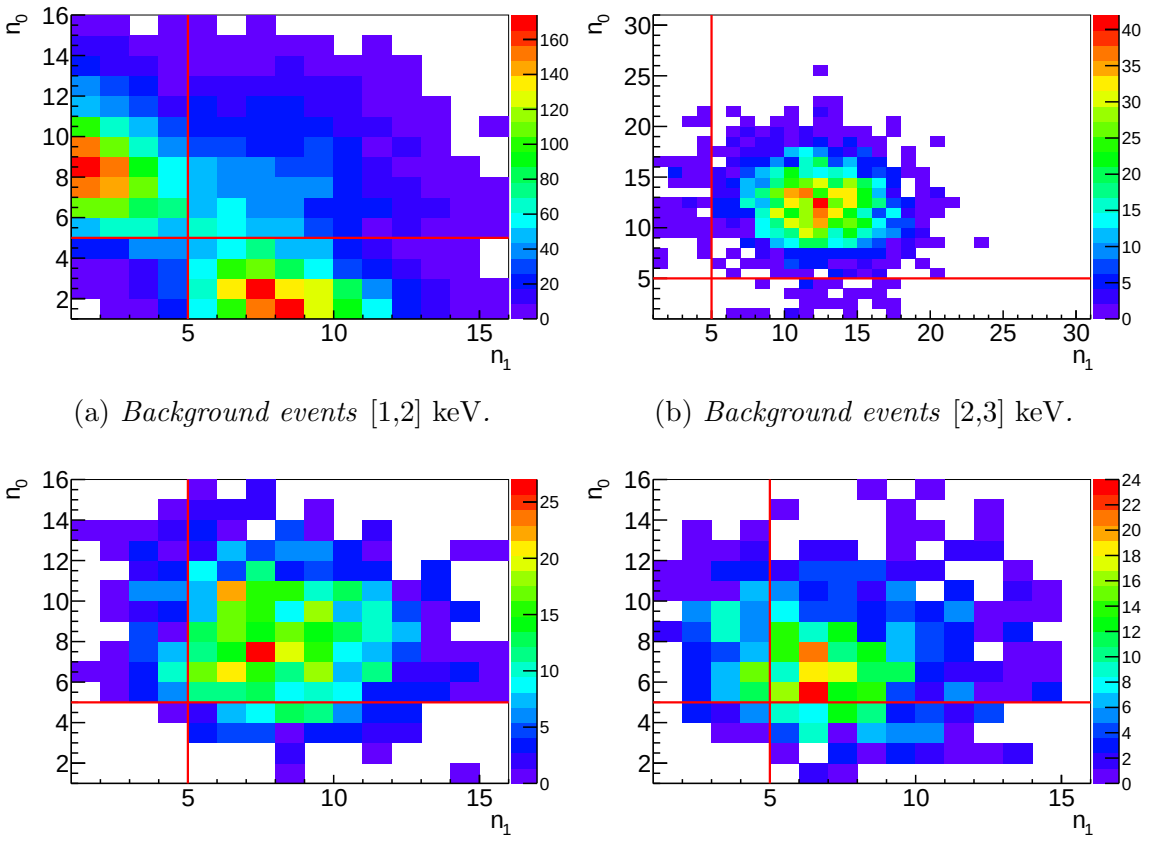

(a) *Background events* [1,2] keV.

(b) *Background events* [2,3] keV.

(c) ^{109}*Cd events* [1,2] keV.

(d) ^{22}*Na coincidence* [1,2] keV.

Figure 3.6: *Distribution in the* (n_0, n_1) *plane (i.e., number of peaks detected by the algorithm for each of the two PMT signals from the same module) for: (a)* $\sim$*10% unblinded data background events with energy between 1 and 2 keV; (b) same but for events with energy between 2 and 3 keV; (c)* ^{109}*Cd calibration events with energy between 1 and 2 keV; (d) bulk scintillation 0.87 keV events from* ^{22}*Na decay selected by coincidence with a 1274.5 keV deposition in another crystal (3 years statistics).*

are collected, so the mean time interval between them increases, thus reducing the efficiency of the trigger by impossing the coincidence requirement between both PMTs.

Given the high light collection and large coincidence window (200 ns), a significant trigger efficiency reduction above 1 keV is not expected for ANAIS–112. As reported in Ref. [228], ^{22}Na and ^{40}K coincidence events allowed to experimentally measured the trigger efficiency for previous ANAIS prototypes in set-ups having two or three modules and a slightly different readout. Very high trigger efficiency was observed then, of 98% above 1.5 keV, and as far as the same DAQ hardware/software is used in ANAIS–112, differences in trigger efficiency in the present set-up are not expected.

To quantify the trigger efficiency a Monte Carlo technique described in Ref. [15] is used: for every detector, $6{\times}10^4$ events of random energy E between 0 and 6 keV are simulated. Basically, for each simulated event, the number of photoelectrons in a PMT is selected according to a Poisson distribution with mean given by $E \times LC(d, PMT)$, where $LC(d, PMT)$ is the measured light collection for that detector and PMT (see Table 2.10). The phe are simulated as Gaussian peaks of widths between 5 and 6 ns, depending on the detector. The arrival time of every phe is sampled from an exponential probability density function with τ=230 ns, as for NaI(Tl) scintillating signals, and their amplitudes are sampled from the SER amplitude distribution of the corresponding PMT. Then, the trigger efficiency as a function of energy is calculated as the number of events having the first phe identified in every PMT above the trigger threshold and within 200 ns divided by the total number of simulated events generated for that energy. The result is depicted in Figure 3.7. As expected, the efficiency is larger than 98% down to 1 keV. The small differences among the detectors are only due to the spread in light collection and phe width.

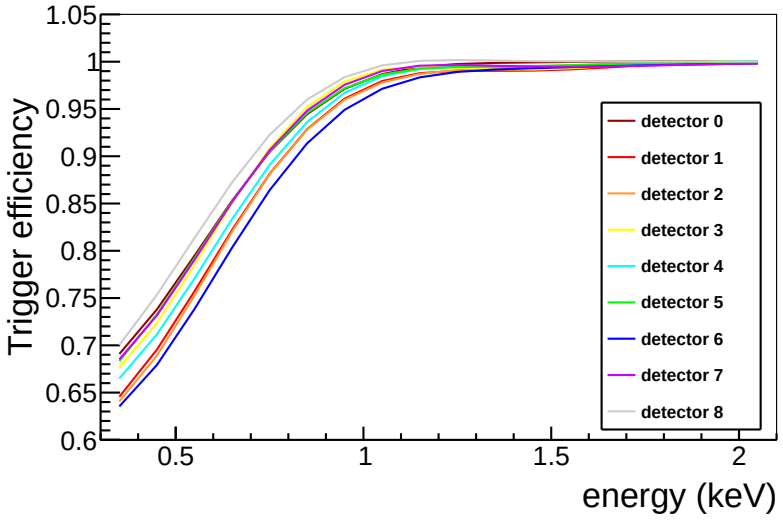

Figure 3.7: *Trigger efficiency for every detector, calculated from the measured light collected by a Monte Carlo technique.*

3.2.2 PSV cut efficiency

From Equation 3.3, the definition of the PSV variable provides the efficiency for every cut value, but it is only valid in the energy region in which the means and covariances are calculated, that is, between 1 and 2 keV. Instead of changing the variable definition for every energy range, the same definition is kept and the effi-

ciency of the cut is calculated as a function of energy. For this purpose, the ^{22}Na and ^{40}K low energy populations selected in coincidence with a 1274.5 keV or 1460.8 keV γ in another detector are used. It is decided to use the ^{22}Na/^{40}K events accumulated during the three years of measurement to reduce the statistical uncertainty in the efficiency estimate. In order to check that using the three years of data in the calculation of the center $\vec{\boldsymbol{\mu}}$ is equivalent to estimate the center of the ellipsoid in the ANAIS–112 physics-run data separately, the stability of the mean value of the P_1 and $\log(\mu_p)$ parameters for every detector are shown in Figures 3.8 and 3.9, respectively. Black dots represent the mean value estimated in each run, whereas red points correspond to the mean value using full statistics.

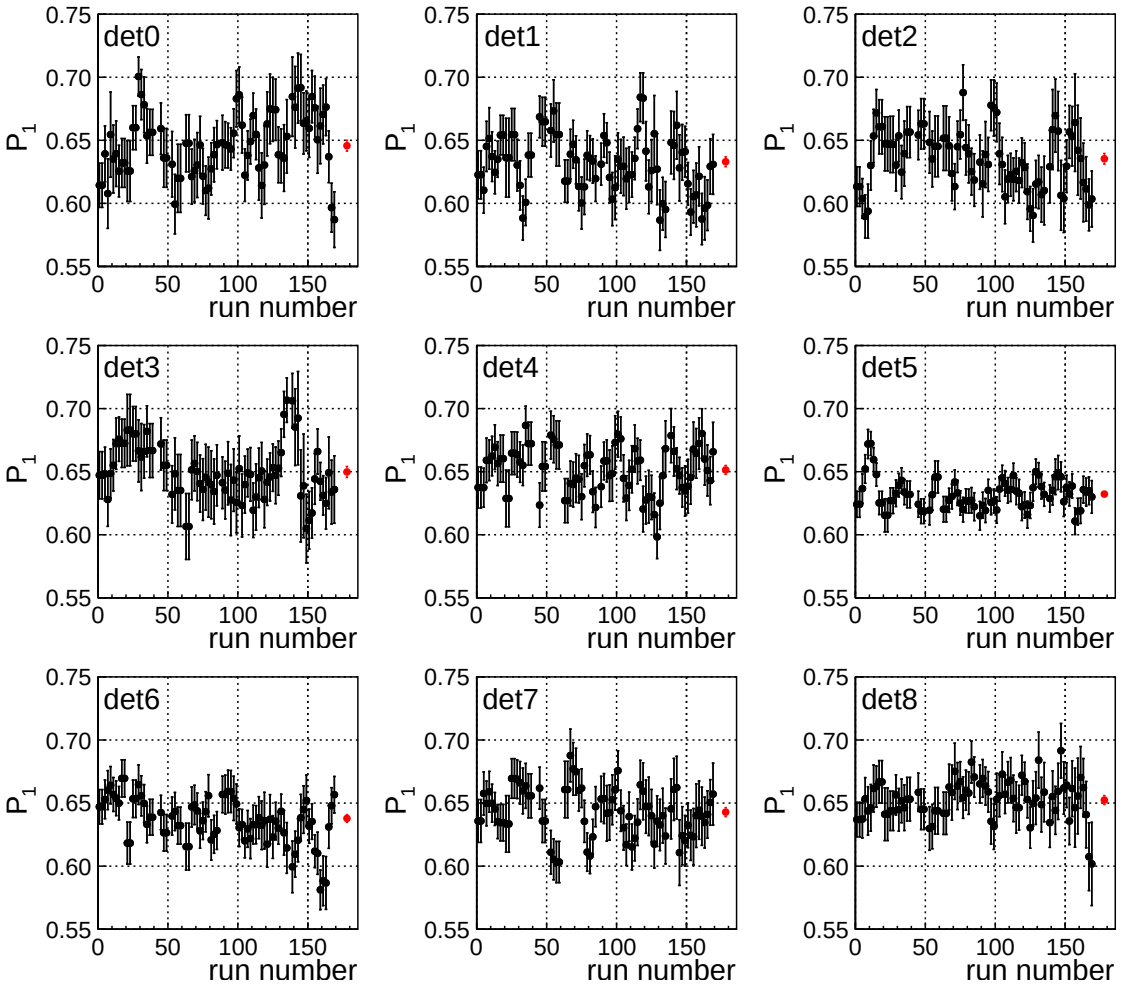

Figure 3.8: *Stability of the P_1 parameter calculated on the $^{22}Na/^{40}K$ coincidence events in [1,2] keV energy region for each run and detector (black dots). Red points represent the mean value using full statistics.*

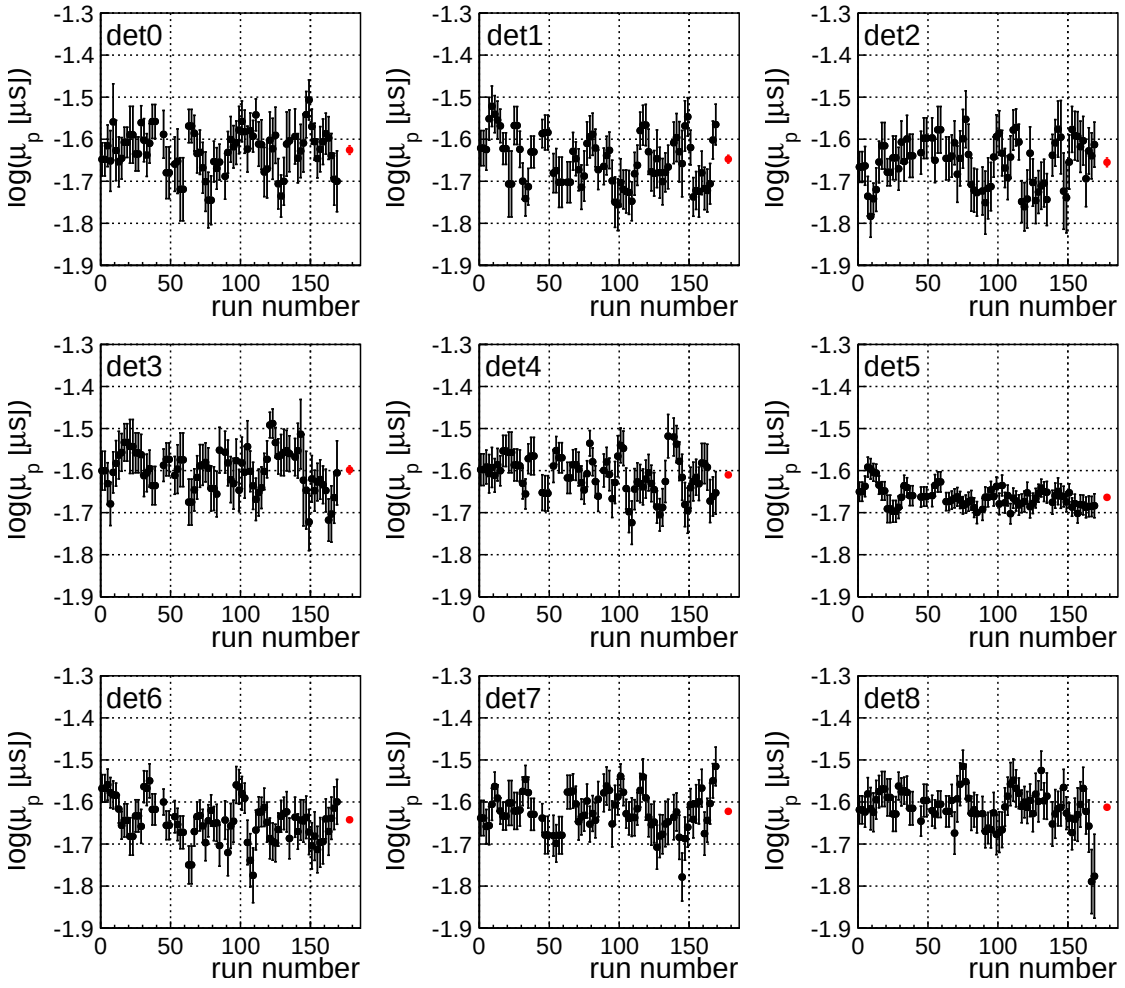

Figure 3.9: *Stability of the* $\log(\mu_p)$ *parameter calculated on the* $^{22}Na/^{40}K$ *coincidence events in [1,2] keV energy region for each run and detector (black dots). Red points represent the mean value using full statistics.*

Figure 3.10 shows the distribution of these low energy events of detector D1 along the first three years of data taking in the PSA parameters plane for three energy ranges. In the first one (1-2 keV), $\vec{\boldsymbol{\mu}}$ and $\boldsymbol{V}$ are calculated and PSV_{cut}=3 is fixed (red ellipse) in order to have a 77.7% efficiency at that energy. This calculation is done for every detector independently. As commented in Section 2.7.2, the ^{22}Na and ^{40}K populations are polluted with fast (Cherenkov-like) events in the PMT in coincidence with a γ in one of the crystals [196]. Consequently, to avoid these events, P_1>0.4 is required before calculating $\vec{\boldsymbol{\mu}}$ and $\boldsymbol{V}$ (see projections along the P_1 and $\log(\mu_p)$ axis in Figure 3.10a). Then, the efficiency is computed in 1 keV bins for larger energies as the number of ^{22}Na/^{40}K events in the ellipsoid divided by the total number of ^{22}Na/^{40}K events having P_1>0.4. The results are shown in

Figure 3.11. They are very similar for all the ANAIS–112 modules, with efficiency increasing from 77.7% at 1.5 keV (fixed by the PSV_{cut} choice) up to 96% at 2.5 keV and 98% at 3.5 keV. The statistical uncertainties in the efficiency, due to the small number of ^{22}Na/^{40}K coincident events in each module, are of the order of 1.5% in [1,2] keV for all the modules.

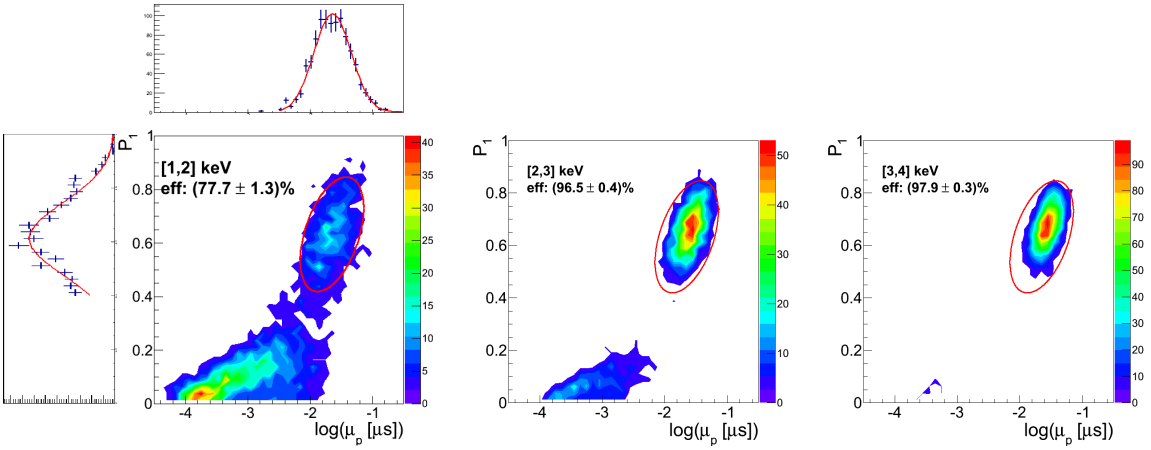

(a) (b) (c)

Figure 3.10: *Distribution of the events at low energy selected by coincidence with a 1274.5 keV or 1460.8 keV γ in another detector in the $(P_1, \log(\mu_p))$ plane. The three panels correspond to [1,2] keV (a), [2,3] keV (b) and [3,4] keV (c) energy regions. The red line corresponds to PSV=3. In panel (a), the projections of P_1 and $\log(\mu_p)$ variables are also shown in left and top panels, respectively, and the fitting to single Gaussian lineshapes, considering only P_1>0.4 events, which supports the bivariate analysis carried out.*

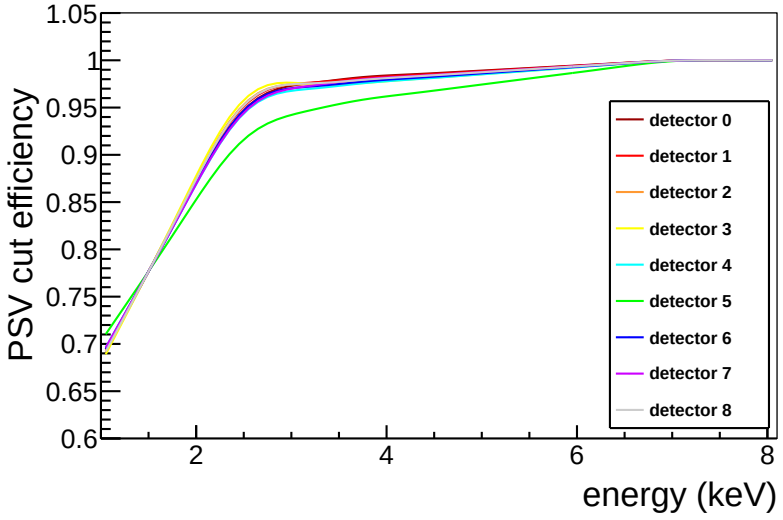

Figure 3.11: *PSV cut efficiency for every detector, calculated from the distribution of the ^{22}Na/^{40}K bulk events selected in coincidence with a high energy γ.*

This procedure to estimate acceptance efficiencies is not valid for energies larger than ∼4 keV, since there are very few events selected by the coincidence condition (see Figure 2.22). In order to extend the efficiency calculation up to 10 keV, the Monte Carlo simulation described in Section 3.2.1 is used. The consistency between MC and the data was verified in Ref. [15].

3.2.3 Asymmetry cut efficiency

The efficiency of the asymmetry cut (more than 4 peaks identified by the algorithm at every PMT) is evaluated using all the ^{109}Cd calibration events accumulated along the first three years of calibration runs to have enough events in the [1,2] keV energy region. To do so, the number of events surviving the cut are divided by the total number of events, as a function of energy. Results are displayed in Figure 3.12. The efficiency is equal to one down to 2 keV, and then it decreases steeply down to 0.2-0.45 at 1 keV, depending on the detector. This energy, 1 keV, has been chosen as common analysis threshold for all the modules, considering the acceptance efficiency of this filtering, which is the most restrictive.

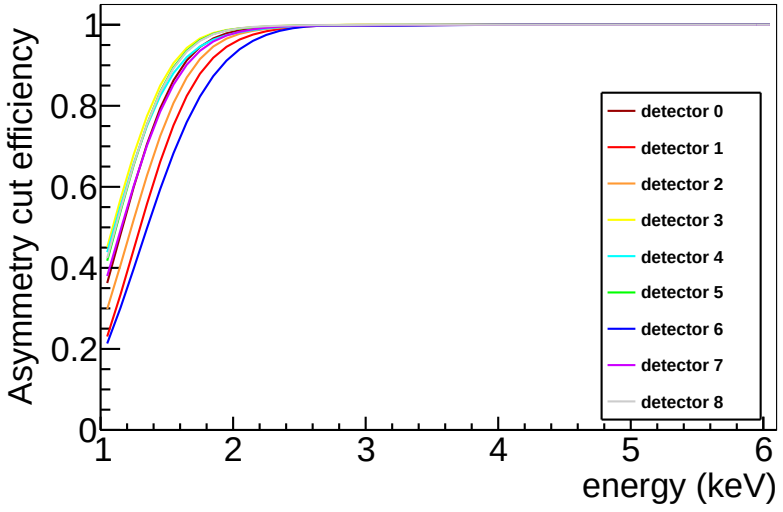

Figure 3.12: *Asymmetry cut efficiency for every detector, calculated in ^{109}Cd calibration runs.*

The consistency of the procedure is checked with the ^{22}Na and ^{40}K populations selected by coincidence. These events are not polluted with the asymmetric population, as shown in Figure 3.6. Figure 3.13 compares for each detector the coincidence low energy spectra, accumulated during the three years of data taking, obtained after applying the PSV cut and correcting for the corresponding efficiency (red points)

with the one obtained after applying also the asymmetry cut and correcting for the corresponding efficiency (black points). The agreement is excellent for all detectors down to 1.2 keV. Below this energy there is a discrepancy for some of the detectors (mainly D0, D1, D2 and D6) up to 18% at 1 keV.

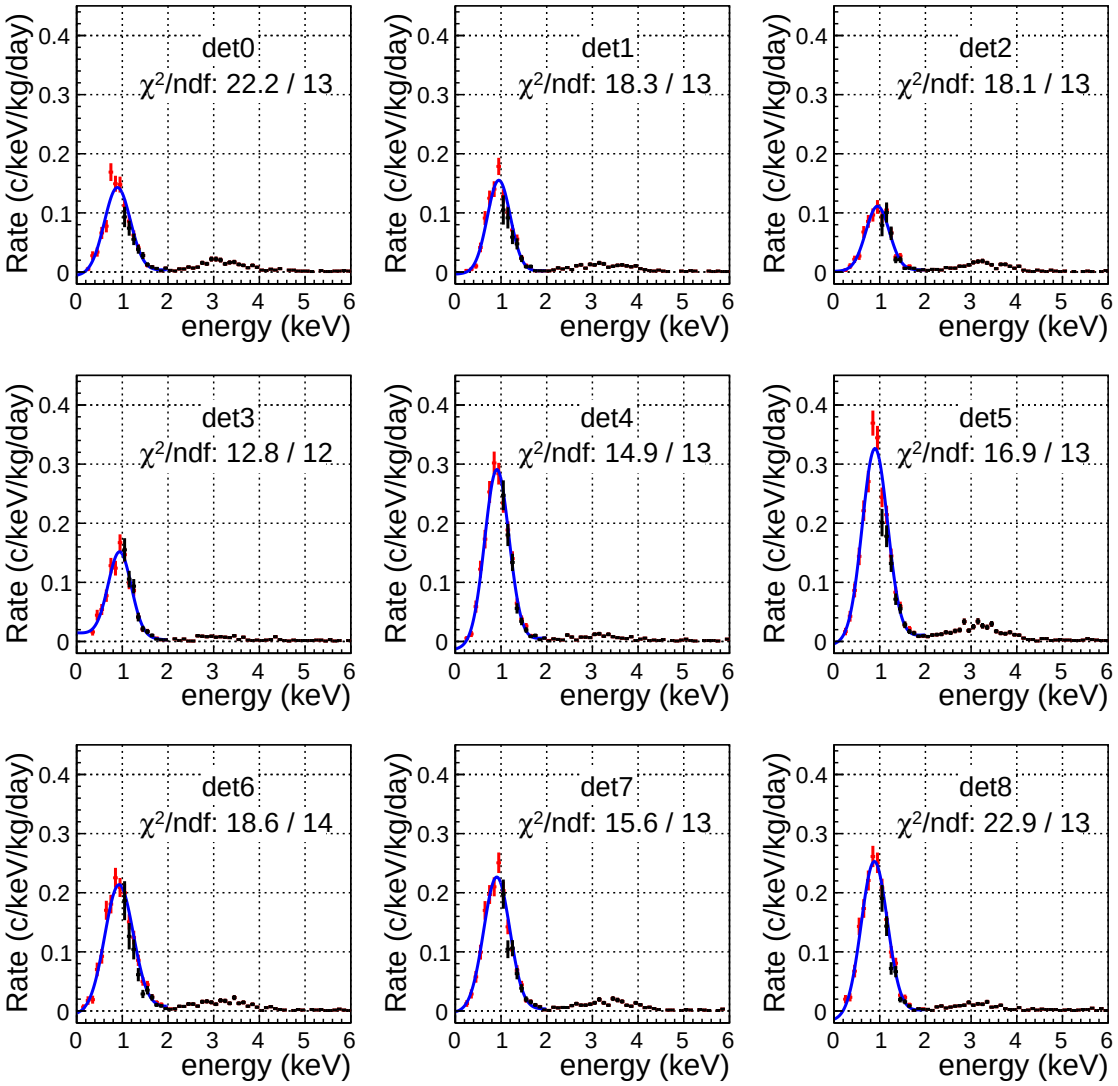

Figure 3.13: *Low energy spectra of the nine modules in coincidence with a high energy gamma between 1215 and 1335 keV in a second module. Red points: Data selected by the PSV cut and corrected with the corresponding efficiency (PSV and trigger). Black points: In addition to the previous one, the asymmetry cut and the corresponding efficiency correction is applied. Blue line: gaussian fit to the red points. The chi-squared of the fit is also displayed.*

3.2.4 Total detection efficiency

Finally, the total efficiency for the selection of dark matter compatible events in every ANAIS–112 detector is calculated by multiplying the three efficiencies (see Equation 3.4). The trigger efficiency has been estimated from MC simulations, and the efficiencies of the pulse shape and asymmetry cuts have been evaluated from the 3.2 and 0.87 keV events selected by the coincidence with the high energy gammas following ^{40}K and ^{22}Na decays, and ^{109}Cd calibration events, respectively, accumulated for all the analyzed exposure. Figure 3.14 shows total detection efficiencies for each ANAIS–112 detector, and it can be observed that efficiency ranges from 0.15 to 0.30 at 1 keV, depending on the detector, increases up to 0.80 at 2 keV, and is nearly 1 at 4 keV for all the modules. Statistical uncertainties in the total efficiency vary from 1 to 3% at 1 keV down to 0.1% at 6 keV.

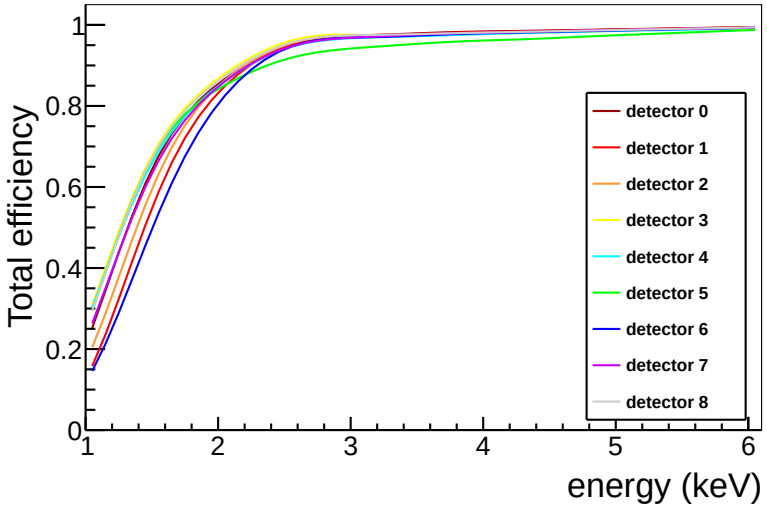

Figure 3.14: *Total efficiency, obtained as the product of the trigger, pulse shape cut and asymmetry cut efficiencies.*

3.3 Low energy spectrum

Figure 3.15 shows the energy spectra in the region of interest corresponding to the ∼10% unblinded data for each of the detectors in anticoincidence (single-hit events) after event selection and efficiency correction. A detailed analysis of the different background contributions, based on MC simulations of quantified radioactive contaminants, is reported in Ref. [196]. The background in the ROI is dominated by the internal contamination of the NaI(Tl) crystals themselves, and varies depending on the detector as do their powder purification procedures, crystal growing protocols

and starting time of underground storage. The main internal background contributions come from ^{40}K, ^{210}Pb (contaminants present in the starting powder, and presumably entering into the powder purification or growing procedures through ^{222}Rn, respectively), and ^{22}Na and ^{3}H (having cosmogenic origin). In all detectors the ^{40}K peak at 3.2 keV is clearly visible. The background level at 2 keV ranges from 2 to 5 c/keV/kg/d, depending on the detector, and then increases up to 7–13 c/keV/kg/d at 1 keV. Corresponding values for the single-hit total spectrum of DAMA/LIBRA–phase 2 are 1 and 1.8 c/keV/kg/d, respectively [7].

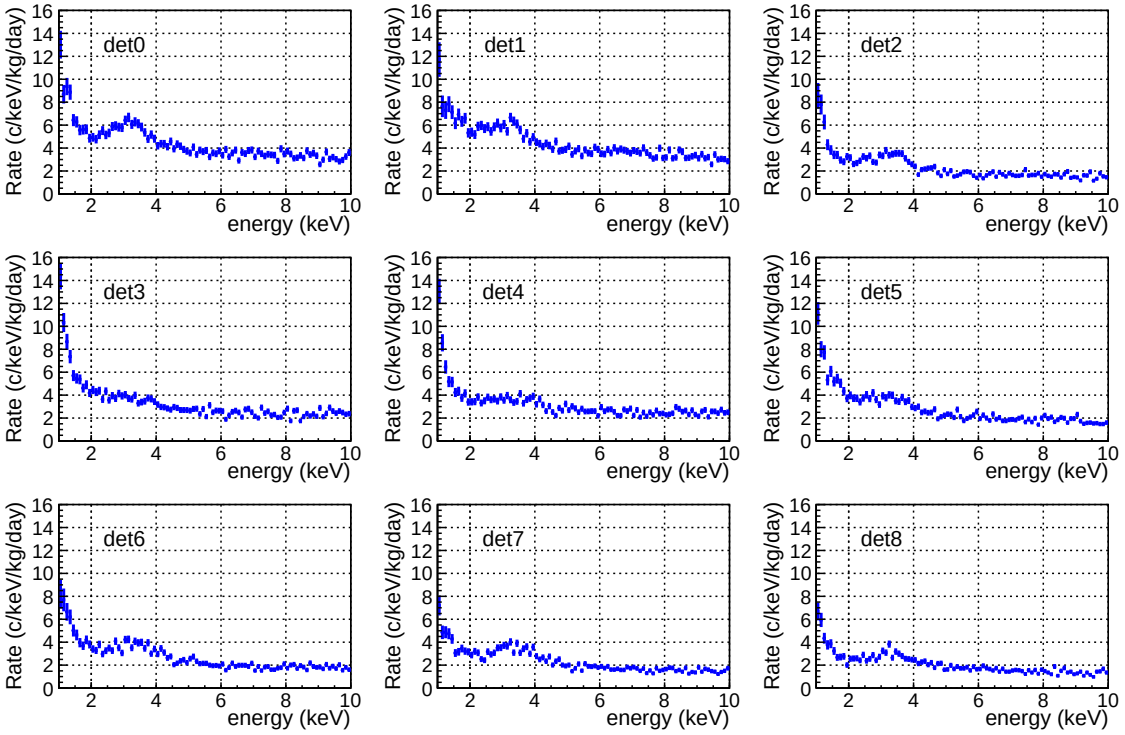

Figure 3.15: *Anticoincidence energy spectrum measured in the ROI after filtering and efficiency correction for each detector, corresponding to the ∼10% unblinded data. The ^{40}K peak at 3.2 keV is clearly visible.*

The total anticoincidence background (adding up all the nine detectors) below 10 keV for the ∼10% unblinded data is shown in Figure 3.16. The background level at 1 and 2 keV is 10 and 4 c/keV/kg/d, respectively.

Finally, a comparison between the total anticoincidence background in the energy region below 100 keV for the unblinded data before (blue points) and after applying the filtering and the corresponding efficiency correction (red points) is shown in Figure 3.17. This energy region is also dominated by the internal contamination of the crystal, with a prominent peak at ∼50 keV coming from ^{210}Pb. The small peak

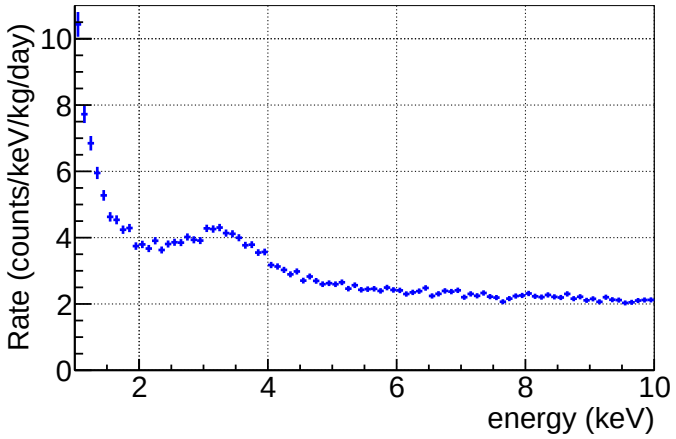

Figure 3.16: *Total anticoincidence energy spectrum of ANAIS–112 at low energy after filtering and efficiency correction, corresponding to the ∼10% unblinded data. The ^{40}K peak at 3.2 keV is clearly visible.*

at ∼26 keV originated by ^{109}Cd and ^{113}Sn cosmogenic isotopes ($T_{1/2}$ = 461.9 and 115.1 days, respectively) is also visible. It can be observed that non-bulk scintillation events clearly dominates the rate in the region of interest, and their correct identification is a key point in this kind of experiments. Above 100 keV (see Figure 2.21) the background is dominated by the PMTs radioactive contamination.

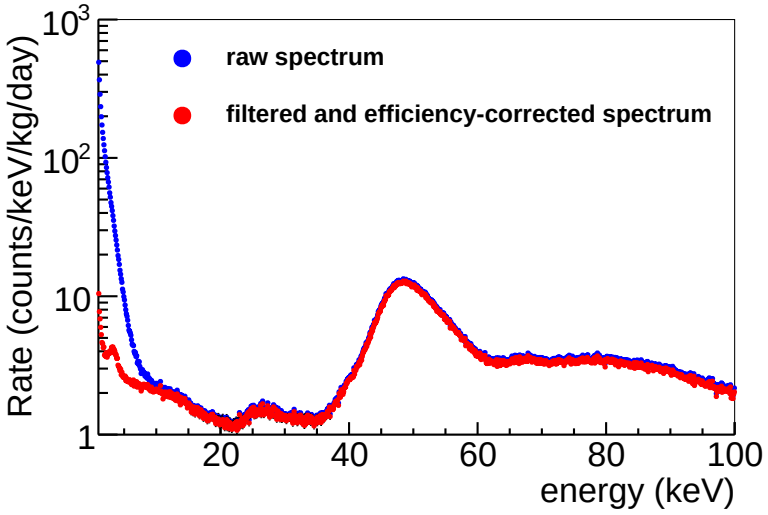

Figure 3.17: *Blue points: total anticoincidence energy spectrum (all detectors) corresponding to the ∼10% unblinded data in the energy region from 0 to 100 keV. Red points: same, but after applying the event selection criteria and correcting for efficiency. Main features identified in this spectrum correspond to the decay of isotopes found in the crystals: ^{210}Pb (around 50 keV), ^{109}Cd and ^{113}Sn (from 20 to 30 keV) of cosmogenic origin, and ^{40}K (around 3 keV).*

Chapter 4

Sensitivity prospects

In this chapter, the expected sensitivity of the ANAIS–112 experiment to the annual modulation observed by DAMA/LIBRA is analyzed. Using the same target and technique than DAMA/LIBRA collaboration, ANAIS–112 is able to test the DAMA/LIBRA result in a model independet way, looking for a signal in the same energy region where DAMA/LIBRA does. This study was developed during my Master's Dissertation [169] from the data of the D0, D1 and D2 modules, and considering as the only source of uncertainty, the purely statistical. Afterwards, the result obtained from the data of all ANAIS–112 detectors was published in Ref. [16]. Here, the procedure followed in the respective publications is summarized, and other sources of uncertainty are taken into consideration, such as that associated with the acceptance efficiency, or the low energy calibration itself. In addition, a Monte Carlo simulation has also been developed to check the consistency of the results, and the expected sensitivity when combining the ANAIS–112 data with those of COSINE–100 has been estimated.

In Section 4.1, a model independent modulation in the interaction rate is searched, i.e. without assumptions about the origin and characteristics of the signal other than the one-year period and the 152.5-days phase. Subsequently, in Section 4.2, it will be considered the particular case of a modulation induced by galactic halo dark matter particles in conventional WIMP-DM scenario. Finally, it will be concluded that ANAIS–112 can prove the DAMA/LIBRA result in a model independent way at 3σ C.L. in 5 years of data taking, having a significant discovery potential if the modulation signal is effectively due to dark matter particles.

4.1 Model independent modulation

In this section, it is analyzed if the ANAIS experiment is sensitive to the annual modulation signal observed by DAMA/LIBRA in different background scenarios. Firstly, the background level is supposed to remain constant over time; and secondly, a background level that decreases with time will be considered. The reason behind this choice is the presence of some radioactive isotopes in the ANAIS–112 NaI(Tl) modules, like ^{22}Na ($T_{1/2} = 2.6$ yr) and long-lived isotopes as ^{210}Pb ($T_{1/2} = 22.2$ yr) and maybe ^{3}H ($T_{1/2} = 12.3$ yr). In some of the modules short-lived cosmogenic isotopes have also been identified (see Section 2.10).

4.1.1 Constant background

As a first approach, constant background is considered, then the normalized rate of events (in c/keV/kg/d units) can be expressed as:

$$B(\tau) = R_0 + S_m \cos\tau, \tag{4.1}$$

where R_0 is the mean annual rate and $\tau = 2\pi(t - t_0)/T$.

The test statistic [234] to evaluate the null ($S_m = 0$) and the alternative ($S_m \neq 0$) hypothesis is the least squares estimator of the amplitude, $\hat{S}_m$, with expected value $E(\hat{S}_m) = S_m$ and variance $var(\hat{S}_m)$. Asymptotically, $\hat{S}_m$ follows a normal distribution.

In order to estimate the ANAIS–112 sensitivity to the annual modulation signal, a two parameter linear least-squares fit of Equation 4.1 for n time bins is carried out, where the dependent variable B_i is the measured rate in the i^{th} time bin τ_i and the independent variable is $\cos\tau_i$. In matrix form:

$$\vec{\mathcal{B}} = \mathcal{M}\vec{\mathcal{P}} \Longrightarrow \begin{pmatrix} B_1 \\ \vdots \\ B_n \end{pmatrix} = \begin{pmatrix} 1 & \cos\tau_1 \\ \vdots & \vdots \\ 1 & \cos\tau_n \end{pmatrix} \begin{pmatrix} R_0 \\ S_m \end{pmatrix} \tag{4.2}$$

The covariance matrix of parameters, $Cov(\mathcal{P})$, is the inverse of the matrix $\mathcal{M}^T\mathcal{W}\mathcal{M}$ [235], where $\mathcal{W} = diag(w_1, ..., w_n)$ is the diagonal matrix of weights $w_i = 1/var(B_i) \equiv 1/\sigma_i^2$ because all B_i are independent of each other.

$$\mathcal{M}^T\mathcal{W}\mathcal{M} = \begin{pmatrix} \sum_i w_i & \sum_i w_i \cos\tau_i \\ \sum_i w_i \cos\tau_i & \sum_i w_i \cos^2\tau_i \end{pmatrix} \tag{4.3}$$

$$Cov(\mathcal{P}) \equiv (\mathcal{M}^T\mathcal{W}\mathcal{M})^{-1} = \frac{1}{det(\mathcal{M}^T\mathcal{W}\mathcal{M})} \begin{pmatrix} \sum_i w_i \cos^2\tau_i & -\sum_i w_i \cos\tau_i \\ -\sum_i w_i \cos\tau_i & \sum_i w_i \end{pmatrix} \tag{4.4}$$

being $det(\mathcal{M}^T\mathcal{W}\mathcal{M})$ the determinant of the matrix $\mathcal{M}^T\mathcal{W}\mathcal{M}$:

$$det(\mathcal{M}^T\mathcal{W}\mathcal{M}) = \sum_i w_i \cdot \sum_i w_i \cos^2\tau_i - \left(\sum_i w_i \cos\tau_i\right)^2 \tag{4.5}$$

The element $Cov(\mathcal{P})_{22}$ corresponds to the variance of the modulation amplitude,

$$var(\hat{S}_m) = \frac{\sum_i w_i}{\sum_i w_i \cdot \sum_i w_i \cos^2\tau_i - \left(\sum_i w_i \cos\tau_i\right)^2} \tag{4.6}$$

Under the constant background assumption, all weights w_i are equal ($w_i = w_0 \equiv 1/\sigma_0^2$), thus the variance of the modulation amplitude is simplified as:

$$var(\hat{S}_m) = \frac{nw_0}{nw_0^2 \sum_i \cos^2\tau_i - w_0^2 \left(\sum_i \cos\tau_i\right)^2} = \sigma_0^2 \cdot \frac{n}{n\sum_i \cos^2\tau_i - \left(\sum_i \cos\tau_i\right)^2} \tag{4.7}$$

As already demonstrated in Ref. [169] and [16], particularly interesting is the case in which an integer number of periods is measured, since the previous equation is reduced to an expression that only depends on the background variance and the number of time bins.

$$var(\hat{S}_m) = \frac{2\sigma_0^2}{n} \tag{4.8}$$

If N_{ij}^k is the number of observed events (Poisson distributed) in the i^{th} time bin and j^{th} energy bin of detector k, and ε_j^k is the fraction of true events remaining after the cuts to reject the noise and select true events in the j^{th} energy bin of detector k (note that the acceptance efficiency ε_j^k has been estimated using full statistics, so it is time-independent):

$$B_{ij}^k = \frac{N_{ij}^k/\varepsilon_j^k}{\delta E_j \cdot m_k \cdot \Delta t_i} \tag{4.9}$$

where m_k is the mass of the detector k, δE_j and Δt_i are the width of the energy and live time bins, respectively. All ANAIS–112 detectors have the same mass

($m_k = m = 12.5$ kg), and equally-spaced bins in energy and time are considered ($\delta E = 0.1$ keV, Δt). Then, the background variance may be written as:

$$var(B_{ij}^k) = \frac{B_{ij}^k/\varepsilon_j^k}{\delta E \cdot m \cdot \Delta t} + \frac{(B_{ij}^k)^2 var(\varepsilon_j^k)}{(\varepsilon_j^k)^2} \tag{4.10}$$

being the first term, the variance due to Poisson statistics, and the second term, the variance related to efficiency.

So, the total background level in the i^{th} time bin is obtained by integrating the N energy bins and adding up all the $N_{det} = 9$ detectors as follows:

$$B_i = \frac{1}{N}\frac{1}{N_{det}}\sum_{j=1}^{N}\sum_{k=1}^{N_{det}} B_{ij}^k \tag{4.11}$$

As a result, the total background variance of the i^{th} time bin is

$$var(B_i) = \frac{1}{N^2}\frac{1}{N_{det}^2}\sum_{j=1}^{N}\sum_{k=1}^{N_{det}} var(B_{ij}^k) = \frac{\langle B_i/\varepsilon\rangle}{\Delta E \cdot M \cdot \Delta t} + \left\langle \frac{B_i^2 var(\varepsilon)}{\varepsilon^2} \right\rangle \tag{4.12}$$

where $M = N_{det} \cdot m = 112.5$ kg is the total detection mass, $\Delta E = N \cdot \delta E$ is the energy window and

$$\begin{aligned} \langle B_i/\varepsilon\rangle &= \frac{1}{N}\frac{1}{N_{det}}\sum_{j=1}^{N}\sum_{k=1}^{N_{det}} \frac{B_{ij}^k}{\varepsilon_j^k} \\ \left\langle \frac{B_i^2 var(\varepsilon)}{\varepsilon^2} \right\rangle &= \frac{1}{N^2}\frac{1}{N_{det}^2}\sum_{j=1}^{N}\sum_{k=1}^{N_{det}} \frac{(B_{ij}^k)^2 var(\varepsilon_j^k)}{(\varepsilon_j^k)^2} \end{aligned} \tag{4.13}$$

Table 4.1 shows the total efficiency-corrected background of the nine ANAIS–112 detectors in [1,6] and [2,6] keV energy regions estimated from the average of the ∼10% unblinded data of the first year of data taking (see Section 2.6). The relevant quantities for background variance evaluation, $\langle B/\varepsilon\rangle$ and $\langle B^2 var(\varepsilon)/\varepsilon^2\rangle$, for every module and the average values for ANAIS–112 are also shown in Table 4.1 (note that, under the constant background hypothesis, the index i can be relaxed in both quantities). The variance due to acceptance efficiency is observed to be negligible compared to statistical variance in both energy ranges. For instance, considering 10-days time bins, the variance due to Poisson statistics is $(9.74 \pm 0.09) \cdot 10^{-4}$ (c/keV/kg/d)^2 ($(7.58 \pm 0.04) \cdot 10^{-4}$ (c/keV/kg/d)^2) in [1,6] keV ([2,6] keV),

two (three) orders of magnitude greater than the variance related to acceptance efficiency.

	[1,6] keV			[2,6] keV		
Detector	B (c/keV/kg/d)	$\langle B/\varepsilon\rangle$ (c/keV/kg/d)	$\langle B^2 var(\varepsilon)/\varepsilon^2\rangle$ (c/keV/kg/d)^2	B (c/keV/kg/d)	$\langle B/\varepsilon\rangle$ (c/keV/kg/d)	$\langle B^2 var(\varepsilon)/\varepsilon^2\rangle$ (c/keV/kg/d)^2
D0	5.29±0.06	7.14±0.13	$(1.39 \pm 0.12) \cdot 10^{-4}$	4.75±0.06	4.90±0.06	$(8.91 \pm 0.40) \cdot 10^{-6}$
D1	5.30±0.07	8.36±0.26	$(0.95 \pm 0.10) \cdot 10^{-4}$	4.80±0.06	4.96±0.06	$(9.42 \pm 0.40) \cdot 10^{-6}$
D2	2.96±0.05	4.68±0.16	$(0.62 \pm 0.08) \cdot 10^{-4}$	2.53±0.04	2.62±0.04	$(3.20 \pm 0.19) \cdot 10^{-6}$
D3	4.06±0.05	5.53±0.11	$(1.41 \pm 0.12) \cdot 10^{-4}$	3.30±0.05	3.40±0.05	$(7.56 \pm 0.36) \cdot 10^{-6}$
D4	3.73±0.05	5.06±0.10	$(0.63 \pm 0.06) \cdot 10^{-4}$	3.20±0.05	3.32±0.05	$(6.02 \pm 0.26) \cdot 10^{-6}$
D5	3.66±0.05	5.00±0.10	$(0.21 \pm 0.02) \cdot 10^{-4}$	3.02±0.04	3.20±0.05	$(3.49 \pm 0.15) \cdot 10^{-6}$
D6	3.48±0.06	6.11±0.23	$(0.34 \pm 0.04) \cdot 10^{-4}$	3.00±0.04	3.12±0.05	$(3.19 \pm 0.16) \cdot 10^{-6}$
D7	2.99±0.05	4.02±0.10	$(0.29 \pm 0.03) \cdot 10^{-4}$	2.69±0.04	2.79±0.04	$(2.77 \pm 0.15) \cdot 10^{-6}$
D8	2.64±0.04	3.45±0.08	$(0.27 \pm 0.03) \cdot 10^{-4}$	2.35±0.04	2.42±0.04	$(2.20 \pm 0.12) \cdot 10^{-6}$
ANAIS-112	3.79±0.02	5.48±0.05	$(7.54 \pm 0.28) \cdot 10^{-6}$	3.29±0.02	3.41±0.02	$(5.77 \pm 0.10) \cdot 10^{-7}$

Table 4.1: *Measured ∼10% of unblinded background [1,6] and [2,6] keV energy intervals for all modules after filtering and efficiency correction have been applied. The relevant quantities for variance evaluation, $\langle B/\varepsilon\rangle$ and $\langle B^2 var(\varepsilon)/\varepsilon^2\rangle$, are also shown. Finally, the average values for ANAIS–112 are listed in the last row.*

The ANAIS–112 sensitivity to the annual modulation signal measured by DAMA/LIBRA collaboration is determined by the standard deviation of the modulation amplitude estimator, $\sigma(\hat{S}_m) = \sqrt{var(\hat{S}_m)}$. Under the constant background assumption, Equation 4.7 is used to estimate $\sigma(\hat{S}_m)$ at a given exposure from the measured background and detection efficiency. Then, we quote our sensitivity to DAMA/LIBRA result as the ratio between S_m^{DAMA} and $\sigma(\hat{S}_m)$, which directly gives in σ units the C.L. at which we can test the DAMA/LIBRA signal.

$$\mathcal{S}(\hat{S}_m, t) = \frac{S_m^{\mathrm{DAMA}}}{\sigma(\hat{S}_m)} \tag{4.14}$$

Figure 4.1 (dark blue lines) displays our sensitivity projection calculated following Equation 4.7 and considering a ten-day time binning for the two studied energy ranges, whereas the blue bands represent the 68% uncertainty in S_m^{DAMA} as reported in Section 1.4.4.1. The black dots are the sensitivities derived from reported ANAIS–112 best fits (see Section 5.2.1.1), including a systematic error estimated by changing the time binning from 1 to 20 days, and considering the systematics in the efficiency [15]. The results agree with our estimates, confirming the ANAIS–112 projected sensitivity to the DAMA/LIBRA result. A 3σ sensitivity should be at reach in 4–5 years of data taking.

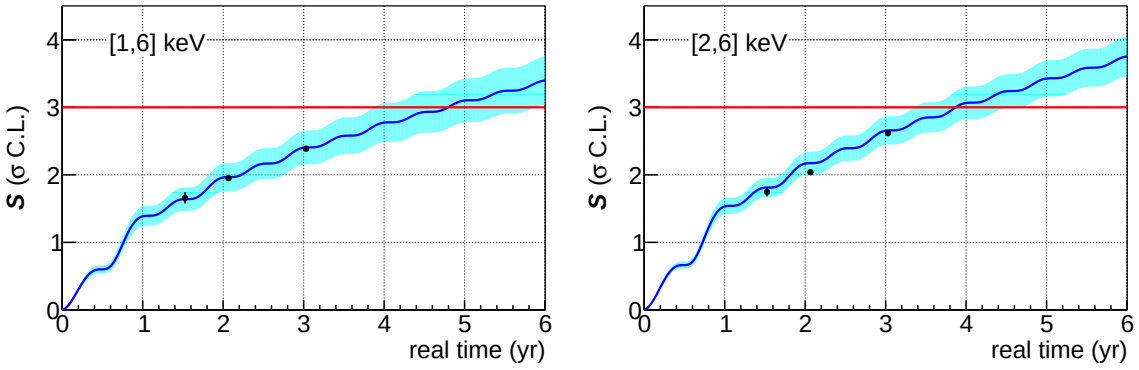

(a) (b)

Figure 4.1: *ANAIS–112 sensitivity to the DAMA/LIBRA signal in σ C.L. units as a function of real time in the [1,6] keV (a) and [2,6] keV (b) energy regions under constant background assumption. The black dots are the sensitivities derived from reported ANAIS–112 best fits (see Section 5.2.1.1). The blue bands represent the 68% C.L. DAMA/LIBRA uncertainty.*

4.1.1.1 Segmented detector

In order to evaluate the impact of detector segmentation on the sensitivity projection, each detector is considered independently. In this way, the normalized background in the i^{th} time bin of detector k is obtained by integrating the N energy bins such that:

$$B_i^k = \frac{1}{N}\sum_{j=1}^{N} B_{ij}^k \tag{4.15}$$

and the background variance of the k^{th} detector in the i^{th} time bin may be written as:

$$var(B_i^k) = \frac{1}{N^2}\sum_{j=1}^{N} var(B_{ij}^k) = \frac{\langle B_i/\varepsilon\rangle^k}{\Delta E\cdot m\cdot \Delta t} + \left\langle \frac{B_i^2 var(\varepsilon)}{\varepsilon^2}\right\rangle^k \tag{4.16}$$

where $m = 12.5$ kg is the mass of one module and

$$\begin{aligned} \langle B_i/\varepsilon\rangle^k &= \frac{1}{N}\sum_{j=1}^{N}\frac{B_{ij}^k}{\varepsilon_j^k} \\ \left\langle \frac{B_i^2 var(\varepsilon)}{\varepsilon^2}\right\rangle^k &= \frac{1}{N^2}\sum_{j=1}^{N}\frac{(B_{ij}^k)^2 var(\varepsilon_j^k)}{(\varepsilon_j^k)^2} \end{aligned} \tag{4.17}$$

For each detector k, we can estimate the variance of the modulation amplitude $\hat{S}_m^k$ combining Equations 4.7 and 4.16. Therefore, the estimator $\hat{S}_m$ with N_{det} detectors is the weighted mean of the N_{det} $\hat{S}_m^k$ and its variance is:

$$var(\hat{S}_m) = \left(\sum_{k=1}^{N_{det}} \frac{1}{var(\hat{S}_m^k)} \right)^{-1} \tag{4.18}$$

Figure 4.2 shows the sensitivity projection considering a single 112.5 kg detector (blue line) compared to the segmentation of the 112.5 kg in 9 modules (red line) for both [1,6] and [2,6] keV energy regions. It can be observed that a segmented detector improves slightly the expected sensitivity in both energy ranges, being this progress greater as the exposure increases. In order to quantify this improvement, the sensitivity projections for each year of real time are also collected in Table 4.2. It is concluded that the improvement factor is constant over time.

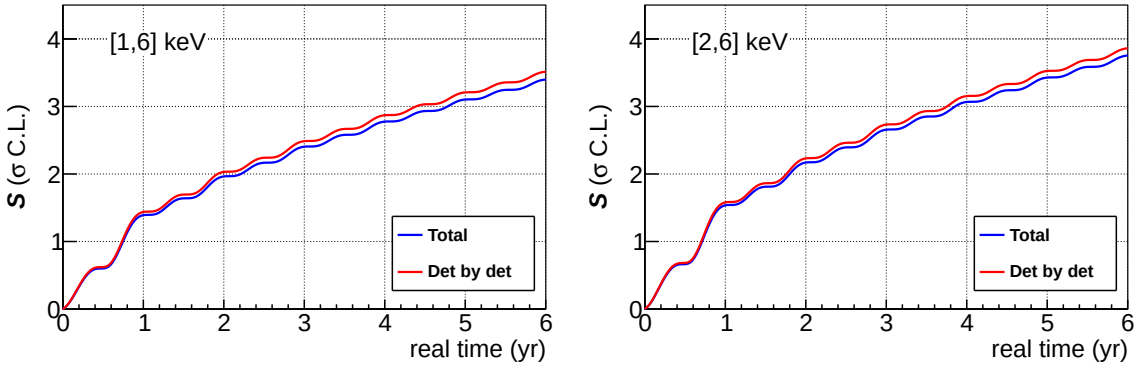

(a) (b)

Figure 4.2: *ANAIS–112 sensitivity to the DAMA/LIBRA signal in σ C.L. units as a function of real time in the [1,6] keV (a) and [2,6] keV (b) energy regions in constant background scenario. The blue lines show our sensitivity projection considering a single 112.5 kg detector, whereas the red lines display the expected sensitivity from segmented detector.*

4.1.1.2 Covariance between time bins

So far, we have considered that there is no covariance between time bins, because we have assumed that the interaction rate at different time bins follows Poisson statistics and is not correlated. However, the ANAIS–112 efficiency has been estimated using full statistics (see Section 3.2), consequently, a correlation among time bins appears. We shall now evaluate the effect of the covariance between time bins on the projected sensitivity. For this purpose, we take into account that there is no

	[1,6] keV			[2,6] keV		
Real time (years)	$\mathcal{S}$ (σ C.L.)	$\mathcal{S}$ segmented (σ C.L.)	$\mathcal{S}$ ratio (%)	$\mathcal{S}$ (σ C.L.)	$\mathcal{S}$ segmented (σ C.L.)	$\mathcal{S}$ ratio (%)
1	1.3861	1.4333	3.41	1.5314	1.5749	2.84
2	1.9613	2.0281	3.41	2.1669	2.2285	2.84
3	2.4016	2.4834	3.41	2.6535	2.7289	2.84
4	2.7736	2.8681	3.41	3.0645	3.1516	2.84
5	3.1007	3.2063	3.41	3.4258	3.5232	2.84
6	3.3970	3.5127	3.41	3.7532	3.8599	2.84

Table 4.2: *ANAIS–112 sensitivity to the DAMA/LIBRA signal in [1,6] and [2,6] keV energy regions for a single 112.5 kg detector and for a segmented detector in constant background scenario. The ratio of the latter with respect to the former is also shown.*

correlation between the efficiency measured for the same detector for different energy bins, and the efficiency of a detector is independent of that of another detector, i.e. $Cov(\varepsilon_j^k, \varepsilon_{j'}^{k'}) = Cov(\varepsilon_j^k, \varepsilon_{j'}^{k'})\delta_{jj'}\delta_{kk'}$. Therefore, the covariance of the background between two time bins i and i' is:

$$\begin{aligned} Cov(B_i, B_{i'}) &= \sum_{j,k}\sum_{j',k'} \frac{\partial B_i}{\partial \varepsilon_j^k}\frac{\partial B_{i'}}{\partial \varepsilon_{j'}^{k'}} Cov(\varepsilon_j^k, \varepsilon_{j'}^{k'}) = \sum_{j,k} \frac{\partial B_i}{\partial \varepsilon_j^k}\frac{\partial B_{i'}}{\partial \varepsilon_j^k} var(\varepsilon_j^k) \\ &= \frac{1}{N^2}\frac{1}{N_{det}^2}\sum_{j=1}^{N}\sum_{k=1}^{N_{det}} \frac{N_{ij}^k N_{i'j}^k/(\varepsilon_j^k)^2}{(\delta E\cdot m\cdot \Delta t)^2} var(\varepsilon_j^k) = \left\langle \frac{B^2 var(\varepsilon)}{\varepsilon^2} \right\rangle \end{aligned} \tag{4.19}$$

because $N_{ij}^k = N_{i'j}^k$ if constant background is assumed (see Equation 4.13). In this way, if we denote by σ_0^2 the variance due to Poisson statistics and δ is the variance due to efficiency, the covariance matrix of the background for n time bins is

$$Cov(\mathcal{B}) = \begin{pmatrix} \sigma_0^2+\delta & & \delta \\ & \ddots & \\ \delta & & \sigma_0^2+\delta \end{pmatrix} \Longrightarrow \mathcal{W} = (Cov(\mathcal{B}))^{-1} = \begin{pmatrix} w & & \widetilde{w} \\ & \ddots & \\ \widetilde{w} & & w \end{pmatrix} \tag{4.20}$$

being

$$w = \frac{\sigma_0^2+(n-1)\delta}{\sigma_0^2(\sigma_0^2+n\delta)} \qquad\qquad \widetilde{w} = -\frac{\delta}{\sigma_0^2(\sigma_0^2+n\delta)} \tag{4.21}$$

Thus, taking into account covariance between time bins, Equation 4.3 translates into:

$$\mathcal{M}^T\mathcal{W}\mathcal{M} = \begin{pmatrix} n[w+(n-1)\widetilde{w}] & [w+(n-1)\widetilde{w}]\sum_i \cos\tau_i \\ [w+(n-1)\widetilde{w}]\sum_i \cos\tau_i & (w-\widetilde{w})\sum_i \cos^2\tau_i + \widetilde{w}\left(\sum_i \cos\tau_i\right)^2 \end{pmatrix} \tag{4.22}$$

The element $(2,2)$ of the inverse matrix $(\mathcal{M}^T\mathcal{W}\mathcal{M})^{-1}$ corresponds to the variance of the modulation amplitude,

$$\begin{aligned} var(\hat{S}_m) &= \frac{n}{n(w-\widetilde{w})\sum_i \cos^2\tau_i - (w-\widetilde{w})\left(\sum_i \cos\tau_i\right)^2} \\ &= \sigma_0^2 \cdot \frac{n}{n\sum_i \cos^2\tau_i - \left(\sum_i \cos\tau_i\right)^2} \end{aligned} \tag{4.23}$$

Comparing Equation 4.23 with Equation 4.7, we conclude that the covariance between time bins due to the efficiency has no impact on the sensitivity projection.

4.1.2 Decreasing background

As commented before, ANAIS background in the ROI is expected to decrease over time because of the presence of radioactive isotopes in NaI(Tl) crystals, in particular, ^{210}Pb, ^{3}H and ^{22}Na are the most significant contributions. Short-lived cosmogenically activated isotopes are still present in the bulk of the last received crystals, contributing as background in the ROI. As a result, the time evolution of the background is not a simple exponential, but a sum of different components decaying exponentially. Both the exponential function and the sum of exponentials are non-linear functions in the parameters, so the method followed in the previous section could not be used. Nevertheless, taking advantage of the fact that the exponential function can be approximated by a straight line in a certain time interval, we will use a combination of two straight lines to model the time behaviour of the background. In particular, we will obtain the sensitivity projection using the data taken during the first year of ANAIS–112 and then we will independently estimate the sensitivity with the data corresponding to the third year of measurement. Finally, the sensitivity is estimated conservatively considering the minimum of both projections over time. Thus, the efficiency-corrected rate of events modelled by a straight line with a modulated component can be written as:

$$B(t) = R_0 + R_1 t + S_m \cos\tau \tag{4.24}$$

In this case, a three parameter linear least-squares fit of Equation 4.24 for n time bins is carried out to estimate the ANAIS–112 sensitivity to the annual modulation signal. In matrix form:

$$\vec{\mathcal{B}} = \mathcal{M}\vec{\mathcal{P}} \Longrightarrow \begin{pmatrix} B_1 \\ \vdots \\ B_n \end{pmatrix} = \begin{pmatrix} 1 & t_1 & \cos\tau_1 \\ \vdots & \vdots & \vdots \\ 1 & t_n & \cos\tau_n \end{pmatrix} \begin{pmatrix} R_0 \\ R_1 \\ S_m \end{pmatrix} \tag{4.25}$$

and the inverse of the covariance matrix of parameters:

$$\mathcal{M}^T\mathcal{W}\mathcal{M} = \begin{pmatrix} \sum_i w_i & \sum_i w_i t_i & \sum_i w_i \cos\tau_i \\ \sum_i w_i t_i & \sum_i w_i t_i^2 & \sum_i w_i t_i \cos\tau_i \\ \sum_i w_i \cos\tau_i & \sum_i w_i t_i \cos\tau_i & \sum_i w_i \cos^2\tau_i \end{pmatrix} \tag{4.26}$$

where the weights $w_i = 1/var(B_i)$ are no longer constant. In these conditions, and neglecting the contribution of the uncertainty of efficiency to the total background variance, Equation 4.12 translates into:

$$var(B_i) = \frac{\langle B/\varepsilon \rangle (t_i)}{\Delta E \cdot M \cdot \Delta t} \tag{4.27}$$

where the quantity $\langle B/\varepsilon \rangle$ is assumed to decrease linearly in the form:

$$\langle B/\varepsilon \rangle (t) = p_0 + p_1 t. \tag{4.28}$$

Figure 4.3 shows the time evolution of $\langle B/\varepsilon \rangle$ for the ANAIS–112 data corresponding to the first year in ten-day time binning in [1,6] and [2,6] keV energy regions. The fit to a straight line is also displayed in the figure, as well as the parameter and chi-square values in the fit panel. Table 4.3 collects the fit parameter values for both the first and third years of ANAIS–112 data.

Energy region	Year	p_0 (c/keV/kg/d)	p_1 (c/keV/kg/d/d)
[1,6] keV	1	5.578 ± 0.029	$(-8.1 \pm 1.4) \cdot 10^{-4}$
	3	5.54 ± 0.12	$(-6.6 \pm 1.3) \cdot 10^{-4}$
[2,6] keV	1	3.532 ± 0.010	$(-6.40 \pm 0.48) \cdot 10^{-4}$
	3	3.353 ± 0.040	$(-2.49 \pm 0.43) \cdot 10^{-4}$

Table 4.3: *Summary of fit results to Equation 4.28 in [1,6] and [2,6] keV energy regions for the first and third years of ANAIS–112 data.*

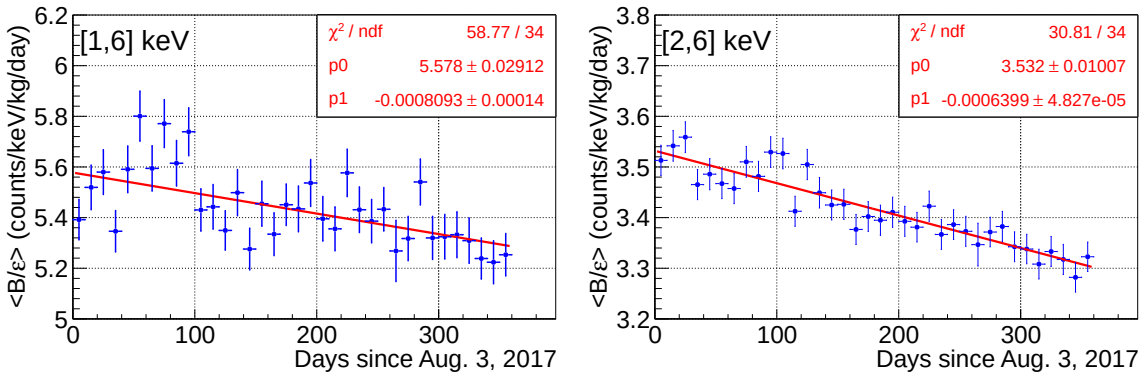

(a) (b)

Figure 4.3: *Fit of* $\langle B/\varepsilon \rangle (t)$ *quantity for ten-day time-binned first year data in the [1,6] keV (a) and [2,6] keV (b) energy regions. The chi-square value is shown in the fit panel.*

Finally, remembering that covariance matrix of parameters is $(\mathcal{M}^T \mathcal{W} \mathcal{M})^{-1}$, the variance of the modulation amplitude corresponds to the element $(3,3)$ such that:

$$var(\hat{S}_m) = \frac{\sum_i w_i \cdot \sum_i w_i t_i^2 - \left(\sum_i w_i t_i\right)^2}{det(\mathcal{M}^T \mathcal{W} \mathcal{M})} \tag{4.29}$$

where

$$\begin{aligned} det(\mathcal{M}^T \mathcal{W} \mathcal{M}) = & \sum_i w_i \cos^2 \tau_i \cdot \left[\sum_i w_i \cdot \sum_i w_i t_i^2 - \left(\sum_i w_i t_i\right)^2\right] \\ & + \sum_i w_i \cos \tau_i \cdot \left[\sum_i w_i t_i \cdot \sum_i w_i t_i \cos \tau_i - \sum_i w_i \cos \tau_i \cdot \sum_i w_i t_i^2\right] \\ & - \sum_i w_i t_i \cos \tau_i \cdot \left[\sum_i w_i \cdot \sum_i w_i t_i \cos \tau_i - \sum_i w_i t_i \cdot \sum_i w_i \cos \tau_i\right] \end{aligned} \tag{4.30}$$

Figure 4.4 shows the sensitivity projection estimated following Equation 4.29 from the data of the first year (blue line) and from the data of the third year (red line) for both [1,6] and [2,6] keV energy regions. It can be seen that both curves overlap at the beginning, whereas for time periods greater than 4–5 years, the estimate obtained using the data corresponding to the first year slightly overestimates the sensitivity in [1,6] keV and more significantly in [2,6] keV. This is because the background decreases faster in the first year than in the third one (as expected because the bakground is a combination of components decaying exponentially), and therefore, the sensitivity is overestimated when extrapolating the time behaviour of the background during the first year. As a result, it is decided to take the minimum of both curves over time as the final estimate of sensitivity. It should be noted that the sensitivity thus calculated will still be slightly overestimated from the fourth year,

but by a very small amount that can be corrected using the data collected later by ANAIS–112.

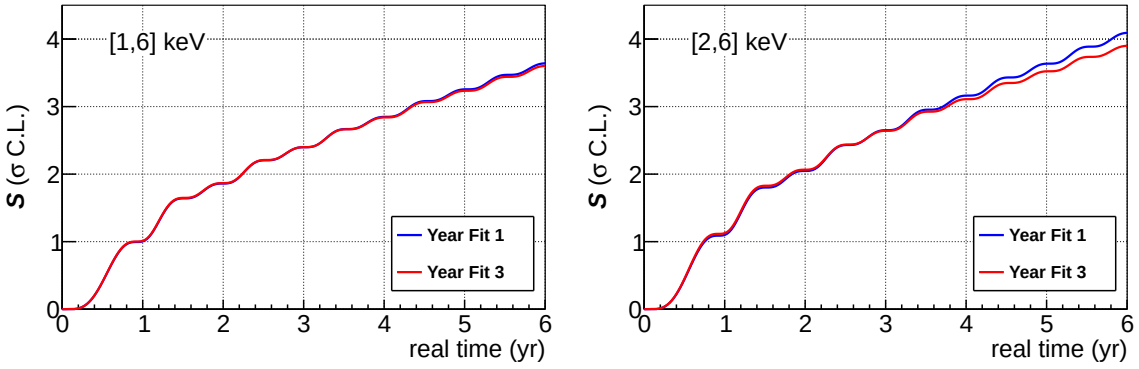

(a) (b)

Figure 4.4: *ANAIS–112 sensitivity to the DAMA/LIBRA signal in σ C.L. units as a function of real time in the [1,6] keV (a) and [2,6] keV (b) energy regions in linear decreasing background scenario. The blue lines show our sensitivity projection considering data from the first year of data taking, whereas the red lines display the expected sensitivity using data from the third year.*

Finally, Figure 4.5 (dark blue lines) displays our sensitivity projection calculated following the procedure described above and considering a ten-day time binning for the two studied energy ranges, whereas the blue bands represent the 68% uncertainty in S_m^{DAMA} as reported in Section 1.4.4.1. The black dots are the sensitivities derived from reported ANAIS–112 best fits (see Section 5.2.1.1), including a systematic error estimated by changing the time binning from 1 to 20 days, and considering the systematics in the efficiency [15]. Comparing this projection with that of constant background assumption (see Figure 4.1), we observe that linear background better reproduces results in [2,6] keV energy region. The results agree with our estimates, confirming the ANAIS–112 projected sensitivity to the DAMA/LIBRA result. A 3σ sensitivity should be at reach in 4–5 years of data taking.

4.1.2.1 Segmented detector

So as to assess the effect of detector segmentation on the sensitivity projection considering linear decreasing background, $\langle B/\varepsilon \rangle (t)$ function in Equation 4.27 is modelled for each detector independently. As an example, Figures 4.6 and 4.7 show ten-day time-binned first year data fitted to straight line for ANAIS–112 nine detectors in the [1,6] and [2,6] keV energy regions, respectively; the same has been calculated for the data corresponding to the third year.

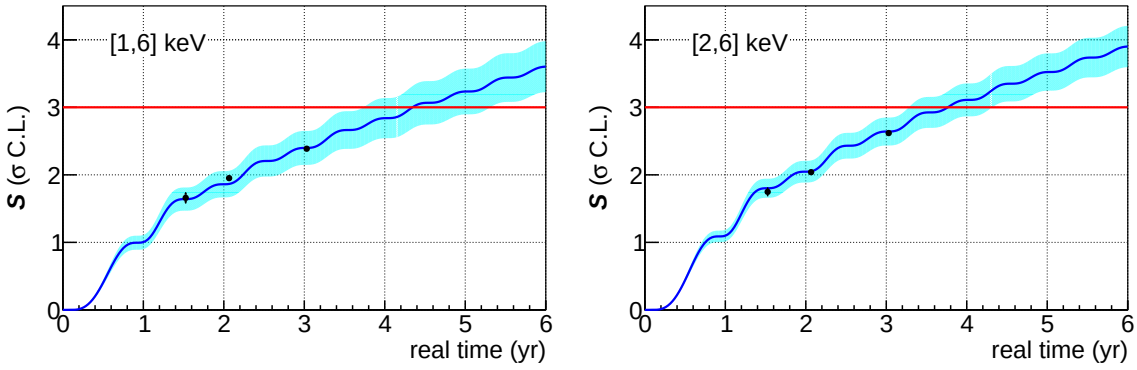

(a) (b)

Figure 4.5: *ANAIS–112 sensitivity to the DAMA/LIBRA signal in σ C.L. units as a function of real time in the [1,6] keV (a) and [2,6] keV (b) energy regions considering linear decreasing background. The black dots are the sensitivities derived from ANAIS–112 best fits (see Section 5.2.1.1). The blue bands represent the 68% C.L. DAMA/LIBRA uncertainty.*

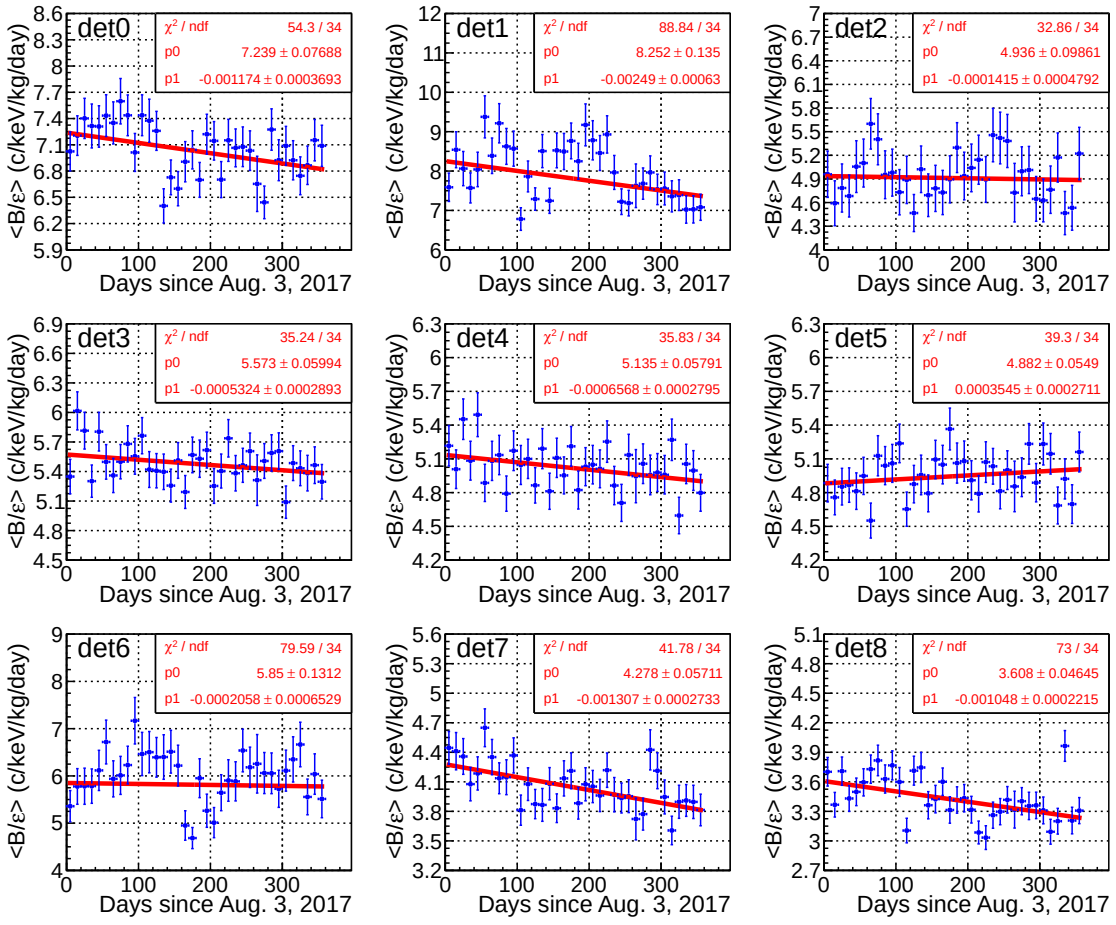

Figure 4.6: *Fit of $\langle B/\varepsilon \rangle (t)$ function for ten-day time-binned first year data in the [1,6] keV energy region. The chi-square values are shown in the fit panel.*

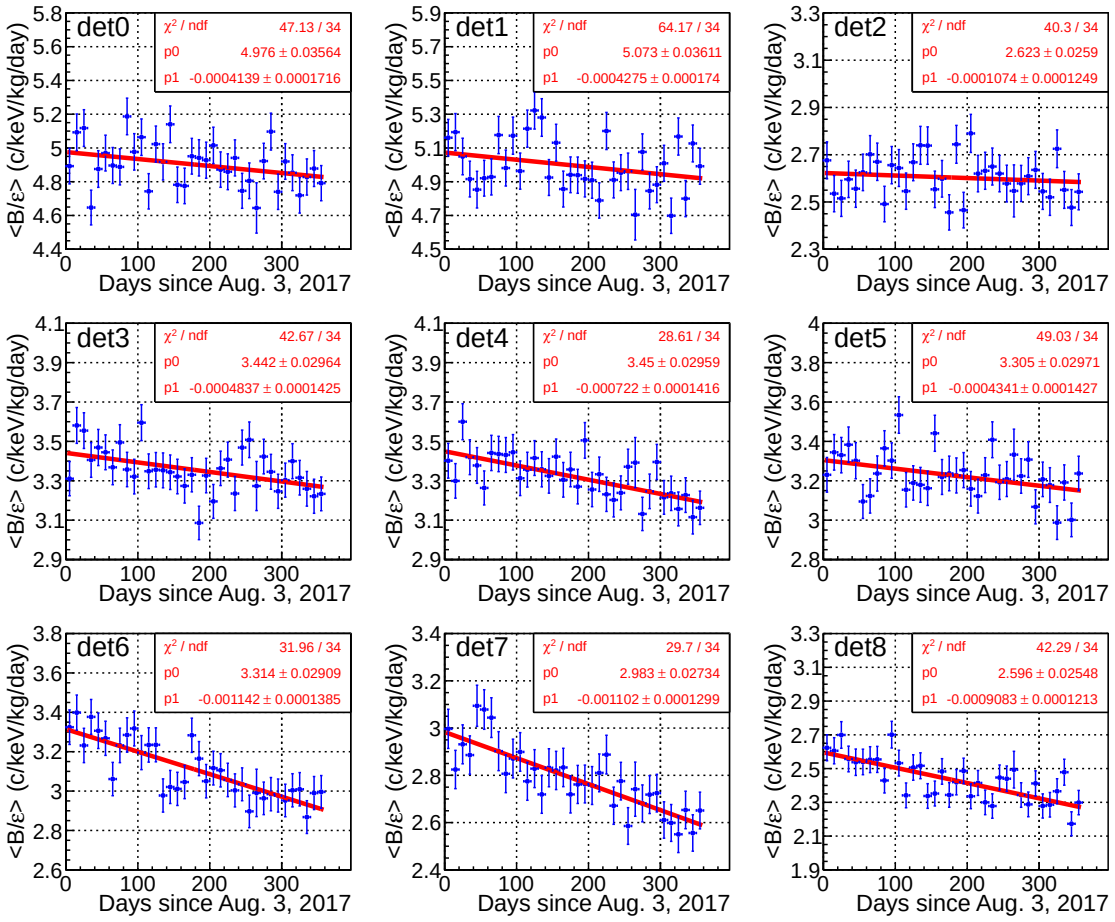

Figure 4.7: *Fit of* $\langle B/\varepsilon \rangle (t)$ *function for ten-day time-binned first year data in the [2,6] keV energy region. The chi-square values are shown in the fit panel.*

Thus, the variance of the modulation amplitude for one detector, $\hat{S}_m^k$, in decreasing background scenario, can be estimated combining Equations 4.27 and 4.29 for the data measured during the first and third years of ANAIS–112. In this way, the variance estimator of the modulation amplitude with N_{det} detectors follows Equation 4.18. Again, the final sensitivity is calculated as the lowest sensitivity of those obtained with the data from the first and third years. Figure 4.8 shows the sensitivity projection considering a single 112.5 kg detector (blue line) compared to the segmentation of the 112.5 kg in 9 modules (red line) for both [1,6] and [2,6] keV energy regions. As in the constant background scenario, we observe that a segmented detector improves slightly the expected sensitivity in both energy ranges, being this progress greater as the exposure increases. In order to quantify this improvement, the sensitivity projections for each year of real time are also collected in Table 4.4. It is concluded that the improvement factor increases slightly over time.

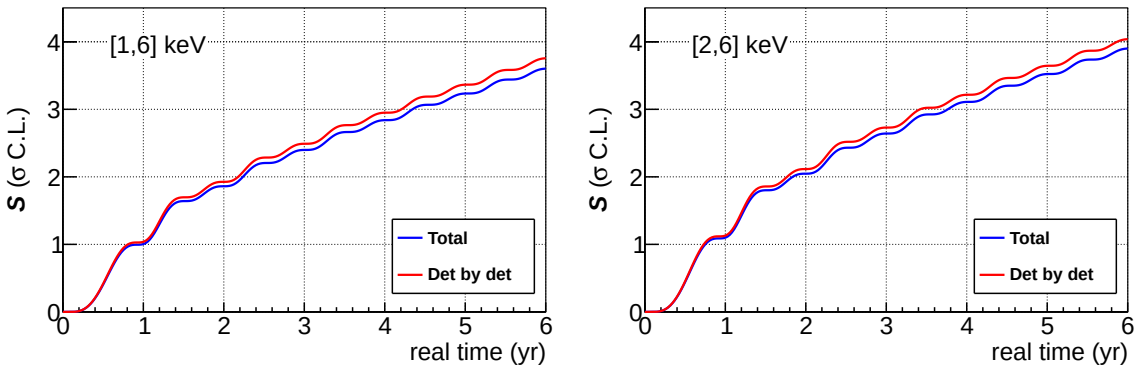

(a) (b)

Figure 4.8: *ANAIS–112 sensitivity to the DAMA/LIBRA signal in σ C.L. units as a function of real time in the [1,6] keV (a) and [2,6] keV (b) energy regions in linear decreasing background scenario. The blue lines show our sensitivity projection considering a single 112.5 kg detector, whereas the red lines display the expected sensitivity from segmented detector.*

	[1,6] keV			[2,6] keV		
Real time (years)	$\mathcal{S}$ (σ C.L.)	$\mathcal{S}$ segmented (σ C.L.)	$\mathcal{S}$ ratio (%)	$\mathcal{S}$ (σ C.L.)	$\mathcal{S}$ segmented (σ C.L.)	$\mathcal{S}$ ratio (%)
1	1.0044	1.0380	3.35	1.0991	1.1301	2.82
2	1.8606	1.9259	3.51	2.0467	2.1153	3.35
3	2.3986	2.4901	3.81	2.6414	2.7300	3.35
4	2.8393	2.9498	3.89	3.1096	3.2153	3.40
5	3.2342	3.3651	4.05	3.5225	3.6447	3.47
6	3.6021	3.7559	4.27	3.9000	4.0387	3.56

Table 4.4: *ANAIS–112 sensitivity to the DAMA/LIBRA signal in [1,6] and [2,6] keV energy regions for a single 112.5 kg detector and for a segmented detector in decreasing background scenario. The ratio of the latter with respect to the former is also shown.*

4.1.3 Consistency check using Monte Carlo simulation

As previously mentioned, the method used in Sections 4.1.1 and 4.1.2 to calculate the sensitivity projection is only valid when the function modelling the time evolution of the rate of events is linear in the parameters. The sensitivity estimated in this way is in agreement with the results obtained from the analysis of the annual modulation in

the ANAIS–112 data to date. However, extrapolations to longer periods of time lead to an underestimation of the sensitivity when considering the constant background hypothesis, or to an overestimation when a decreasing background combining two straight lines is assumed. This discrepancy can be solved by fitting the rate of events to an exponential function, which has demonstrated to successfully reproduce the time evolution of the ANAIS–112 background (see Section 5.2.1.1). As the exponential function is non-linear, the analytical method can no longer be used, and instead a Monte Carlo simulation can be exploited.

The time evolution of the rate of events modelled by an exponential decay with a modulated component can be written as:

$$B(\tau) = R_0 \cdot \left(1 + f e^{-t/\tau_d}\right) + S_m \cos\tau, \tag{4.31}$$

where R_0, f, τ_d and S_m are free parameters. The best fit results of the three years of ANAIS–112 data to Equation 4.31 for both [1,6] and [2,6] keV energy regions are gathered in Table 4.5 (more details on fitting the ANAIS–112 background to this equation are given in Section 5.2.1.1). For each energy region, these values define the function to be exploited using the Monte Carlo technique. In particular, for each ten-day time bin i, a Gaussian distribution of mean μ_i and standard deviation σ_i is sampled. The mean value μ_i in the i^{th} time bin is computed by evaluating the non-modulated exponential function at the center of the time bin t_i, whereas the standard deviation σ_i is obtained by multiplying the mean value μ_i by the expected relative error for the rate of events at t_i. The relative error in the rate of events for ANAIS–112 in [1,6] and [2,6] keV energy regions is shown in Figure 4.9, and is clearly time-dependent. This time behaviour is successfully reproduced by fitting to a straight line (in red). The best fit values are also displayed in the figure. In this way, the standard deviation of the modulation amplitude in the i^{th} time bin is estimated by fitting the simulated rates of events up to said time bin to Equation 4.31.

Energy region	R_0 (c/keV/kg/d)	f	τ_d (days)
[1,6] keV	3.147±0.069	0.239±0.025	1009±150
[2,6] keV	2.823±0.041	0.208±0.016	816±110

Table 4.5: *Best fit results of the three years of ANAIS–112 data to Equation 4.31 for both [1,6] and [2,6] keV energy regions.*

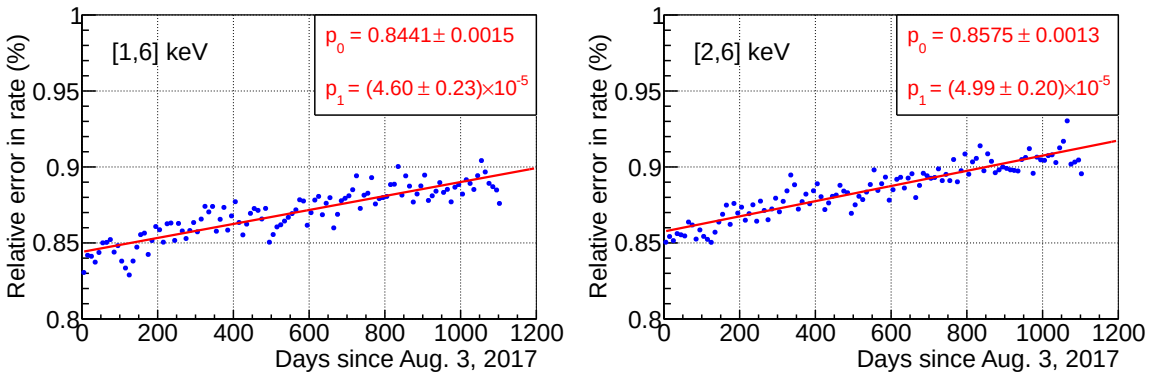

(a) (b)

Figure 4.9: *Relative error in the rate of events of ANAIS–112 for a ten-day time binning as a function of time in the [1,6] keV (a) and [2,6] keV (b) energy regions. The fit to a straight line is shown in red and the best fit values are also displayed.*

Finally, Figure 4.10 (dark blue lines) displays our sensitivity projection calculated following Equation 4.31 and considering a ten-day time binning for the two studied energy ranges, whereas the blue bands represent the 68% uncertainty in S_m^{DAMA} as reported in Section 1.4.4.1. The black dots are the sensitivities derived from reported ANAIS–112 best fits (see Section 5.2.1.1), including a systematic error estimated by changing the time binning from 1 to 20 days, and considering the systematics in the efficiency [15]. The results perfectly agree with our estimates, confirming in the short term the ANAIS–112 projected sensitivity to the DAMA/LIBRA result. In the longer term, the sensitivity obtained with this method is between those obtained when considering the constant background and decreasing background combining two straight lines scenarios, as expected. Table 4.6 summarizes the sensitivity projections using the three methods. In any case, a 3σ sensitivity should be at reach in 4–5 years of data taking for both energy regions.

	[1,6] keV			[2,6] keV		
Real time	$\mathcal{S}$ (σ C.L.) using			$\mathcal{S}$ (σ C.L.) using		
(years)	Eq. 4.1	Eq. 4.24	Eq. 4.31	Eq. 4.1	Eq. 4.24	Eq. 4.31
4	2.77	2.84	2.84	3.06	3.11	3.11
5	3.10	3.23	3.21	3.43	3.52	3.50
6	3.40	3.60	3.54	3.75	3.90	3.84

Table 4.6: *ANAIS–112 sensitivity projection to the DAMA/LIBRA signal in [1,6] and [2,6] keV energy regions considering the three background scenarios: constant (Equation 4.1), decreasing combining two straight lines (Equation 4.24) and exponentially decreasing (Equation 4.31).*

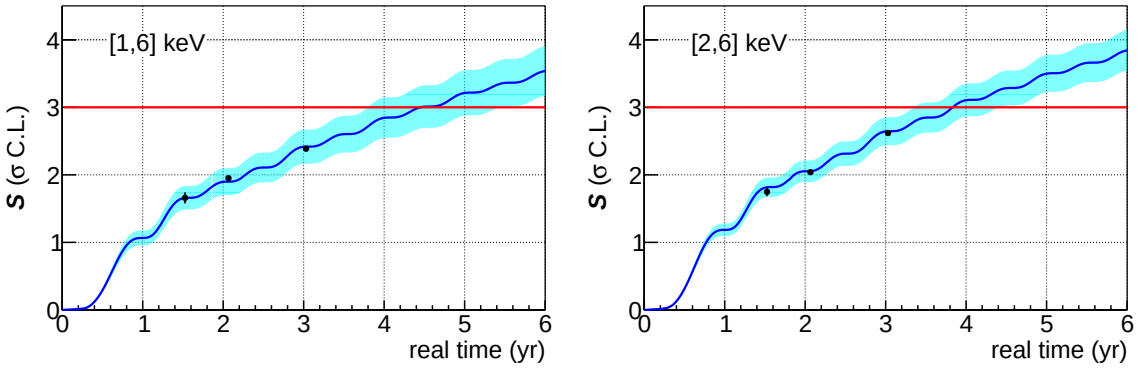

(a) (b)

Figure 4.10: *ANAIS–112 sensitivity to the DAMA/LIBRA signal in σ C.L. units as a function of real time in the [1,6] keV (a) and [2,6] keV (b) energy regions considering exponentially decreasing background. The black dots are the sensitivities derived from ANAIS–112 best fits (see Section 5.2.1.1). The blue bands represent the 68% C.L. DAMA/LIBRA uncertainty.*

4.1.4 Calibration effect on sensitivity

Low energy calibration is performed by unweighted linear fit to four calibration points: two internal lines due to ^{22}Na (0.87 keV) and ^{40}K (3.20 keV) and two external lines coming from ^{109}Cd source (11.9 and 22.6 keV) as described in Section 2.7.2. The uncertainty in the position of the ^{22}Na and ^{40}K peaks is much higher than that of the ^{109}Cd peaks due to the low number of ^{22}Na/^{40}K events. This uncertainty in determining the center of the peaks implies an uncertainty in the energy assigned to each event, and its subsequent binning in the spectrum. The net effect is that there is a non-Poisson term in the variance and a covariance between the bin contents. In order to estimate the impact of the calibration procedure on the sensitivity projection, a Monte Carlo simulation has been carried out. Specifically, for each ten-day time bin and detector, the position of the ^{22}Na/^{40}K (^{109}Cd) calibration points has been sampled from a Gaussian distribution with mean value the corresponding to the median (mean) position of the peaks, and standard deviation equal to the respective uncertainty of the peaks. Then, an unweighted linear fit on the expected energies against the simulated positions of the peaks is performed using a linear function. This process is repeated 4×10^3 times, and the variance of the rate of events in each time bin due to the calibration method is estimated by calculating the variance of the total integral rate in the [1,6] and [2,6] keV energy regions from the ANAIS–112 background data corresponding to the full first year. As an example, Figure 4.11 shows the distribution of the total integral rate with respect to the mean value in the first ten-day time bin for both [1,6] and [2,6] keV energy regions.

Table 4.7 summarizes the contributions from both the statistics and the calibration to the uncertainty of the total rate of events in [1,6] and [2,6] keV energy ranges. The calibration uncertainty has been found to be slightly greater than half the statistical uncertainty between 1 and 6 keV because of the ^{22}Na component near the energy threshold, whereas it accounts for only about 6% of the total variance of the rate for the energy range from 2 to 6 keV. In addition, the covariance between time bins results to be negligible.

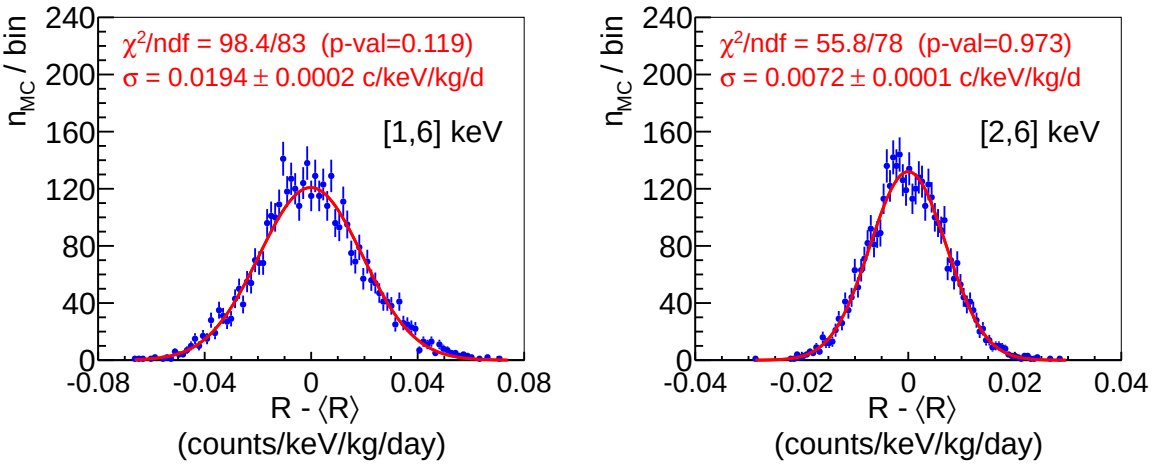

(a) (b)

Figure 4.11: *Distribution of the total integral rate with respect to the mean value in the first ten-day time bin of the first year of ANAIS–112 for both [1,6] keV (a) and [2,6] keV (b) energy regions. The best fit of the standard deviation is also shown.*

Energy region	Stat. unc. (c/keV/kg/d)	Cal. unc. (c/keV/kg/d)	Fraction of total variance (%)
[1,6] keV	0.0324±0.0004	0.0189±0.0006	25.5
[2,6] keV	0.0289±0.0003	0.0075±0.0002	6.5

Table 4.7: *Total event rate uncertainty separated into its contribution due to statistics and calibration for [1,6] and [2,6] keV energy regions. The fraction of the total variance corresponding to the uncertainty in the calibration is also reported.*

Figure 4.12 shows the sensitivity projection in the exponentially decreasing background scenario taking into account (red line) and not (blue line) the uncertainty due to the low energy calibration procedure used in ANAIS–112 for both [1,6] and [2,6] keV energy regions. It can be observed that when this new source of uncertainty is added, the expected sensitivity is slightly lower in [2,6] keV and quite lower in

[1,6] keV energy window. Specific values of the sensitivity projections in these conditions for each year of real time can be found in Table 4.8. It can be concluded that by adding the uncertainty due to the calibration method, the expected sensitivity decreases by approximately 10% in [1,6] keV and only 3% in [2,6] keV energy region. It is worth remembering that when considering the segmentation of ANAIS–112 in nine detectors, the sensitivity increased in the order of 3%, so that the reduction of the sensitivity by adding the uncertainty in the calibration would be in any case less than the previous values.

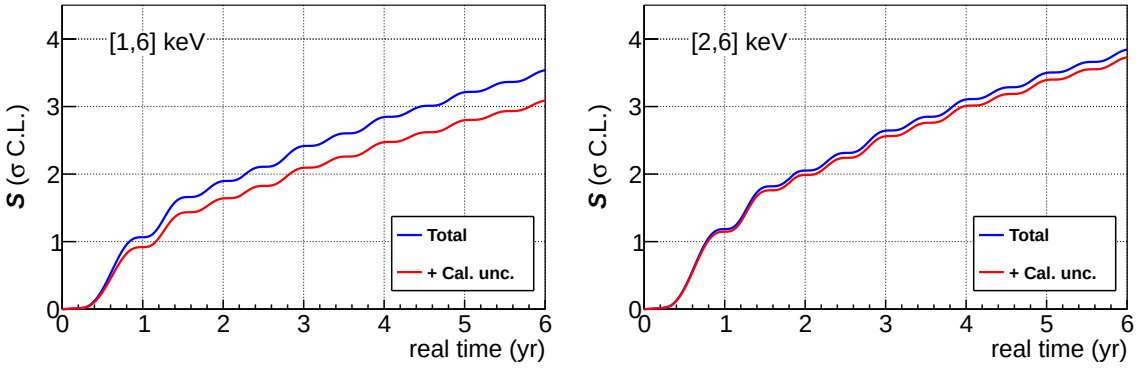

(a) (b)

Figure 4.12: *ANAIS–112 sensitivity to the DAMA/LIBRA signal in σ C.L. units as a function of real time in the [1,6] keV (a) and [2,6] keV (b) energy regions. The blue lines show our sensitivity projection considering variance due to Poisson statistics and efficiency correction, whereas the red lines display the expected sensitivity considering also the variance due to the calibration method.*

	[1,6] keV			[2,6] keV		
Real time (years)	$\mathcal{S}$ (σ C.L.)	$\mathcal{S}$ cal. (σ C.L.)	$\mathcal{S}$ ratio (%)	$\mathcal{S}$ (σ C.L.)	$\mathcal{S}$ cal. (σ C.L.)	$\mathcal{S}$ ratio (%)
1	1.0651	0.9183	-13.8	1.1850	1.1462	-3.27
2	1.8964	1.6404	-13.5	2.0529	1.9873	-3.20
3	2.4148	2.0936	-13.3	2.6427	2.5599	-3.13
4	2.8448	2.4720	-13.1	3.1058	3.0104	-3.08
5	3.2124	2.7978	-12.9	3.4985	3.3929	-3.02
6	3.5379	3.0879	-12.7	3.8435	3.7296	-2.96

Table 4.8: *ANAIS–112 sensitivity to the DAMA/LIBRA signal in [1,6] and [2,6] keV energy regions taking into consideration and not the uncertainty due to the calibration method in the exponentially decreasing background scenario. The ratio of the latter with respect to the former is also shown.*

4.1.5 Combined sensitivity with COSINE–100

As has been commented throughout the chapter, the estimates of the ANAIS–112 sensitivity to the DAMA/LIBRA signal have been confirmed after the analysis searching for the annual modulation carried out with 1.5, 2 and 3 years of data. As a result, ANAIS–112 will be able to detect the annual modulation singled out by DAMA/LIBRA at 3σ level after the scheduled 5 year of data taking in both [1,6] and [2,6] keV energy regions. This goal could be achieved earlier if the ANAIS–112 data are combined with those of other experiments searching for the annual modulation reported by DAMA/LIBRA using NaI(Tl) as a target. In particular, the COSINE–100 experiment has also published results on annual modulation in the [2,6] keV energy region after accumulating an exposure of 97.7 kg×yr (see Section 1.4.4.2). Both experiments have similar background levels and duty cycles, but the total active mass of COSINE–100 is 61.4 kg, almost half the mass of ANAIS–112. Consequently, the sensitivity to annual modulation achieved by COSINE–100 is lower despite starting data collection about ten months earlier than ANAIS–112.

From the published information on backgrounds, effective mass and duty cycle [177], we can estimate the COSINE–100 sensitivity to the annual modulation signal in the constant background scenario using Equations 4.7 and 4.12. The results are shown in green in Figure 4.13 together with those obtained by ANAIS–112 (in blue), where the beginning of the ANAIS–112 data collection has been considered as the origin of time. The combined sensitivity is calculated from the standard deviation of the modulation amplitude estimators from both experiments using the weighted standard deviation formula, and is displayed in red in the figure. As can be observed, the sensitivity at 3σ level would be reached around 2.5 years from the beginning of ANAIS–112, that is, at the beginning of 2020, and after 4.5 years the 4σ sensitivity would be achieved. Nevertheless, COSINE–100 collaboration has not updated the results on annual modulation since July 2019.

4.2 Model dependent modulation

As mentioned in Section 1.4.4, the annual modulation signal reported by DAMA/LIBRA is compatible with that expected for galactic halo dark matter particles. Owing to the Earth's rotation around the Sun, the expected differential rate of WIMP's scatterings off the target's nucleus changes periodically in time following approximately the Equation 1.28 in the SHM. The theoretical inputs introduced in the evaluation of the WIMP-nucleus elastic scattering and all the parameters entering in the halo velocity distribution makes S_0 and S_m functions rather model dependent.

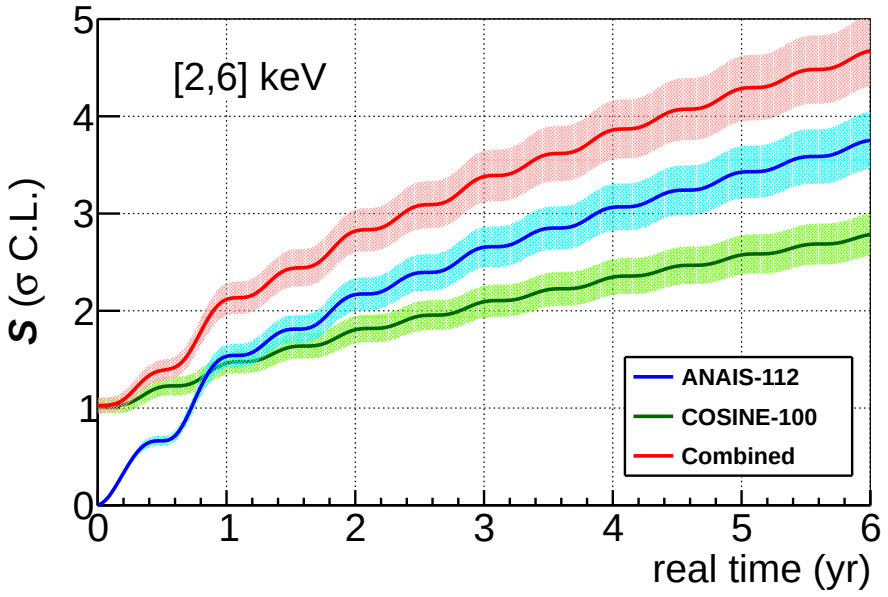

Figure 4.13: *ANAIS–112 (blue), COSINE–100 (green) and combined (red) sensitivity to the DAMA/LIBRA signal in σ C.L. units as a function of real time in the [2,6] keV energy region under the constant background assumption. The beginning of the ANAIS–112 data taking has been taken as the origin of time. The coloured bands represent the 68% C.L. DAMA/LIBRA uncertainty.*

Given a set of experimental count rates N_{ij} representing the number of events collected on the i^{th} time bin and j^{th} energy bin, the mean value of N_{ij} is

$$\langle N_{ij} \rangle = [b_j + S_{0,j} + S_{m,j} \cos \tau_i] \, M \Delta t_i \delta E_j \varepsilon_j, \tag{4.32}$$

where the b_j and $S_{0,j} + S_{m,j} \cos \tau_i$ represent the average background and the dark matter expected signal in the j^{th} energy bin, respectively, in number of counts per unit of detector mass, time and interval of collected energy. The $S_{0,j}$ and $S_{m,j}$ parameters are expressed in terms of the WIMP mass m_W and of the point-like WIMP-nucleus cross section σ.

The procedure to extract a modulated signal within a given period and phase from a set of measured count rates has been discussed by several authors [118, 236–238]. The maximum-likelihood estimation method is the most commonly used procedure to compare theory with the measured data. In particular, we use as test statistics the likelihood ratio [239]

$$\frac{\mathcal{L}(S_{m,j}|\sigma, m_W)}{\mathcal{L}(S_{m,j}|\hat{\sigma}, \hat{m}_W)} \tag{4.33}$$

where $\mathcal{L}$ is the likelihood function, and $\hat{\sigma}$ and $\hat{m}_W$ are the values of the parameters that maximize the likelihood for the observed $S_{m,j}$. The denominator of the above equation is the maximum likelihood value, so the value of the likelihood ratio is between 0 and 1. As shown in Ref. [239, 240], the likelihood ratio test is asympotically equivalent to test the difference between the χ^2_{min} of the null ($\sigma = 0$) and alternative ($\sigma \neq 0$) hypotheses. The minimum of:

$$\chi^2(\sigma, m_W) = \sum_{j=1}^{N} \frac{\left(\hat{S}_{m,j} - S_{m,j}(\sigma, m_W)\right)^2}{var(\hat{S}_{m,j})} \tag{4.34}$$

has to be evaluated for $\sigma = 0$ and $\sigma \neq 0$. If $\sigma = 0$, the quantity

$$\Delta\chi^2 = \chi^2(\sigma = 0, m_W)_{min} - \chi^2(\sigma, m_W)_{min} \tag{4.35}$$

is distributed as a χ^2_ν variable with $\nu = 2$ degrees of freedom. On the other hand, if $\sigma \neq 0$, $\Delta\chi^2$ is a non-central $\chi'^2_{(\nu,\lambda)}$ with $\nu = 1$ degree of freedom, expected value

$$\left\langle \Delta\chi^2 \right\rangle = \frac{1}{2} \sum_{j=1}^{N} \frac{S^2_{m,j} \cdot \delta E_j \cdot \varepsilon_j}{B_j} \cdot M \cdot L_T \cdot \alpha + 2, \tag{4.36}$$

and non-central parameter $\lambda = \langle \Delta\chi^2 \rangle - 1$. L_T corresponds to total live time and $\alpha = \frac{2}{L_T} \sum_i \cos^2 \tau_i$, such that $\alpha = 1$ when full period of data taking is considered.

The segmented detector can also be incorporated to the test, obtaining

$$\left\langle \Delta\chi^2 \right\rangle = \frac{1}{2} \sum_{j=1}^{N} \sum_{k=1}^{N_{det}} \frac{(S^k_{m,j})^2 \cdot \delta E_j \cdot \varepsilon^k_j}{B^k_j} \cdot m_k \cdot L_T \cdot \alpha + 2. \tag{4.37}$$

The statistical interpretation of the so-called sensitivity plot (m_W, σ) is obtained from the degree of overlapping between the $\Delta\chi^2$ distributions in the two cases: absence and presence of modulation. For the sake of illustration, Figure 4.14 displays a chi-square distribution with two degrees of freedom (in red) together with a non-central chi-square distribution with one degree of freedom and non-central parameter $\lambda = 11.8$ (in blue), i.e $\langle \Delta\chi^2 \rangle = 12.8$.

Equations 4.36 and 4.37 allow us to estimate the needed exposure $ML_T\alpha$ so as to observe a modulation effect with a given probability. For instance, $\langle \Delta\chi^2 \rangle = 12.8$ corresponds to a 90% probability to see an effect at least at the 90% C.L. In the same

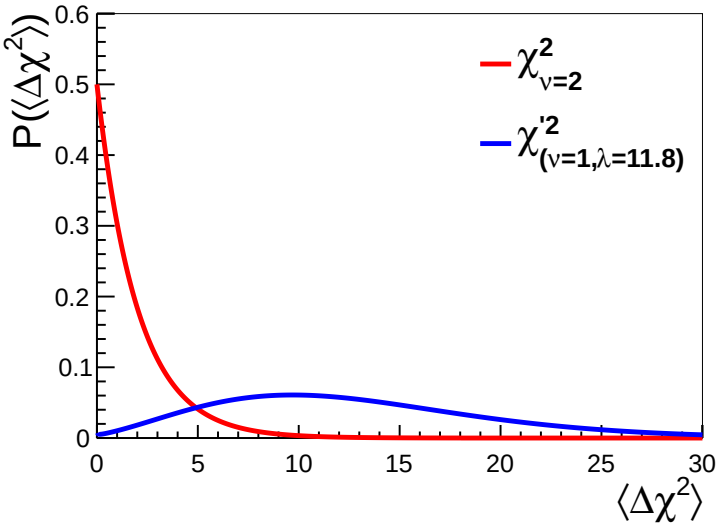

Figure 4.14: *Chi-square distribution with two degrees of freedom (red) and non-central chi-square distribution with one degree of freedom and non-central parameter* $\lambda = 11.8$ *(blue).*

way, a less demanding value of $\langle \Delta\chi^2 \rangle = 5.6$ would give a 50% probability to see an effect at the 90% C.L. or more. Once a required $\langle \Delta\chi^2 \rangle$ is chosen, a sensitivity plot may be obtained by showing the curves of constant $ML_T\alpha$ on the plane $m_W - \sigma$. Other situations are summarized in Table 4.9, where $\langle \Delta\chi^2 \rangle$ is tabulated as a function of the fraction of experiments where absence of modulation can be excluded (rows), and the required C.L. (columns). This procedure allows to see in a compact way the masses and exposures needed to explore each different region of the WIMP $m_W - \sigma$ parameter space.

The projected sensitivity of ANAIS–112 to dark matter annual modulation assuming SI interactions has been evaluated following the aforementioned procedure.

In the calculation of the sensitivity plots, we take the differential rate defined by Equation 1.25 for each of species of the target material (Na, I), the local dark matter density $\rho = 0.3$ GeV/cm^3 (standard halo model assumption), the most probable WIMP velocity $v_0 = 220$ km/s and the escape velocity $v_{esc} = 650$ km/s. We consider the spin-independent WIMP interaction, using the Helm nuclear form factor (see Equation 1.20) and $Q_{Na} = 0.30$ and $Q_I = 0.09$ for the sodium and iodine quenching factors, respectively. The resolution of ANAIS–112 is given by $\sigma = -0.060 + 0.3525\sqrt{E}$ for 1keV $< E <$ 6keV (see Figure 2.25) and the Earth velocity is defined in Equation 1.27.

	90%	**95%**	**99%**	**99.5%**	**99.9%**
50%	5.6	7.0	10.2	11.6	14.8
60%	6.8	8.3	11.8	13.3	16.8
70%	8.1	9.9	13.7	15.3	19.0
80%	9.9	11.8	16.0	17.8	21.8
90%	12.8	14.9	19.6	21.6	26.0
95%	15.4	17.8	22.9	25.0	29.8
99%	21.0	23.8	29.7	32.2	37.5

Table 4.9: *Parameter $\langle \Delta\chi^2 \rangle$ as a function of the required confidence level to exclude the absence of modulation (columns) and the fraction of successful experiments (rows). From Ref. [240].*

Figure 4.15 shows the sensitivity plots for [1,6] keV (a) and [2,6] keV (b) energy regions considering the efficiency-corrected background tabulated in Table 4.1. Both of them have been obtained requiring 90% C.L. and 90% of succesful experiments and assuming 5 years of data taking. Segmented detector has also been considered. Orange areas represent DAMA/LIBRA modulation regions at 90%, 3σ and 5σ levels [119]. It is worth noting that the DAMA regions displayed in the plot correspond to the fit of the data measured by DAMA/NaI and DAMA/LIBRA-phase1 between 2 and 6 keV, and are taken only as reference. As commented in Section 1.4.4.1, there is a discrepancy in the interpretation of the DAMA signal in the spin-independent interaction scenario when combining these data with those obtained by DAMA/LIBRA-phase2 in [2,6] keV energy region, or when considering those reported by DAMA/LIBRA-phase2 between 1 and 6 keV. In any case, the regions singled out by DAMA/LIBRA are within our reach. Consequently, we conclude that after 5 years of measurement, ANAIS–112 can detect the annual modulation in the 3σ region compatible with the DAMA/LIBRA result.

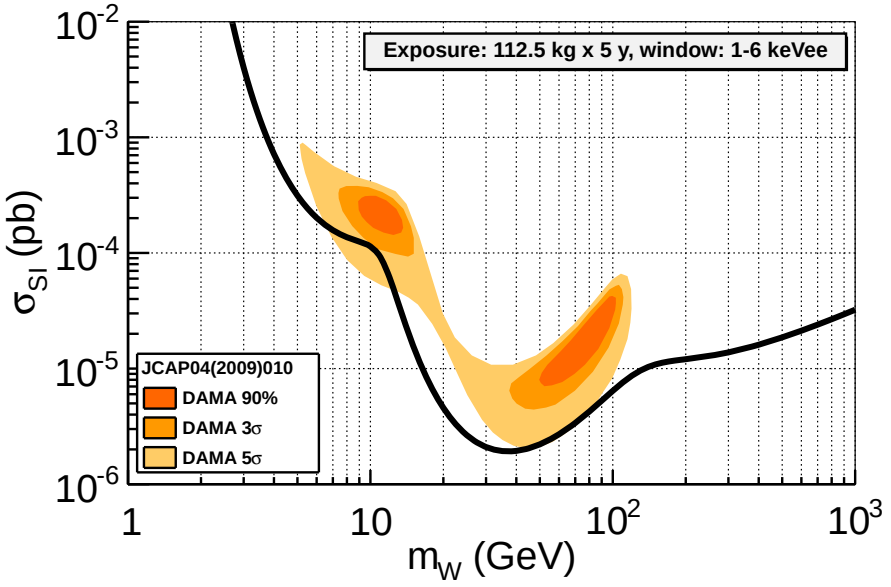

(a)

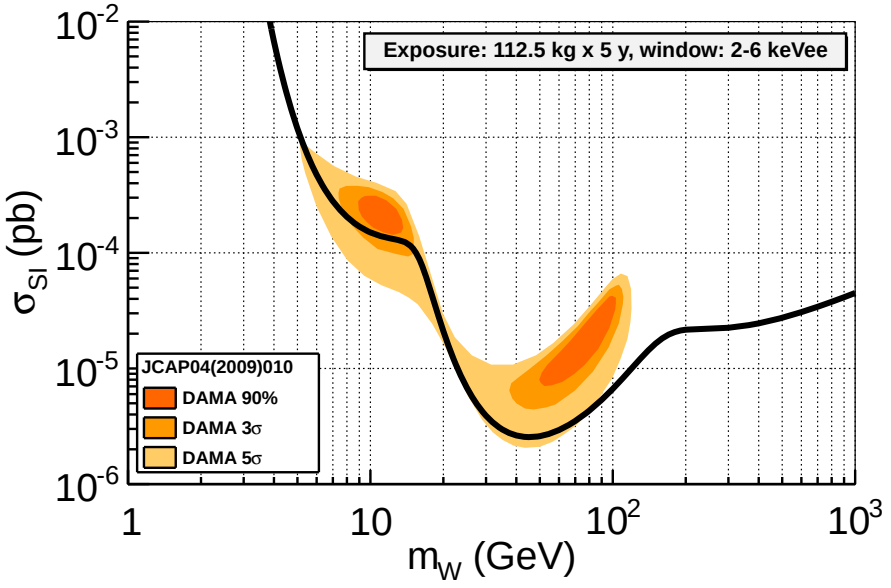

(b)

Figure 4.15: *Sensitivity plot in the $\sigma_{SI} - m_W$ plane for ANAIS–112 experiment for [1,6] keV (a) and [2,6] keV (b) energy regions and 5 years of data taking corresponding to a detection limit at 90% C.L. with a critical limit at 90% C.L. Segmented detector has also been considered. In addition, DAMA/LIBRA regions at 90%, 3σ and 5σ [119] are shown as orange areas.*

Chapter 5

Annual modulation search with 3 years of data

ANAIS–112 started taking data in the dark matter mode on the 3^{rd} of August 2017, and is currently running. The excellent duty cycle of ANAIS–112 has allowed to accumulate more than 95% of live time for all the nine modules (see Section 2.1.4), guaranteeing a perfect coverage of the whole year-periods for the annual modulation analysis. Following the designed blind strategy for the analysis of ANAIS–112 data (see Section 2.6), energy and time distribution from single-hit events in the region of interest (from 1 to 6 keV) were kept blinded since the beginning of the data taking. After the first year of data taking, $\sim$10% of these events (randomly selected from the whole year) were unblinded for fine tuning the events selection procedures, general background assessment and sensitivity estimates [15, 16, 196]. The designed analysis protocol has been applied for model independent annual modulation study after 1.5, 2 and 3 years of data taking, unblinding the corresponding ROI events. These results, corresponding to exposures of 157.55, 220.69 and 322.82 kg$\times$yr [203, 241, 242], respectively, are compatible with the absence of modulation and confirm our sensitivity projections, whereas producing some tension with DAMA/LIBRA annual modulation result.

This chapter reviews the analysis of the annual modulation corresponding to the three years of ANAIS–112 data through an independent analysis derived from the different form of data aggregation with respect to the standard analysis. In addition, different fitting procedures of background evolution are considered in order to evaluate the possible presence of systematic effects in the analysis protocols. Specific control populations for which no modulation is expected are used to monitor the stabilitiy of the event selection efficiencies and to verify the agreement between the background model and data (see Section 5.1). Afterwards, the results of the model

independent annual modulation analysis in the same energy regions as DAMA/LIBRA published results (from 1 to 6 keV and from 2 to 6 keV) are presented in Section 5.2. This section also includes the energy dependence of modulation amplitude, a phase-free annual modulation analysis and the segmentation in detectors for annual modulation search.

5.1 Control populations

Independent control populations for which no modulation is expected are studied in order to monitor the stability of the event selection efficiencies, check the agreement between the background model and data, and test any possible systematic due to the specific fitting procedures. Firstly, Figure 5.1 shows the low energy coincident events in any modules (events with multiplicity equal to or greater than 2) attributed to the K-shell electron binding energy following electron capture in cosmogenic ^{22}Na (0.87 keV) and internal ^{40}K (3.2 keV) in one of the modules, and the corresponding high energy gamma ray (1274.5 and 1460.8 keV, respectively) interaction and finally full absorption in other modules. The radioactive disintegration of ^{22}Na ($T_{1/2}$ =2.6 yr) has been fitted to an exponential decay shown in red in Figure 5.1a. The fit provides a mean life of 1481±65 days (with p-value=0.26), corresponding to a half-life period of 2.81±0.12 yr, and being found at 1.7σ from the ^{22}Na half-life. However, the ^{40}K events have been fitted to a constant rate because the half-life of ^{40}K is $T_{1/2} = 1.25 \times 10^9$ yr [243]. The result of the fit can be seen in Figure 5.1b and is compatible with a constant rate with p-value=0.35.

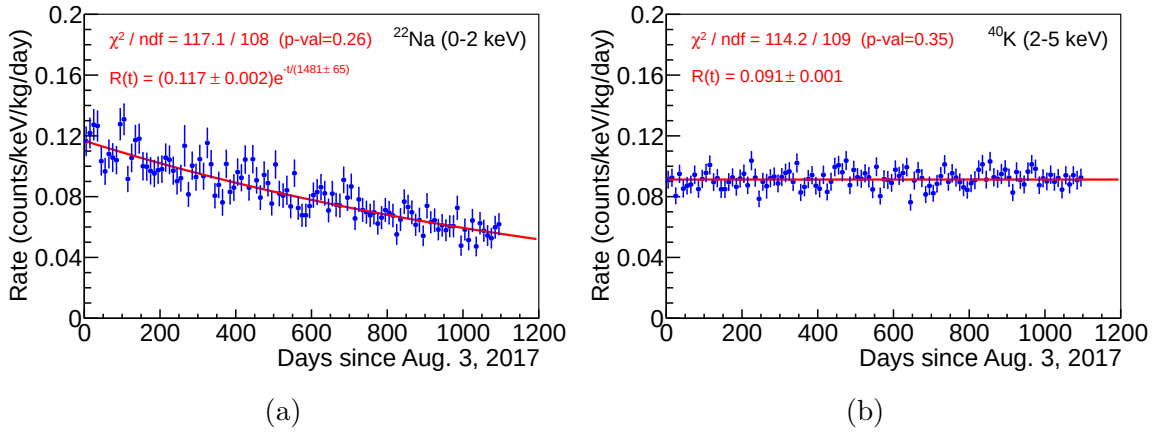

(a) (b)

Figure 5.1: *Time evolution of the rate of events attributed to ^{22}Na (a) and ^{40}K (b) at low energy identified by the coincidence with the corresponding high energy gamma in other modules.*

In order to confirm the background understanding and account for possible systematic effects that could appear over time, other control populations related to the time evolution of the rate of events of multiple-hit events in the region of interest or single-hit events out of the ROI are investigated. The time evolution of the total rate of events corresponding to single-hit events (labelled M1, i.e., multiplicity equal to 1) in the [6,10] keV region is shown in Figure 5.2a. The time dependence is fitted to an exponential decay plus a constant term (red line) and provides a lifetime of 1814±707 days with p-value=0.89. The green line of the figure corresponds to the prediction of the background model for the evolution of the corresponding rate of events, corrected by a normalization factor, f, in order to better reproduce the observations. This factor is also displayed in the figure and is at the level of a few percent. The same, but for events corresponding to single-hit events in the [10,20] keV energy region is shown in Figure 5.2b. In this case, the result of the fit provides a lifetime of 1508±489 days with p-value=0.07. The rate evolution is also well described by the background model. Finally, the time evolution of the total rate of events corresponding to multiple-hit events (labelled M2, i.e., multiplicity equal to 2) in the region of interest from 1 to 6 keV is shown in Figure 5.2c. The result of the fit provides a lifetime of 371±71 days with p-value=0.07, and the background model reproduces satisfactorily M2 events in [1,6] keV.

5.2 Annual modulation analysis

In this section, the annual modulation analysis corresponding to three years of ANAIS–112 data is carried out. For this purpose, the scintillating events after applying all the developed filtering protocols described in Chapter 3 from the 3^{rd} of August 2017 to the 13^{th} of August 2020, amounting to 322.82 kg×yr, are used. The approach followed in previous ANAIS–112 papers [203, 241, 242] is reviewed through an independent fit of the data with the same filtering procedure, and different fitting procedures of background evolution are considered in order to evaluate the possible presence of systematic effects in the analysis protocols. It has to be highlighted that any time-dependent systematic effect which might be originated from environmental factors or detector instability like gain, calibration or light yield is well controlled for this analysis as discussed in Section 2.9.

For a direct comparison with the DAMA/LIBRA results [7], the model independent analysis searching for annual modulation is performed in the same energy regions explored by DAMA/LIBRA collaboration ([1,6] and [2,6] keV), fixing the period to 1 year and the maximum of the modulation to the 2^{nd} of June. How-

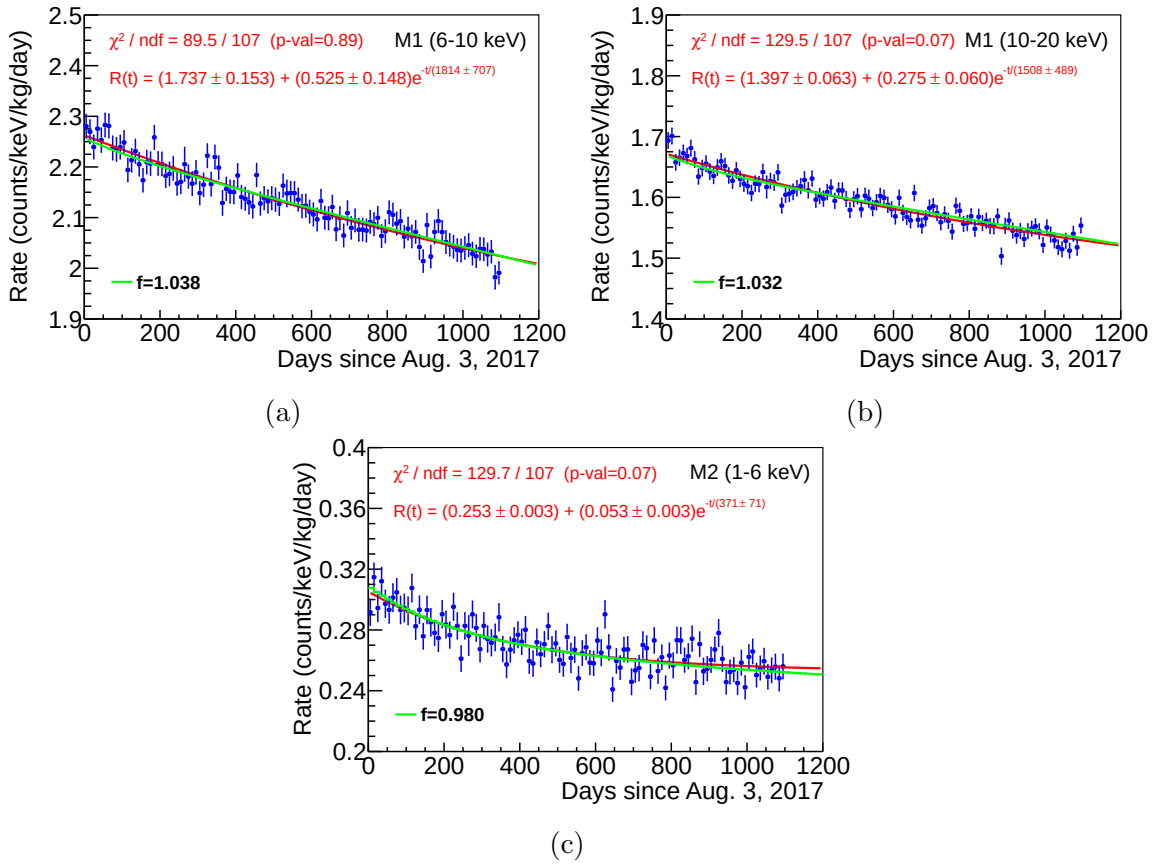

Figure 5.2: *Time evolution of the rate corresponding to M1 events in [6,10] keV (a) and [10-20] keV (b), and M2 events in [1,6] keV (c). All rates have been fitted to an exponential decay plus a constant term (red line) and compared with the background model estimates (green line), after normalizing by a factor f also displayed in panels.*

ever, the analysis approach followed by ANAIS–112 is quite different from that of DAMA/LIBRA, which is based on the subtraction of the average detection rate in 1 keV energy bins inside the region of interest in their defined annual cycles [170]. As shown in the previous section, ANAIS–112 background is clearly time-dependent (just as DAMA/LIBRA, but the collaboration has never published such a dependency), so this approach could produce a time modulation in data as an artefact due to the interaction between a time-dependent rate and the analysis method [244, 245]. Because of that, the used fitting procedure allows to include time-dependent backgrounds in a consistent way as no subtraction of any component before the fitting is imposed, as it is detailed in subsequent section.

One of the most important assets of ANAIS–112 in the search for the annual modulation is the very high duty cycle achieved (see Table 2.1). This excellent duty

cycle guarantees a perfect coverage of the whole year-periods, reducing possible systematic contributions in the annual modulation analysis. Detailed information about the three annual cycles by ANAIS–112 is reported in Table 5.1. Using the live time distribution (day by day) along the annual cycles of data taking, the mean value of the squared cosine is $\alpha = \langle \cos^2 \omega(t - t_0) \rangle$ and the mean value of the cosine is $\beta = \langle \cos \omega(t - t_0) \rangle$, where $\omega = 2\pi/365$ days^{-1} and $t_0 = 152.5$ days (i.e., the 2^{nd} of June). These parameters should be 0.5 and 0.0, respectively, for a perfect coverage of the whole year-periods.

Annual cycle	Time period	Exposure (kg×yr)	α	β
1	03/08/2017 - 31/07/2018	104.83	0.50129	-0.01303
2	01/08/2018 - 01/08/2019	107.33	0.50144	0.00171
3	02/08/2019 - 13/08/2020	110.66	0.48734	0.01049
Total	03/08/2017 - 13/08/2020	322.82	0.49656	-0.00007

Table 5.1: *Details about the annual cycles of ANAIS–112. The mean value of the squared cosine is* $\alpha = \langle \cos^2 \omega(t - t_0) \rangle$ *and the mean value of the cosine is* $\beta = \langle \cos \omega(t - t_0) \rangle$. *These parameters should be 0.5 and 0.0, respectively, for a perfect coverage of the whole year-periods.*

5.2.1 Modulation fit model and results

The results of the model independent analysis searching for annual modulation in the same energy regions reported by DAMA/LIBRA collaboration (from 1 to 6 keV and from 2 to 6 keV) are presented below. In order to perform a direct comparison with the results singled out by DAMA/LIBRA with one free parameter, the period and phase are fixed to 1 year and the 2^{nd} of June, respectively.

To evaluate the statistical significance of a possible modulation in ANAIS–112 data, a least-squares method adding the nine detectors grouped in 10-days time bins is used. The χ^2 function is:

$$\chi^2 = \sum_i \frac{(R_i - \mathcal{R}(t_i))^2}{\sigma_i^2}, \tag{5.1}$$

where R_i is the rate of events in the time bin t_i after correcting the measured number of events by the detector efficiency (in c/keV/kg/d units), σ_i is the corresponding

uncertainty of the observed rate of events, and $\mathcal{R}(t_i)$ is the expected rate of events at that time bin, that can be written as:

$$\mathcal{R}(t_i) = R_T(t_i) + S_m \cos\omega(t_i - t_0). \tag{5.2}$$

$R_T(t_i)$ is the expected rate of any non-modulated component, S_m is the modulation amplitude, $\omega = 2\pi/365$ days^{-1} and $t_0 = -62.17$ days (corresponding the cosine maximum to the 2^{nd} of June, when taking as time origin the 3^{rd} of August), while S_m is fixed to 0 for the null hypothesis and left unconstrained (positive or negative) for the modulation hypothesis.

The possible presence of systematic effects in the analysis protocols is evaluated below considering four different fitting procedures of background evolution.

5.2.1.1 Exponential model

In the first approach, the time evolution of the rate of events is modelled by an exponential decay, following the ANAIS–112 established analysis in Ref. [203, 241, 242]:

$$R_T(t_i) = R_0 \cdot (1 + fe^{-t_i/\tau}), \tag{5.3}$$

being R_0, f and τ free parameters.

The results of the χ^2 minimization following Equation 5.3 are shown in Figure 5.3 for [1,6] keV (a) and [2,6] keV (b) energy regions. The χ^2 and p-values of the fit for the null (modulation) hypothesis are also shown in red (green), together with the best fit for S_m. In order to emphasise the presence or absence of modulation, the data with the constant and exponential terms subtracted (residuals) are plotted in Figures 5.3c and 5.3d for [1,6] and [2,6] keV, respectively. In the [2,6] keV energy region, data are well described by the null hypothesis (p-value of 0.305). Smaller p-value (0.073) is obtained in [1,6] keV energy range. For the modulation hypothesis, the best fit modulation amplitudes compatible with zero at $\sim 1\sigma$ are obtained in both cases. The standard deviation of the modulation amplitude $\sigma(S_m)$ is 0.0044 c/keV/kg/d in [1,6] keV and 0.0039 c/keV/kg/d in [2,6] keV, which are consistent with the sensitivity estimates for ANAIS–112 from the previous chapter. The best fit values are also gathered in Tables 5.2 and 5.4.

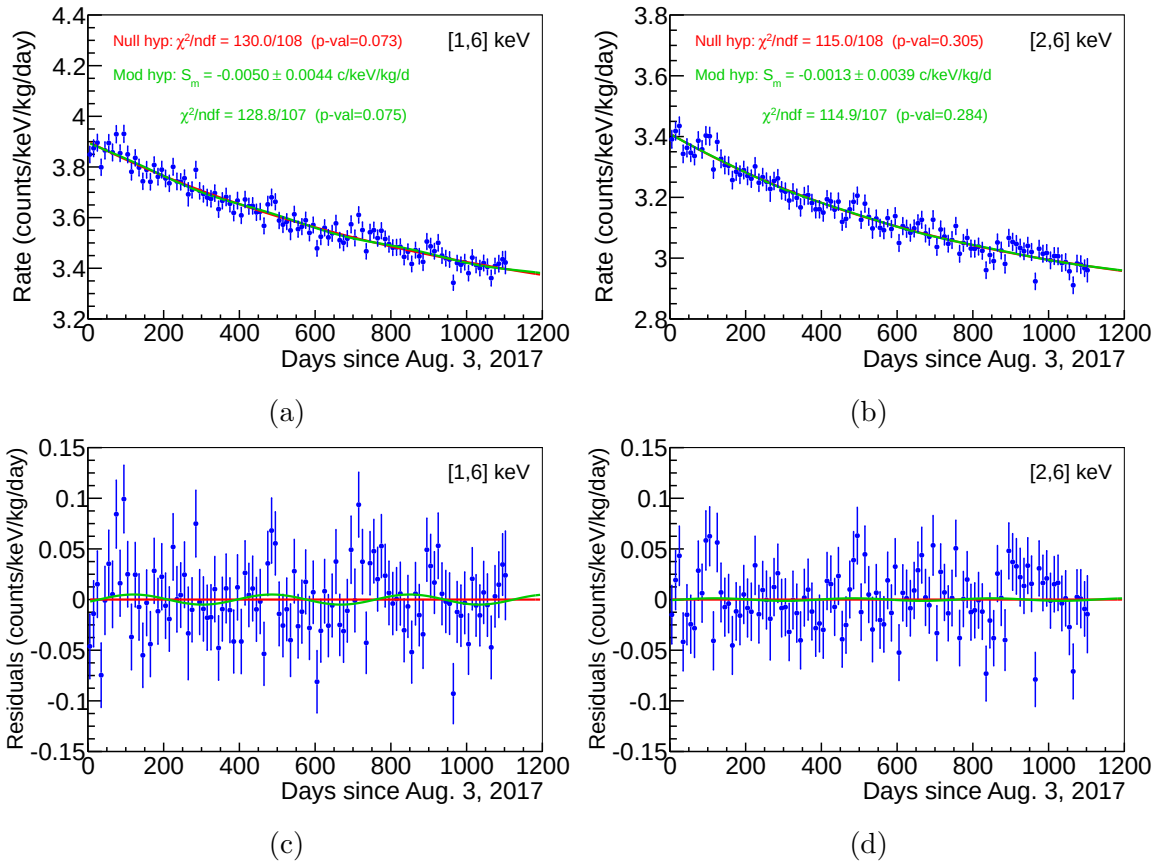

Figure 5.3: *ANAIS–112 fit results for three years of data in [1,6] keV (a) and [2,6] keV (b) energy regions, both in the modulation (green) and null hypotheses (red) when the background is described by Equation 5.3. Panels (c) and (d): the same, but after subtracting the constant and exponential functions fitted to Equation 5.3. Best fit S_m, χ^2 and p-values are also shown.*

Using the aforementioned approach, the ANAIS–112 best fit results have been published after 1.5, 2 and 3 years of data taking [203, 241, 242]. Table 5.2 collects these best fits together with the results reported by DAMA project [170] and COSINE–100 [177] experiment. DAMA project combines the results obtained in three different configurations: DAMA/NaI, DAMA/LIBRA-phase1 and DAMA/LIBRA-phase2 in [2,6] keV energy region, but only DAMA/LIBRA-phase2 has been able to explore energies below 2 keV. COSINE–100 has not published results in [1,6] keV energy range because the analysis threshold was established at 2 keV. The result obtained from the combination of the ANAIS–112 and COSINE–100 best fits can also be seen in Table 5.2, for which the weighted mean and variance formulas have been used. Given the low exposure of COSINE–100 relative to that of ANAIS–112, the combined result barely improves the sensitivity of ANAIS–112 by

15% between 2 and 6 keV. Furthermore, Figure 5.4 summarizes the best fit values of ANAIS–112 annual modulation analysis with 1.5, 2 and 3 years of exposure in comparison with DAMA/LIBRA result. After 3 years of measurement, the ANAIS–112 best fits are incompatible with DAMA/LIBRA result at 3.5σ (2.9σ), for a sensitivity of 2.4σ (2.6σ) at [1,6] keV ([2,6] keV).

Energy region	Experiment	Exposure (kg×yr)	χ^2 / NDF	p-value	S_m (c/keV/kg/d)
[1,6] keV	ANAIS–112	157.55	62.0 / 52	0.161	-0.0015±0.0063
		213.83	88.0 / 71	0.084	-0.0036±0.0054
		313.95	130.9 / 106	0.051	-0.0045±0.0044
	ANAIS–112 (This work)	313.95	128.8 / 107	0.051	-0.0050±0.0044
	DAMA/LIBRA-phase2	1126.40	50.0 / 51	0.513	0.0105±0.0011
[2,6] keV	ANAIS–112	157.55	47.4 / 52	0.655	-0.0044±0.0058
		213.83	67.0 / 71	0.613	-0.0029±0.0050
		313.95	115.7 / 106	0.245	-0.0008±0.0039
	ANAIS–112 (This work)	313.95	114.9 / 107	0.284	-0.0013±0.0039
	COSINE–100	97.70	175.6 / 175	0.473	0.0083±0.0068
	ANAIS–112+COSINE–100	411.65			0.0011±0.0034
	DAMA project	2462.09	113.8 / 138	0.935	0.0102±0.0008

Table 5.2: *Summary of the fit results to Equation 5.3 for the modulation hypothesis in [1,6] and [2,6] keV energy regions for ANAIS–112 after 1.5, 2 and 3 years of exposure [203, 241, 242], as well as the result for 3 years using the independent analysis followed in this work. The DAMA/LIBRA results [170] and the COSINE–100 result [177] are also shown.*

5.2.1.2 Quadratic model

In the second approach, the time evolution of the rate of events is modelled by a second degree polynomial function:

$$R_T(t_i) = R_0 + R_1 t_i + R_2 t_i^2, \tag{5.4}$$

where R_0, R_1 and R_2 are free parameters. In this case, the least squares estimator for the parameters is unbiased because the rate is linear in all the parameters [234], while the least squares estimator for R_0, f and τ in Equation 5.3 is generally biased due to the non-linearity of the rate in the parameters [246, 247].

Following Equation 5.4, the results of the χ^2 minimization for [1,6] and [2,6] keV energy regions are shown in Figures 5.5a and 5.5b, respectively. The χ^2 and p-values

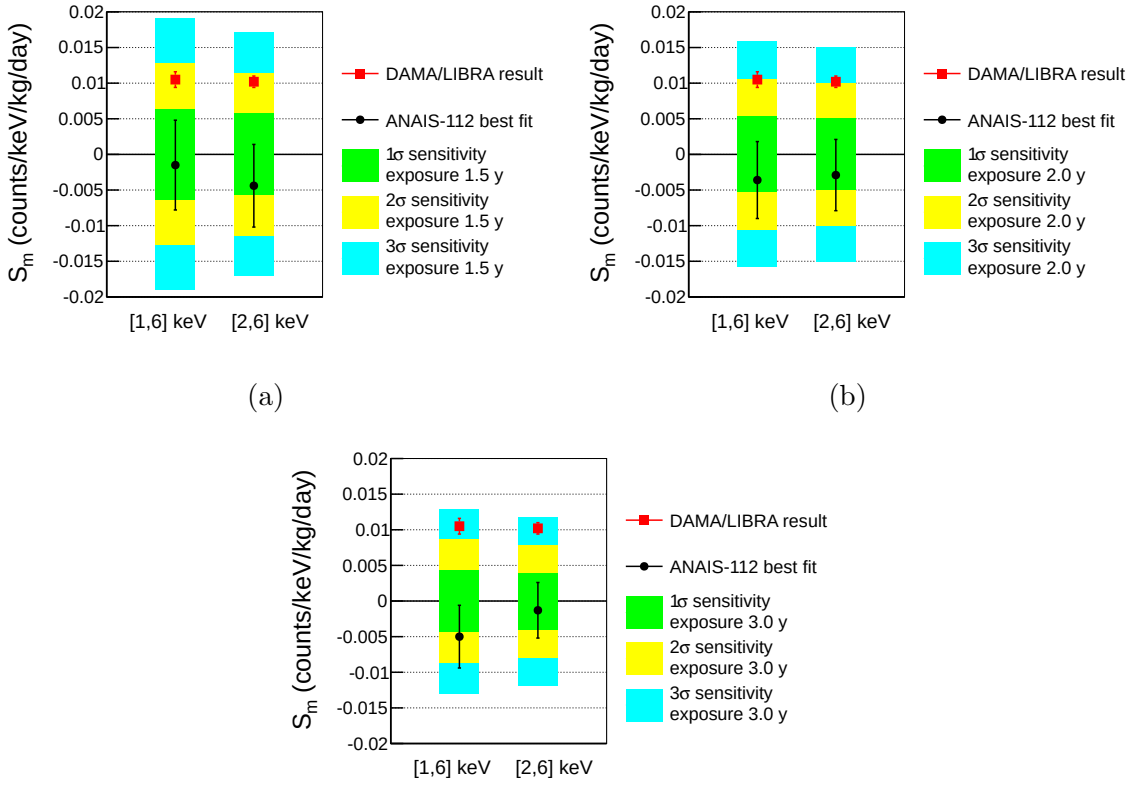

Figure 5.4: *Comparison between the ANAIS–112 best fits (in black) on annual modulation using data from 1.5 years (a), 2 years (b) and 3 years (c) and the DAMA/LIBRA modulation result (in red). Estimated sensitivity is shown at different confidence levels as coloured bands: green at 1σ, yellow at 2σ, and cyan at 3σ.*

of the fit for the null (modulation) hypothesis are also shown in red (green), together with the best fit for S_m. Panels 5.5c and 5.5d represent the residual counting rate for [1,6] and [2,6] keV, respectively, after non-modulated components have been subtracted. The null hypothesis is well supported by the χ^2 test in [2,6] keV energy region, with χ^2/NDF=117.8/108 (p-value=0.245), but provides a poorer description in [1,6] keV energy range, with χ^2/NDF=130.8/108 (p-value=0.067). The best fits for the modulation hypothesis are $S_m = -0.0021 \pm 0.0039$ c/keV/kg/d and -0.0057 ± 0.0044 c/keV/kg/d for [2,6] and [1,6] keV, respectively, both compatible with zero at $\sim 1\sigma$. The best fit values are also collected in Table 5.4.

5.2.1.3 Piecewise-defined straight lines model

When the three years of measurements are analyzed independently, the best description for the time evolution of the rate of events is obtained by fitting to a straight

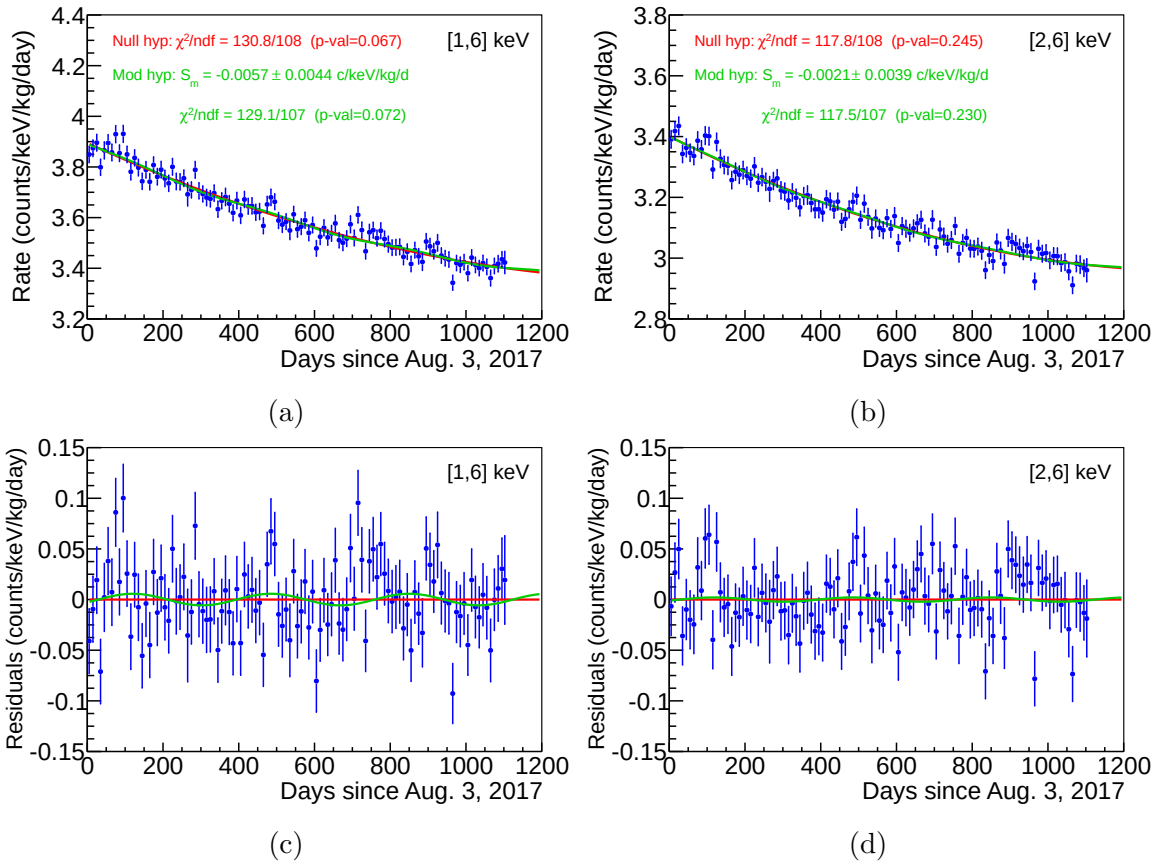

Figure 5.5: *ANAIS–112 fit results for three years of data in [1,6] keV (a) and [2,6] keV (b) energy regions, both in the modulation (green) and null hypotheses (red) when the background is described by Equation 5.4. Panels (c) and (d): the same, but after subtracting the second degree polynomial function fitted to Equation 5.4. Best fit S_m, χ^2 and p-values are also shown.*

line. However, this no longer occurs when the three years are considered together (see Table 5.3). A solution to this problem could be to consider a piecewise-defined function, in which each annual cycle is described by a first degree polynomial. Consequently, in this novel third approach, the time evolution of the rate of events is fitted to Equation 5.5.

$$R_T(t_i) = \begin{cases} R_0 + R_1 t_i & \text{if} \quad 0 \leq t_i \leq 360 \text{ days} \\ R_0' + R_2 t_i & \text{if } 360 < t_i \leq 730 \text{ days} \\ R_0'' + R_3 t_i & \text{if } 730 < t_i \leq 1105 \text{ days} \end{cases} \tag{5.5}$$

Here, R_0, R_1, R_2 and R_3 are free parameters. Parameters R_0' and R_0'' are completely determined by imposing the condition of continuity in the change of annualities (t_1=360 days and t_2=730 days). In particular, $R_0' = R_0 + (R_1 - R_2) \cdot t_1$ and $R_0'' = R_0 + R_1 t_1 + R_2 \cdot (t_2 - t_1) - R_3 t_2$.

Energy region	Year	χ^2 / NDF	p-value	R_0 (c/keV/kg/d)	R_1 (c/keV/kg/d/d)
[1,6] keV	1	43.9 / 34	0.118	3.897±0.011	$(-6.45 \pm 0.52) \cdot 10^{-4}$
	2	46.4 / 35	0.094	3.802±0.027	$(-3.96 \pm 0.49) \cdot 10^{-4}$
	3	38.7 / 36	0.348	3.772±0.043	$(-3.49 \pm 0.47) \cdot 10^{-4}$
	1–3	173.2 / 109	0.000	3.850±0.006	$(-4.45 \pm 0.10) \cdot 10^{-4}$
[2,6] keV	1	30.8 / 34	0.625	3.408±0.010	$(-6.23 \pm 0.46) \cdot 10^{-4}$
	2	33.5 / 35	0.540	3.305±0.024	$(-3.24 \pm 0.43) \cdot 10^{-4}$
	3	46.9 / 36	0.106	3.234±0.038	$(-2.40 \pm 0.41) \cdot 10^{-4}$
	1–3	175.3 / 109	0.000	3.355±0.005	$(-3.81 \pm 0.09) \cdot 10^{-4}$

Table 5.3: *Summary of the fit results to a straight line R_0+R_1t for the null hypothesis in [1,6] and [2,6] keV energy regions for the three years of ANAIS–112 data when each year is analyzed independently as well as when they are analyzed together.*

Figures 5.6a and 5.6b show the results of the χ^2 minimization following Equation 5.5 for [1,6] and [2,6] keV energy regions, respectively. The χ^2 and p-values of the fit for the null (modulation) hypothesis are also shown in red (green), together with the best fit for S_m. Panels (c) and (d) from Figure 5.6 depict the residual counting rate for [1,6] and [2,6] keV, respectively, after non-modulated components have been subtracted. In the [2,6] keV energy region, data are well described by the null hypothesis (p-value of 0.347). Smaller p-value (0.070) is obtained in [1,6] keV energy range. For the modulation hypothesis, the best fits modulation amplitudes are $S_m = 0.0012 \pm 0.0040$ c/keV/kg/d and -0.0026 ± 0.0045 c/keV/kg/d for [2,6] and [1,6] keV, respectively, both compatible with zero at 1σ. The best fit values are listed in Table 5.4.

5.2.1.4 Monte Carlo model

Finally and for completeness, it is summarized here a fourth approach which was used in the analysis of the time evolution of the rate of events in ANAIS–112 in Ref. [203]. This approach exploits the Monte Carlo background model of ANAIS–112 [196] so as to compute the background evolution in time (which is not a simple exponential as it is a sum of different components). This evolution is converted into a function $R_T^{MC}(t)$, so the rate of events can be expressed as:

$$R_T(t_i) = R_0 \cdot (1 + f R_T^{MC}(t_i)) \tag{5.6}$$

being R_0 and f free parameters.

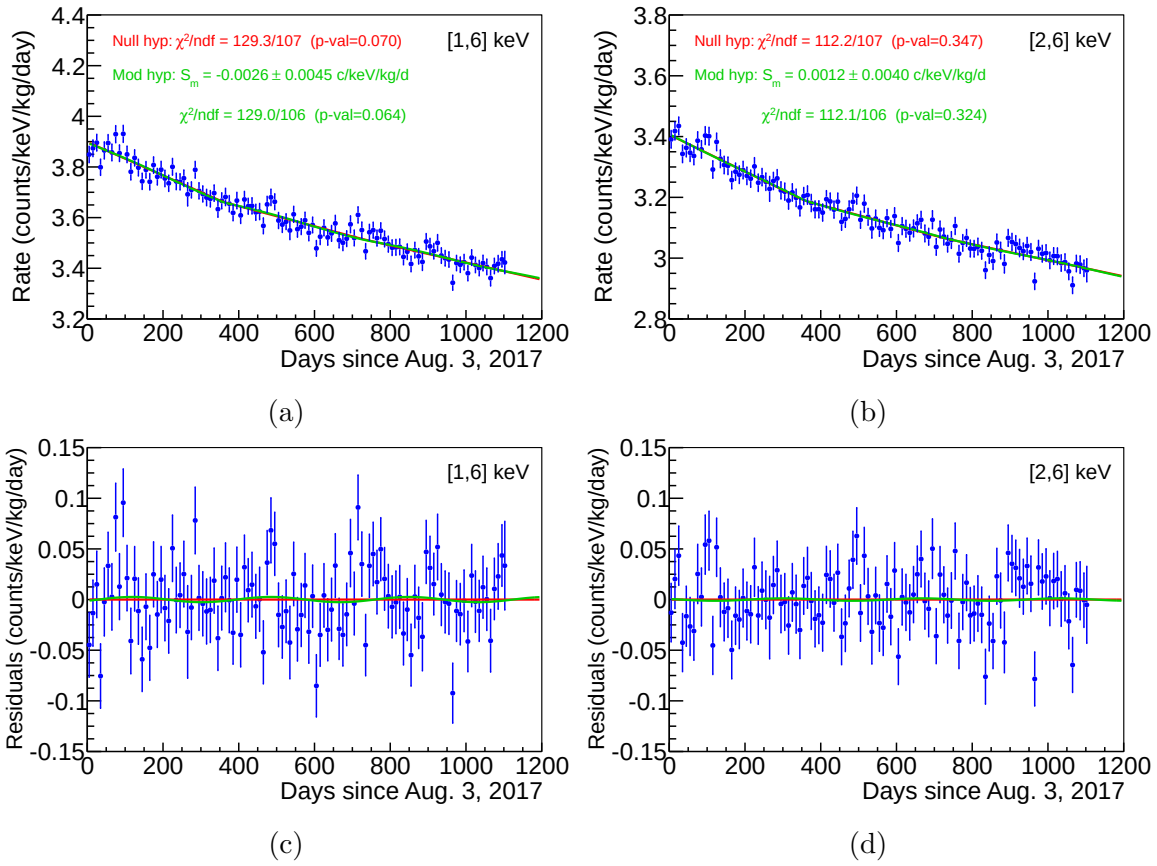

Figure 5.6: *ANAIS–112 fit results for three years of data in [1,6] keV (a) and [2,6] keV (b) energy regions, both in the modulation (green) and null hypotheses (red) when the background is described by Equation 5.5. Panels (c) and (d): the same, but after subtracting the piecewise function fitted to Equation 5.5. Best fit S_m, χ^2 and p-values are also shown.*

Table 5.4 summarizes the annual modulation results from three years of exposure of ANAIS–112 for [1,6] and [2,6] keV energy regions following the four aforementioned approaches. It is worth remarking that Equation 5.5 has one more nuisance parameter than Equations 5.3 and 5.4, while Equation 5.6 has only two nuisance parameters. The exponential decay provides the best description for the time evolution of the rate of events in [1,6] keV energy region, whereas the piecewise-defined function is the one that best supports the evolution of the rate of events in time between 2 and 6 keV. For the modulation hypothesis, the best fit modulation amplitudes are compatible with zero at $\sim 1\sigma$ in all cases. The standard deviation of the modulation amplitude $\sigma(S_m)$ is the same for the four background modelling approaches in [1,6] and [2,6] keV energy regions. In addition, Table 5.5 lists the nuisance parameters obtained in the different fitting procedures.

Fit model	χ^2 / NDF null hyp	p-value null hyp	χ^2 / NDF mod hyp	p-value mod hyp	nuisance params	S_m (c/keV/kg/d)
From 1 to 6 keV						
Exponential Eq. 5.3	130.0 / 108	0.073	128.8 / 107	0.075	3	-0.0050±0.0044
Polynomial-2 Eq. 5.4	130.8 / 108	0.067	129.1 / 107	0.072	3	-0.0057±0.0044
Piecewise Eq. 5.5	129.3 / 107	0.070	129.0 / 106	0.064	4	-0.0026±0.0045
MC Eq. 5.6	143.1 / 108	0.013	142.5 / 107	0.012	2	-0.0036±0.0044
From 2 to 6 keV						
Exponential Eq. 5.3	115.0 / 108	0.305	114.9 / 107	0.284	3	-0.0013±0.0039
Polynomial-2 Eq. 5.4	117.8 / 108	0.245	117.5 / 107	0.230	3	-0.0021±0.0039
Piecewise Eq. 5.5	112.2 / 107	0.347	112.1 / 106	0.324	4	0.0012±0.0040
MC Eq. 5.6	120.8 / 108	0.188	120.8 / 107	0.171	2	0.0004±0.0039

Table 5.4: *Summary of the fits searching for an annual modulation with fixed period and phase in the three years of ANAIS–112 data for different background modelling.*

The results perfectly agree with the sensitivity estimates for ANAIS–112 in both energy regions (see Figure 4.10a for [1,6] keV and Figure 4.10b for [2,6] keV), confirming the ANAIS–112 projected sensitivity to the DAMA/LIBRA result. A 3σ sensitivity should be at reach before completing the scheduled 5 years of data-taking.

5.2.2 Modulation amplitude variation with energy

The energy distribution of the modulation amplitude as a function of the detected energy, $S_m(E)$, is a powerful tool to investigate the nature of a potential dark matter candidate in model dependent analyses. Positive signal reported by DAMA/LIBRA is only present below 6 keV. Above this energy, the modulation amplitude values are compatible with zero. In fact, the S_m values in the [6,20] keV energy interval have random fluctuations around zero with χ^2 equal to 29.8 for 28 degrees of freedom (upper tail probability of 37%) in the case of DAMA/LIBRA-phase2 [7].

From 1 to 6 keV				
Fit model	Exponential Eq. 5.3	Polynomial-2 Eq. 5.4	Piecewise Eq. 5.5	MC Eq. 5.6
R_0 (c/keV/kg/d)	3.147±0.069	3.894±0.009	3.897±0.010	3.605±0.003
f	0.239±0.025	-	-	0.85±0.02
τ (d)	1009±150	-	-	-
R_1 (c/keV/kg/d/d)	-	$(-6.85 \pm 0.38) \cdot 10^{-4}$	$(-6.54 \pm 0.41) \cdot 10^{-4}$	-
R_2 (c/keV/kg/d/d)	-	-	$(-4.00 \pm 0.31) \cdot 10^{-4}$	-
R_2 (c/keV/kg/d/d^2)	-	$(2.18 \pm 0.33) \cdot 10^{-7}$	-	-
R_3 (c/keV/kg/d/d)	-	-	$(-3.34 \pm 0.37) \cdot 10^{-4}$	-

From 2 to 6 keV				
Fit model	Exponential Eq. 5.3	Polynomial-2 Eq. 5.4	Piecewise Eq. 5.5	MC Eq. 5.6
R_0 (c/keV/kg/d)	2.823±0.041	3.400±0.008	3.407±0.009	3.145±0.003
f	0.208±0.016	-	-	0.91±0.02
τ (d)	816±110	-	-	-
R_1 (c/keV/kg/d/d)	-	$(-6.29 \pm 0.34) \cdot 10^{-4}$	$(-6.09 \pm 0.36) \cdot 10^{-4}$	-
R_2 (c/keV/kg/d/d)	-	-	$(-3.33 \pm 0.28) \cdot 10^{-4}$	-
R_2 (c/keV/kg/d/d^2)	-	$(2.24 \pm 0.29) \cdot 10^{-7}$	-	-
R_3 (c/keV/kg/d/d)	-	-	$(-2.66 \pm 0.33) \cdot 10^{-4}$	-

Table 5.5: *Summary of the nuisance parameters obtained in the fits searching for an annual modulation with fixed period and phase in the three years of ANAIS–112 data for different background modelling. Note that the R_2 parameter has different units according to the fit model used.*

Figure 5.7 presents the best fit amplitudes, S_m, from three years of exposure of ANAIS–112 calculated per 1 keV energy bins following Equation 5.3, from 1 to 20 keV (bottom panel, black dots), together with the DAMA/LIBRA-phase2 modulation amplitudes extracted from Ref. [7] (red triangles). The top panel shows the p-values for the null (open squares) and modulation hypotheses (closed circles) for every energy bin. All the modulation amplitudes below 20 keV are compatible with zero and, in general, p-values for the null hypothesis are slightly larger than those of the modulation hypothesis. The 1σ and 2σ bands shown in the figure are obtained from the sensitivity estimates (see Section 4.1) for three years of exposure of ANAIS–112.

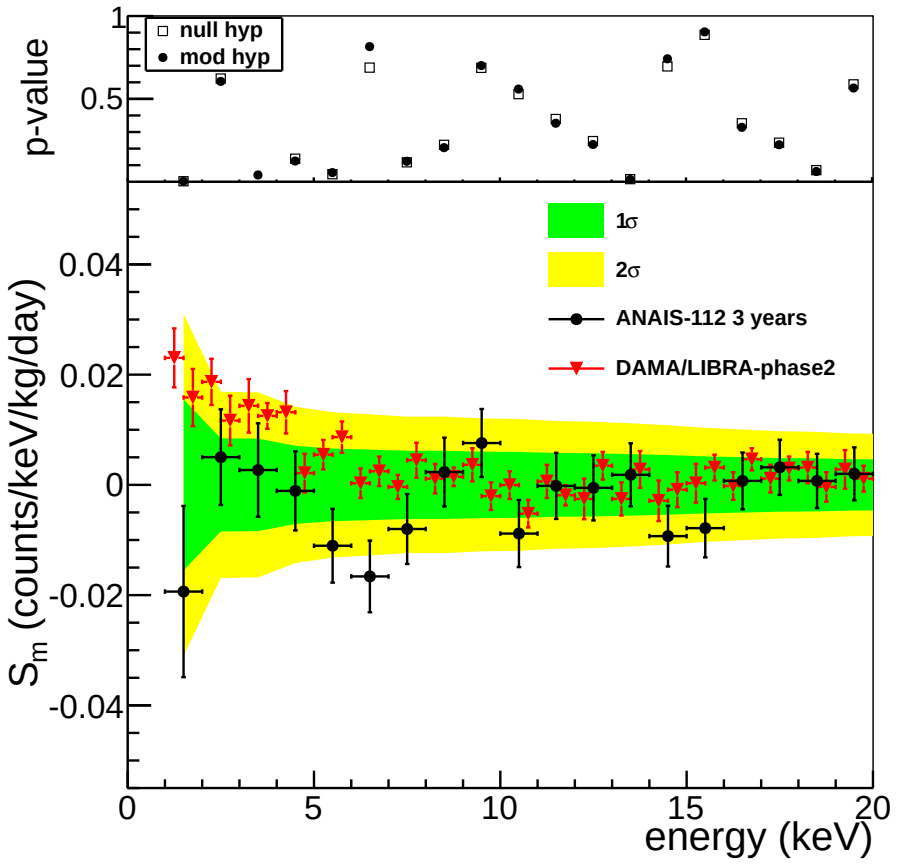

Figure 5.7: *Modulation amplitude per 1 keV energy bins combining data from all the modules. The corresponding DAMA/LIBRA result [7] is shown for reference, as well as the 1σ and 2σ ANAIS–112 bands derived from sensitivity estimates (see Section 4.1). Top panel compares the p-values of the fits to Equation 5.3 with those corresponding to the null hypothesis for every energy bin.*

5.2.3 Phase-free annual modulation analysis

In the analysis presented in previous sections, the period and the phase of the possible annual modulation signal have been set to 1 year and -62.17 days (corresponding to the 2^{nd} of June), respectively. An extension of this analysis is considered below, in which the time evolution of the rate of events from ANAIS–112 is fitted to Equation 5.3, where the modulated component has the period fixed to 1 year and both the modulation amplitude and the phase are taken as free parameters. The best fits are shown as black dots in Figures 5.8a and 5.8b for [1,6] and [2,6] keV energy regions, respectively. Exclusion contours at 1, 2 and 3σ are also depicted as green, yellow and cyan coloured bands, respectively. It is worth noting that due to the periodicity of the cosine function, a signal with modulation amplitude S_m at $t = t_0$ is just as

valid as one with amplitude $-S_m$ at $t = t_0 \pm T/2$ ($T = 365$ days), which leads to odd contour plots (and best fit solutions) with respect to an origin at $t = t_0 \pm T/4$. The ANAIS–112 best fits are $\sim 3\sigma$ away from DAMA/LIBRA result (shown as red points), but it has to be remarked that in this case the fit is biased, as would generally be expected due to the non-linearity of the model in the parameters [246, 247]. Table 5.6 collects the ANAIS–112 best fits in [1,6] and [2,6] keV energy ranges for phase-free annual modulation analysis.

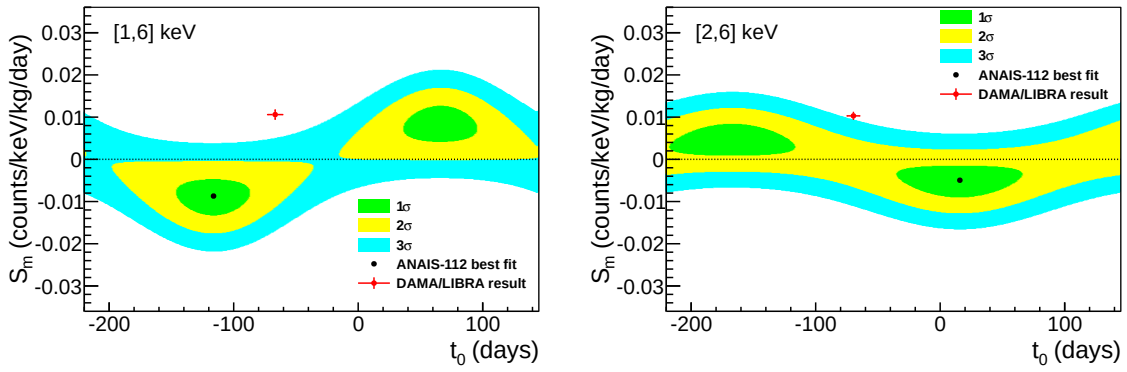

(a) (b)

Figure 5.8: *Best fit results for three years of data (black points) in [1,6] keV (a) and [2,6] keV (b) energy regions in the (t_0,S_m) plane for the exponential fitting procedure (see Equation 5.3). Exclusion contours at 1, 2 and 3σ are depicted as green, yellow and cyan coloured bands, respectively. DAMA/LIBRA results are shown for comparison in red.*

Energy region	χ^2 / NDF	p-value	S_m (c/keV/kg/d)	t_0 (days)
[1,6] keV	126.2 / 106	0.088	-0.0087±0.0044	-116±29
[2,6] keV	113.3 / 106	0.296	-0.0050±0.0038	16±46

Table 5.6: *Best fit results from three years exposure of ANAIS–112 with period fixed to 1 year and unconstrained phase. The evolution of rate of events is modelled by Equation 5.3. Note that with a phase shift of $+T/2$ ($-T/2$) in [1,6] keV ([2,6] keV), the same value would be obtained for the modulation amplitude, but with a changed of sign.*

In order to estimate the expected bias in absence of modulation, Equation 5.2 can be alternatively written as:

$$\mathcal{R}(t_i) = R_T(t_i) + A\cos\omega t_i + B\sin\omega t_i, \tag{5.7}$$

where $\phi = \omega t_0$, $A = S_m \cos\phi$ and $B = S_m \sin\phi$. The pair of parameters (A,B) can be interpreted as cartesian coordinates, and (S_m,ϕ) as their corresponding polar coordinates. In the simplest case in which $R_T(t_i)$ is time independent, the equation is linear in all parameters and thus their least squares estimator (LSE) is unbiased; however, the non-linearity of ϕ in Equation 5.2 is very likely to imply a bias in the LSE for S_m and ϕ [234]. If data are evenly distributed along an integer number of year-periods, the covariance matrix of parameters is diagonal and the estimators of A and B have the same variance, σ^2. Moreover, whether there is not any modulated component, the estimators of A and B are independent normal distributions with mean zero and variance σ^2. Taking these considerations into account, the bias of the LSE of S_m can be calculated through the joint probability of (A,B):

$$P(A,B)dAdB = \frac{1}{\sqrt{2\pi}\sigma} e^{-A^2/2\sigma^2} \frac{1}{\sqrt{2\pi}\sigma} e^{-B^2/2\sigma^2} dAdB, \tag{5.8}$$

which, in polar coordinates (S_m,ϕ), can be written as:

$$P(S_m,\phi)dS_m d\phi = \frac{1}{2\pi\sigma^2} e^{-S_m^2/2\sigma^2} S_m dS_m d\phi. \tag{5.9}$$

So, the expectation value of the modulation amplitude $S_m = +\sqrt{A^2+B^2}$ is:

$$\begin{aligned} E(S_m) &= \int_{-\infty}^{\infty}\int_{-\infty}^{\infty} S_m P(A,B)dAdB \\ &= \int_0^{\infty}\int_0^{2\pi} S_m P(S_m,\phi)S_m dS_m d\phi = \sqrt{\frac{\pi}{2}}\cdot\sigma. \end{aligned} \tag{5.10}$$

In this way, the expected bias in absence of modulation is $\sqrt{\pi/2}\cdot\sigma$, being σ the standard deviation of the estimator of the amplitudes A and B in Equation 5.7. This result translates into a bias of $\pm$ 0.0055 ($\pm$ 0.0049) c/keV/kg/d in [1,6] ([2,6]) keV energy region, depending on whether the modulation amplitude is positive or negative, respectively. Correcting the best fits (see Table 5.6) with the calculated bias, results compatible with no modulation are obtained in both energy ranges.

A similar procedure can be used to estimate the expected bias in the presence of a modulation with amplitude $S_{m,0}$ and phase ϕ_0. Again, the pair of parameters (A,B) in Equation 5.7 can be interpreted as cartesian coordinates, and (S_m,ϕ) as their corresponding polar coordinates. In this case, the expected value of A and B is no longer zero, but generally has a value of A_0 and B_0, respectively, such that $S_{m,0} = \sqrt{A_0^2 + B_0^2}$. To simplify calculations and without losing generality, a coordinate change can be made by rotating an angle with $\tan\phi_0 = B_0/A_0$ around the origin of the coordinates, so that $A_0 = S_{m,0}$ and $B_0 = 0$. In these conditions, the joint probability of (A,B) is:

$$P(A,B)dAdB = \frac{1}{\sqrt{2\pi}\sigma} e^{-(A-S_{m,0})^2/2\sigma^2} \frac{1}{\sqrt{2\pi}\sigma} e^{-B^2/2\sigma^2} dAdB, \tag{5.11}$$

which can be written in polar coordinates as follows:

$$P(S_m,\phi)dS_m d\phi = \frac{1}{2\pi\sigma^2} e^{-(S_m^2 - 2S_{m,0}S_m\cos\phi + S_{m,0}^2)/2\sigma^2} S_m dS_m d\phi. \tag{5.12}$$

Consequently, the expected value of the modulation amplitude ($S_m > 0$) is:

$$\begin{aligned} E(S_m) &= \int_0^\infty \int_0^{2\pi} S_m P(S_m,\phi) S_m dS_m d\phi \\ &= \frac{1}{2\pi\sigma^2} \int_0^\infty e^{-\frac{S_m^2 + S_{m,0}^2}{2\sigma^2}} S_m^2 dS_m \int_0^{2\pi} e^{\frac{S_{m,0}S_m\cos\phi}{\sigma^2}} d\phi \\ &= \sqrt{\frac{\pi}{2}} \frac{1}{2\sigma} e^{-S_{m,0}^2/4\sigma^2} \left[\left(S_{m,0}^2 + 2\sigma^2\right) I_0\left(\frac{S_{m,0}^2}{4\sigma^2}\right) + S_{m,0}^2 I_1\left(\frac{S_{m,0}^2}{4\sigma^2}\right) \right] \end{aligned} \tag{5.13}$$

where $I_\alpha(x)$ are the modified Bessel functions of the first kind of order α and are defined as [248]:

$$I_\alpha(x) = \sum_{k=0}^{\infty} \frac{1}{k!\Gamma(k+\alpha+1)} \left(\frac{x}{2}\right)^{2k+\alpha} \tag{5.14}$$

$$I_0(x) = 1 + \frac{x^2}{2} + \frac{x^4}{2^2 4^2} + ... \qquad I_1(x) = \frac{x}{2} + \frac{x^3}{2^2 4} + \frac{x^5}{2^2 4^2 6} + ... \tag{5.15}$$

It is worth remarking that when the modulation amplitude is much greater than the standard deviation, the bias is negligible. For example, if $S_m \sim 2\sigma$, the bias is of the order of 13%, whereas if $S_m \sim 3\sigma$, the bias is less than 5%. For ANAIS–112, Equation 5.13 implies a bias of ± 0.0012 (± 0.0017) c/keV/kg/d in [1,6] ([2,6]) keV

energy region, depending on whether the modulation amplitude is positive or negative, respectively. Correcting these values with the calculated bias, results consistent with no modulation to less than 2σ are obtained in both energy ranges.

5.2.4 Segmented detector for annual modulation search

According to the ANAIS–112 sensitivity estimates described in Chapter 4, considering the nine detectors independently improves the expected sensitivity to the annual modulation signal in both energy regions (from 1 to 6 keV and from 2 to 6 keV), because the differences between the background and the acceptance efficiency of each detector take action. Therefore, the summation in the χ^2 expression is also performed over detectors:

$$\chi^2 = \sum_{k=1}^{N_{det}} \sum_i \left(\frac{R_i^k - \mathcal{R}^k(t_i)}{\sigma_i^k} \right)^2, \tag{5.16}$$

where R_i^k is the rate of events for the k^{th} detector in the i^{th} time bin after correcting the measured number of events by the detector efficiency (in c/keV/kg/d units), σ_i^k is the corresponding uncertainty of the observed rate of events in detector k, and $\mathcal{R}^k(t_i)$ is the expected rate of events for detector k at that time bin, which can be written as:

$$\mathcal{R}^k(t_i) = R_T^k(t_i) + S_m^k \cos\omega(t_i - t_0). \tag{5.17}$$

$R_T^k(t_i)$ is the expected rate of any non-modulated component of detector k, S_m^k is the modulation amplitude in the k^{th} detector, $\omega = 2\pi/365$ days^{-1} and $t_0 = -62.17$ days, while S_m^k is fixed to 0 for the null hypothesis and left unconstrained (positive or negative) for the modulation hypothesis. In order to combine the modulation amplitudes obtained considering each detector independently, the weighted mean of the nine S_m^k is carried out.

The different fitting procedures of background evolution followed in Section 5.2.1 are evaluated below for segmented detector. In the first approach, the time evolution of the rate of events is modelled by an exponential decay:

$$R_T^k(t_i) = R_0^k \cdot (1 + f^k e^{-t_i/\tau^k}), \tag{5.18}$$

being R_0^k, f^k and τ^k free parameters.

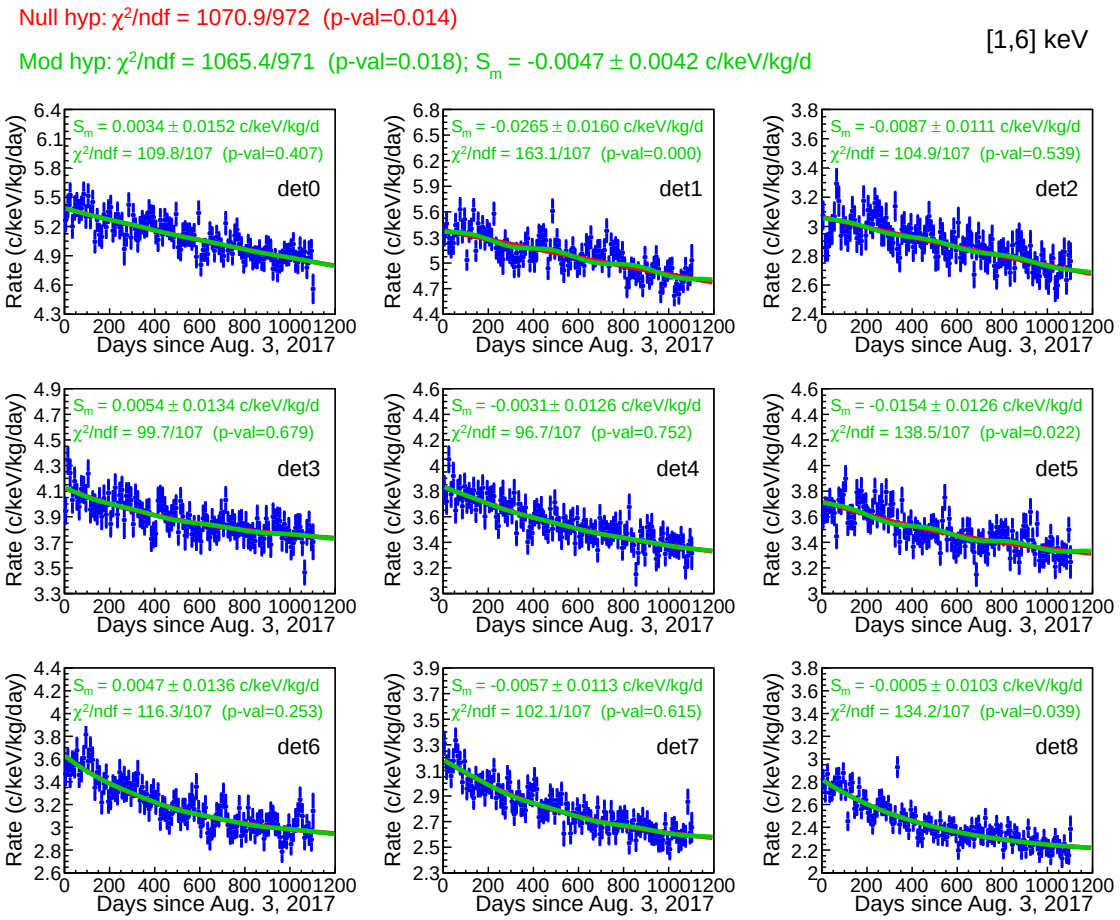

Figure 5.9: *Results of the fit of the nine modules data using Equation 5.18 in [1,6] keV energy region, in the modulation (green) and null hypotheses (red). Best fit S_m, χ^2 and p-values are also shown.*

The results of the χ^2 minimization following Equation 5.18 are shown in Figures 5.9 and 5.10 for [1,6] keV and [2,6] keV energy regions, respectively. The χ^2 and p-values of the fit for the null (modulation) hypothesis are also shown in red (green) at the top, together with the best fit for S_m. The best fits for the modulation hypothesis are also calculated separately for the data of every module and displayed in the legend of each panel. The null hypothesis is well supported by the χ^2 test in [2,6] keV energy region, with χ^2/NDF=1006.9/972 (p-value=0.212), but provides a poorer description in [1,6] keV energy range, with χ^2/NDF=1070.9/972 (p-value=0.014). The best fits for the modulation hypothesis are $S_m = -0.0006 \pm 0.0038$ c/keV/kg/d and -0.0047 ± 0.0042 c/keV/kg/d for [2,6] and [1,6] keV, respectively, both compatible with zero at $\sim 1\sigma$. It is worth to note that in general the fits obtained for the individual detectors are good, with p-values larger than 0.05 in all cases except for D1 and D5 in both energy regions and D8 in [1,6] keV. The results are compatible with those obtained adding the nine detectors (Equation 5.3), with slightly lower values

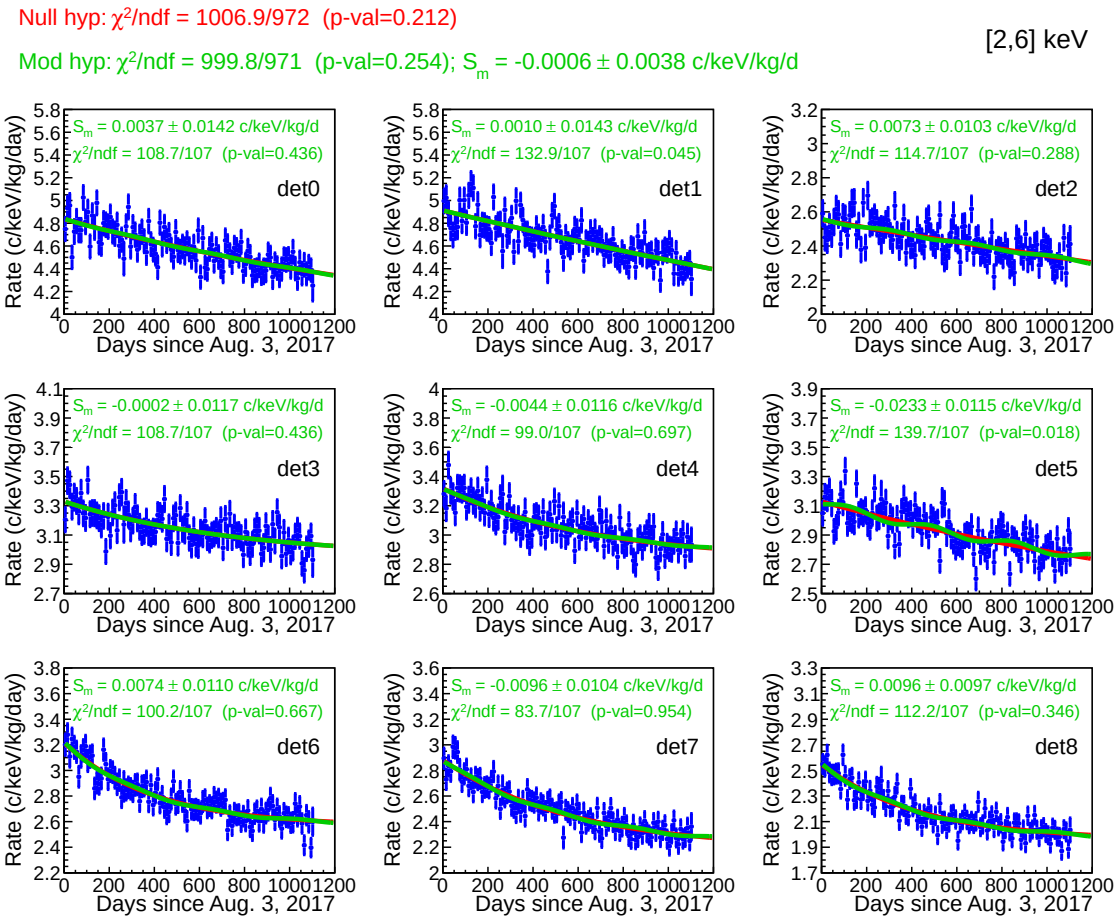

Figure 5.10: *Results of the fit of the nine modules data using Equation 5.18 in [2,6] keV energy region, in the modulation (green) and null hypotheses (red). Best fit S_m, χ^2 and p-values are also shown.*

of $\sigma(S_m)$ in this case in [1,6] and [2,6] keV energy regions, as expected from the sensitivity expectations (see Sections 4.1.1.1 and 4.1.2.1). The best fit values are also collected in Tables 5.7 and 5.8 for [1,6] and [2,6] keV energy regions, respectively.

The modulation amplitudes S_m^k integrated in the energy ranges [1,6] and [2,6] keV for each of the nine detectors from three years of exposure of ANAIS–112 are shown as black dots in Figures 5.11a and 5.11b, respectively. They have random fluctuations around the weighted averaged value (red point) confirmed by the χ^2/NDF equal to 4.2/8 (7.1/8) in [1,6] keV ([2,6] keV) energy region. The 1σ and 2σ bands are also shown as green and yellow shaded areas, respectively.

In the second approach, the time evolution of the rate of events is modelled by a second degree polynomial function:

$$R_T^k(t_i) = R_0^k + R_1^k t_i + R_2^k t_i^2, \tag{5.19}$$

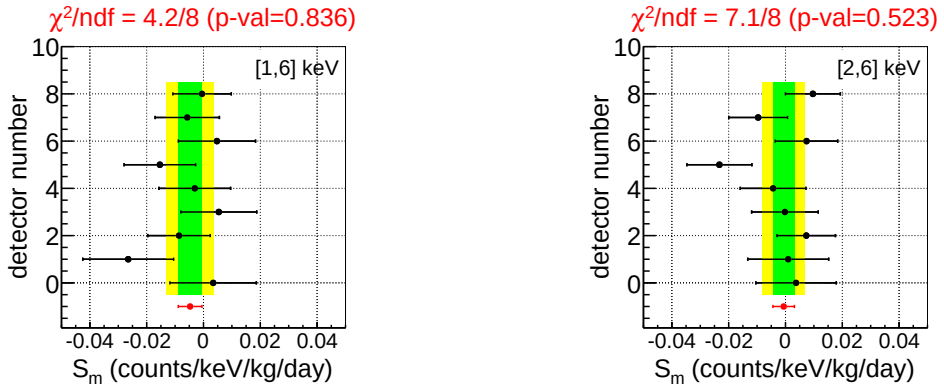

(a) (b)

Figure 5.11: *Modulation amplitudes S_m integrated in the [1,6] keV (a) and [2,6] keV (b) energy ranges for each of the 9 detectors from three years exposure of ANAIS–112. The uncertainties are at 1σ confidence level. The weighted averaged point is shown in red, whereas 1σ and 2σ bands are shown as green and yellow shaded areas, respectively. The χ^2 and p-values are also reported.*

where R_0^k, R_1^k and R_2^k are free parameters. The results of the χ^2 minimization following Equation 5.19 are gathered in Tables 5.7 and 5.8 for [1,6] and [2,6] keV energy regions, respectively. The best fits for the modulation hypothesis are compatible with zero at $\sim$1σ in both energy regions and are also consistent with those obtained adding the nine detectors (Equation 5.4), with slightly lower values of $\sigma(S_m)$ in this case in the [1,6] and [2,6] keV energy regions, as expected from the sensitivity expectations.

In the third approach, the time evolution of the rate of events is fitting to Equation 5.20.

$$R_T^k(t_i) = \begin{cases} R_0^k + R_1^k t_i & \text{if} \quad 0 \leq t_i \leq 360 \text{ days} \\ R_0^{k\prime} + R_2^k t_i & \text{if } 360 < t_i \leq 730 \text{ days} \\ R_0^{k\prime\prime} + R_3^k t_i & \text{if } 730 < t_i \leq 1105 \text{ days} \end{cases} \tag{5.20}$$

Here, R_0^k, R_1^k, R_2^k and R_3^k are free parameters. Parameters $R_0^{k\prime}$ and $R_0^{k\prime\prime}$ are completely determined by imposing the condition of continuity in the change of annualities (t_1=360 days and t_2=730 days). In particular, $R_0^{k\prime} = R_0^k + (R_1^k - R_2^k) \cdot t_1$ and $R_0^{k\prime\prime} = R_0^k + R_1^k t_1 + R_2^k \cdot (t_2 - t_1) - R_3^k t_2$. As in the two previous approaches, the results of the χ^2 minimization following Equation 5.20 are found in Tables 5.7 and 5.8 for [1,6] and [2,6] keV energy regions, respectively. In both energy ranges, the best fits for the modulation hypothesis are consistent with the absence of modulation at 1σ.

Finally, the fourth approach (extracted from Ref. [203]) exploits the Monte Carlo background model of ANAIS–112 [196] so as to compute the background evolution in time. This evolution is converted into a function $R_T^{MC,k}(t)$, so the rate of events can be expressed as:

$$\mathcal{R}^k(t_i) = R_0^k \cdot (1 + f^k R_T^{MC,k}(t_i)) + S_m \cos\omega(t_i - t_0). \tag{5.21}$$

being R_0^k, f^k and S_m free parameters. As expected from the sensitivity estimates, the results obtained from the χ^2 minimization following Equation 5.21 are compatible with those obtained adding the nine detectors (Equation 5.6), with slightly lower values of $\sigma(S_m)$ in this case for both [1,6] and [2,6] keV energy regions. These best fit values are listed in Tables 5.7 and 5.8 for [1,6] and [2,6] keV energy regions, respectively.

Tables 5.7 and 5.8 summarize the annual modulation results from three years of exposure of ANAIS–112 for [1,6] and [2,6] keV energy regions, respectively, following the four aforementioned approaches. The piecewise-defined function provides the best description for the time evolution of the rate of events in both energy regions, but closely followed by the exponential decay, which is the fitting procedure established in ANAIS–112 publications [203, 241, 242]. For the modulation hypothesis, the best fit modulation amplitudes are compatible with zero at $\sim 1\sigma$ in all cases. The standard deviation of the modulation amplitude $\sigma(S_m)$ is roughly the same for the four background modelling approaches in [1,6] and [2,6] keV energy regions.

Regarding the search for a systematic effect in the ANAIS–112 data due to the background fitting procedure, it can be concluded that, after studying four different models for the time evolution of the ANAIS–112 rate of events, compatible results have been obtained in all cases, both considering the total background of the experiment and evaluating the background of each detector independently. These results are consistent with the absence of modulation in both [1,6] and [2,6] keV energy regions. Moreover, the results perfectly agree with the sensitivity estimates for ANAIS–112 in both energy regions, reaching higher sensitivity when segmentation in the nine detectors is considered and confirming the ANAIS–112 projected sensitivity to the DAMA/LIBRA result. A 3σ sensitivity should be at reach before completing the scheduled 5 years of data-taking.

From 1 to 6 keV				
Fit model	detector	χ^2 / NDF mod hyp	p-value mod hyp	S_m (c/keV/kg/d)
Exponential Eq. 5.18	0	109.8 / 107	0.407	0.0034±0.0152
	1	163.1 / 107	0.000	-0.0265±0.0160
	2	104.9 / 107	0.538	-0.0086±0.0110
	3	99.7 / 107	0.679	0.0054±0.0134
	4	96.7 / 107	0.752	-0.0031±0.0126
	5	138.5 / 107	0.022	-0.0154±0.0126
	6	116.3 / 107	0.253	0.0047±0.0136
	7	102.1 / 107	0.615	-0.0057±0.0113
	8	134.2 / 107	0.039	-0.0005±0.0103
	all	1065.4 / 971	0.018	-0.0047±0.0042
Polynomial-2 Eq. 5.19	0	109.8 / 107	0.408	0.0032±0.0152
	1	161.3 / 107	0.001	-0.0251±0.0161
	2	103.7 / 107	0.572	-0.0074±0.0126
	3	100.2 / 107	0.665	0.0044±0.0134
	4	97.0 / 107	0.745	-0.0038±0.0127
	5	137.8 / 107	0.024	-0.0164±0.0126
	6	114.8 / 107	0.286	0.0011±0.0137
	7	102.8 / 107	0.598	-0.0079±0.0114
	8	138.4 / 107	0.022	-0.0029±0.0103
	all	1065.8 / 971	0.018	-0.0057±0.0043
Piecewise Eq. 5.20	0	109.5 / 106	0.387	0.0016±0.0155
	1	154.0 / 106	0.002	-0.0153±0.0166
	2	103.0 / 106	0.565	-0.0105±0.0129
	3	99.4 / 106	0.661	0.0087±0.0137
	4	95.9 / 106	0.749	0.0007±0.0129
	5	136.2 / 106	0.026	-0.0171±0.0129
	6	115.5 / 106	0.249	0.0051±0.0139
	7	104.5 / 106	0.522	-0.0038±0.0116
	8	133.2 / 106	0.038	0.0061±0.0105
	all	1051.2 / 962	0.023	-0.0021±0.0044
PDF Eq. 5.21	all	1075.2 / 971	0.011	-0.0034±0.0042

Table 5.7: *Summary of the fits of the nine modules data searching for an annual modulation with fixed period and phase in [1,6] keV energy region from three years exposure of ANAIS–112 for different background modelling.*

From 2 to 6 keV				
Fit model	detector	χ^2 / NDF mod hyp	p-value mod hyp	S_m (c/keV/kg/d)
Exponential Eq. 5.18	0	108.7 / 107	0.436	0.0037±0.0142
	1	132.9 / 107	0.045	0.0010±0.0143
	2	114.7 / 107	0.288	0.0073±0.0103
	3	108.7 / 107	0.436	-0.0002±0.0117
	4	99.0 / 107	0.697	-0.0044±0.0116
	5	139.7 / 107	0.018	-0.0233±0.0115
	6	100.2 / 107	0.667	0.0074±0.0110
	7	83.7 / 107	0.954	-0.0096±0.0104
	8	112.2 / 107	0.346	0.0096±0.0097
	all	999.8 / 971	0.254	-0.0006±0.0038
Polynomial-2 Eq. 5.19	0	108.6 / 107	0.438	0.0035±0.0142
	1	132.9 / 107	0.045	0.0011±0.0143
	2	114.7 / 107	0.288	0.0074±0.0104
	3	109.3 / 107	0.421	-0.0006±0.0118
	4	99.5 / 107	0.685	-0.0056±0.0116
	5	139.5 / 107	0.019	-0.0236±0.0115
	6	106.9 / 107	0.485	0.0036±0.0111
	7	84.7 / 107	0.945	-0.0120±0.0104
	8	118.7 / 107	0.206	0.0070±0.0097
	all	1014.8 / 971	0.160	-0.0020±0.0038
Piecewise Eq. 5.20	0	108.6 / 106	0.413	0.0035±0.0145
	1	132.4 / 106	0.042	0.0034±0.0146
	2	114.2 / 106	0.276	0.0061±0.0106
	3	107.8 / 106	0.434	0.0036±0.0120
	4	96.5 / 106	0.736	0.0004±0.0119
	5	133.2 / 106	0.038	-0.0291±0.0117
	6	100.4 / 106	0.636	0.0130±0.0113
	7	84.2 / 106	0.942	-0.0065±0.0106
	8	110.5 / 106	0.363	0.0166±0.0099
	all	987.6 / 962	0.276	0.0017±0.0039
PDF Eq. 5.21	all	1018.2 / 971	0.143	0.0003±0.0037

Table 5.8: *Summary of the fits of the nine modules data searching for an annual modulation with fixed period and phase in [2,6] keV energy region from three years exposure of ANAIS–112 for different background modelling.*

Chapter 6

Machine Learning for optimizing ANAIS–112 results

The background models of ANAIS–112 detectors provide a good overall description of measured data at all energy ranges above 2 keV and at different analysis conditions (coincidence or anticoincidence); nevertheless, below this energy, there is some discrepancy (see Section 2.10). In particular, the model does not explain 54% of the measured rate in the region from 1 to 2 keV, but the deviation is of only 10.7% from 2 to 6 keV (see Table 2.12). The unexplained events below 2 keV could be attributed to non-bulk scintillation events which have not been rejected by our filtering protocols, or to background sources not included in the described model. In order to better understand (and, in case, reject) these types of events, a machine learning technique based on a multivariate analysis called Boosted Decision Tree (BDT) [249–253] has been implemented.

In this chapter, we describe a new PMT-related noise rejection algorithm based on the BDT technique developed to improve ANAIS–112 results in the very low energy region. Firstly, the different triggered pulses observed in the low energy region for the ANAIS–112 experiment are presented in Section 6.1. Subsequently, in Section 6.2, the BDT training procedure is described in detail. In particular, the two-steps training, the preselection cuts for training populations, the input parameters and the validation of the BDT output. Finally, the event selection based on BDT response and the comparison with the background model are presented (Sections 6.2.3 and 6.2.5, respectively), as well as the sensitivity improvement to the annual modulation signal observed by DAMA/LIBRA (Section 6.2.6) and the reanalysis of the three years of ANAIS–112 data searching for annual modulation using the BDT method (Section 6.2.7).

6.1 Event types

The events triggered by the ANAIS–112 data acquisition system can be classified in three main categories, depending on the shape of the total pulse, calculated as the addition of the individual pulses of the two photomultipliers, as shown in Figure 6.1. Waveforms from the detector are recorded when both PMTs on a crystal register signals whose amplitude is above the single photoelectron within 200 ns (see Section 2.4). In Figure 6.1a, we can observe the average waveform from the ANAIS–112 PMT tubes for calibration events below 10 keV that passed the trigger condition. They are clearly signal-like scintillating events in NaI(Tl) crystal, with fast rise and then slow fall-off with a decay time of about 230 ns. These types of events are easily distinguished from Cherenkov emission of radioactive contamination in the PMT (see Figure 6.1b) because the latter are dominated by the temporal behaviour of the PMT response (tens of ns range). So, we can reject fast PMT noise by using different variables related to charge and time (see Section 3.1.2). However, below 2 keV, there are some non-bulk scintillation events with temporal parameters similar to that of bulk NaI(Tl) ones due to the low number of photoelectrons, and difficult to discriminate by the pulse shape cut. An example of this unusual type of events can be seen in Figure 6.1c, where the average waveform has been computed for PMT noise events with P_1>0.4 from the Blank module (see Equation 3.1). As described in Section 2.11, this module is similar to the ANAIS–112 modules having two PMTs (identical to those used in ANAIS–112 modules) coupled to quartz optical windows at both sides, but without NaI(Tl) crystal, so all triggered pulses have non-bulk origin.

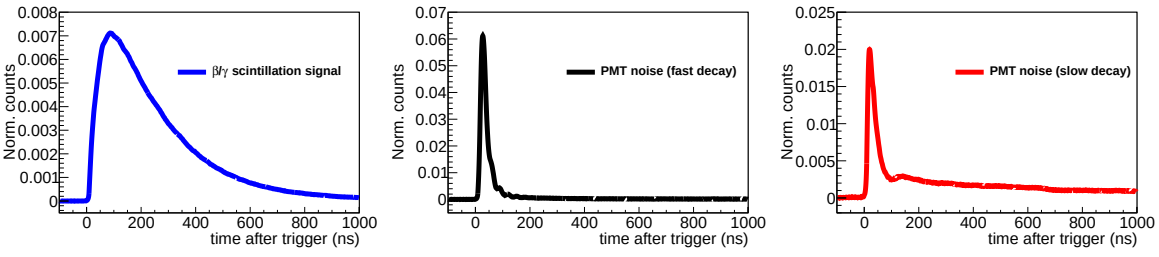

(a) (b) (c)

Figure 6.1: *Average waveforms from the ANAIS–112 PMT tubes for events below 10 keV that passed the trigger condition. The left panel shows signal like scintillating events in NaI(Tl) crystal (a), with fast rise and then slow fall-off with a decay time of about 230 ns. The middle panel shows fast PMT noise events with decay time of tens of ns (b). Finally, the right panel shows PMT noise events from the Blank module with decay time compatible with that of NaI(Tl) scintillator (c).*

Figure 6.2 shows the average waveform for the events from the Blank module with P_1>0.4 (solid and wide red line), together with those background events below 2 keV that, having P_1>0.4, present a strong asymmetry in the light sharing among both PMTs (solid and narrow black line). We can see that both waveforms have the same temporal behaviour, strongly supporting the idea of the non-bulk origin of most of the events in the [1,2] keV region. Therefore, the events from the Blank module will be very useful to define parameters related to the shape of the pulse in order to reject non-bulk events.

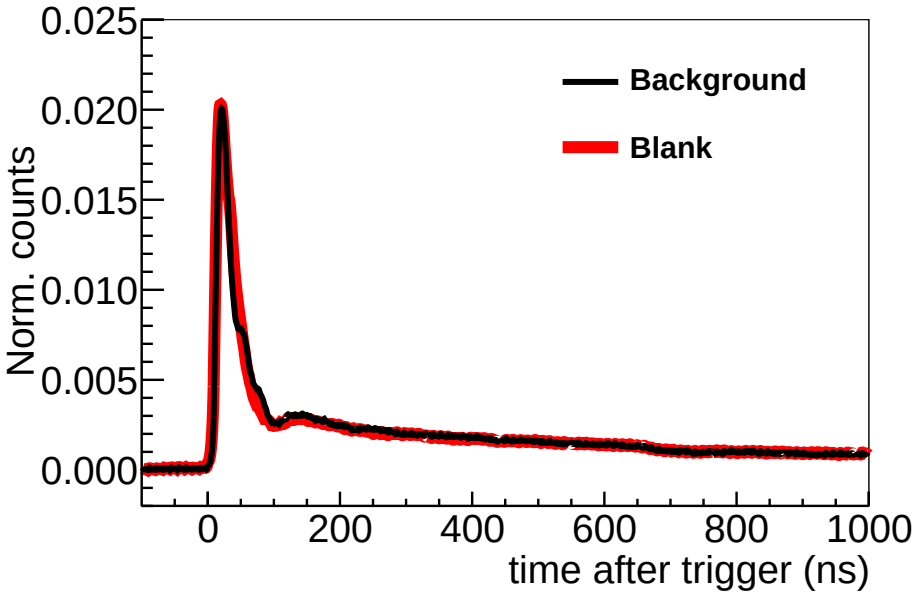

Figure 6.2: *Average waveforms adding the two PMT signals for events from the Blank module with P_1>0.4 (solid and wide red line) and from asymmetric background events below 2 keV with P_1>0.4 (solid and narrow black line). Both of them have very similar temporal behaviour.*

As described in Section 3.1.2, the parameters defined on the total pulse shape in the ANAIS–112 filtering protocols are P_1 and $\log(\mu_p)$ (see Equation 3.2). Both parameters are combined into a single pulse shape analysis variable called PSV (see Equation 3.3). In Figure 6.3, the distribution of coincidence events below 2 keV in the P_1–$\log(\mu_p)$ plane is shown in magenta, and the same for the events from the Blank module is shown in black. We observe that above P_1>0.4, both populations overlap, so the PSV cut is insufficient, but, on the other hand, the asymmetry cut based on the number of peaks is so restrictive that the efficiency at 1 keV is very limited. In order to improve the rejection of non-bulk events below 2 keV, a multivariable analysis based on a BDT has been developed.

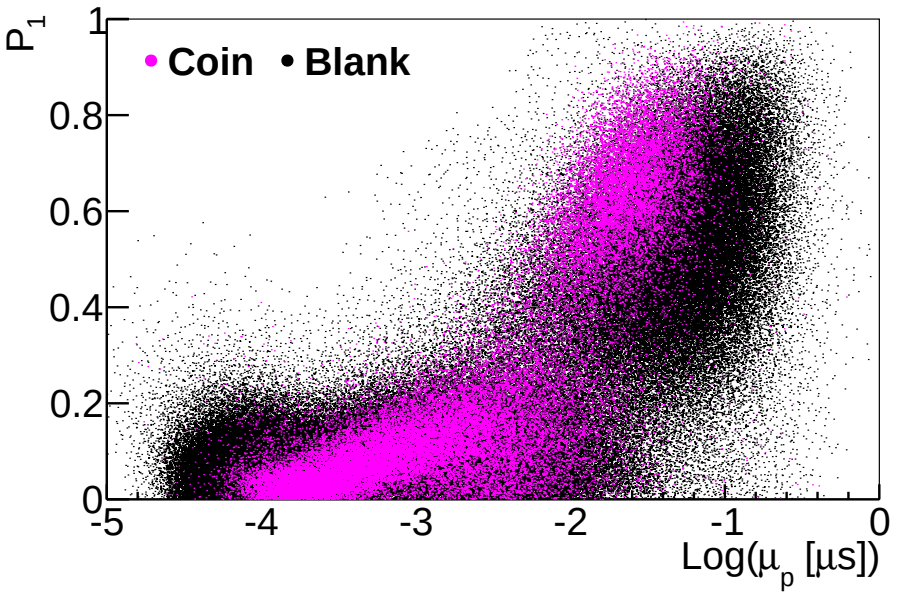

Figure 6.3: *Distribution of coincidence events below 2 keV (magenta) and events from the Blank module (black) in the* P_1–$\log(\mu_p)$ *plane.*

6.2 Multivariate analysis: Boosted Decision Tree

In this work, a multivariate analysis using a BDT technique has been performed for more efficient noise rejection. Taking into account the correlations between individual input parameters, the BDT method allows us to combine several weak discriminating variables into a single powerful discriminator, which gives better separation than one variable alone. Basically, decision trees consist in extending a simple cut-based analysis into a multivariate technique in which each event is analysed by means of yes/no decisions taken on a single variable at a time that are repeated until a stopping criterion is fulfilled. Most events do not have all characteristics of either signal or background, because otherwise the signal could be extracted with an analysis with a few criteria. Therefore, decision tree does not reject right away events that fail a criterion, but checks whether other criteria may help to classify these events properly [253].

Mathematically, decision trees have a binary structure with two classes: signal and background. An example is shown in Figure 6.4. A decision tree is trained in a successive manner starting from an initial node: the root node. Consider this root node constituted by a sample of signal (s_i) and background (b_j) events, each with weights w_i^s and w_j^b, respectively, described by a set $\vec{x}_i$ of variables. Then, starting from this root node, the BDT algorithm proceeds as follows [253]:

1. If the node satisfies any stopping criterion, declare it as terminal (that is, a leaf) and exit the algorithm.
2. Sort all events according to the value of each variable in $\vec{x}_i$ in increasing order.
3. For each variable, find the splitting value that gives the best separation between two children: one with mostly signal events and the other with mostly background events. If the separation cannot be improved by any splitting, turn the node into a leaf and exit the algorithm.
4. Select the variable and splitting value leading to the best separation and split the node in two new nodes (branches), one containing events that fail the criterion and one with events that satisfy it.
5. Apply recursively from step 1 on each node.

At each node, all variables can be considered, even if they have been used in a previous iteration: this allows to find intervals of interest in a particular variable, instead of limiting oneself to using each variable only once.

The output from a single decision tree for an event corresponds to the value associated to the terminal leaf. There are several conventions used for the value attached to a leaf. We use a binary answer, signal or background depending on whether the purity is above or below a specified critical value. The purity is defined as $p = \frac{s}{s+b}$, where s (b) is the sum of weigths of signal (background) events that ended up in this leaf during training. If $p > 0.5$, $+1$ is attached to the leaf and is classified as signal, otherwise the leaf is set to -1 and labeled as background. Conventionally, the sums of weights of signal and background events are chosen equal to one before starting the training, giving the root node a purity of 0.5, an equal mix of signal and background. During training, it is crucial to evaluate what is the best separation between signal and background events, that is, how a node is split into two. The goodness of this separation is measured through the so-called impurity function, which is maximum when there is no separation (an equal mix of signal and background) and minimum when the separation is perfect (nodes with either only signal or only background events). In our particular case, the chosen impurity function is the Gini Index, defined by $p \cdot (1 - p)$ [254]. Since the splitting criterion is always a cut on a single variable, the training procedure chooses the variable and cut value that maximizes the increase in the impurity function between the parent node and the sum of the two daughter nodes, weighted by their relative fraction of events. In principle, the splitting could continue until each leaf node contains only signal or only background events, which could suggest that perfect discrimination

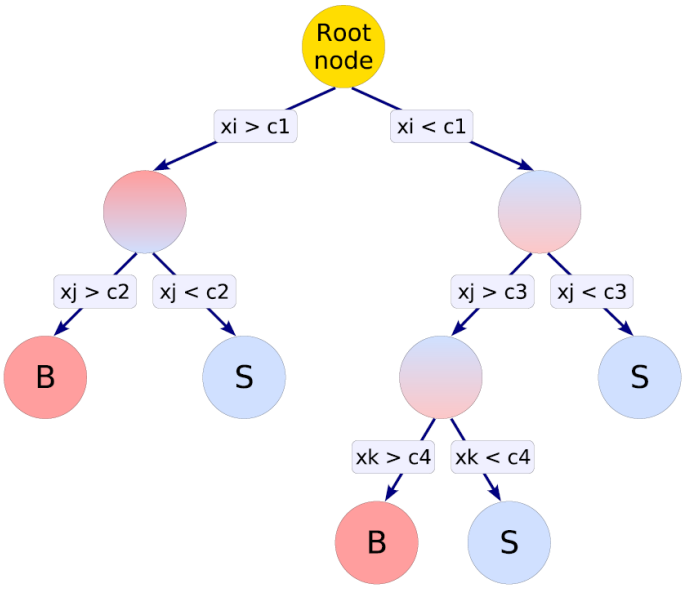

Figure 6.4: *Schematic view of a decision tree. Starting from the root node, a sequence of binary splits using the discriminating variables $\vec{x}_i$ is applied to the data. Each split uses the variable that at this node gives the best separation between signal and background when being cut on (cut c_p). The same variable may thus be used at several nodes, while others might not be used at all. The leaf nodes at the bottom end of the tree are labeled "S" for signal and "B" for background depending on the majority of events that end up in the respective nodes. From Ref. [254].*

is achievable. However, such a decision tree would be strongly overtrained. One way to avoid overtraining is to establish a certain stopping criterion at some point, declaring such nodes as terminal leaves. For example, this can be done by limiting the tree depth during the tree building proccess (training).

The boosting of a decision tree [250] extends the aforementioned concept from one tree to several trees which form a forest. The trees are derived from the same training ensemble by reweighting events, and are finally combined into a single classifier which is given by a weighted average of the individual decision trees. Boosting stabilizes the response of the decision trees with respect to fluctuations in the training sample and is able to considerably enhance the performance with regard to a single tree. Thanks to the averaging, the BDT output becomes quasi-continuous, mitigating one of the limitations of single decision trees. In particular, we use AdaBoost [250] to implement the boosting algorithm. AdaBoost stands for adaptive boosting, referring to the fact that the learning procedure adjusts itself to the training data in order to classify it better. Events that were misclassified during the training of a decision tree

are given a higher event weight in the training of the following tree. Starting with the original event weights (all equal to $1/N$, being N the number of training events) when training the first decision tree, the subsequent tree is trained using a modified event sample where the weights of previously misclassified events are multiplied by a common boost weight α_1: $w_i \rightarrow \alpha_1 \cdot w_i$. The boost weight is derived from the fraction of misclassified events f_1 of the previous tree, $\alpha_1 = \frac{1-f_1}{f_1} \geq 1$. The weights of the entire event sample are then renormalised such that the sum of weights remains constant. After training the second tree, the sample will again be reweighted and another tree be grown. This process will be repeated until a certain number of trees have been grown. If we denote the result of an individual classifier as $T(\vec{x}_i)$, with encoded for signal and background as $T(\vec{x}_i) = +1$ and -1, respectively, adaptive boosting yields a response defined by:

$$BDT(\vec{x}_i) = \frac{1}{nTrees} \sum_{j=1}^{nTrees} \ln(\alpha_j) \cdot T_j(\vec{x}_i), \tag{6.1}$$

where $nTrees$ is the number of trees in the forest. Small (large) values for $BDT(\vec{x}_i)$ indicate a background-like (signal-like) event. This boosting algorithm performs best on small individual decision trees with a depth as small as 2 or 3 layers. The performance is often further enhanced by forcing a slow training and allowing a larger number of boost steps instead. The learning rate of the AdaBoost algorithm is controlled by a parameter β giving as an exponent to the boost weight: $\alpha \rightarrow \alpha^\beta$.

For the implementation of BDT in ANAIS–112, we use the Toolkit for Multivariate Data Analysis (TMVA) package [254] integrated in ROOT. The default values for the maximum depth of the decision tree ($maxDepth$) and the learning rate (β) have been selected, whereas a scan in the number of trees ($nTrees$) has been performed to determine the value that minimizes the background between 1 and 2 keV for the same training population. The choice of the configurable parameters can be found in Table 6.1.

Parameter	Value
maxDepth	3
β	0.5
nTrees	850

Table 6.1: *Configurable parameters used in the implementation of BDT in ANAIS–112.*

We follow a two-steps training strategy to discriminate the real scintillation events (signal-like events) from the low energy PMT-noise events (background-like):

- **Training phase 1: Pulse shape**. In this first phase, we try to extract the scintillation events considering input parameters only depending on the shape of the total pulse from the two PMTs. As training populations, low energy ^{109}Cd calibration events are used as a pure scintillation signal sample, whereas events from the Blank module are used as noise sample (see Section 6.2.1).

- **Training phase 2: Asymmetry**. In this second phase, we will use as input parameters those that describe the asymmetry in the light sharing among both PMTs for low energy events to separate the signal from the noise. Again, ^{109}Cd calibration events will be used as signal sample; however, since one of the input variables utilised cannot be defined for the Blank module events (as will be explained later), the physics-run data are used as noise sample for training BDT. As discussed above, they are dominated by PMT noise-like events in the very low energy region (see Section 6.2.2).

6.2.1 Training phase 1

We train two independent boosted decision trees to separate signal events from noise events. In the first phase of BDT training, parameters exclusively depending on the shape of the pulse obtained adding the two PMT signals are considered as input variables (see Section 6.2.1.2). Low energy ^{109}Cd calibration events are used to model the scintillation sample, while events from the Blank module are used as noise sample. The most challenging aspect of a BDT training is to obtain pure event samples that are used to model the scintillation and PMT-noise events. Therefore, in the following section, a series of preselection cuts on the training populations are defined to extract representative samples of signal and noise.

6.2.1.1 Preselection cuts

There are different processes by which PMTs generate low energy signals like noises due to the low hardware trigger threshold. Some of the mechanism can be: ultraviolet and/or visible photons directly produced inside the PMTs by U, Th or K radioactive decays; a flash caused by the charge accumulation somewhere in the PMT due to the high voltage supply; accidental coincidences between two PMTs originated by PMT dark currents and able to pass the trigger condition; or an afterpulse from large pulses produced by ionized residual gas inside the PMT. These PMT-generated noise signals are not only present in the physics-run data, but are

also found, although to a lower rate, in the ^{109}Cd calibration runs. Consequently, dedicated preselection criteria are required to obtain a sample of real scintillation-like events.

Firstly, we focus on ^{109}Cd calibration events with energies between 1 and 2 keV triggered within the 200 ns coincidence window. The distribution of calibration events in P_1 parameter as a function of energy (see Figure 3.4) shows a remarkably spread below 2 keV. The events with low P_1 value are due to fast pulses (see Figure 3.3b), while those with P_1 close to 1, are events with a large amount of light concentrated in a few ns, but in which the DAQ system has triggered before this flash (see Figure 6.5a). For this reason, we select the calibration events with P_1>0.35 and P_1<0.90 as possible scintillation candidates.

In the same way that occurs with events with P_1>0.90, there are also events in which the entire signal from one of the PMTs is concentrated in a few ns, but added to the signal from the other PMT, they have a global P_1 within the aforementioned range of acceptance (see Figure 6.5b). Because of this, we decide to define a new P_1 variable on each PMT via, P_{10} (P_{11}) for PMT0 (PMT1), which allows us to discriminate these events. Figure 6.6 shows the distribution of these variables for the calibration events (upper panels) and background events (lower panels) between 1 and 2 keV (panels to the left) and from 2 to 3 keV (panels to the right). We observe that calibration events are clustered around $P_{10} = P_{11} = 0.60$, but the dispersion in [1,2] keV is much greater than in [2,3] keV. To eliminate this type of events, we impose $P_{10}, P_{11} > 0.15$ for scintillation-like events selection.

The P_1, P_{10} and P_{11} parameters are unsatisfactory to obtain a free-noise sample of scintillation events, since possible phosphorescences with very large mean time are well-distributed in the former parameters (see Figure 6.5c). Therefore, following Equation 3.2, we define a new μ_p variable on each PMT, μ_{p0} (μ_{p1}) for PMT0 (PMT1), to rule out this type of event. Figure 6.7 shows the scatter plot of these variables for the calibration events (upper panels) and background events (lower panels) between 1 and 2 keV (panels to the left) and from 2 to 3 keV (panels to the right). We can see that calibration events are clustered around $\mu_{p0} = \mu_{p1} = 180$ ns, being the spread greater between 1 and 2 keV than from 2 to 3 keV. So as to select the events that model the scintillation signal, we choose $\mu_{p0}, \mu_{p1} < 400$ ns.

Thus, our scintillation events sample is constituted by the ^{109}Cd calibration events between 1 and 2 keV corresponding to the the first three years of measurement that,

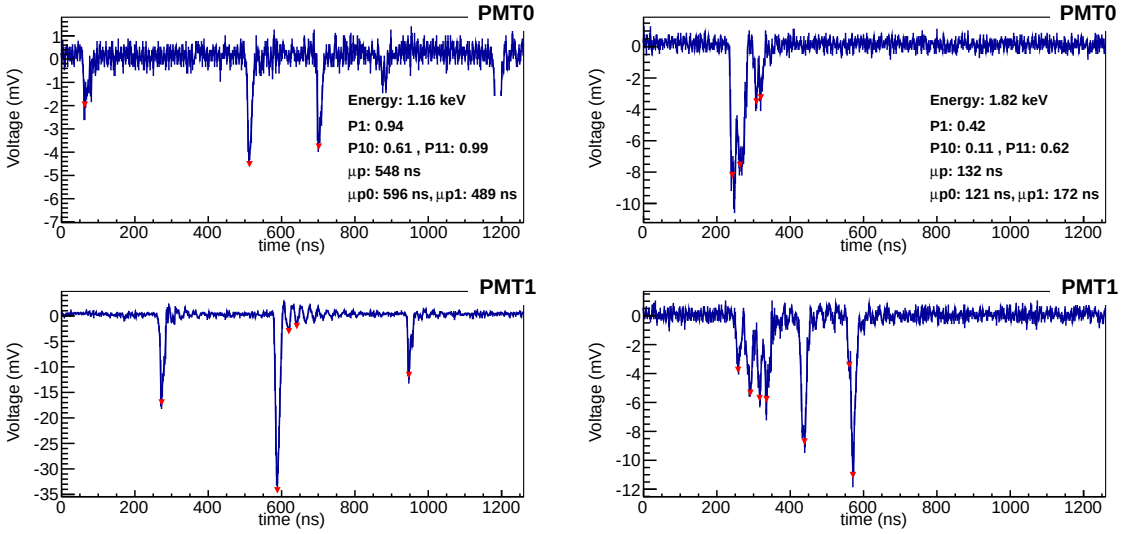

(a) $P_1 > 0.90$.

(b) $P_{10} < 0.15$.

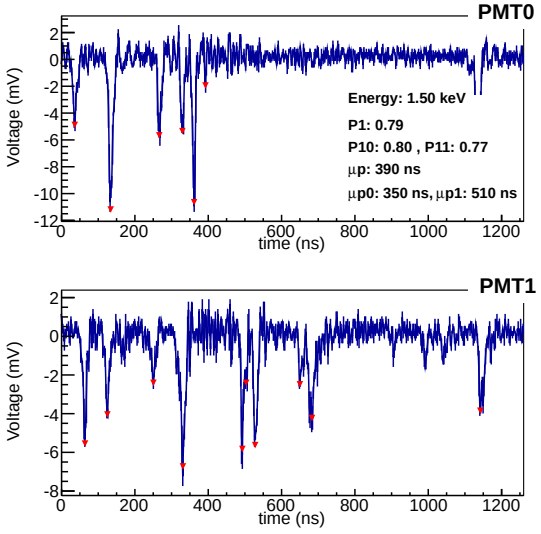

(c) $\mu_{p1} > 400$ ns.

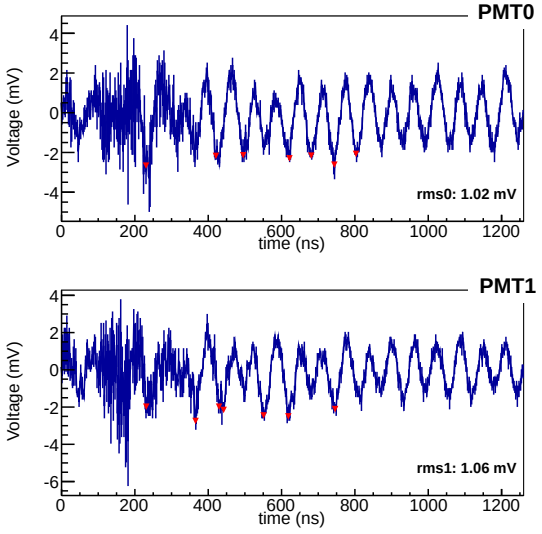

(d) $rms_0, rms_1 > 1$ mV.

Figure 6.5: *Examples of PMT-noise low energy digitized pulses. The two traces at each panel correspond to the two PMT signals, while the legend display the energy of the event and global and single trace P_1 and μ_p parameters (a-c) or the RMS of the baseline (d). Red triangles: phe identified by the peak-searching algorithm. Panel (a): event from ^{109}Cd calibration run with $P_1 > 0.90$. Panel (b): event from ^{109}Cd calibration run with $P_{10} < 0.15$, but a suitable P_1 value. Panel (c): event from ^{109}Cd calibration run with $\mu_{p1} > 400$ ns, but well-distributed in P_1, P_{10} and P_{11}. Panel (d): electrical noise from Blank module data with $rms_0, rms_1 > 0.60$ mV.*

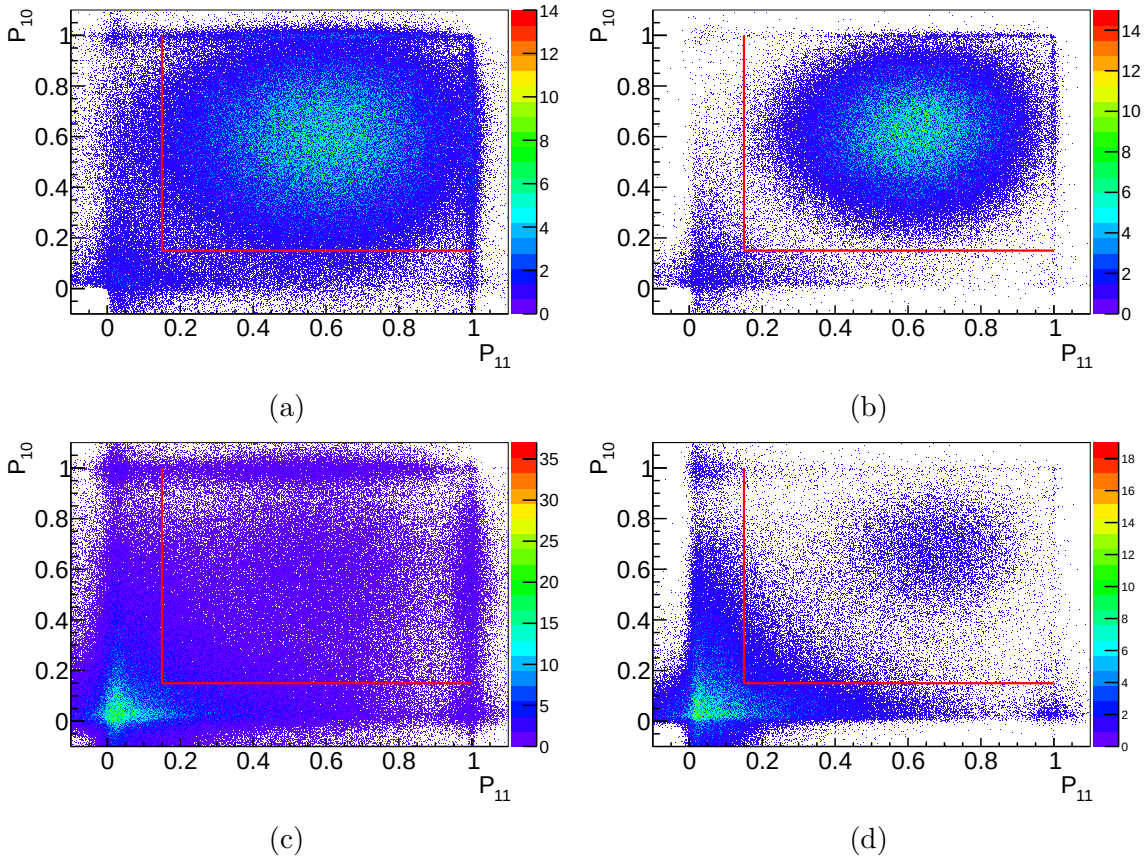

Figure 6.6: *Scatter plot (P_{10} vs P_{11}) showing events from ^{109}Cd calibration runs between 1 and 2 keV (a) and from 2 to 3 keV (b). Panels (c) and (d): the same, but for background events of the ∼10% unblinded data. Red lines show the established preselection cut:* $P_{10}, P_{11} > 0.15$.

in the 200 ns coincidence window, satisfy: $0.35 < P_1 < 0.90$, $P_{10} > 0.15$, $P_{11} > 0.15$, $\mu_{p0} < 400$ ns and $\mu_{p1} < 400$ ns.

To model a set of PMT-noise events, we use data from the Blank module accumulated from the 12^{th} of February 2019 to the 13^{th} of August 2020. Events equivalent to energies between 1 and 2 keV are those that satisfy $10 < nphe_0 + nphe_1 < 28$ (see Section 2.11). Some of these events correspond to electrical noise (see Figure 6.5d), which we can remove based on the RMS of the baseline. Figure 6.8 shows the RMS for each PMT signal of the Blank module, and most of the events are observed to be clustered around $rms_0 = rms_1 = 0.30$ mV, but there is a population of events with RMS of the order of one or more millivolts. By impossing $rms_0, rms_1 < 0.60$ mV, we select a population of PMT-noise events free of electical noise.

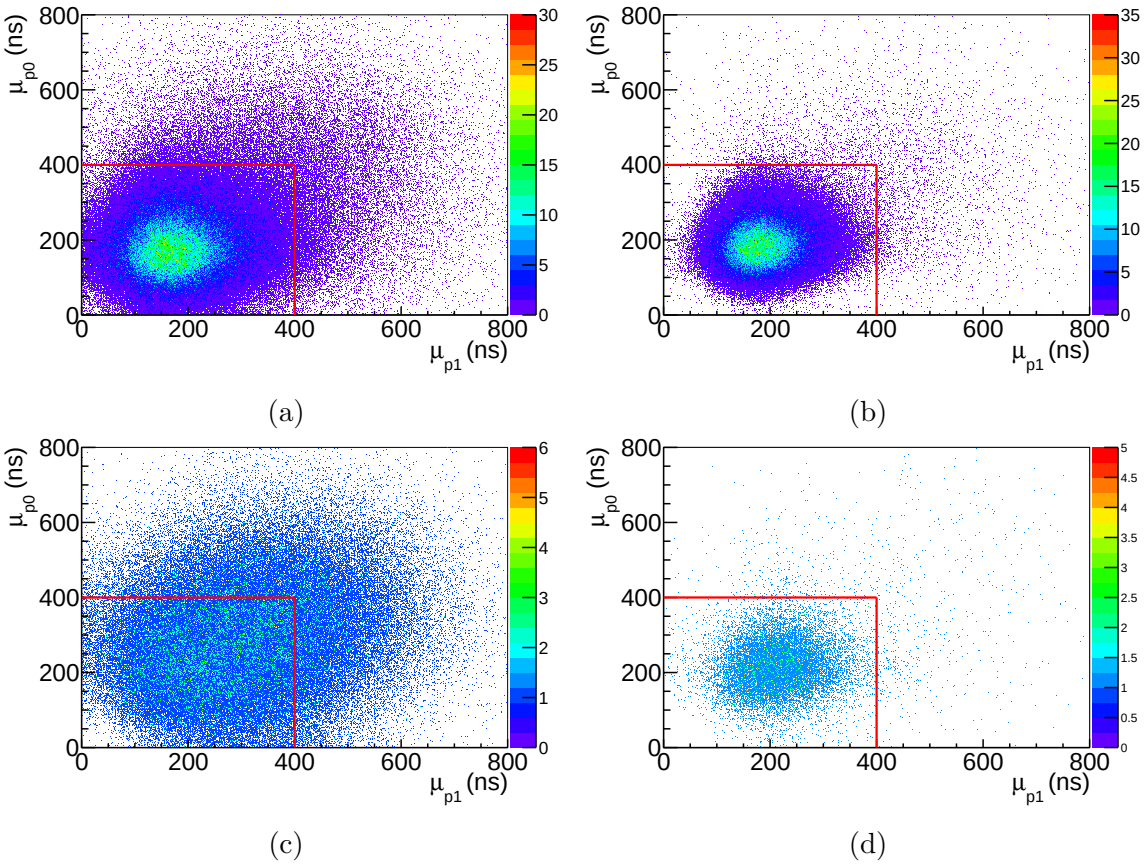

Figure 6.7: *Scatter plot (μ_{p0} vs μ_{p1}) showing events from ^{109}Cd calibration runs in [1,2] keV (a) and [2,3] keV (b) energy regions. Panels (c) and (d): the same, but for background events of the ∼10% unblinded data. Red lines show the chosen preselection cut: $\mu_{p0}, \mu_{p1} < 400$ ns.*

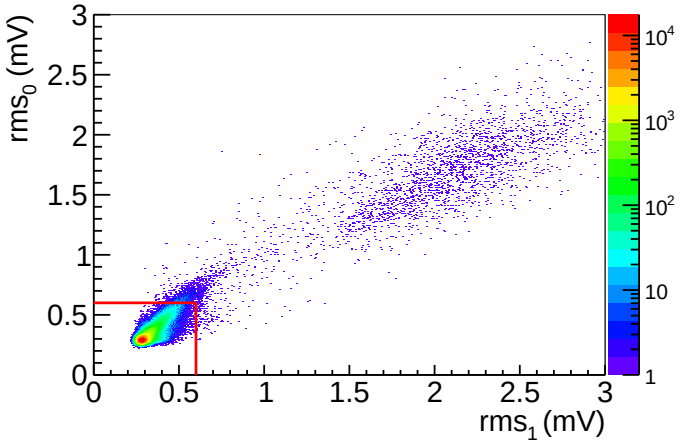

Figure 6.8: *Distribution of the RMS of the baseline for each PMT signal from Blank-runs data. Most of the events are clustered around $rms_0 = rms_1 = 0.30$ mV, but there are some events with rms greater than 1 mV. Red lines show the preselection cut impossed to remove this electrical noise: $rms_0, rms_1 < 0.60$ mV.*

6.2.1.2 Input variables

The training populations for scintillation and noise events have been determined, now we must define the input variables for the BDT. For a decision tree, all variables are treated equal, regardless of the order in which they are presented. The order of events in the training samples is also irrelevant. If variables are not discriminating, they will simply be ignored and will not add any noise to the decision tree. Moreover, variables do not need to be regularise with decision trees unlike other multivariate techniques. For decision trees, the CPU consumption scales as $nN \log N$ with n variables and N training events [253].

The input variables used in BDT training are listed as below:

1. Slow charge (P_1): a fractional charge in [100 ns, 600 ns] window to total charge in [0 ns, 600 ns] window for the total pulse,

$$P_1 = \frac{\sum_{t=100\text{ ns}}^{t=600\text{ ns}}(S_0(t) + S_1(t))}{\sum_{t=0\text{ ns}}^{t=600\text{ ns}}(S_0(t) + S_1(t))}, \tag{6.2}$$

   where $S_0(t)$ ($S_1(t)$) is the pulse amplitude at time t after the trigger position for waveform S_0 (S_1) of PMT0 (PMT1).

2. Fast charge (P_2): a fractional charge in [0 ns, 50 ns] window to total charge in [0 ns, 600 ns] window for the total pulse, i.e.,

$$P_2 = \frac{\sum_{t=0\text{ ns}}^{t=50\text{ ns}}(S_0(t) + S_1(t))}{\sum_{t=0\text{ ns}}^{t=600\text{ ns}}(S_0(t) + S_1(t))}. \tag{6.3}$$

3. Mean time (μ_p): amplitude-weighted mean time of the individual photoelectrons arrival times in the digitized window for summed pulse

$$\mu_p = \frac{\sum_i A_i t_i}{\sum_i A_i}, \tag{6.4}$$

   being A_i and t_i the amplitude and time of the phe identified in the pulse trace, respectively.

4. Charge accumulated pulse (CAP): integral of the cumulative distribution of the total pulse up to a certain time after the trigger position.

$$CAP_x = \frac{\sum_{t=0\text{ ns}}^{t=x\text{ ns}}(S_0(t) + S_1(t))}{\sum_{t=0\text{ ns}}^{t=t_{max}}(S_0(t) + S_1(t))}, \tag{6.5}$$

where x is the upper limit of summation and t_{max} the end of the pulse. In particular, we use $x = 50, 100, 200, 300, 400, 500, 600, 700$ and 800 ns. Figure 6.9 shows the cumulative distribution function for pulses from Figure 6.1, that is, scintillation events (blue), fast PMT-noise events (black) and slow decay PMT-noise events (red). We can observe, for instance, that 90% of the total charge is reached after 150 ns for fast PMT-noise events, 500 ns for scintillation events and 750 ns for slow decay PMT-noise events.

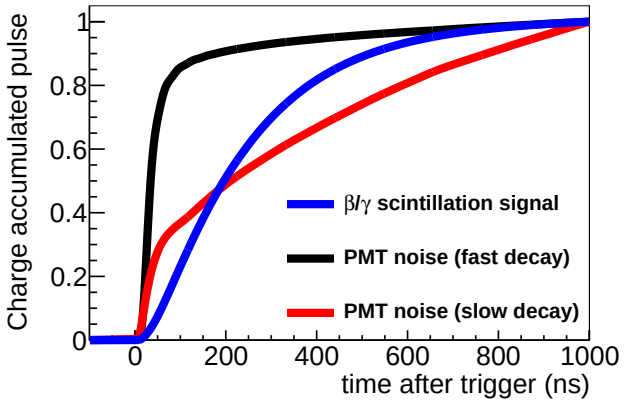

Figure 6.9: *Cumulative distribution of the total pulse for different events below 10 keV that passed the trigger condition. Blue line shows scintillation-like events in NaI(Tl) crystal, black line shows fast PMT-noise events and red line shows PMT-noise events from the Blank module with decay time compatible with that of NaI(Tl) scintillator.*

6.2.1.3 Training and BDT output

We have carried out a 850-trees training to develop a BDT score which can discriminate scintillation signal from PMT-noise more efficiently. The scintillation-like signal model is obtained from the preselected ^{109}Cd calibration sample, and Blank module data containing large PMT-induced noise events are used as background sample (see Section 6.2.1.1). The noise rejection variables defined in the previous section are used as the training variables. All crystals are trained at the same time on a single BDT. Table 6.2 lists the separation signal/background of the input variables before training (2^{nd} column) and the variable ranking after training (3^{rd} column). The ranking of the BDT input variables is derived by counting how often the variables are used to split decision tree nodes, and by weighting each split occurrence by the separation gain-squared it has achieved and by the number of events in the node [254]. The top variable in the table is the best ranked. In particular, the variables used in the ANAIS–112 standard analysis (P_1 and μ_p) have a high discriminating power, although the new defined variable CAP_{50} is even better than μ_p.

Variable	Variable separation before training (%)	Variable ranking after training (%)
P_1	68.95	17.40
CAP_{50}	66.96	13.26
μ_p	64.87	9.06
CAP_{200}	47.05	8.65
CAP_{400}	12.88	7.96
CAP_{800}	6.78	7.71
CAP_{300}	27.03	7.63
CAP_{100}	63.78	7.45
CAP_{600}	6.15	6.80
CAP_{500}	7.32	6.75
CAP_{700}	6.50	5.92
P_2	0.89	1.41

Table 6.2: *Signal/background separation of input variables before training and variable ranking after training. The top variable is the best ranked.*

The result of the training generates the new BDT parameter, capable of separating a large amount of noise events from scintillation events. Figure 6.10a shows the BDT distribution for both ^{109}Cd calibration events (in red) and background events of the ∼10% unblinded data (in black) in the [1,2] keV energy region. We can observe an accumulation of events around BDT=−0.45, which mostly corresponds to fast PMT-noise events. The excess of events around BDT=−0.35 is due to very large mean time, and the peak observed around BDT=−0.05 is associated with asymmetric events. The BDT score as a function of energy of the ∼10% unblinded background is shown in Figure 6.10b, and displays a clear separation between scintillation and fast PMT-noise events for energies greater than 2 keV. The events placed in the lower band are PMT-induced noise events and those with higher BDT value (above 0) are real scintillation events.

6.2.2 Training phase 2

In the first training phase, we have performed a BDT parameter to separate scintillation events from PMT-noise events using variables exclusively depending on the shape of the summed pulse. After that, we train a second boosted decision tree in order to improve the rejection of the asymmetric events observed in the background data below 2 keV (see Figure 6.2). In this second phase, we take into account

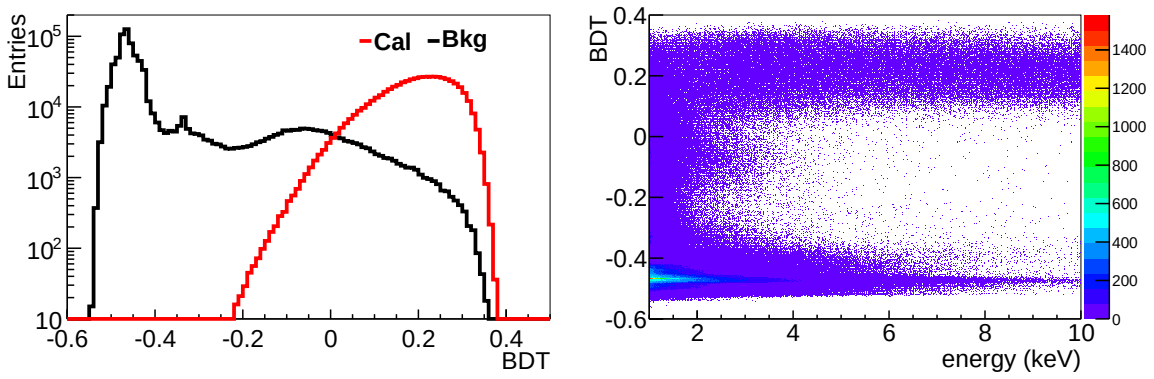

(a) (b)

Figure 6.10: *Panel (a): BDT distribution for ^{109}Cd calibration events (red line) and background events of the ∼10% unblinded data (black line) in the [1,2] keV energy region. The three excesses of events in background data around BDT=−0.45, −0.35 and −0.05 are related to fast PMT-noise events, large mean time events and asymmetric events, respectively. Panel (b): BDT response as a function of energy of the ∼10% unblinded dark matter search data. The events located in the lower band are PMT-generated noise events and real scintillation events are in the higher band.*

parameters related to the asymmetry in the light sharing among both PMTs as input variables (see Section 6.2.2.2). Low energy ^{109}Cd calibration events are used again to model the scintillation sample; nevertheless, since one of the input variables utilised cannot be defined for the Blank module events, the physics-run data (totally dominated by PMT noise-like events below 2 keV) are used as noise sample. In the following section, we define the preselection cuts on the training populations to obtain representative samples of signal and noise for this training phase.

6.2.2.1 Preselection cuts

To extract real scintillation sample for this training phase, we select ^{109}Cd calibration events between 1 and 2 keV which lie above BDT>0.05 (see red line in Figure 6.10a). On the other hand, 12.9 days corresponding to the 3^{rd} dark matter run (from the 17^{th} of August 2017 to the 31^{st} of August 2017), which are dominantly PMT noise-like events, are used as the noise sample for training the second BDT, hereinafter denoted by BDT2. This background run has been chosen because it does not contain any of the days belonging to the ∼10% unblinded data from the first year. The latter will be used as the test population for the algorithm. It is worth noting that the sample for the noise amounting 1% of the full analysis data and therefore little bias is expected.

6.2.2.2 Input variables

Once the training populations for scintillation-like and noise-like events have been designed, we define the input parameters for this second training phase. The input variables used in the BDT2 training are:

1. Asymmetry in area (Asyarea): quotient between the charge partition among both PMTs and the total charge corrected by the corresponding mean value of asymmetry in area for each detector. That is:

$$Asyarea = \frac{area_0 - area_1}{area_0 + area_1} - \langle A \rangle \,, \tag{6.6}$$

   where $area_0$ ($area_1$) is the total charge for PMT0 (PMT1) signal, and $\langle A \rangle$ is the mean value of the ratio between the area difference between signals versus total area, estimated from ^{109}Cd calibration events for each detector, in 1 keV energy bins, and for each data run. It is worth emphasizing that $\langle A \rangle$ is not distributed around zero because of the different gain in the PMTs. Figure 6.11 shows the $\langle A \rangle$ distribution for detector D1 from the first ^{109}Cd calibration run in 1 keV bins. Data have been fitted to Gaussian lineshapes and fit results are shown in the fit panels. Since the Blank module cannot be calibrated in energy (it does not house a NaI(Tl) crystal), the $\langle A \rangle$ parameter cannot be estimated and, consequently, the *Asyarea* variable cannot be defined.

2. Number of peaks identified by peak-finding algorithm in PMT0 trace (n_0).

3. Number of peaks detected by peak-searching algorithm in PMT1 signal (n_1).

Note that decision trees can deal easily with both continuous and discrete variables, simultaneously [253].

6.2.2.3 Training and BDT2 output

We have grown 850 trees to perform a BDT2 score which is able to reject PMT-noise events from scintillation signal more efficiently than the filtering protocols established for ANAIS–112. The real scintillation sample is extracted from the pre-cut ^{109}Cd calibration data and low energy background events, which are dominated by PMT-generated noise events, are used as noise sample (see Section 6.2.2.1). The noise rejection parameters defined in Section 6.2.2.2 are used as the training variables for the second training phase. All crystals are trained at the same time on a single BDT2. Table 6.3 lists the separation signal/background of input variables before training (2^{nd} column) and the variable ranking after training (3^{rd} column). The top variable is the best ranked.

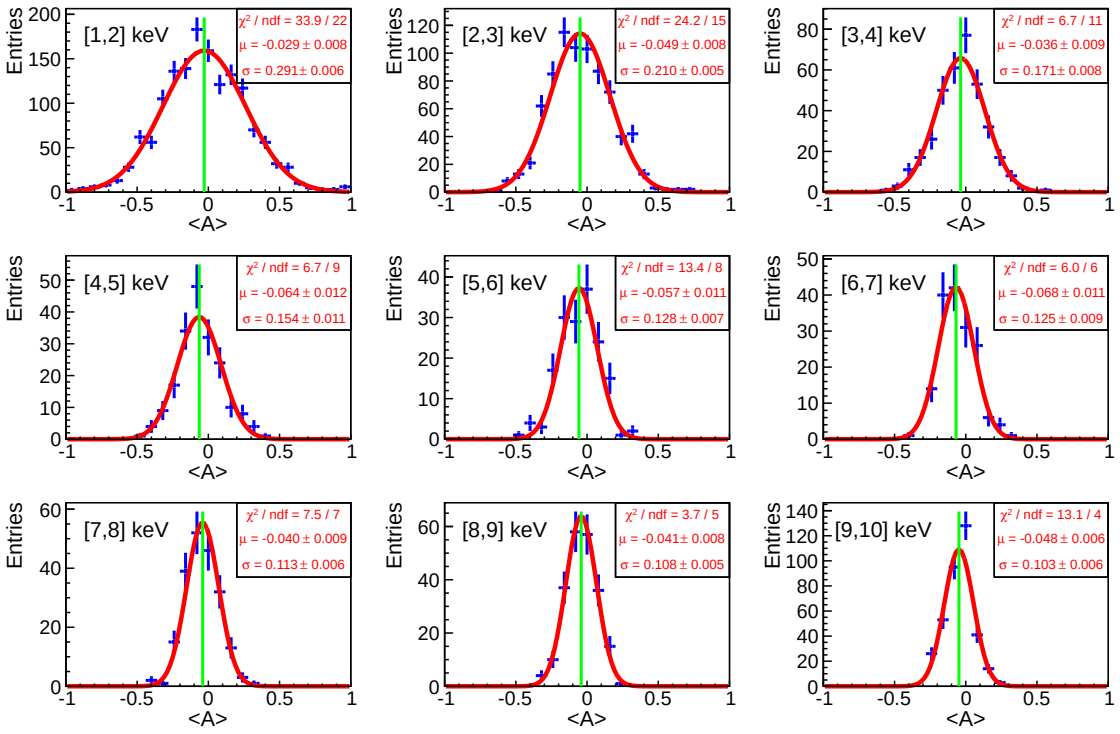

Figure 6.11: $\langle A \rangle$ *distribution for detector D1 from the first* ^{109}*Cd calibration run in 1 keV bins. Data are fitted to Gaussian lineshapes, showing fit results in the panels.*

Variable	Variable separation before training (%)	Variable ranking after training (%)
n_0	40.43	33.80
n_1	36.86	33.68
Asyarea	42.66	32.52

Table 6.3: *Signal/background separation of input variables before training and variable ranking after training in the second phase. The top variable is the best ranked.*

The training result provides the new BDT2 variable, which combined with the previous BDT parameter, will allow us to better discriminate noise events from scintillation events. In Figure 6.12, the two-dimensional scatter plots of the BDT vs BDT2 outputs for both dark matter search data (upper panels) and ^{109}Cd calibration events (lower panels) between 1 and 2 keV (panels to the left) and from 2 to 3 keV (panels to the right) are shown. Events that are above and to the right of the solid red lines in the figure are retained (see Section 6.2.3). As commented in Section 6.2.1.3, background events around BDT$\simeq -0.45$ mostly correspond to

fast PMT-noise events, which can be either symmetric (higher BDT2 values) or asymmetric events (lower BDT2 values). The excess of background events around BDT=−0.35 is due to very large mean time, and can be easily removed using BDT parameter. The background events clustered around BDT=−0.05 and BDT2=−0.10 have strong asymmetry. Some of them are not present neither in the ^{109}Cd calibration sample (Figure 6.12d) nor in the dark matter runs (Figure 6.12b) for energies above 2 keV, and can be rejected using only BDT variable. Nevertheless, for those with BDT>0 and BDT2<0, which only appear below 2 keV, it is mandatory to use both BDT variables to be removed. This type of events are in larger quantity in the physics-run data than in the calibration runs, and correspond to the events defined in Figure 6.1c, which have decay time compatible with that of NaI(Tl) scintillator but present a strong asymmetry in the light sharing among both PMTs.

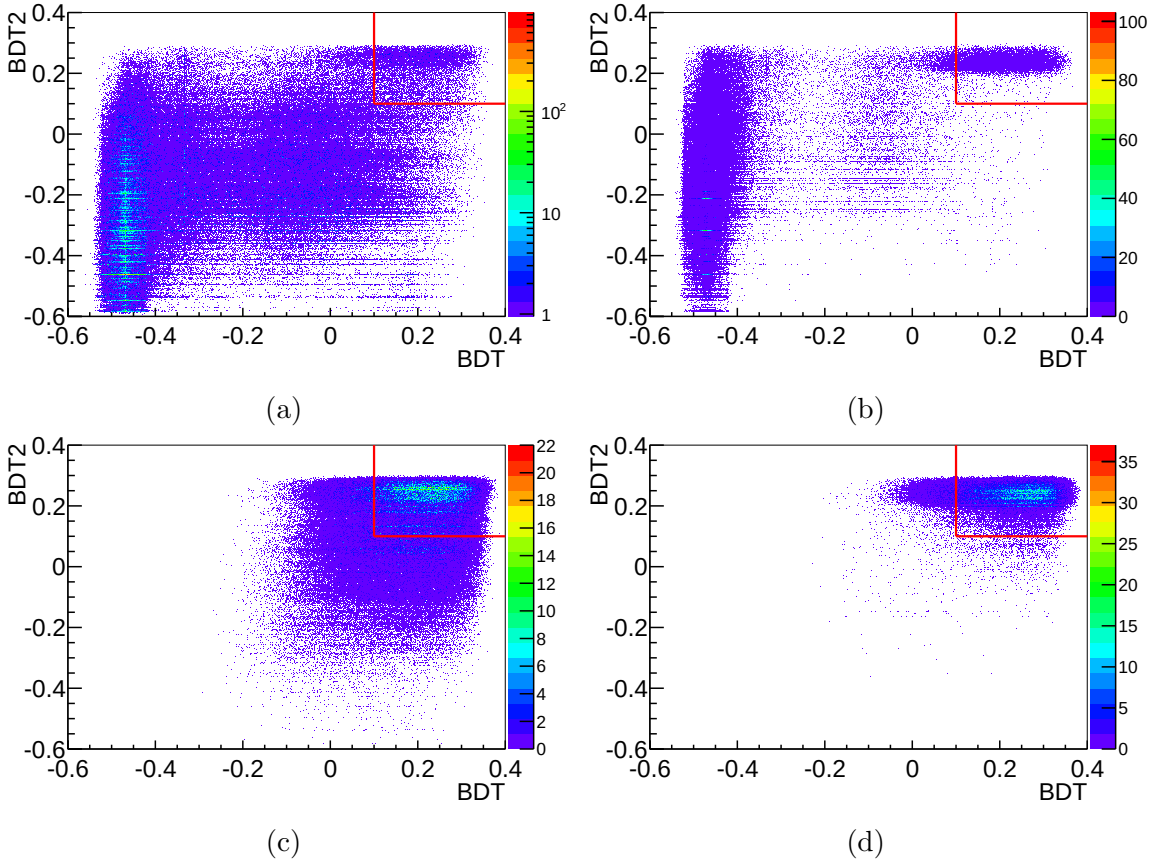

Figure 6.12: *Scatter plot (BDT2 vs BDT) showing events from background events of the ∼10% unblinded data in [1,2] keV (a) and [2,3] keV (b) energy regions. Panels (c) and (d): the same, but for ^{109}Cd calibration runs preselected following Section 6.2.1.1. The events to the right and above the solid red lines are selected as real scintillation events.*

6.2.3 Event selection

We have designed a set of preselection cuts on the ^{109}Cd calibration data to collect the scintillation signal sample for BDT training (Section 6.2.1.1). Straight line cuts on BDT and BDT2 parameters are used for final event selection (Figure 6.12). This BDT-BDT2 selection has been optimized to ensure the lowest total corrected background in [1,2] keV from ∼10% unblinded data, guaranteeing acceptance efficiencies equal to or greater than those obtained with current ANAIS–112 filtering protocols (see Section 3.2.4). We select BDT>0.10 and BDT2>0.10, and the corresponding efficiency is estimated for each detector independently by using ^{109}Cd calibration single-hit events. The ratio of the events which passed over signal selection to the total preselected events is the acceptance efficiency. The efficiency of BDT-BDT2 cut for each module is shown in red in Figure 6.13, and it is observed that they are equal to or higher than those obtained by ANAIS–112 filtering protocols (shown in green in the figure). Furthermore, we use the ^{22}Na and ^{40}K low energy populations selected in coincidence with a 1274.5 keV or 1460.8 keV γ to cross-check the consistency of the selection criteria and efficiency estimation (depicted in blue in Figure 6.13). It has to be remarked that the uncertainty in the latter efficiencies is higher due to the low number of ^{22}Na and ^{40}K coincidence events.

The ∼10% unblinded data of the first year of data taking, amounting to 31.9 days live time, is used for background understanding. The single-hit energy spectra in the ROI for the nine ANAIS–112 detectors after event selection and efficiency correction are shown in red in Figure 6.14. In all detectors the ^{40}K peak at 3.2 keV is clearly visible. The background level at 2 keV ranges from 2 to 4 c/keV/kg/d, depending on the detector, and then increases up to 3–8 c/keV/kg/d at 1 keV. For comparison, the anticoincidence spectra using the established ANAIS–112 filtering procedure is depicted with black dots in the figure. We can observe that the BDT-BDT2 method developed significantly improves the efficiency-corrected background below 2 keV for all detectors with respect to that obtained by the procedure described in Chapter 3. To see this better, the total anticoincidence background spectrum below 10 keV is shown in red (black) for BDT-BDT2 (previous ANAIS–112) filter in Figure 6.15. The background level at 1 and 2 keV is 5.5 and 3.5 c/keV/kg/d, respectively. The integral rate from 1 to 2 keV is 5.77±0.06 and 4.24±0.05 c/keV/kg/d for the ANAIS–112 filtering procedure and the BDT-BDT2 method, respectively, which represents a reduction of the background of 26.5%.

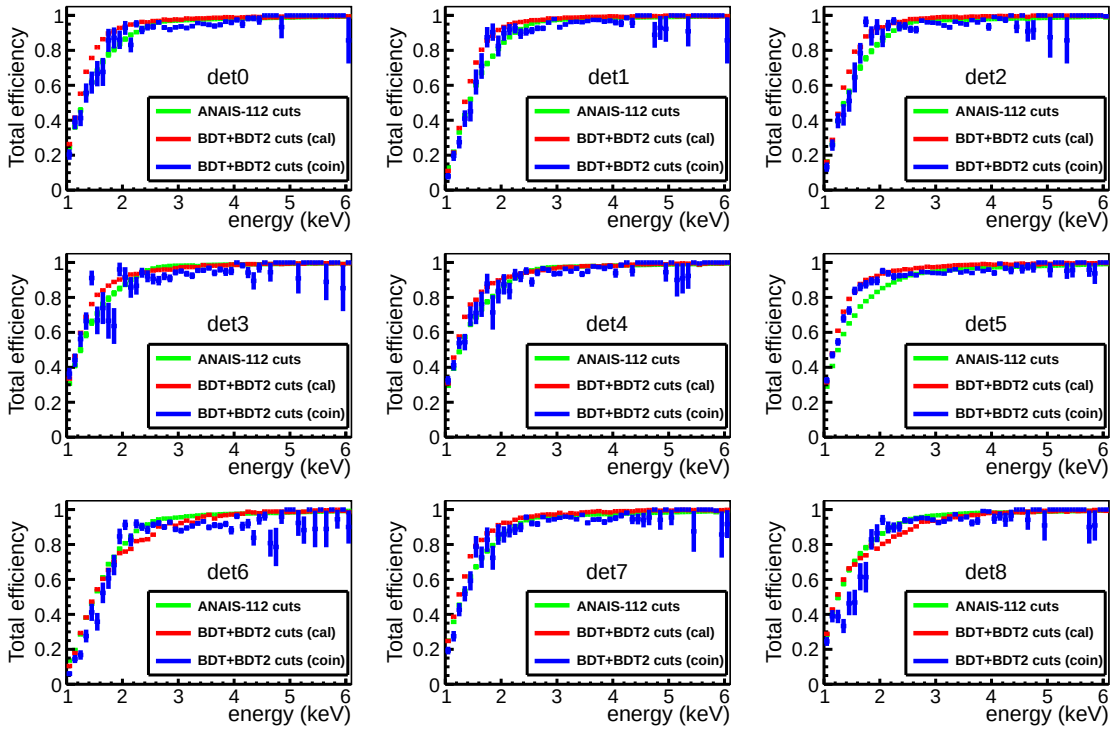

Figure 6.13: *In red: total efficiency for each ANAIS–112 detector, obtained as the product of the trigger and BDT-BDT2 cut efficiencies, estimated from* ^{109}*Cd calibration events. In blue: the same, but estimated from* ^{22}*Na and* ^{40}*K low energy populations selected in coincidence with the high energy gamma. Total efficiency obtained with ANAIS–112 filtering protocols are shown in green for comparison.*

6.2.4 BDT output validation

Although the BDT-BDT2 method gives a good event separation between scintillation and noise events, the validation of boosted decision trees becomes mandatory in order to ensure that calibration events used in the training behave in the same way as those in the background runs. To do this, the distribution of the input variables of the scintillation-like events in the ^{109}Cd calibration sample used for the BDT training is compared with that of the events selected from the independent physics-run data. Figure 6.16 shows the validation of the 15 input variables used to construct the BDT and BDT2. The solid black line is the raw background, while the solid red line is the preselected ^{109}Cd calibration data. After the BDT-BDT2 selection, scintillation-like events from the physics-run (^{109}Cd calibration) data are shown as solid gray (magenta) lines. We can observe that there is a good agreement in the shape of distributions for variables between ^{109}Cd calibration events and the selected scintillation data. The consistency between the two independent samples provides an indirect validation of the procedure.

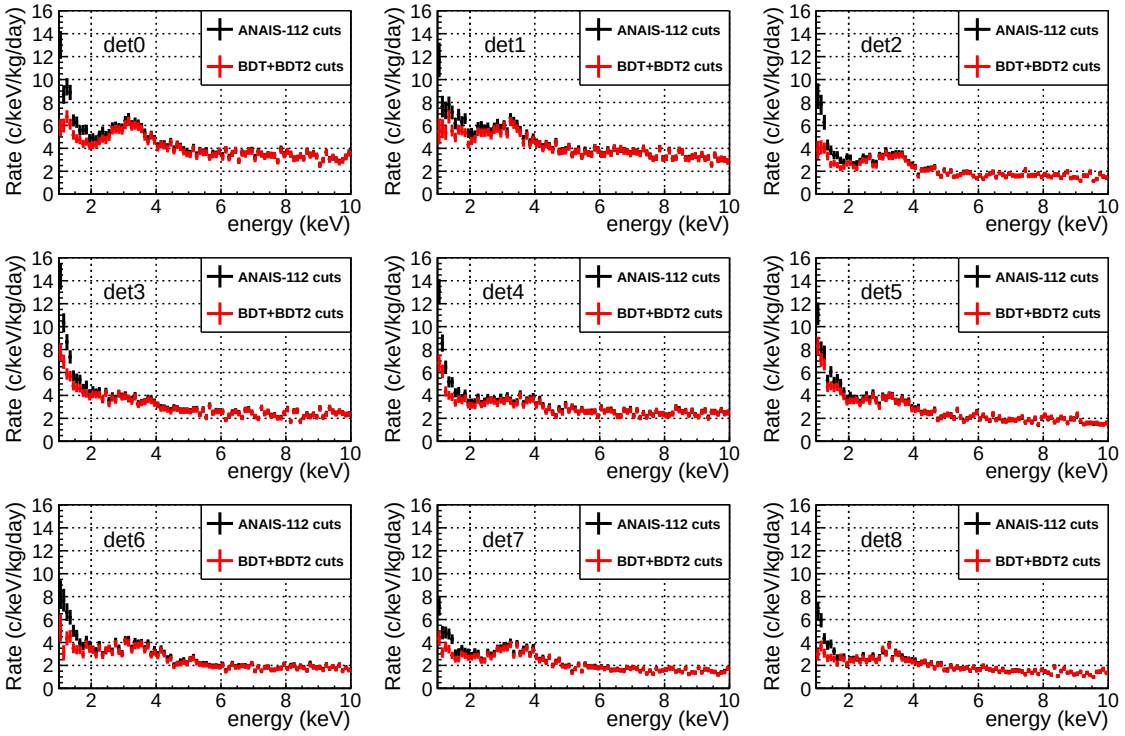

Figure 6.14: *In red: anticoincidence energy spectrum measured in the ROI for each detector after BDT-BDT2 event selection and efficiency correction, corresponding to the ∼10% unblinded data. In black: the same, but using ANAIS–112 filtering procedure described in Chapter 3. The* ^{40}K *peak at* 3.2 *keV is clearly visible.*

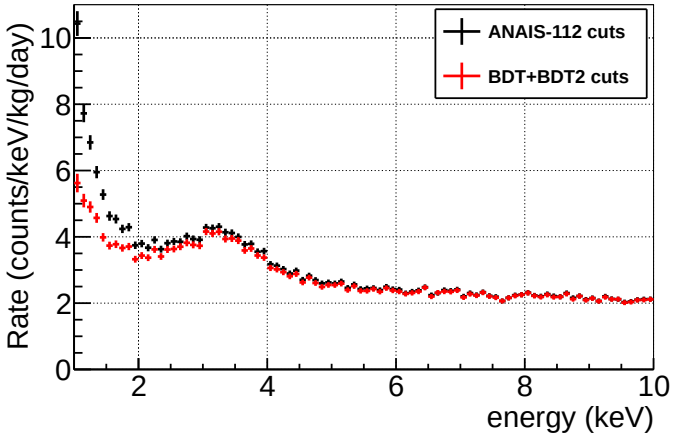

Figure 6.15: *In red: total anticoincidence energy spectrum measured in the ROI after BDT-BDT2 event selection and efficiency correction, corresponding to the ∼10% unblinded data. In black: the same, but using ANAIS–112 filtering procedure described in Chapter 3. The* ^{40}K *peak at* 3.2 *keV is clearly visible.*

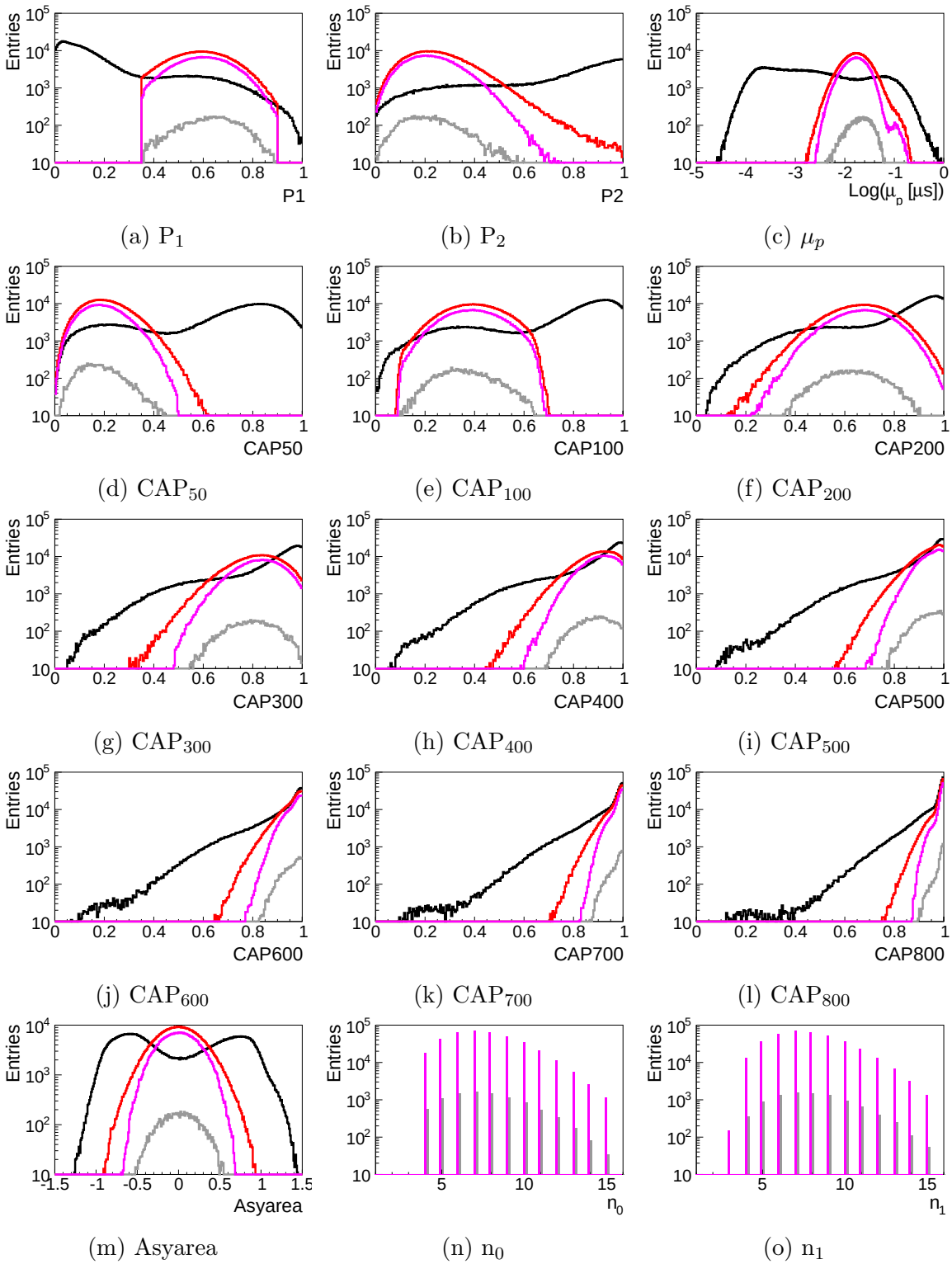

(a) P_1 (b) P_2 (c) μ_p

(d) CAP_{50} (e) CAP_{100} (f) CAP_{200}

(g) CAP_{300} (h) CAP_{400} (i) CAP_{500}

(j) CAP_{600} (k) CAP_{700} (l) CAP_{800}

(m) Asyarea (n) n_0 (o) n_1

Figure 6.16: *Distribution of the 15 input parameters used to validate BDT-BDT2 output response. The black and red lines correspond to physics-run and* ^{109}*Cd calibration data before the BDT-BDT2 selection, respectively. After applying BDT-BDT2 criterion, scintillating-like events from the physics-run data are shown as gray line, whereas selected* ^{109}*Cd calibration events are shown in magenta.*

6.2.5 Comparison with background model

A robust background understanding is essential for experiments demanding ultra low background conditions, such as in experiments seeking rare events (see Section 2.10). The validation of the background model against the experimental data obtained after the BDT-BDT2 event selection and efficiency correction is presented in Table 6.4. The table lists the measured rates for each detector in ANAIS–112 in the region from 1 to 6 keV, corresponding to the ∼10% of unblinded data, in comparison with the corresponding simulation and deviations; the statistical uncertainty of simulated rates for these low energy windows is at the level or below 1%. The background models developed agree very well with the data above 2 keV, but below this energy there is some discrepancy. From Table 6.4, it can be seen that the model does not explain 37% of the measured rate in the region from 1 to 2 keV, but the deviation is of only 7.0% from 2 to 6 keV. If we compare the discrepancy between the background model and the data after filtering with the BDT method with those obtained with the ANAIS–112 filtering protocols described in Chapter 3, we observe that the BDT method presents less deviation both between 1 and 2 keV and from 2 to 6 keV; in particular, 37% and 7.0% compared to the 54% and 10.7% obtained so far, respectively. Although the result obtained with the boosted decision trees is better than that obtained with the ANAIS–112 filtering procedure, there are still unexplained events below 2 keV. These events could be related either with non-bulk scintillation events which have not been rejected by our BDT-BDT2 filtering procedure, or some background sources which have not been taken into consideration in our model. More work is underway in order to develop additional procedures for the rejection of the remaining PMT-noise events.

In Figure 6.17, the comparison for the low energy region for anticoincidence spectra of each ANAIS–112 detector using the ∼10% of unblinded data of the first year of data taking is shown. We can see that detectors D3 and D5 present the greatest disagreement with respect to the model. The same, but for total anticoincidence spectrum is depicted in Figure 6.18.

Detector	[1,2] keV			[2,6] keV		
	Measurement (c/keV/kg/d)	Simulation (c/keV/kg/d)	Deviation (%)	Measurement (c/keV/kg/d)	Simulation (c/keV/kg/d)	Deviation (%)
D0	5.26±0.15	4.37	-17	4.54±0.05	4.53	-0.1
D1	5.46±0.19	4.36	-20	4.59±0.05	4.46	-2.9
D2	3.05±0.14	1.84	-40	2.41±0.04	2.27	-5.8
D3	5.26±0.15	2.77	-47	3.20±0.05	2.97	-7.2
D4	4.26±0.14	2.73	-36	3.07±0.04	2.88	-6.2
D5	5.28±0.15	1.84	-65	2.92±0.04	2.34	-19.9
D6	3.77±0.18	2.04	-46	2.86±0.04	2.42	-15.1
D7	3.09±0.12	2.03	-34	2.58±0.04	2.42	-6.1
D8	2.72±0.11	1.94	-29	2.29±0.04	2.18	-5.0
ANAIS-112	4.24±0.05	2.66	-37	3.16±0.02	2.94	-7.0

Table 6.4: *Measured rates after BDT-BDT2 filtering and efficiency correction in the regions from 1 to 2 keV and 2 to 6 keV for each ANAIS–112 detector and on average, from the ∼10% of unblinded data of the first year of data taking. The corresponding simulated rates and their deviation from the measurement are also presented.*

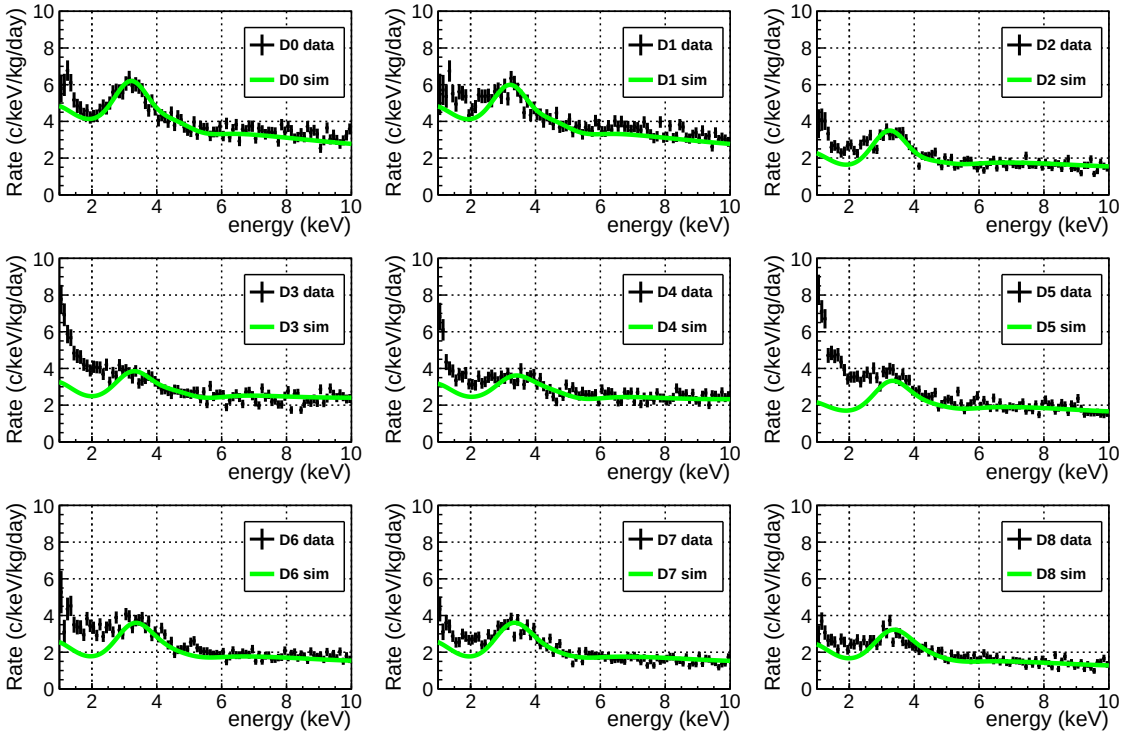

Figure 6.17: *Comparison of the anticoincidence energy spectra in the region of interest measured for each detector (black dots) with the corresponding background model summing all the simulated contributions (green line). The shown data correspond to the ∼10% of unblinded data of the first year of data taking after BDT-BDT2 filtering and efficiency correction.*

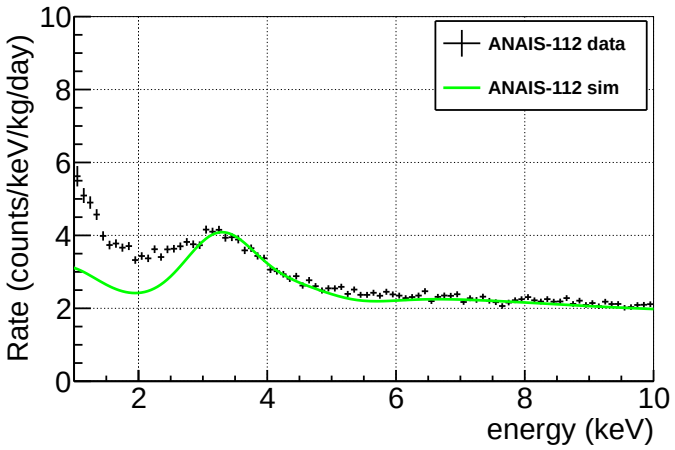

Figure 6.18: *Comparison of the total anticoincidence energy spectrum in the region of interest (black dots) with the corresponding background model summing all the simulated contributions (green line). The shown data correspond to the ∼10% of unblinded data of the first year of data taking after BDT-BDT2 filtering and efficiency correction.*

6.2.6 Sensitivity improvement with BDT

In this section, the projected sensitivity of the ANAIS–112 experiment to the annual modulation observed by DAMA/LIBRA using the developed boosted decision tree technique is evaluated in both model dependent and independent scenarios. The background reduction between 2 and 6 keV is only 4.0%, so the change in projected sensitivity is expected to be small. We have a robust background understanding in this energy region. On the other hand, the background reduction in [1,2] keV energy range is 26.5%, which translates into 10.9% reduction from 1 to 6 keV.

For model independent modulation, we follow the procedure described in Section 4.1.3 to estimate the expected sensitivity. The time evolution of the rate of events is modelled by an exponential decay with a modulated component as:

$$B(\tau) = R_0 \cdot \left(1 + f e^{-t/\tau_d}\right) + S_m \cos\tau, \tag{6.7}$$

where R_0, f, τ_d and S_m are free parameters. The best fit results of the three years of ANAIS–112 data to Equation 6.7 for both [1,6] and [2,6] keV energy regions are gathered in Table 6.5. For each energy region, these values define the function to be exploited using the Monte Carlo technique. Figure 6.19 (dark blue lines) displays our sensitivity projection calculated following Equation 6.7 and considering a ten-day time binning for the two studied energy ranges, whereas the blue bands represent the 68% uncertainty in S_m^{DAMA} as reported in Section 1.4.4.1. The black dots are

the sensitivities derived from the reanalysis of the three years of ANAIS–112 data searching for annual modulation using the BDT method (see Section 6.2.7). The results agree with our estimates, confirming the ANAIS–112 projected sensitivity to the DAMA/LIBRA result. With this filtering procedure, the goal of reaching a 3σ sensitivity to the DAMA/LIBRA signal is achieved in 4 years of data taking in both energy regions, even 1 year ahead of schedule. Figure 6.20 shows the sensitivity projection considering the ANAIS–112 filtering protocols (blue line) compared to the BDT method (red line) for both [1,6] and [2,6] keV energy regions. It can be observed that the BDT technique improves moderately (slightly) the expected sensitivity in the [1,6] ([2,6]) keV energy range, being this progress greater as the exposure increases. In particular, using the BDT method for the low energy events selection improves the sensitivity between 1 and 6 keV by 11.6% with respect to that obtained with the established ANAIS–112 filtering protocols. This improvement is only 2.7% between 2 and 6 keV.

Energy region	R_0 (c/keV/kg/d)	f	τ_d (days)
[1,6] keV	2.854±0.044	0.227±0.017	845±105
[2,6] keV	2.678±0.044	0.220±0.018	862±116

Table 6.5: *Best fit results of the three years of ANAIS–112 data to Equation 6.7 for both [1,6] and [2,6] keV energy regions.*

In the particular case that the annual modulation is induced by the dark matter particles of the galactic halo, the projected sensitivity of ANAIS–112 using the BDT filtering procedure and assuming SI interactions is evaluated following the procedure described in Section 4.2. The background reduction between 2 and 6 keV is so small that the change in projected sensitivity is less than the thickness of the black line in Figure 4.15b and, therefore, will not be drawn. Figure 6.21 shows in magenta the expected sensitivity for [1,6] keV energy window considering the efficiency-corrected background using the BDT method (see Table 6.4), in comparison with that obtained taking into consideration the corresponding background after filtering and efficiency correction using the ANAIS–112 event selection (in black, see Table 2.12). Both of them have been obtained requiring 90% C.L. and 90% of succesful experiments and asumming 5 years of data taking. Segmented detector has also been considered. We can observe a slight improvement in the whole range of WIMP masses shown. We conclude that after the scheduled 5 years of data-taking, ANAIS–112 can detect the annual modulation in the 3σ region compatible with the DAMA/LIBRA result.

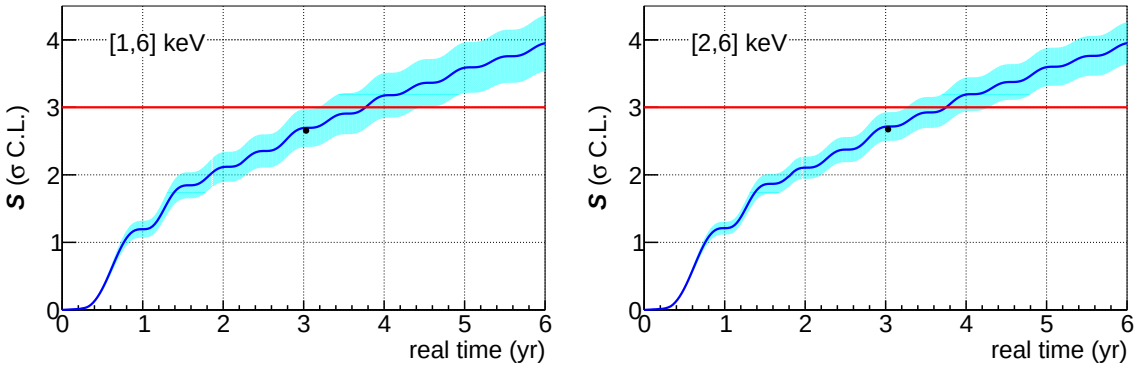

(a) (b)

Figure 6.19: *ANAIS–112 sensitivity to the DAMA/LIBRA signal in σ C.L. units as a function of real time in the [1,6] keV (a) and [2,6] keV (b) energy regions considering exponentially decreasing background after applying the BDT-BDT2 event selection. The black dots are the sensitivities derived from the reanalysis of the three years of ANAIS–112 data using the BDT method (see Section 6.2.7). The blue bands represent the 68% C.L. DAMA/LIBRA uncertainty.*

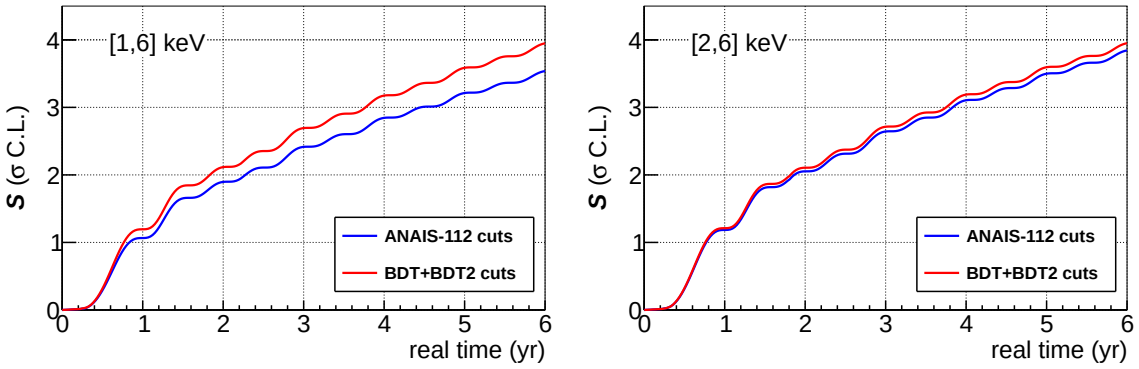

(a) (b)

Figure 6.20: *ANAIS–112 sensitivity to the DAMA/LIBRA signal in σ C.L. units as a function of real time in the [1,6] keV (a) and [2,6] keV (b) energy regions considering exponentially decreasing background. The blue lines show our sensitivity projection derived from applying the established ANAIS–112 filtering procedure, whereas the red lines display the expected sensitivity from applying the BDT method.*

6.2.7 Annual modulation analysis with BDT

Finally, the reanalysis of the three years of ANAIS–112 data searching for annual modulation using the BDT method is carried out. In order to do this, we follow the procedure described in Section 5.2.1.1. After selecting the low energy events using

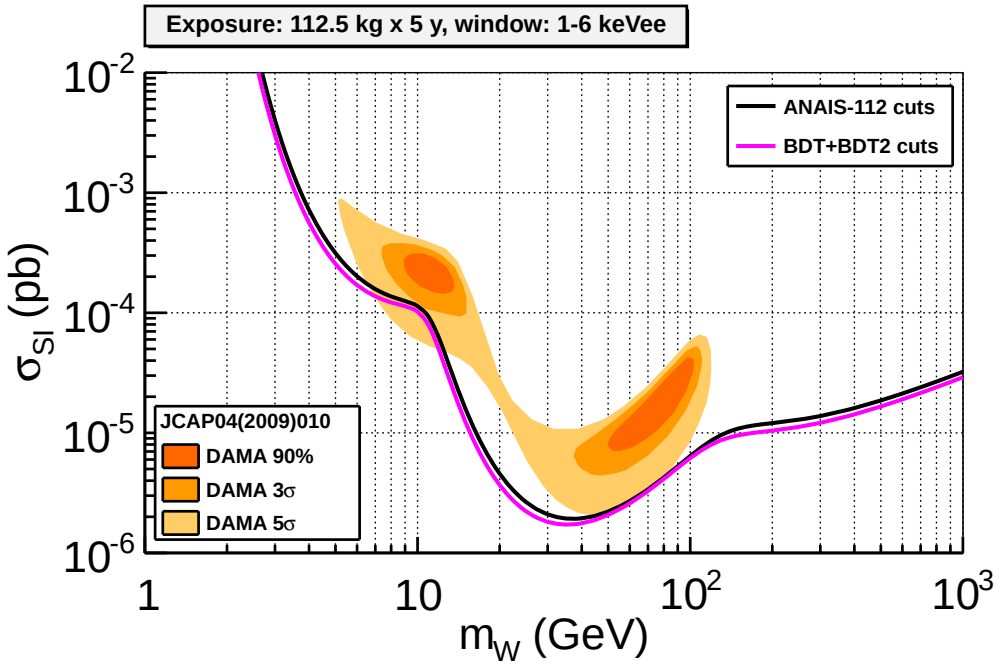

Figure 6.21: *Sensitivity plot in the $\sigma_{SI} - m_W$ plane for ANAIS–112 experiment for [1,6] keV energy region and 5 years of data taking corresponding to a detection limit at 90% C.L. with a critical limit at 90% C.L. Segmented detector has been also considered. In addition, DAMA/LIBRA regions at 90%, 3σ and 5σ [119] are shown as orange areas.*

the BDT technique and applying the corresponding efficiency correction, the time evolution of the resulting rate of events is modelled by an exponential decay with a modulated component as:

$$\mathcal{R}(t_i) = R_0 \cdot (1 + f e^{-t_i/\tau_d}) + S_m \cos\omega(t_i - t_0), \tag{6.8}$$

where $\mathcal{R}(t_i)$ is the expected rate of events in the time bin t_i, R_0, f and τ_d are free parameters, while the modulation amplitude S_m is fixed to 0 for the null hypothesis and left unconstrained (positive or negative) for the modulation hypothesis; $\omega = 2\pi/365$ days^{-1} and $t_0 = -62.17$ days (corresponding the cosine maximum to the 2^{nd} of June, when taking as time origin the 3^{rd} of August).

The results of the χ^2 minimization following Equation 6.8 are shown in Figure 6.22 for [1,6] keV (a) and [2,6] keV (b) energy regions. The χ^2 and p-values of the fit for the null (modulation) hypothesis are also shown in red (green), together with the best fit for S_m. Panels 6.22c and 6.22d represent the residual counting rate for [1,6] and [2,6] keV, respectively, after non-modulated components have been sub-

tracted. The null hypothesis is well supported by the χ^2 test in both energy regions, with χ^2/NDF=115.1/108 (p-value=0.303) from 1 to 6 keV and χ^2/NDF=114.9/108 (p-value=0.307) between 2 and 6 keV. The best fits for the modulation hypothesis are $S_m = -0.0031 \pm 0.0040$ c/keV/kg/d and 0.0009 ± 0.0038 c/keV/kg/d for [1,6] and [2,6] keV, respectively, both compatible with zero at 1σ, and incompatible with DAMA/LIBRA result at 3.4σ (2.4σ), for a present sensitivity of 2.6σ (2.7σ) at [1,6] keV ([2,6] keV). The sensitivity achieved is consistent with the sensitivity estimates for ANAIS–112 from the previous section. The best fit values are also collected in Table 6.6. In addition, Table 6.5 lists the nuisance parameters obtained in the fitting procedure.

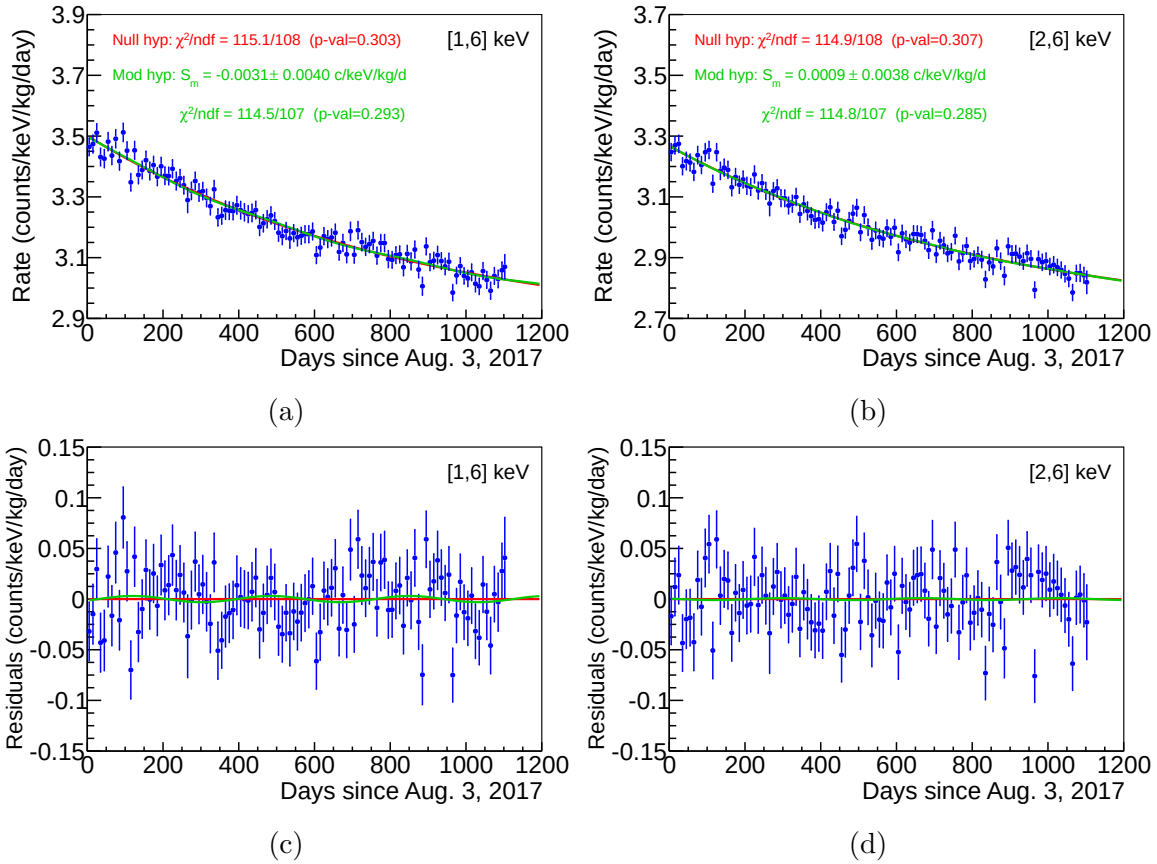

Figure 6.22: *ANAIS–112 fit results for three years of data in [1,6] keV (a) and [2,6] keV (b) energy regions, both in the modulation (green) and null hypotheses (red) when the background is described by Equation 6.8. Panels (c) and (d): the same, but after subtracting the constant and exponential functions fitted to Equation 6.8. Best fit S_m, χ^2 and p-values are also shown.*

Energy region	χ^2 / NDF null hyp	p-value null hyp	χ^2 / NDF mod hyp	p-value mod hyp	S_m (c/keV/kg/d)
[1,6] keV	115.1 / 108	0.303	114.5 / 107	0.293	-0.0031±0.0040
[2,6] keV	114.9 / 108	0.307	114.8 / 107	0.285	0.0009±0.0038

Table 6.6: *Summary of the fit results to Equation 6.8 for the null and modulation hypotheses in [1,6] and [2,6] keV regions for the three years of ANAIS–112 data.*

Figure 6.23 summarizes the results obtained by fitting the total ANAIS–112 rate of events to an exponential function with a modulated component in both [1,6] and [2,6] keV energy regions. On the one hand, the results obtained for the standard deviation of the modulation amplitude after applying the cuts established in the ANAIS–112 publications are shown with black circles. On the other hand, the results obtained when using the BDT method as the filtering protocol for low energy events are shown as red squares. It can be observed that the results obtained with the BDT method present a lower standard deviation of the modulation amplitude in both energy regions, leading to a higher sensitivity to the annual modulation signal. In particular, using the boosted decision tree as the filtering procedure in ANAIS–112 implies an increase of 9.1% in the sensitivity to the annual modulation signal in the energy region between 1 and 6 keV, and an increase of 2.6% between 2 and 6 keV. In view of the potential of the machine learning technique for bulk NaI(Tl) low energy events selection in the ANAIS–112 experiment, the boosted decision tree will be incorporated to ANAIS official analysis.

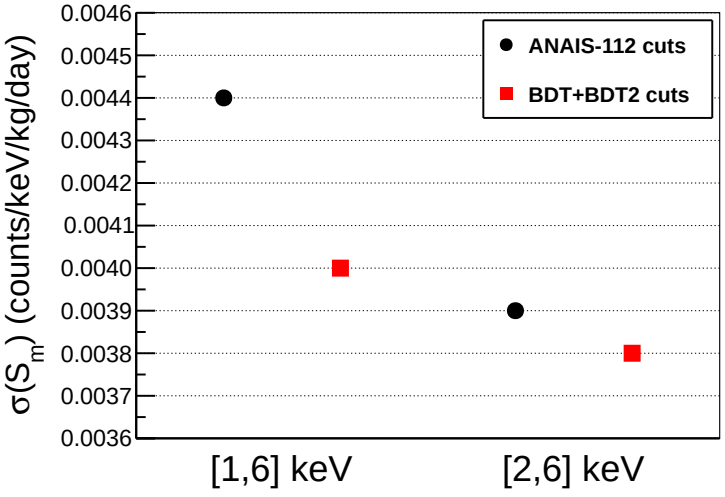

Figure 6.23: *Comparison of the results obtained when fitting the total background of ANAIS–112 derived from the application of the cuts described in Chapter 3 (black circles) and after the application of the new BDT method for event selection (red squares). The results are shown for the [1,6] and [2,6] keV energy regions.*

Summary and conclusions

Despite constituting about 85% of the total amount of matter in the universe, the nature of dark matter still remains one of the most puzzling questions in Fundamental Physics today. Its existence is inferred from a large amount of cosmological and astrophysical observations at very different length scales, from the galaxy rotation curves to the cosmic microwave background anisotropies. All these evidences are based on the gravitational interactions produced between ordinary and dark matter and restricts the nature of dark matter. It has to be non-baryonic, weakly interacting with ordinary matter and non-relativistic (cold dark matter). As there is no particle of the Standard Model that fulfils all these requirements, a plethora of candidates have been proposed beyond the Standard Model of Particle Physics. Axions and WIMPs (Weakly Interacting Massive Particles) are among the preferred.

Different experimental strategies have been applied in order to detect the elusive dark matter particles. They are based on the indirect and direct detection, as well as the production at colliders. Indirect searches are based on the detection of annihilation products of dark matter particles. Direct search attempts to detect nuclear recoils produced by the elastic scattering of dark matter particles in the target nuclei of the detector. The elastic scattering of WIMPs with masses in the 10–100 GeV would produce typical nuclear recoils energies in the range of 1–100 keV. Such recoil energy of the detector's target nuclei could be measured with different techinques.

Several experiments based on different and complementary technologies have been devoted to the direct detection of dark matter. Depending on the channels used to measure the recoil energy of the detector's target nuclei, these experiments use from scintillating crystals or germanium detectors to noble liquid-gas TPCs. In spite of the wide experimental effort devoted to the understanding of the dark matter nature, no unambiguous answer has been reported until now. Only the DAMA/LIBRA experiment, which uses NaI(Tl) crystal detectors at the Gran Sasso National Laboratory (LNGS) in Italy, has provided a long-standing positive result: the observation

of a highly statistically significant annual modulation in the detection rate, which is compatible with that expected for galactic halo dark matter particles. This result has neither been reproduced by any other experiment, nor ruled out in a model independent way. Other experiments using the same target are crucial to ascertain whether the DAMA/LIBRA positive signal is a signature of the halo dark matter particles or due to some systematic artefact.

The ANAIS experiment is intended to search for dark matter annual modulation with ultrapure NaI(Tl) scintillators at the Canfranc Underground Laboratory (LSC) in Spain, in order to provide a model independent confirmation of the signal reported by the DAMA/LIBRA collaboration using the same target and technique. It has been necessary to use ultrapure NaI(Tl) crystals, carefully select external radiopure materials and properly shield the detectors from external radiation. Robust noise filtering protocols are also essential to ensure the quality of low energy events. After more than twenty years operating different ANAIS prototypes, the full ANAIS experiment set-up (ANAIS–112) with 112.5 kg NaI(Tl) was installed at LSC Hall B in 2017. ANAIS–112 started data taking in "dark matter search" mode on the 3^{rd} of August 2017. Since then, ANAIS–112 has been taking data continuously, achieving an average live time of 95%. This long exposure, together with the stability of the operational conditions of ANAIS–112, are essential to guarantee a enough statistical significance in the search for a seasonal variation. Thanks to the outstanding light collection of all the modules, in the order of 15 photoelectrons/keV, and the good low energy calibration, ANAIS–112 has successfully set its energy threshold at 1 keV. ANAIS–112 has also demonstrated to reach a low enough background level in the region of interest to explore the signal singled out by DAMA/LIBRA.

This work focuses on the analysis of the data acquired by ANAIS–112 during its first three years of measurement. A complete description of the elements of the experimental ANAIS–112 set-up is conducted, as well as the most relevant experimental parameters. The experiment performance over the three years is also presented. The sensitivity of the experiment to the annual modulation signal of DAMA/LIBRA has been evaluated taking into account different sources of uncertainty and considering different background scenarios. The three years of data have been analyzed searching for the dark matter annual modulation using different fit functions and studying different control populations to rule out possible systematic effects. Finally, a new filtering procedure for low-energy noise events has been developed using machine learning techniques and it has been applied to reanalyze the three years of data in the search for the annual modulation signal.

It has been studied the evolution of some data acquisition parameters and different environmental parameters whose variations could mimic an annual modulation.

- A very stable behaviour during the three years of data taking has been observed; only some PMTs needed some voltage adjustment and, thanks to the periodic energy calibration, the possible gain drifts have been successfully corrected.

- A seasonal variation in the radon concentration and humidity in the laboratory air outside the ANAIS–112 shielding has been identified, which is compatible with an annual modulation, but whose maximum is reached almost two months later than the expected for dark matter modulation.

- The radon content in the air filling the inner volume of the ANAIS–112 shielding has also been evaluated by screening the same nitrogen gas used for the flushing into the ANAIS shielding using an HPGe detector at LSC. An upper limit of 0.04 Bq/m^3 at 95% C.L. has been estimated, observing a small seasonal variation with low statistical significance. Even if this modulation represented 100% of the ^{222}Rn content inside the ANAIS–112 shielding, its contribution to the ANAIS modulation would be $< 2.7 \cdot 10^{-4}$ c/keV/kg/d in the region of [1,6] keV, being negligible compared to the expected modulation deduced from the DAMA/LIBRA result ($\sim 10^{-2}$ c/keV/kg/d).

- Analyzing the muons crossing the ANAIS–112 veto system, an annual modulation in the coincident muon rates between two different faces has also been observed. This modulation peaks almost one month later than expected for dark matter. However, these muon-related events are rejected by imposing a condition on the time elapsed since the last interaction of a muon in the veto system.

The expected sensitivity of the ANAIS–112 experiment to the annual modulation observed by DAMA/LIBRA has been calculated taking into consideration several sources of uncertainty and assuming different background scenarios.

- Sources of uncertainty included are the purely statistical, that associated with the acceptance efficiency, or the low energy calibration itself. The uncertainty due to efficiency has resulted to be negligible compared to the statistical one. The uncertainty due to the calibration method decreases the expected sensitivity by approximately 10% in [1,6] keV and only 3% in [2,6] keV energy region.

- An analytical formula has been derived to compute the sensitivity to the modulation signal when the background remains constant or decreases linearly with time. The sensitivity estimated in this way is in agreement with the results obtained from the analysis of the annual modulation in the ANAIS–112 data to date.

- A Monte Carlo simulation has also been developed to check the consistency of the results and to evaluate the long-term sensitivity projections. The 3σ sensitivity goal will be reached in the scheduled 5 years of data taking for both energy regions.

- This sensitivity can increase even more if the ANAIS–112 data are combined with those of other experiments searching for the annual modulation reported by DAMA/LIBRA using NaI(Tl) as a target. In particular, the combined sensitivity of ANAIS–112 and COSINE–100 in the energy region between 2 and 6 keV has been determined, concluding that the sensitivity at 3σ level would have been reached around 2.5 years from the beginning of ANAIS–112, that is, at the beginning of 2020, and after 4.5 years the 4σ sensitivity would be achieved (February 2022).

An independent analysis of the annual modulation corresponding to the three years of ANAIS–112 data has been performed from a different data aggregation as a cross-checking of the ANAIS standard analysis. In addition, four different fitting procedures of background evolution have been considered in order to evaluate the possible presence of systematic effects in the analysis protocols.

- Compatible results have been obtained in all cases, both considering the total background of the experiment and evaluating the background of each detector independently.

- These results are consistent with the absence of modulation in both [1,6] and [2,6] keV energy regions.

- In turn, the ANAIS–112 best fits are incompatible with DAMA/LIBRA result at 3.6σ (2.8σ), for a sensitivity of 2.5σ (2.7σ) at [1,6] keV ([2,6] keV).

Finally, a new low-energy noise event filtering protocol based on a multivariate analysis called Boosted Decision Tree (BDT) has been developed. Even though the ANAIS background model satisfactorily reproduces the measured data at all energy ranges above 2 keV and at different analysis conditions (coincidence or anticoincidence), the model is unable to explain 54% of the detected rate between 1 and 2 keV. This new event selection method is intended to explain the excess of events

observed below 2 keV, improving the discrimination between bulk scintillation and noise events.

- A detailed study of all the elements participating in a supervised machine learning algorithm, such as training populations and input variables, has been carried out, and the response of the algorithm to training events has been validated.

- A two-phase strategy for BDT training has been followed. In the first one, only the parameters dependent on the shape of the total pulse from the two PMTs were taken into account. While in the second phase, those variables that describe the asymmetry in the light sharing among both PMTs have been considered.

- Using the BDT selection criterion, the background level between 1 and 2 keV has been significantly reduced by 26.5% without affecting efficiency.

- Comparing this result with the background model, it is observed that the model still does not explain 37% of the measured rate between 1 and 2 keV. These unexplained events could be related either with non-bulk scintillation events which have not been rejected by the BDT filtering procedure, or some background sources which have not been taken into consideration in our model. Both ideas will be explored in the near future to try to understand the origin of this discrepancy.

- Using the boosted decision tree as the filtering procedure in ANAIS–112 implies an increase of 9.1% in the sensitivity to the annual modulation signal in the energy region between 1 and 6 keV, and an increase of 2.6% between 2 and 6 keV. The projected sensitivity is in perfect agreement with the results obtained by reanalyzing the three years of ANAIS–112 data in search for the annual modulation signal observed by DAMA/LIBRA. These results are compatible with the absence of modulation in both [1,6] and [2,6] keV energy regions, and incompatible with DAMA/LIBRA result at 3.4σ (2.4σ), for a present sensitivity of 2.6σ (2.7σ) at [1,6] keV ([2,6] keV).

As a result of the remarkable results achieved in this work, the boosted decision tree will be incorporated to ANAIS official analysis for bulk NaI(Tl) low energy events selection.

Resumen y conclusiones

A pesar de constituir alrededor del 85 % de la cantidad de materia total del universo, la naturaleza de la materia oscura sigue siendo uno de los mayores enigmas de la Física Fundamental en la actualidad. Su existencia se infiere a partir de una gran cantidad de observaciones cosmológicas y astrofísicas a escalas de longitud muy diferentes, desde las curvas de rotación de galaxias hasta las anisotropías de la radiación de fondo de microondas. Todas estas evidencias están basadas en las interacciones gravitatorias producidas entre la materia ordinaria y la materia oscura, y restringen la naturaleza de la materia oscura. Se trata de materia no bariónica y fría (o no relativista en el momento de formación de las estructuras que hoy dominan nuestro universo), que debe interaccionar débilmente con la materia ordinaria. Dado que no existe ninguna partícula del Modelo Estándar que satisfaga todos estos requisitos, se han propuesto numerosos candidatos más allá del Modelo Estándar de la Física de Partículas. Entre los preferidos se encuentran los axiones y los WIMPs (partículas masivas débilmente interactuantes).

Se han aplicado distintas estrategias experimentales para tratar de detectar las esquivas partículas de materia oscura. Éstas se basan en la detección directa e indirecta, así como en su creación en colisionadores de partículas. Las búsquedas indirectas están basadas en la detección de los productos de aniquilación de las partículas de materia oscura, mientras que la búsqueda directa trata de detectar los retrocesos nucleares producidos por la colisión elástica de las partículas de materia oscura en los núcleos blanco del detector. La dispersión elástica de WIMPs con masas entre los 10 y 100 GeV poduciría retrocesos nucleares con energías en el rango de 1 a 100 keV. Tales energías de retroceso podrían ser medidas con diferentes técnicas.

Diversos experimentos basados en tecnologías distintas y complementarias han sido destinados a la detección directa de la materia oscura. Dependiendo de los canales utilizados para medir la energía de retroceso de los núcleos blanco del detector, estos experimentos usan desde cristales centelleadores o detectores de germanio hasta cámaras de proyección temporal (TPCs) de doble fase (líquido-gas) basadas en

elementos nobles. A pesar del gran esfuerzo experimental dedicado a la comprensión de la naturaleza de la materia oscura, hasta ahora no se ha proporcionado una respuesta irrefutable a este problema. Sólo el experimento DAMA/LIBRA, que utiliza detectores centelleadores de NaI(Tl) en el Laboratorio Nacional del Gran Sasso (LNGS) en Italia, ha presentado un resultado positivo: la observación de una modulación anual con alta significancia estadísitica en el ritmo de detección, que es compatible con la esperada para las partículas de materia oscura del halo galáctico. Este resultado no ha sido reproducido por ningún otro experimento, ni tampoco descartado de forma independiente del modelo de WIMP. Otros experimentos que utilicen el mismo blanco material son cruciales para determinar si la señal positiva de DAMA/LIBRA es una señal distintiva de las partículas de materia oscura del halo galáctico o se debe a algún artefacto sistemático.

El experimento ANAIS está destinado a la búsqueda de la modulación anual de la materia oscura con centelleadores ultrapuros de NaI(Tl) en el Laboratorio Subterráneo de Canfranc (LSC) en España, con el fin de proporcionar una confirmación independiente del modelo de la señal presentada por la colaboración DAMA/LIBRA utilizando el mismo blanco y la misma técnica. Ha sido necesario utilizar cristales ultrapuros de NaI(Tl), seleccionar cuidadosamente los materiales externos en términos de radiopureza y proteger adecuadamente los detectores de la radiación externa. Para garantizar la calidad de los sucesos de baja energía, es fundamental también implementar protocolos de filtrado de ruido sólidos. Tras más de veinte años operando distintos prototipos de ANAIS, el montaje completo del experimento ANAIS (ANAIS–112) con 112.5 kg de NaI(Tl) se instaló en el Hall B del LSC en 2017. ANAIS–112 comenzó la toma de datos en busca de la materia oscura el 3 de agosto de 2017. Desde entonces, ANAIS–112 ha estado tomando datos ininterrumpidamente, logrando alcanzar un tiempo vivo promedio del 95 %. Esta gran exposición, unida a la estabilidad de las condiciones operacionales de ANAIS–112, son esenciales para garantizar una significancia estadística suficiente en la búsqueda de un fenómeno estacional. Gracias a la excelente recolección de luz de todos los módulos, del orden de 15 fotoelectrones/keV, y a la buena calibración en baja energía, ANAIS–112 ha situado su umbral de energía en 1 keV satisfactoriamente. ANAIS–112 también ha demostrado alcanzar un nivel de fondo suficientemente bajo en la región de interés para explorar la señal encontrada por DAMA/LIBRA.

Este trabajo se centra en el análisis de los datos adquiridos por ANAIS–112 durante sus primeros tres años de medida. Se realiza una descripción completa de los elementos que configuran el montaje experimental de ANAIS–112, así como de los parámetros experimentales más relevantes. También se presenta el rendimiento del

experimento durante los tres años. Se ha evaluado la sensibilidad del experimento a la señal de modulación anual de DAMA/LIBRA teniendo en cuenta distintas fuentes de incertidumbre y considerando diferentes escenarios de fondo. Se han analizado los tres años de datos en busca de la modulación anual de la materia oscura utilizando distintas funciones de ajuste y estudiando diversas poblaciones de control con el fin de descartar posibles efectos sistemáticos. Por último, se ha desarrollado un nuevo procedimiento de filtrado de sucesos de ruido de baja energía utilizando técnicas de aprendizaje automático y se ha aplicado para reanalizar los tres años de datos en busca de la señal de modulación anual.

Se ha estudiado la evolución de algunos parámetros de adquisición y diferentes parámetros ambientales cuyas variaciones podrían imitar una modulación anual.

- Se ha observado un comportamiento muy estable durante los tres años de toma de datos; sólo algunos PMTs necesitaron algún ajuste de voltaje y, gracias a la calibración en energía periódica, se han corregido satisfactoriamente las posibles desviaciones de la ganancia.

- Se ha identificado una variación estacional en la concentración de radón y en la humedad del aire del laboratorio externo al blindaje de ANAIS–112, que es compatible con una modulación anual, pero cuyo máximo se alcanza casi dos meses después de lo esperado para la modulación de la materia oscura.

- También se ha evaluado el contenido de radón presente en el aire de la cavidad interna del blindaje de ANAIS–112 analizando el gas nitrógeno utilizado para purgar el blindaje de ANAIS–112 mediante un detector de germanio hiperpuro (HPGe) del LSC. Se ha estimado un límite superior de 0.04 $\mathrm{Bq/m^3}$ al 95 % C.L., observándose una pequeña variación estacional con baja significancia estadística. Aunque esta modulación representara el 100 % del contenido de ^{222}Rn dentro del blindaje de ANAIS–112, su contribución a la modulación de ANAIS sería $< 2{,}7 \cdot 10^{-4}$ c/keV/kg/d en la región de [1,6] keV, siendo despreciable frente a la modulación que se esperaría a partir del resultado de DAMA/LIBRA ($\sim 10^{-2}$ c/keV/kg/d).

- Al analizar los muones que atraviesan el sistema de veto de ANAIS–112, también se ha observado una modulación anual en los ritmos de coincidencia de muones entre dos caras diferentes. Esta modulación alcanza su máximo casi un mes después de lo esperado para la materia oscura. No obstante, estos sucesos relacionados con los muones son eliminados al imponer un corte en el tiempo transcurrido desde la última interacción de un muon en el sistema de veto.

La sensibilidad esperada del experimento ANAIS–112 a la modulación anual observada por DAMA/LIBRA se ha calculado teniendo en cuenta diversas fuentes de incertidumbre y suponiendo distintos escenarios de fondo.

- Entre las fuentes de incertidumbre se incluyen: la puramente estadística, aquella asociada a la eficiencia de aceptación de sucesos, o la debida a la propia calibración de la baja energía. La incertidumbre debida a la eficiencia ha resultado ser despreciable frente a la estadística. La incertidumbre debida al método de calibración disminuye la sensibilidad esperada en aproximadamente un 10 % en [1,6] keV y sólo un 3 % en la región de energía [2,6] keV.

- Se ha deducido una fórmula analítica para calcular la sensibilidad a la señal de modulación cuando el fondo permanece constante o disminuye linealmente con el tiempo. La sensibilidad estimada de esta manera concuerda con los resultados obtenidos en el análisis de la modulación anual de los datos de ANAIS–112 hasta la fecha.

- También se ha desarrollado una simulación de Monte Carlo para comprobar la consistencia de los resultados y evaluar las proyecciones de sensibilidad a largo plazo. Se alcanzará el objetivo de sensibilidad de 3σ en ambas regiones energéticas dentro de los 5 años programados de toma de datos.

- Esta sensibilidad puede aumentar aún más si los datos obtenidos por ANAIS–112 se combinan con los de otros experimentos que buscan la modulación anual señalada por DAMA/LIBRA utilizando NaI(Tl) como blanco. En concreto, se ha determinado la sensibilidad combinada de ANAIS–112 y COSINE–100 en la región energética entre 2 y 6 keV, concluyendo que la sensibilidad a 3σ se habría alcanzado en torno a 2.5 años después del comienzo de ANAIS–112, es decir, a principios de 2020, y tras 4.5 años se alcanzaría la sensibilidad a 4σ (febrero de 2022).

Se ha realizado un análisis independiente de la modulación anual correspondiente a los tres años de datos de ANAIS–112 a partir de una agregación de datos distinta, que ha servido como verificación cruzada del análisis estándar realizado por ANAIS. Además, se han considerado cuatro procedimientos de ajuste diferentes para la evolución del fondo con el fin de evaluar la posible presencia de efectos sistemáticos en los protocolos de análisis.

- Se han obtenido resultados compatibles en todos los casos, tanto considerando el fondo total del experimento como evaluando el fondo de cada detector de forma independiente.

- Estos resultados son consistentes con la ausencia de modulación en las regiones de energía [1,6] y [2,6] keV.

- A su vez, los resultados de ANAIS–112 son incompatibles con el obtenido por DAMA/LIBRA a 3.6σ (2.8σ), para una sensibilidad de 2.5σ (2.7σ) en [1,6] keV ([2,6] keV).

Por último, se ha desarrollado un nuevo protocolo de filtrado de sucesos de ruido de baja energía basado en un análisis multivariante denominado árbol de decisión ampliado (BDT). A pesar de que el modelo de fondo de ANAIS reproduce satisfactoriamente los datos medidos en todos los rangos de energía por encima de 2 keV y en distintas condiciones de análisis (coincidencia o anticoincidencia), el modelo es incapaz de explicar el 54 % del ritmo detectado entre 1 y 2 keV. Con este nuevo método de selección de sucesos se pretende dar explicación al exceso de sucesos observados por debajo de 2 keV, mejorando la discriminación entre sucesos de centelleo y sucesos de ruido.

- Se ha llevado a cabo un estudio detallado de todos los elementos que participan en un algoritmo de aprendizaje automático supervisado, como las poblaciones de entrenamiento y las variables de entrada, y se ha validado la respuesta del algoritmo ante los sucesos de entrenamiento.

- Se ha seguido una estrategia en dos fases para el entrenamiento del árbol. En la primera de ellas, se ha atendido sólo a parámetros dependientes de la forma del pulso suma de los dos fotomultiplicadores. Mientras que en la segunda fase, se han considerado aquellas variables que describen la asimetría en el reparto de luz entre ambos fotomultiplicadores.

- Utilizando el criterio de selección basado en el BDT, el nivel de fondo entre 1 y 2 keV se ha reducido significativamente en un 26.5 % sin afectar a la eficiencia.

- Comparando este resultado con el modelo de fondo, se observa que el modelo sigue sin explicar el 37 % del ritmo medido entre 1 y 2 keV. Este inexplicable exceso de sucesos podría estar relacionado con sucesos no originados en el cristal de NaI(Tl) que no han sido eliminados por el procedimiento de filtrado del BDT, o con algunas fuentes de fondo no consideradas en nuestro modelo. Ambas ideas van a ser exploradas en el futuro próximo para tratar de entender el origen de esta discrepancia.

- El uso del árbol de decisión ampliado como procedimiento de filtrado en ANAIS–112 implica un incremento del 9.1 % en la sensibilidad a la señal de modulación anual en la región de energía entre 1 y 6 keV, y un aumento del

2.6 % entre 2 y 6 keV. La sensibilidad proyectada concuerda perfectamente con los resultados obtenidos al reanalizar los tres años de datos de ANAIS–112 en busca de la señal de modulación anual observada por DAMA/LIBRA. Estos resultados son compatibles con la ausencia de modulación en las regiones de energía [1,6] y [2,6] keV, e incompatibles con el obtenido por DAMA/LIBRA a 3.4σ (2.4σ), para una sensibilidad de 2.6σ (2.7σ) en [1,6] keV ([2,6] keV).

Como consecuencia de los resultados notables obtenidos en este trabajo, el árbol de decisión ampliado se incorporará al análisis oficial de ANAIS para la selección de sucesos de baja energía del cristal de NaI(Tl).

Agradecimientos

En estas líneas quiero mostrar mi agradecimiento a las personas que directa o indirectamente han formado parte de mi crecimiento, tanto a nivel personal como profesional, y han contribuido a hacer posible este trabajo de investigación.

En primer lugar, me gustaría dar las gracias a mi director de tesis, Jorge Puimedón, mentor y referente, que me ha llevado de la mano en este camino del conocimiento, haciéndome parar, admirar y disfrutar de todas las vistas. Gracias, Jorge, por saber transmitirme parte de tu gran sabiduría, por todas las charlas siempre enriquecedoras y, sobre todo, por haber confiado en mí desde el primer momento; contigo esta andadura ha sido más sencilla.

Gracias a mi director de tesis, Miguel Ángel Oliván, por introducirme en el apasionante mundo del aprendizaje automático, por su disponibilidad para aclararme dudas incluso en días festivos y por su ayuda en la gestión de mi estancia de investigación.

También me gustaría mostrar un agradecimiento especial a María Martínez, incansable y excelente investigadora, que me ha acompañado, ayudado y animado a continuar en la investigación desde su regreso a Zaragoza. Te agradezco de verdad que hayas contado conmigo en todo momento.

A Eduardo García, por sus enseñanzas, ánimo y gran calidad humana. A Susana Cebrián, por su preciada ayuda con las simulaciones, su excepcional trato y su ejemplar forma de trabajar. A Alfonso Ortiz de Solórzano, por los viajes a Canfranc y el entusiasmo que transmite por el laboratorio. A Javier Mena por su ayuda y a Ysrael Ortigoza por sus consejos.

Me gustaría acordarme también de Theopisti Dafni e Igor García, por creer en mí y darme una oportunidad sin apenas conocerme. Encantado de haber formado parte de vuestro proyecto de investigación. Estaré siempre agradecido a Theopisti

también por las innumerables charlas que hemos tenido, sus consejos y su disposición a escuchar mi punto de vista para organizar las prácticas de laboratorio.

Al resto de compañeros de prácticas de laboratorio (Javier Jiménez, Javier Galán y David Díez), a mis compañeros de despacho (Paco Iguaz y Héctor Mirallas), a todas las personas que han participado en la organización del Día de la Materia Oscura y otras actividades de divulgación durante estos años y al personal del Laboratorio Subterráneo de Canfranc por su colaboración y ayuda.

También quisiera agradecer la acogida y el trato del departamento de Integración de TIC de la Fundación CIRCE durante mi estancia de investigación, especialmente a Alberto por su paciencia y colaboración.

Por último, en el terreno más personal, me gustaría dar las gracias a mis amigos y a mi familia; en especial a mi madre, por ser el pilar fundamental de mi vida, por su apoyo incondicional y por todo lo que me ha enseñado a lo largo de mi vida. Gracias de todo corazón.

Acknowledgements

This work has been financially supported by the Spanish Ministerio de Economía y Competitividad and the European Regional Development Fund (MINECO-FEDER) under Grant No. FPA2017-83133-P; the Ministerio de Ciencia e Innovación – Agencia Estatal de Investigación under Grant No. PID2019-104374GB-I00; the Consolider-Ingenio 2010 Programme under Grants No. MultiDark CSD2009-00064 and No. CPAN CSD2007-00042; the Laboratorio Subterráneo de Canfranc (LSC) Consortium; and the Gobierno de Aragón and the European Social Fund (Group in Nuclear and Astroparticle Physics, GIFNA). The support of the Spanish Red Consolider MultiDark FPA2017-90566-REDC is also appreciated. Technical support from LSC and GIFNA staff through all stages of this work is worth of acknowledgement, too. Finally, the warm hospitality received from the CIRCE's ICT Integration Department during the research stage is gratefully acknowledged.

This PhD dissertation has been possible thanks to the Gobierno de Aragón Programa de Fomento de la Investigación in its call for recruitment of predoctoral research staff in training for the period 2016-2020, cofinanced with the Programa Operativo FSE Aragón 2014-2020.

Bibliography

[1] N. Aghanim et al. Planck 2018 results - VI. Cosmological parameters. *Astronomy&Astrophysics*, 641:A6, 2020, doi:10.1051/0004-6361/201833910.

[2] L. Baudis. Dark matter detection. *Journal of Physics G: Nuclear and Particle Physics*, 43(4):044001, March 2016, doi:10.1088/0954-3899/43/4/044001.

[3] C. Tao. Dark Matter searches: an overview. *Journal of Instrumentation*, 15(06):C06054–C06054, June 2020, doi:10.1088/1748-0221/15/06/c06054.

[4] R. Bernabei et al. First results from DAMA/LIBRA and the combined results with DAMA/NaI. *The European Physical Journal C*, 56(3):333–355, August 2008, doi:10.1140/epjc/s10052-008-0662-y.

[5] R. Bernabei et al. New results from DAMA/LIBRA. *The European Physical Journal C*, 67(1–2):39–49, March 2010, doi:10.1140/epjc/s10052-010-1303-9.

[6] R. Bernabei et al. Final model independent result of DAMA/LIBRA-phase1. *The European Physical Journal C*, 73(12):2648, November 2013, doi:10.1140/epjc/s10052-013-2648-7.

[7] R. Bernabei et al. First model independent results from DAMA/LIBRA-phase2. *Nuclear Physics and Atomic Energy*, 19(4):307–325, 2019, doi:10.15407/jnpae2018.04.307.

[8] R. Agnese et al. New Results from the Search for Low-Mass Weakly Interacting Massive Particles with the CDMS Low Ionization Threshold Experiment. *Physical Review Letters*, 116:071301, February 2016, doi:10.1103/PhysRevLett.116.071301.

[9] A. H. Abdelhameed et al. First results from the CRESST-III low-mass dark matter program. *Physical Review D*, 100:102002, November 2019, doi:10.1103/PhysRevD.100.102002.

[10] E. Armengaud et al. Searching for low-mass dark matter particles with a massive Ge bolometer operated above ground. *Physical Review D*, 99:082003, April 2019, doi:10.1103/PhysRevD.99.082003.

[11] H. S. Lee et al. Search for low-mass dark matter with CsI(Tl) crystal detectors. *Physical Review D*, 90:052006, September 2014, doi:10.1103/PhysRevD.90.052006.

[12] D. S. Akerib et al. First Results from the LUX Dark Matter Experiment at the Sanford Underground Research Facility. *Physical Review Letters*, 112:091303, March 2014, doi:10.1103/PhysRevLett.112.091303.

[13] C. B. Krauss. PICO–60 Results and PICO–40L Status. *Journal of Physics: Conference Series*, 1468:012043, February 2020, doi:10.1088/1742-6596/1468/1/012043.

[14] E. Aprile et al. Dark Matter Search Results from a One Ton-Year Exposure of XENON1T. *Physical Review Letters*, 121:111302, September 2018, doi:10.1103/PhysRevLett.121.111302.

[15] J. Amaré et al. Performance of ANAIS–112 experiment after the first year of data taking. *The European Physical Journal C*, 79(228), 2019, doi:10.1140/epjc/s10052-019-6697-4.

[16] I. Coarasa et al. ANAIS–112 sensitivity in the search for dark matter annual modulation. *The European Physical Journal C*, 79(233), 2019, doi:10.1140/epjc/s10052-019-6733-4.

[17] G. Adhikari et al. Initial performance of the COSINE–100 experiment. *The European Physical Journal C*, 78(2):107, 2018, doi:10.1140/epjc/s10052-018-5590-x.

[18] M. Antonello et al. The SABRE project and the SABRE Proof-of-Principle. *The European Physical Journal C*, 79(4):363, 2019, doi:10.1140/epjc/s10052-019-6860-y.

[19] G. Angloher et al. The COSINUS project: perspectives of a NaI scintillating calorimeter for dark matter search. *The European Physical Journal C*, 76(8):441, 2016, doi:10.1140/epjc/s10052-016-4278-3.

[20] K. Fushimi et al. Development of highly radiopure NaI(Tl) scintillator for PICOLON dark matter search project. *Progress of Theoretical and Experimental Physics*, 2021(4), February 2021, doi:10.1093/ptep/ptab020.

[21] S. Carroll. The cosmological constant. *Living Reviews in Relativity*, 4, May 2000, doi:10.12942/lrr-2001-1.

[22] P. J. E. Peebles and B. Ratra. The cosmological constant and dark energy. *Rev. Mod. Phys.*, 75:559–606, April 2003, doi:10.1103/RevModPhys.75.559.

[23] P. Bull et al. Beyond ΛCDM: Problems, solutions, and the road ahead. *Physics of the Dark Universe*, 12:56–99, 2016, doi:10.1016/j.dark.2016.02.001.

[24] A. Arbey and F. Mahmoudi. Dark matter and the early Universe: A review. *Progress in Particle and Nuclear Physics*, 119:103865, 2021, doi:10.1016/j.ppnp.2021.103865.

[25] L. Perivolaropoulos and F. Skara. Challenges for ΛCDM: An update, 2021. arXiv:2105.05208.

[26] A. G. Riess et al. Observational Evidence from Supernovae for an Accelerating Universe and a Cosmological Constant. *The Astronomical Journal*, 116(3):1009–1038, September 1998, doi:10.1086/300499.

[27] S. Perlmutter et al. Measurements of Ω and Λ from 42 High-Redshift Supernovae. *The Astrophysical Journal*, 517(2):565–586, June 1999, doi:10.1086/307221.

[28] L. Page et al. First-Year Wilkinson Microwave Anisotropy Probe (WMAP) Observations: Interpretation of the TT and TE Angular Power Spectrum Peaks. *The Astrophysical Journal Supplement Series*, 148(1):233–241, September 2003, doi:10.1086/377224.

[29] F. Bernardeau, S. Colombi, E. G. naga, and R. Scoccimarro. Large-scale structure of the universe and cosmological perturbation theory. *Physics Reports*, 367(1):1–248, 2002, doi:10.1016/S0370-1573(02)00135-7.

[30] D. N. Schramm and M. S. Turner. Big-bang nucleosynthesis enters the precision era. *Review of Modern Physics*, 70:303–318, January 1998, doi:10.1103/RevModPhys.70.303.

[31] G. Steigman. Primordial Nucleosynthesis in the Precision Cosmology Era. *Annual Review of Nuclear and Particle Science*, 57(1):463–491, 2007, doi:10.1146/annurev.nucl.56.080805.140437.

[32] F. Iocco et al. Primordial nucleosynthesis: From precision cosmology to fundamental physics. *Physics Reports*, 472(1):1–76, March 2009, doi:10.1016/j.physrep.2009.02.002.

[33] R. H. Cyburt, B. D. Fields, K. A. Olive, and T.-H. Yeh. Big bang nucleosynthesis: Present status. *Review of Modern Physics*, 88:015004, February 2016, doi:10.1103/RevModPhys.88.015004.

[34] E. Hubble. A relation between distance and radial velocity among extragalactic nebulae. *Proceedings of the National Academy of Sciences*, 15(3):168–173, 1929, doi:10.1073/pnas.15.3.168.

[35] E. Hubble and M. L. Humason. The Velocity-Distance Relation among Extra-Galactic Nebulae. *Astrophysical Journal*, 74:43, July 1931, doi:10.1086/143323.

[36] G. Lemaître. The Beginning of the World from the Point of View of Quantum Theory. *Nature*, 127(3210):706, May 1931, doi:10.1038/127706b0.

[37] G. Lemaître. *The Primeval Atom – An Essay on Cosmology*. D. Van Nostrand Co, 1946.

[38] G. Gamow. Expanding Universe and the Origin of Elements. *Physical Review*, 70:572–573, October 1946, doi:10.1103/PhysRev.70.572.2.

[39] R. A. Alpher, H. Bethe, and G. Gamow. The Origin of Chemical Elements. *Physical Review*, 73:803–804, April 1948, doi:10.1103/PhysRev.73.803.

[40] M. Tanabashi et al. Review of Particle Physics. *Physical Review D*, 98:030001, August 2018, doi:10.1103/PhysRevD.98.030001.

[41] Particle Data Group. Big-Bang Cosmology. `https://pdg.lbl.gov/2020/reviews/rpp2020-rev-bbang-cosmology.pdf`.

[42] R. A. Alpher and R. C. Herman. On the Relative Abundance of the Elements. *Physical Review*, 74:1737–1742, December 1948, doi:10.1103/PhysRev.74.1737.

[43] R. A. Alpher and R. C. Herman. Remarks on the Evolution of the Expanding Universe. *Physical Review*, 75:1089–1095, April 1949, doi:10.1103/PhysRev.75.1089.

[44] A. A. Penzias and R. W. Wilson. A Measurement of Excess Antenna Temperature at 4080 Mc/s. *Astroparticle Physics*, 142:419–421, July 1965, doi:10.1086/148307.

[45] D. J. Fixsen. THE TEMPERATURE OF THE COSMIC MICROWAVE BACKGROUND. *The Astrophysical Journal*, 707(2):916–920, November 2009, doi:10.1088/0004-637x/707/2/916.

[46] J. A. Peacock. *Cosmological Physics*. Cambridge University Press, 1998.

[47] S. Weinberg. *Cosmology*. Oxford University Press Inc., New York, 2008.

[48] T.-P. Cheng. *Relativity, gravitation and cosmology: a basic introduction*. Oxford University Press, Oxford, 2nd edition, 2010.

[49] A. H. Guth. Inflationary universe: A possible solution to the horizon and flatness problems. *Physical Review D*, 23:347–356, January 1981, doi:10.1103/PhysRevD.23.347.

[50] C. L. Bennett et al. NINE-YEAR WILKINSON MICROWAVE ANISOTROPY PROBE (WMAP) OBSERVATIONS: FINAL MAPS AND RESULTS. *The Astrophysical Journal Supplement Series*, 208(2):20, September 2013, doi:10.1088/0067-0049/208/2/20.

[51] G. Hinshaw et al. NINE-YEAR WILKINSON MICROWAVE ANISOTROPY PROBE (WMAP) OBSERVATIONS: COSMOLOGICAL PARAMETER RESULTS. *The Astrophysical Journal Supplement Series*, 208(2):19, September 2013, doi:10.1088/0067-0049/208/2/19.

[52] J. C. Kapteyn. First Attempt at a Theory of the Arrangement and Motion of the Sidereal System. *Astrophysical Journal*, 55:302, May 1922, doi:10.1086/142670.

[53] F. Zwicky. Die Rotverschiebung von extragalaktischen Nebeln. *Helvetica Physica Acta*, 6:110–127, January 1933.

[54] V. C. Rubin, J. Ford, W. K., and N. Thonnard. Extended rotation curves of high-luminosity spiral galaxies. IV. Systematic dynamical properties, Sa $\rightarrow$ Sc. *Astrophysical Journal*, 225:L107–L111, November 1978, doi:10.1086/182804.

[55] E. E. Richards et al. Baryonic distributions in the dark matter halo of NGC 5005. *Monthly Notices of the Royal Astronomical Society*, 449(4):3981–3996, April 2015, doi:10.1093/mnras/stv568.

[56] K. G. Begeman, A. H. Broeils, and R. H. Sanders. Extended rotation curves of spiral galaxies: dark haloes and modified dynamics. *Monthly Notices of the Royal Astronomical Society*, 249(3):523–537, April 1991, doi:10.1093/mnras/249.3.523.

[57] G. Bertone, D. Hooper, and J. Silk. Particle dark matter: evidence, candidates and constraints. *Physics Reports*, 405(5):279–390, January 2005, doi:10.1016/j.physrep.2004.08.031.

[58] K. Freese. Review of Observational Evidence for Dark Matter in the Universe and in upcoming searches for Dark Stars. *EAS Publications Series*, 36:113–126, May 2009, doi:10.1051/eas/0936016.

[59] D. Clowe, A. Gonzalez, and M. Markevitch. Weak-Lensing Mass Reconstruction of the Interacting Cluster 1E 0657-558: Direct Evidence for the Existence of Dark Matter. *The Astrophysical Journal*, 604(2):596–603, April 2004, doi:10.1086/381970.

[60] D. Clowe et al. A Direct Empirical Proof of the Existence of Dark Matter. *The Astrophysical Journal*, 648(2):L109–L113, August 2006, doi:10.1086/508162.

[61] X-ray: NASA/CXC/CfA/M.Markevitch et al.; Optical: NASA/STScI; Magellan/U.Arizona/D.Clowe et al.; Lensing Map: NASA/STScI; ESO WFI; Magellan/U.Arizona/D.Clowe et al. Visible-Light and X-Ray Composite Image of Galaxy Cluster 1E 0657-556, 2006. `http://hubblesite.org/newscenter/archive/releases/2006/39/image/a/`.

[62] W. Hu, N. Sugiyama, and J. Silk. The Physics of microwave background anisotropies. *Nature*, 386:37–43, 1997, doi:10.1038/386037a0.

[63] W. Hu and S. Dodelson. Cosmic Microwave Background Anisotropies. *Annual Review of Astronomy and Astrophysics*, 40(1):171–216, 2002, doi:10.1146/annurev.astro.40.060401.093926.

[64] G. F. Smoot et al. Structure in the COBE Differential Microwave Radiometer First-Year Maps. *Astrophysical Journal Letters*, 396:L1, September 1992, doi:10.1086/186504.

[65] N. Aghanim et al. Planck 2018 results - I. Overview and the cosmological legacy of Planck. *Astronomy&Astrophysics*, 641:A1, 2020, doi:10.1051/0004-6361/201833880.

[66] Y. Akrami et al. Planck 2018 results - X. Constraints on inflation. *Astronomy&Astrophysics*, 641:A10, 2020, doi:10.1051/0004-6361/201833887.

[67] R. H. Cyburt, B. D. Fields, and K. A. Olive. An update on the big bang nucleosynthesis prediction for ^{7}Li: the problem worsens. *Journal of Cosmology and Astroparticle Physics*, 2008(11):012, November 2008, doi:10.1088/1475-7516/2008/11/012.

[68] B. D. Fields. The Primordial Lithium Problem. *Annual Review of Nuclear and Particle Science*, 61(1):47–68, May 2011, doi:10.1146/annurev-nucl-102010-130445.

[69] G. Bertone and D. Hooper. History of dark matter. *Rev. Mod. Phys.*, 90:045002, October 2018, doi:10.1103/RevModPhys.90.045002.

[70] M. Milgrom. A modification of the Newtonian dynamics as a possible alternative to the hidden mass hypothesis. *Astrophysical Journal*, 270:365–370, July 1983, doi:10.1086/161130.

[71] J. D. Bekenstein. Relativistic gravitation theory for the modified newtonian dynamics paradigm. *Physical Review D*, 70:083509, October 2004, doi:10.1103/PhysRevD.70.083509.

[72] C. Skordis, D. F. Mota, P. G. Ferreira, and C. Bœhm. Large Scale Structure in Bekenstein's Theory of Relativistic Modified Newtonian Dynamics. *Physical Review Letters*, 96:011301, January 2006, doi:10.1103/PhysRevLett.96.011301.

[73] X.-d. Xu, B. Wang, and P. Zhang. Testing the tensor-vector-scalar theory with the latest cosmological observations. *Physical Review D*, 92:083505, October 2015, doi:10.1103/PhysRevD.92.083505.

[74] P. A. Zyla et al. Review of particle physics. *Progress of Theoretical and Experimental Physics*, 2020(8), August 2020, doi:10.1093/ptep/ptaa104.

[75] K. Freese. Status of dark matter in the universe. *International Journal of Modern Physics D*, 26(06):1730012, 2017, doi:10.1142/S0218271817300129.

[76] G. Bertone and T. M. P. Tait. A new era in the search for dark matter. *Nature*, 562(7725):51–56, 2018, doi:10.1038/s41586-018-0542-z.

[77] R. D. Peccei and H. R. Quinn. Constraints imposed by CP conservation in the presence of pseudoparticles. *Physical Review D*, 16:1791–1797, September 1977, doi:10.1103/PhysRevD.16.1791.

[78] C. Abel et al. Measurement of the permanent electric dipole moment of the neutron. *Physical Review Letters*, 124:081803, February 2020, doi:10.1103/PhysRevLett.124.081803.

[79] N. Du et al. Search for invisible axion dark matter with the axion dark matter experiment. *Physical Review Letters*, 120:151301, April 2018, doi:10.1103/PhysRevLett.120.151301.

[80] T. Braine et al. Extended search for the invisible axion with the axion dark matter experiment. *Physical Review Letters*, 124:101303, March 2020, doi:10.1103/PhysRevLett.124.101303.

[81] V. Anastassopoulos et al. New CAST Limit on the Axion-Photon Interaction. *Nature Physics*, 13:584–590, 2017, doi:10.1038/nphys4109.

[82] T. Dafni et al. Weighing the solar axion. *Physical Review D*, 99:035037, February 2019, doi:10.1103/PhysRevD.99.035037.

[83] G. Steigman and M. S. Turner. Cosmological constraints on the properties of weakly interacting massive particles. *Nuclear Physics B*, 253:375–386, 1985, doi:10.1016/0550-3213(85)90537-1.

[84] H. Nilles. Supersymmetry, supergravity and particle physics. *Physics Reports*, 110(1):1–162, 1984, doi:10.1016/0370-1573(84)90008-5.

[85] D. Hooper and S. Profumo. Dark matter and collider phenomenology of universal extra dimensions. *Physics Reports*, 453(2):29–115, 2007, doi:10.1016/j.physrep.2007.09.003.

[86] A. Boyarsky et al. Sterile neutrino Dark Matter. *Progress in Particle and Nuclear Physics*, 104:1–45, January 2019, doi:10.1016/j.ppnp.2018.07.004.

[87] S. Bird et al. Did LIGO Detect Dark Matter? *Physical Review Letters*, 116:201301, May 2016, doi:10.1103/PhysRevLett.116.201301.

[88] B. Carr, F. Kühnel, and M. Sandstad. Primordial black holes as dark matter. *Physical Review D*, 94:083504, October 2016, doi:10.1103/PhysRevD.94.083504.

[89] B. Carr and F. Kühnel. Primordial Black Holes as Dark Matter: Recent Developments. *Annual Review of Nuclear and Particle Science*, 70:1–40, August 2020, doi:10.1146/annurev-nucl-050520-125911.

[90] G. Aad et al. The ATLAS Experiment at the CERN Large Hadron Collider. *Journal of Instrumentation*, 3(08):S08003–S08003, August 2008, doi:10.1088/1748-0221/3/08/s08003.

[91] S. Chatrchyan et al. The CMS experiment at the CERN LHC. *Journal of Instrumentation*, 3(08):S08004–S08004, August 2008, doi:10.1088/1748-0221/3/08/s08004.

[92] A. Boveia and C. Doglioni. Dark Matter Searches at Colliders. *Annual Review of Nuclear and Particle Science*, 68(1):429–459, 2018, doi:10.1146/annurev-nucl-101917-021008.

[93] N. Trevisani. Collider Searches for Dark Matter (ATLAS + CMS). *Universe*, 4(11), 2018, doi:10.3390/universe4110131.

[94] K. N. Abazajian et al. Strong constraints on thermal relic dark matter from Fermi-LAT observations of the Galactic Center. *Physical Review D*, 102:043012, August 2020, doi:10.1103/PhysRevD.102.043012.

[95] C. Pérez de los Heros. Status, challenges and directions in indirect dark matter searches. *Symmetry*, 12(10), October 2020, doi:10.3390/sym12101648.

[96] V. Acciari et al. A search for dark matter in Triangulum II with the MAGIC telescopes. *Physics of the Dark Universe*, 28:100529, May 2020, doi:10.1016/j.dark.2020.100529.

[97] L. Rinchiuso, E. Moulin, C. Armand, and V. Poireau. Dark Matter search with H.E.S.S. towards ultra-faint dwarf nearby DES satellites of the Milky Way. *Proceedings of Science*, ICRC2019:542, 2020, doi:10.22323/1.358.0542.

[98] B. K. Cantlay and M. Wechakama. Constraints on dark matter annihilation with electron spectrum from VERITAS. *Journal of Physics: Conference Series*, 1380:012071, November 2019, doi:10.1088/1742-6596/1380/1/012071.

[99] D. Hooper and L. Goodenough. Dark matter annihilation in the Galactic Center as seen by the Fermi Gamma Ray Space Telescope. *Physics Letters B*, 697(5):412–428, March 2011, doi:10.1016/j.physletb.2011.02.029.

[100] A. Albert et al. SEARCHING FOR DARK MATTER ANNIHILATION IN RECENTLY DISCOVERED MILKY WAY SATELLITES WITHFERMI-LAT. *The Astrophysical Journal*, 834(2):110, January 2017, doi:10.3847/1538-4357/834/2/110.

[101] R. E. Keeley et al. What the Milky Way's dwarfs tell us about the Galactic Center extended gamma-ray excess. *Physical Review D*, 97:103007, May 2018, doi:10.1103/PhysRevD.97.103007.

[102] M. Actis et al. Design Concepts for the Cherenkov Telescope Array, An Advanced Facility for Ground-Based High-Energy Gamma-Ray Astronomy. *Experimental Astronomy*, 32:193–316, November 2011, doi:10.1007/s10686-011-9247-0.

[103] T. Hassan et al. Monte Carlo performance studies for the site selection of the Cherenkov Telescope Array. *Astroparticle Physics*, 93:76–85, 2017, doi:10.1016/j.astropartphys.2017.05.001.

[104] M. Aartsen et al. Search for neutrinos from decaying dark matter with IceCube. *The European Physical Journal C*, 78, October 2018, doi:10.1140/epjc/s10052-018-6273-3.

[105] A. Albert et al. Search for dark matter towards the Galactic Centre with 11 years of ANTARES data. *Physics Letters B*, 805:135439, 2020, doi:10.1016/j.physletb.2020.135439.

[106] K. Abe et al. Indirect search for dark matter from the Galactic Center and halo with the Super-Kamiokande detector. *Physical Review D*, 102:072002, October 2020, doi:10.1103/PhysRevD.102.072002.

[107] M. G. Aartsen et al. Observation of High-Energy Astrophysical Neutrinos in Three Years of IceCube Data. *Physical Review Letters*, 113:101101, September 2014, doi:10.1103/PhysRevLett.113.101101.

[108] C. Kopper. Observation of Astrophysical Neutrinos in Six Years of IceCube Data. *Proceedings of Science*, ICRC2017:981, 2017, doi:10.22323/1.301.0981.

[109] M. G. Aartsen et al. IceCube-Gen2: the window to the extreme Universe. *Journal of Physics G: Nuclear and Particle Physics*, 48(6):060501, April 2021, doi:10.1088/1361-6471/abbd48.

[110] S. Adrián-Martínez et al. Letter of intent for KM3NeT 2.0. *Journal of Physics G: Nuclear and Particle Physics*, 43(8):084001, June 2016, doi:10.1088/0954-3899/43/8/084001.

[111] K. Abe et al. Physics potentials with the second Hyper-Kamiokande detector in Korea. *Progress of Theoretical and Experimental Physics*, 2018(6), June 2018, doi:10.1093/ptep/pty044.

[112] O. Adriani et al. Ten years of PAMELA in space. *La Rivista del Nuovo Cimento*, 40(10):473–522, September 2017, doi:10.1393/ncr/i2017-10140-x.

[113] M. Aguilar et al. Towards Understanding the Origin of Cosmic-Ray Positrons. *Physical Review Letters*, 122:041102, January 2019, doi:10.1103/PhysRevLett.122.041102.

[114] J. Lewin and P. Smith. Review of mathematics, numerical factors, and corrections for dark matter experiments based on elastic nuclear recoil. *Astroparticle Physics*, 6(1):87–112, December 1996, doi:10.1016/S0927-6505(96)00047-3.

[115] L. Baudis. Direct dark matter detection: The next decade. *Physics of the Dark Universe*, 1(1):94–108, November 2012, doi:10.1016/j.dark.2012.10.006.

[116] M. Schumann. Direct detection of WIMP dark matter: concepts and status. *Journal of Physics G: Nuclear and Particle Physics*, 46(10):103003, August 2019, doi:10.1088/1361-6471/ab2ea5.

[117] R. H. Helm. Inelastic and Elastic Scattering of 187-Mev Electrons from Selected Even-Even Nuclei. *Physical Review*, 104:1466–1475, December 1956, doi:10.1103/PhysRev.104.1466.

[118] K. Freese, J. Frieman, and A. Gould. Signal modulation in cold-dark-matter detection. *Physical Review D*, 37:3388–3405, June 1988, doi:10.1103/PhysRevD.37.3388.

[119] C. Savage, G. Gelmini, P. Gondolo, and K. Freese. Compatibility of DAMA/LIBRA dark matter detection with other searches. *Journal of Cosmology and Astroparticle Physics*, 2009(04):010–010, April 2009, doi:10.1088/1475-7516/2009/04/010.

[120] G. Heusser. Low-Radioactivity Background Techniques. *Annual Review of Nuclear and Particle Science*, 45(1):543–590, December 1995, doi:10.1146/annurev.ns.45.120195.002551.

[121] S. Cebrián. The Role of Small Scale Experiments in the Direct Detection of Dark Matter. *Universe*, 7(4), March 2021, doi:10.3390/universe7040081.

[122] K. Fushimi et al. Application of a large-volume NaI scintillator to search for dark matter. *Physical Review C*, 47:R425–R428, February 1993, doi:10.1103/PhysRevC.47.R425.

[123] N. Spooner et al. The scintillation efficiency of sodium and iodine recoils in a NaI(Tl) detector for dark matter searches. *Physics Letters B*, 321(1):156–160, January 1994, doi:10.1016/0370-2693(94)90343-3.

[124] R. Bernabei et al. New limits on WIMP search with large-mass low-radioactivity NaI(Tl) set-up at Gran Sasso. *Physics Letters B*, 389(4):757–766, December 1996, doi:10.1016/S0370-2693(96)80020-7.

[125] G. Gerbier et al. Pulse shape discrimination and dark matter search with NaI(Tl) scintillator. *Astroparticle Physics*, 11(3):287–302, July 1999, doi:10.1016/S0927-6505(99)00004-3.

[126] J. I. Collar. Quenching and channeling of nuclear recoils in NaI(Tl): Implications for dark-matter searches. *Physical Review C*, 88:035806, September 2013, doi:10.1103/PhysRevC.88.035806.

[127] H. Joo et al. Quenching factor measurement for NaI(Tl) scintillation crystal. *Astroparticle Physics*, 108:50–56, 2019, doi:10.1016/j.astropartphys.2019.01.001.

[128] H. Chagani et al. Measurement of the quenching factor of Na recoils in NaI(Tl). *Journal of Instrumentation*, 3(06):P06003–P06003, June 2008, doi:10.1088/1748-0221/3/06/p06003.

[129] V. Tretyak. Semi-empirical calculation of quenching factors for ions in scintillators. *Astroparticle Physics*, 33(1):40–53, February 2010, doi:10.1016/j.astropartphys.2009.11.002.

[130] C. Cuesta. *ANAIS–0: Feasibility study for a 250 kg NaI(Tl) dark matter search experiment at the Canfranc Underground Laboratory.* PhD thesis, Universidad de Zaragoza, 2013. `https://zaguan.unizar.es/record/12520/files/TESIS-2013-086.pdf`.

[131] A. K. Drukier, K. Freese, and D. N. Spergel. Detecting cold dark-matter candidates. *Physical Review D*, 33:3495–3508, June 1986, doi:10.1103/PhysRevD.33.3495.

[132] D. N. Spergel. Motion of the Earth and the detection of weakly interacting massive particles. *Physical Review D*, 37:1353–1355, March 1988, doi:10.1103/PhysRevD.37.1353.

[133] C. J. Copi, J. Heo, and L. M. Krauss. Directional sensitivity, WIMP detection, and the galactic halo. *Physics Letters B*, 461(1):43–48, August 1999, doi:10.1016/S0370-2693(99)00830-8.

[134] T. Marrodán Undagoitia and L. Rauch. Dark matter direct-detection experiments. *Journal of Physics G: Nuclear and Particle Physics*, 43(1):013001, December 2015, doi:10.1088/0954-3899/43/1/013001.

[135] T. Saab and E. Figueroa-Feliciano. `https://supercdms.slac.stanford.edu/dark-matter-limit-plotter`.

[136] J. Barreto et al. Direct search for low mass dark matter particles with CCDs. *Physics Letters B*, 711(3):264–269, May 2012, doi:10.1016/j.physletb.2012.04.006.

[137] A. Aguilar-Arevalo et al. Constraints on Light Dark Matter Particles Interacting with Electrons from DAMIC at SNOLAB. *Physical Review Letters*, 123:181802, October 2019, doi:10.1103/PhysRevLett.123.181802.

[138] A. Aguilar-Arevalo et al. Results on Low-Mass Weakly Interacting Massive Particles from an 11 kg d Target Exposure of DAMIC at SNOLAB. *Physical Review Letters*, 125:241803, December 2020, doi:10.1103/PhysRevLett.125.241803.

[139] N. Castelló-Mor. DAMIC-M experiment: Thick, silicon CCDs to search for light dark matter. *Nuclear Instruments and Methods in Physics Research Section A: Accelerators, Spectrometers, Detectors and Associated Equipment*, 958:162933, April 2020, doi:10.1016/j.nima.2019.162933.

[140] H. Jiang et al. Limits on Light Weakly Interacting Massive Particles from the First 102.8 kg × day Data of the CDEX-10 Experiment. *Physical Review Letters*, 120:241301, June 2018, doi:10.1103/PhysRevLett.120.241301.

[141] H. Ma et al. Results of direct dark matter detection with CDEX experiment at CJPL. *Journal of Physics: Conference Series*, 1468:012070, February 2020, doi:10.1088/1742-6596/1468/1/012070.

[142] E. Armengaud et al. Performance of the EDELWEISS-III experiment for direct dark matter searches. *Journal of Instrumentation*, 12(08):P08010–P08010, August 2017, doi:10.1088/1748-0221/12/08/p08010.

[143] L. Hehn et al. Improved EDELWEISS-III sensitivity for low-mass WIMPs using a profile likelihood approach. *The European Physical Journal C*, 76, July 2016, doi:10.1140/epjc/s10052-016-4388-y.

[144] E. Armengaud et al. Searches for electron interactions induced by new physics in the EDELWEISS-III germanium bolometers. *Physical Review D*, 98:082004, October 2018, doi:10.1103/PhysRevD.98.082004.

[145] Q. Arnaud et al. First Germanium-Based Constraints on Sub-MeV Dark Matter with the EDELWEISS Experiment. *Physical Review Letters*, 125:141301, October 2020, doi:10.1103/PhysRevLett.125.141301.

[146] R. Agnese et al. Demonstration of Surface Electron Rejection with Interleaved Germanium Detectors for Dark Matter Searches. *Applied Physics Letters*, 103, May 2013, doi:10.1063/1.4826093.

[147] R. Agnese et al. Results from the Super Cryogenic Dark Matter Search Experiment at Soudan. *Physical Review Letters*, 120:061802, February 2018, doi:10.1103/PhysRevLett.120.061802.

[148] D. W. Amaral et al. Constraints on low-mass, relic dark matter candidates from a surface-operated SuperCDMS single-charge sensitive detector. *Physical Review D*, 102:091101, November 2020, doi:10.1103/PhysRevD.102.091101.

[149] R. Strauss et al. A prototype detector for the CRESST-III low-mass dark matter search. *Nuclear Instruments and Methods in Physics Research Section A: Accelerators, Spectrometers, Detectors and Associated Equipment*, 845:414–417, 2017, doi:10.1016/j.nima.2016.06.060.

[150] P.-A. Amaudruz et al. Design and construction of the DEAP-3600 dark matter detector. *Astroparticle Physics*, 108:1–23, March 2019, doi:10.1016/j.astropartphys.2018.09.006.

[151] R. Ajaj et al. Search for dark matter with a 231-day exposure of liquid argon using DEAP-3600 at SNOLAB. *Physical Review D*, 100:022004, July 2019, doi:10.1103/PhysRevD.100.022004.

[152] E. Aprile et al. The XENON1T dark matter experiment. *The European Physical Journal C*, 77(12):881, December 2017, doi:10.1140/epjc/s10052-017-5326-3.

[153] Q. Wang et al. Results of dark matter search using the full PandaX-II exposure. *Chinese Physics C*, 44(12):125001, November 2020, doi:10.1088/1674-1137/abb658.

[154] D. S. Akerib et al. Results from a Search for Dark Matter in the Complete LUX Exposure. *Physical Review Letters*, 118:021303, January 2017, doi:10.1103/PhysRevLett.118.021303.

[155] P. Agnes et al. Low-Mass Dark Matter Search with the DarkSide-50 Experiment. *Physical Review Letters*, 121:081307, August 2018, doi:10.1103/PhysRevLett.121.081307.

[156] E. Aprile et al. Projected WIMP sensitivity of the XENONnT dark matter experiment. *Journal of Cosmology and Astroparticle Physics*, 2020(11):031–031, November 2020, doi:10.1088/1475-7516/2020/11/031.

[157] H. Zhang et al. Dark matter direct search sensitivity of the PandaX-4T experiment. *Science China Physics, Mechanics & Astronomy*, 62:31011, March 2019, doi:10.1007/s11433-018-9259-0.

[158] D. S. Akerib et al. Projected WIMP sensitivity of the LUX-ZEPLIN dark matter experiment. *Phys. Rev. D*, 101:052002, March 2020, doi:10.1103/PhysRevD.101.052002.

[159] C. Aalseth et al. DarkSide-20k: A 20 tonne two-phase LAr TPC for direct dark matter detection at LNGS. *The European Physical Journal Plus*, 133, March 2018, doi:10.1140/epjp/i2018-11973-4.

[160] J. Aalbers et al. DARWIN: towards the ultimate dark matter detector. *Journal of Cosmology and Astroparticle Physics*, 2016(11):017–017, November 2016, doi:10.1088/1475-7516/2016/11/017.

[161] C. Amole et al. Dark matter search results from the complete exposure of the PICO-60 C_3F_8 bubble chamber. *Physical Review D*, 100:022001, July 2019, doi:10.1103/PhysRevD.100.022001.

[162] M. Bressler et al. A buffer-free concept bubble chamber for PICO dark matter searches. *Journal of Instrumentation*, 14(08):P08019–P08019, August 2019, doi:10.1088/1748-0221/14/08/p08019.

[163] G. Alner et al. The DRIFT-II dark matter detector: Design and commissioning. *Nuclear Instruments and Methods in Physics Research Section A: Accelerators, Spectrometers, Detectors and Associated Equipment*, 555(1):173–183, December 2005, doi:10.1016/j.nima.2005.09.011.

[164] J. Battat et al. Low threshold results and limits from the DRIFT directional dark matter detector. *Astroparticle Physics*, 91:65–74, May 2017, doi:10.1016/j.astropartphys.2017.03.007.

[165] J. Battat et al. Improved sensitivity of the DRIFT-IId directional dark matter experiment using machine learning, July 2021.

[166] S. E. Vahsen et al. CYGNUS: Feasibility of a nuclear recoil observatory with directional sensitivity to dark matter and neutrinos, 2020. arXiv:2008.12587.

[167] R. Bernabei and P. Belli. *Annual modulation signature with large mass highly radiopure NaI(Tl)*, pages 370–382. Cambridge University Press, Cambridge, 2010.

[168] F. Froborg and A. R. Duffy. Annual modulation in direct dark matter searches. *Journal of Physics G: Nuclear and Particle Physics*, 47(9):094002, July 2020, doi:10.1088/1361-6471/ab8e93.

[169] I. Coarasa Casas. Sensibilidad y perspectivas del experimento ANAIS. Master's thesis, Universidad de Zaragoza, 2016. `https://zaguan.unizar.es/record/61019/files/TAZ-TFM-2016-118.pdf`.

[170] R. Bernabei et al. The DAMA project: Achievements, implications and perspectives. *Progress in Particle and Nuclear Physics*, 114:103810, 2020, doi:10.1016/j.ppnp.2020.103810.

[171] R. Bernabei et al. Dark matter search. *La Rivista del Nuovo Cimento*, 26N1:1–73, 2003.

[172] Saint-Gobain Home Page. `https://www.saint-gobain.com/en`.

[173] R. Bernabei et al. No role for muons in the DAMA annual modulation results. *The European Physical Journal C*, 72:2064, 2012, doi:10.1140/epjc/s10052-012-2064-4.

[174] R. Bernabei et al. No role for neutrons, muons and solar neutrinos in the DAMA annual modulation results. *The European Physical Journal C*, 74(12):3196, 2014, doi:10.1140/epjc/s10052-014-3196-5.

[175] S. Baum, K. Freese, and C. Kelso. Dark matter implications of DAMA/LIBRA-phase2 results. *Physics Letters B*, 789:262–269, 2019, doi:10.1016/j.physletb.2018.12.036.

[176] G. Adhikari et al. An experiment to search for dark-matter interactions using sodium iodide detectors. *Nature*, 564:83–86, December 2018, doi:10.1038/s41586-018-0739-1.

[177] G. Adhikari et al. Search for a Dark Matter-Induced Annual Modulation Signal in NaI(Tl) with the COSINE–100 Experiment. *Physical Review Letters*, 123:031302, July 2019, doi:10.1103/PhysRevLett.123.031302.

[178] G. Adhikari et al. Lowering the energy threshold in COSINE–100 dark matter searches. *Astroparticle Physics*, 130:102581, 2021, doi:10.1016/j.astropartphys.2021.102581.

[179] K. Shin et al. A facility for mass production of ultra-pure NaI powder for the COSINE–200 experiment. *Journal of Instrumentation*, 15(07):C07031–C07031, July 2020, doi:10.1088/1748-0221/15/07/c07031.

[180] B. Park et al. Development of ultra-pure NaI(Tl) detectors for the COSINE–200 experiment. *The European Physical Journal C*, 80:814, September 2020, doi:10.1140/epjc/s10052-020-8386-8.

[181] M. Sarsa et al. Dark matter searches at the Canfranc tunnel. *Nuclear Physics B-Proceedings Supplements*, 35:154–158, 1994.

[182] M. Sarsa et al. Searching for annual modulations of WIMPs with NaI scintillators. *Physics Letters B*, 386(1):458–462, 1996.

[183] M. Sarsa et al. Results of a search for annual modulation of WIMP signals. *Physical Review D*, 56(4):1856, 1997.

[184] S. Cebrián. *Estudio del fondo radioactivo en experimentos subterráneos de búsqueda de sucesos poco probables: CUORE (Cryogenic underground Observatory for Rare Events) y ANAIS (Annual Modulation with NaI(Tl)).* PhD thesis, Universidad de Zaragoza, 2006.

[185] M. Martínez. *Diseño de un prototipo para un experimento de detección directa de materia oscura mediante modulación anual con centelleadores de ioduro de sodio.* PhD thesis, Universidad de Zaragoza, 2006.

[186] C. Cuesta et al. Analysis of the ^{40}K contamination in NaI(Tl) crystals from different providers in the frame of the ANAIS project. *International Journal of Modern Physics A*, 29(19):1443010, 2014, doi:10.1142/S0217751X14430106.

[187] R. Bernabei et al. The DAMA/LIBRA apparatus. *Nuclear Instruments and Methods in Physics Research Section A: Accelerators, Spectrometers, Detectors and Associated Equipment*, 592(3):297–315, 2008, doi:10.1016/j.nima.2008.04.082.

[188] Alpha Spectra Inc. Home Page. `http://www.alphaspectra.com/`.

[189] J. Amaré et al. Preliminary results of ANAIS–25. *Nuclear Instruments and Methods in Physics Research Section A: Accelerators, Spectrometers, Detectors and Associated Equipment*, 742:187–190, 2014, doi:https://doi.org/10.1016/j.nima.2013.09.019.

[190] J. Amaré et al. Background Model of NaI(Tl) Detectors for the ANAIS Dark Matter Project. DESY-PROC, pages 232–235, Hamburg, June 2015. 11th Patras Workshop on Axions, WIMPs and WISPs, Zaragoza (Spain), 22 June 2015 - 26 June 2015, Verlag Deutsches Elektronen-Synchrotron. doi:10.3204/DESY-PROC-2015-02/villar_patricia.

[191] W. Trzaska et al. Cosmic-ray muon flux at Canfranc Underground Laboratory. *The European Physical Journal C*, 79(721):1–5, August 2019, doi:10.1140/epjc/s10052-019-7239-9.

[192] M. Á. Oliván. *Design, scale-up and characterization of the data acquisition system for the ANAIS dark matter experiment.* PhD thesis, Universidad de

Zaragoza, 2015. https://zaguan.unizar.es/record/48118/files/TESIS-2016-078.pdf.

[193] W. Leo. *Techniques for Nuclear and Particle Physics Experiments: A How-to Approach*. Springer-Verlag, 1994.

[194] G. Knoll. *Radiation Detection and Measurement*. John Wiley & Sons, Inc., New York, 2000.

[195] M. Oliván et al. Light yield determination in large sodium iodide detectors applied in the search for dark matter. *Astroparticle Physics*, 93:86–95, 2017, doi:10.1016/j.astropartphys.2017.06.005.

[196] J. Amaré et al. Analysis of backgrounds for the ANAIS–112 dark matter experiment. *The European Physical Journal C*, 79(412), 2019, doi:10.1140/epjc/s10052-019-6911-4.

[197] G. Adhikari et al. Understanding NaI(Tl) crystal background for dark matter searches. *The European Physical Journal C*, 77(7):437, 2017, doi:10.1140/epjc/s10052-017-5011-6.

[198] P. Adhikari et al. Background model for the nai(tl) crystals in cosine–100. *The European Physical Journal C*, 78:490, 2018, doi:10.1140/epjc/s10052-018-5970-2.

[199] Hamamatsu Photonics Home Page. https://www.hamamatsu.com/eu/en/product/optical-sensors/pmt/about_pmts/index.html.

[200] R. Bernabei et al. Performances of the new high quantum efficiency PMTs in DAMA/LIBRA. *Journal of Instrumentation*, 7:P03009, 2012, doi:10.1088/1748-0221/7/03/P03009.

[201] K. Kim et al. Tests on NaI(Tl) crystals for WIMP search at the Yangyang Underground Laboratory. *Astroparticle Physics*, 62:249–257, 2015, doi:10.1016/j.astropartphys.2014.10.004.

[202] P. Villar. *Background evaluation of the ANAIS dark matter experiment in different configurations: towards a final design*. PhD thesis, Universidad de Zaragoza, 2016. https://zaguan.unizar.es/record/58561/files/TESIS-2017-007.pdf.

[203] J. Amaré et al. Annual modulation results from three-year exposure of ANAIS–112. *Physical Review D*, 103:102005, May 2021, doi:10.1103/PhysRevD.103.102005.

[204] C. Pobes. *Optimización de la respuesta de un sistema multidetector de cristales de centelleo para un experimento de materia oscura (ANAIS)*. PhD thesis, Universidad de Zaragoza, 2006.

[205] N. Agafonova et al. Measurement of the cosmic ray muon flux seasonal variation with the OPERA detector. *Journal of Cosmology and Astroparticle Physics*, 10:003, 2019, doi:10.1088/1475-7516/2019/10/003.

[206] J. Morales et al. The Canfranc Underground Laboratory. Present and Future. In *The Identification of Dark Matter*, pages 447–452. Proceedings of the Fifth International Workshop, Edinburgh, UK, 6-10 September 2004, World Scientific, May 2005. doi:10.1142/9789812701848_0067.

[207] C. Aalseth et al. IGEX ^{76}Ge neutrinoless double-beta decay experiment: Prospects for next generation experiments. *Physical Review D*, 65(9):092007, May 2002, doi:10.1103/PhysRevD.65.092007.

[208] Scionix Home Page. `https://scionix.nl/`.

[209] M. Menon et al. Muon intensities and angular distributions deep underground. *Proceedings of the Physical Society*, 90(3):649–656, March 1967, doi:10.1088/0370-1328/90/3/311.

[210] C. Stockel. A study of muons deep underground. I. Angular distribution and vertical intensity. *Journal of Physics A: General Physics*, 2(6):639–649, November 1969, doi:10.1088/0305-4470/2/6/004.

[211] M. Ambrosio et al. Seasonal variations in the underground muon intensity as seen by MACRO. *Astroparticle Physics*, 7(1):109–124, 1997, doi:10.1016/S0927-6505(97)00011-X.

[212] N. Y. Agafonova et al. Analysis of seasonal variations of the cosmic ray muon flux and neutrons produced by muons in the LVD detector. *Bulletin of the Russian Academy of Sciences: Physics*, 75(3):427–430, 2011, doi:10.3103/S1062873811030063.

[213] P. Desiati. Seasonal Variations of High Energy Cosmic Ray Muons Observed by the IceCube Observatory as a Probe of Kaon/Pion Ratio. In *Proceedings of the 32nd International Cosmic Ray Conference, ICRC 2011*, volume 1, pages 78–81, 2011. doi:10.7529/ICRC2011/V01/0662.

[214] G. Bellini et al. Cosmic-muon flux and annual modulation in Borexino at 3800 m water-equivalent depth. *Journal of Cosmology and Astroparticle Physics*, 2012(05):015, 2012, doi:10.1088/1475-7516/2012/05/015.

[215] P. Adamson et al. Observation of muon intensity variations by season with the MINOS near detector. *Physical Review D*, 90:012010, July 2014, doi:10.1103/PhysRevD.90.012010.

[216] F. Ronga. Seasonal variations of the rate of multiple-muons in the Gran Sasso underground laboratory. *EPJ Web of Conferences*, 136:05004, 2017, doi:10.1051/epjconf/201713605004.

[217] C. Vigorito et al. Underground flux of atmospheric muons and its variations with 25 years of data of the LVD experiment. *Proceedings of Science*, ICRC2017:291, 2018, doi:10.22323/1.301.0291.

[218] M. Agostini et al. Modulations of the cosmic muon signal in ten years of Borexino data. *Journal of Cosmology and Astroparticle Physics*, 02:046, 2019, doi:10.1088/1475-7516/2019/02/046.

[219] N. Agafonova. LVD status report: underground muon physics. *Journal of Physics: Conference Series*, 1690:012101, December 2020, doi:10.1088/1742-6596/1690/1/012101.

[220] H. Prihtiadi et al. Measurement of the cosmic muon annual and diurnal flux variation with the COSINE–100 detector. *Journal of Cosmology and Astroparticle Physics*, 02:013, February 2020, doi:10.1088/1475-7516/2021/02/013.

[221] I. Antcheva et al. ROOT – A C++ framework for petabyte data storage, statistical analysis and visualization. *Computer Physics Communications*, 180(12):2499–2512, 2009, doi:10.1016/j.cpc.2009.08.005. 40 YEARS OF CPC: A celebratory issue focused on quality software for high performance, grid and novel computing architectures.

[222] S. Cebrián et al. Background model for a NaI (Tl) detector devoted to dark matter searches. *Astroparticle Physics*, 37:60–69, 2012, doi:10.1016/j.astropartphys.2012.07.009.

[223] J. Amaré et al. Cosmogenic radionuclide production in NaI(Tl) crystals. *Journal of Cosmology and Astroparticle Physics*, 2015(02):046–046, February 2015, doi:10.1088/1475-7516/2015/02/046.

[224] J. Amaré et al. Assessment of backgrounds of the ANAIS experiment for dark matter direct detection. *The European Physical Journal C*, 76(8):429, 2016, doi:10.1140/epjc/s10052-016-4279-2.

[225] P. Villar et al. Study of the cosmogenic activation in NaI(Tl) crystals within the ANAIS experiment. *International Journal of Modern Physics A*, 33(09):1843006, 2018, doi:10.1142/S0217751X18430066.

[226] S. Cebrián et al. Performances and prospects of the "ROSEBUD" dark matter search experiment. *Astroparticle Physics*, 10(4):361–368, 1999, doi:10.1016/S0927-6505(98)00058-9.

[227] S. Agostinelli et al. GEANT4–a simulation toolkit. *Nuclear Instruments and Methods in Physics Research Section A: Accelerators, Spectrometers, Detectors and Associated Equipment*, 506:250–303, 2003, doi:10.1016/S0168-9002(03)01368-8.

[228] C. Cuesta et al. Bulk NaI(Tl) scintillation low energy events selection with the ANAIS–0 module. *The European Physical Journal C*, 74(11):3150, 2014, doi:10.1140/epjc/s10052-014-3150-6.

[229] C. Cuesta et al. Slow scintillation time constants in NaI(Tl) for different interacting particles. *Optical Materials*, 36(2):316–320, 2013, doi:10.1016/j.optmat.2013.09.015.

[230] J. Amaré et al. Study of scintillation in natural and synthetic quartz and methacrylate. *Optical Materials*, 36(8):1408–1417, 2014, doi:10.1016/j.optmat.2014.03.042.

[231] K. Kim et al. Limits on Interactions between Weakly Interacting Massive Particles and Nucleons Obtained with NaI(Tl) crystal Detectors. *Journal of High Energy Physics*, 03:194, March 2019, doi:10.1007/JHEP03(2019)194.

[232] D. Akimov et al. Observation of light emission from Hamamatsu R11410-20 photomultiplier tubes. *Nuclear Instruments and Methods in Physics Research Section A: Accelerators, Spectrometers, Detectors and Associated Equipment*, 794:1–2, 2015, doi:10.1016/j.nima.2015.04.066.

[233] S. Li et al. Performance of photosensors in the PandaX-I experiment. *Journal of Instrumentation*, 11(02):T02005–T02005, February 2016, doi:10.1088/1748-0221/11/02/t02005.

[234] W. T. Eadie et al. *Statistical methods in experimental physics*. North-Holland, Amsterdam, 1971.

[235] G. Cowan. *Statistical Data Analysis*. Oxford University Press, New York, 1998.

[236] R. Bernabei et al. Searching for wimps by the annual modulation signature. *Physics Letters B*, 424(1):195–201, 1998, doi:10.1016/S0370-2693(98)00172-5.

[237] R. Bernabei et al. On a further search for a yearly modulation of the rate in particle dark matter direct search. *Physics Letters B*, 450:448–455, 1999, doi:10.1016/S0370-2693(99)00091-X.

[238] Y. Ramachers, M. Hirsch, and H. Klapdor-Kleingrothaus. Limitations of modulation analysis for dark matter direct detection experiments. *The European Physical Journal A*, 3(1):93–98, 1998, doi:10.1007/s100500050151.

[239] M. Kendall and A. Stuart. *The advanced theory of statistics*. Hafner Publishing Company, New York, 1961.

[240] S. Cebrián et al. Sensitivity plots for WIMP direct detection using the annual modulation signature. *Astroparticle Physics*, 14(4):339–350, 2001, doi:10.1016/S0927-6505(00)00124-9.

[241] J. Amaré et al. First results on dark matter annual modulation from the ANAIS–112 experiment. *Phys. Rev. Lett.*, 123:031301, July 2019, doi:10.1103/PhysRevLett.123.031301.

[242] J. Amaré et al. ANAIS–112 status: two years results on annual modulation. *Journal of Physics: Conference Series*, 1468:012014, February 2020, doi:10.1088/1742-6596/1468/1/012014.

[243] Laboratoire National Henri Becquerel. `http://www.lnhb.fr/nuclear-data/nuclear-data-table/`.

[244] D. Buttazzo, P. Panci, N. Rossi, and A. Strumia. Annual modulations from secular variations: relaxing DAMA? *Journal of High Energy Physics*, 2020:1–21, April 2020, doi:10.1007/JHEP04(2020)137.

[245] A. Messina, M. Nardecchia, and S. Piacentini. Annual modulations from secular variations: not relaxing DAMA? *Journal of Cosmology and Astroparticle Physics*, 2020(04):037–037, April 2020, doi:10.1088/1475-7516/2020/04/037.

[246] M. J. Box. Bias in Nonlinear Estimation. *Journal of the Royal Statistical Society. Series B (Methodological)*, 33(2):171–201, 1971.

[247] F. Corrêa Alegria. Bias of amplitude estimation using three-parameter sine fitting in the presence of additive noise. *Measurement*, 42(5):748–756, 2009, doi:10.1016/j.measurement.2008.12.006.

[248] J. Liu, S. Lipschutz, and M. Spiegel. *Schaum's Outline of Mathematical Handbook of Formulas and Tables*. McGraw-Hill, US, 4th edition, 2012.

[249] L. Breiman, J. Friedman, R. Olshen, and C. Stone. *Classification and Regression Trees*. Wadsworth, Stamford, 1984.

[250] Y. Freund and R. E. Schapire. Experiments with a new boosting algorithm. In *Proceedings of the Thirteenth International Conference on International Conference on Machine Learning*, ICML'96, pages 148–156, San Francisco, CA, USA, 1996. Morgan Kaufmann Publishers Inc. doi:10.5555/3091696.

[251] B. P. Roe et al. Boosted decision trees as an alternative to artificial neural networks for particle identification. *Nuclear Instruments and Methods in Physics Research Section A: Accelerators, Spectrometers, Detectors and Associated Equipment*, 543(2):577–584, 2005, doi:10.1016/j.nima.2004.12.018.

[252] H.-J. Yang, B. P. Roe, and J. Zhu. Studies of boosted decision trees for MiniBooNE particle identification. *Nuclear Instruments and Methods in Physics Research Section A: Accelerators, Spectrometers, Detectors and Associated Equipment*, 555(1):370–385, 2005, doi:10.1016/j.nima.2005.09.022.

[253] Y. Coadou. Decision trees. *The European Physical Journal Conferences*, 4(02003), 2010, doi:10.1051/epjconf/20100402003.

[254] A. Hocker. TMVA – Toolkit for Multivariate Data Analysis. 2009. arXiv:physics/0703039.